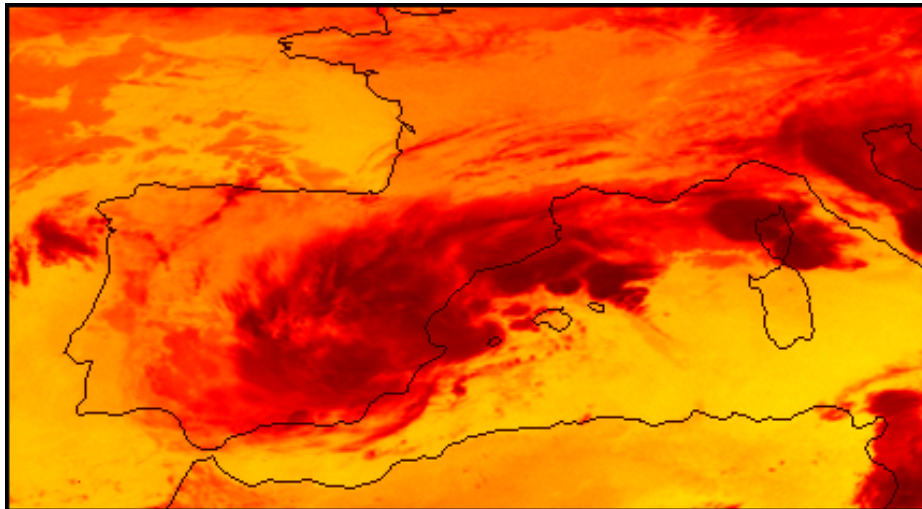




UNIVERSITAT DE LES ILLES BALEARS
DEPARTAMENT DE FÍSICA

*Numerical Simulation of Mesoscale
Processes in the Western Mediterranean:
Environmental Impact and
Natural Hazards*



*Memòria presentada per **Romualdo Romero March**
per optar al Grau de Doctor en Ciències Físiques per la
Universitat de les Illes Balears.*



UNIVERSITAT DE LES ILLES BALEARS
DEPARTAMENT DE FÍSICA

*Numerical Simulation of Mesoscale
Processes in the Western Mediterranean:
Environmental Impact and
Natural Hazards*

*Memòria presentada per **Romualdo Romero March**
per optar al Grau de Doctor en Ciències Físiques per la
Universitat de les Illes Balears.*

*Amb el vist i plau del director de la tesi, **Dr. Climent
Ramis Noguera**, professor titular de la Universitat de
les Illes Balears.*

Climent Ramis Noguera, professor titular de la Universitat de les Illes Balears,

CERTIFICA

Que la present memòria, titulada “NUMERICAL SIMULATION OF MESOSCALE PROCESSES IN THE WESTERN MEDITERRANEAN: ENVIRONMENTAL IMPACT AND NATURAL HAZARDS”, ha estat realitzada per Romualdo Romero March sota la seva direcció al Departament de Física, i que conclueix la Tesi que presenta per optar al Grau de Doctor en Ciències Físiques.

I per que així consti, signa la present a Palma de Mallorca el 2 de Juny de 1998.

Climent Ramis Noguera

A Isabel, a mis padres y hermanos

AGRADECIMIENTOS

El presente trabajo ha sido realizado bajo la dirección del Dr. Climent Ramis, del Departamento de Física de la UIB. Gracias a la confianza depositada en mí, he podido canalizar mi pasión por la Meteorología, habiéndome hecho partícipe desde el fin de Licenciatura de la activa investigación que se desarrolla en el seno del Grupo de Meteorología. Espero, con toda sinceridad, compartir con él durante muchos años más sus conocimientos y labor científica sobre Meteorología Mediterránea.

Quiero extender mi gratitud al resto de componentes y colaboradores científicos del Grupo de Meteorología. En primer lugar, al Prof. Sergio Alonso, por su gran experiencia y constante apoyo. En segundo lugar, a Víctor Homar, que empieza con gran fuerza y cuyo soporte informático siempre le agradeceré. En tercer lugar, a distintos miembros del Centro Meteorológico de Baleares (José Antonio Guijarro, Ana Genovés, Miguel Gayá, Elisa Tudurí), con el deseo de que nuestro trabajo en común se mantenga en el futuro. Al Dr. Jaume Vadell, del Departamento de Biología Ambiental de la UIB, por su ayuda en la clasificación de tipos de suelo para la simulación de la brisa en Mallorca. Y también a Damià Martín y Joan Rosselló, con quienes he compartido agradables momentos. Les debo a todos ellos el magnífico ambiente de trabajo y la constructiva interacción que he tenido el lujo de experimentar.

Agradezco también la dedicación y ayuda en proyectos conjuntos prestada por otros investigadores extranjeros: Dr. Everitt C. Nickerson (NOAA/FSL, Boulder, CO, USA), Drs. Charles A. Doswell III y David J. Stensrud (NOAA/ERL National Severe Storms Laboratory, Norman, OK, USA), Dr. Andrea Buzzi (FISBAT/CNR, Bologna, Italia), Dr. Graham Sumner (Department of Geography, University of Wales, Lampeter, Gales), Dr. Xuhui Cai (University of Peking, China). Nuestra estrecha colaboración ha sido desde luego fructífera para mi formación.

Por supuesto, agradezco a los miembros del Departamento de Física de la UIB, y en especial a los becarios de la Agencia EFE, las grandes facilidades y excelente trato que me han brindado desde un principio.

Por último, quiero hacer constar mi gratitud al Instituto Nacional de Meteorología, por el suministro de los datos meteorológicos tan esenciales para la realización del presente estudio, al Laboratorio de Teledetección de la Universidad de Valladolid, por la cesión de imágenes de satélite, y al Ministerio de Educación y Cultura, por la concesión de una beca de Formación de Personal Investigador que me ha permitido desarrollar parte de este trabajo.

SUMMARY

The meteorological conditions during the summer over the western Mediterranean are normally very favourable for the development of breeze circulation. Over the island of Mallorca, the sea breeze develops often from April to October and almost every day during July and August. There is special interest in studying the environmental impact during the frequent breeze episodes, since the air pollutants released over the coast, where the main urban and industrial centres of the island are located, are easily dragged inland by the current.

On the other hand, the closed characteristic of the Mediterranean sea and the high insolation received during the summer lead to high sea surface temperatures during summer and autumn. This aspect ensures strong water vapour availability in the Mediterranean environment and during that period the Mediterranean air masses present frequently convective instability. Under favorable synoptic conditions, that instability is released in the form of Mesoscale Convective Systems (Riosalido 1990) triggered by the coastal terrain features. Several episodes of devastating rainfalls occur every year in coastal regions of Spain, France and Italy, especially during the autumn, causing many casualties and material losses. Three of such events, referred to as Catalonia (12 November 1988), Piedmont (5 November 1994) and Tarragona (9 and 10 October 1994) events, were selected as case studies.

The general motivation of this research is the development of new understanding about the aforementioned environmental problems. In first place, we apply a mesoscale numerical model (the SALSA model; Nickerson et al. 1986), to study the transport and diffusion during the breeze of non-reactive sulphur dioxide emitted from a power plant located in the north bay of Mallorca, paying special attention to the physical mechanisms responsible for the ground-level concentration. The study is extended to a hypothetical scenario to consider a similar power plant on the south coast. In second place, as a contribution to the pluviometric characterization of Mediterranean Spain, we find (using principal components analysis and cluster analysis) the main spatial patterns controlling significant and torrential daily rainfalls in the region. In the third part of the work, we study the Catalonia, Piedmont and Tarragona heavy precipitation events, with a special emphasis on the spatial distribution of rainfall produced by the SALSA simulations. We analyze the feasibility of mesoscale numerical simulations for this kind of event in the western Mediterranean area, the roles exerted by the orography and evaporation from the sea by means of the factor separation technique of Stein and Alpert (1993), and the performance of two cumulus convection parameterizations (Emanuel 1991; Kain and Fritsch 1990).

The air pollution study for Mallorca under breeze conditions reveals that the convergence line along the centre of the island limits the plume expansion toward the south and deflects its transport toward the Serra de Tramuntana (the major wild area of the island), which acts to block the pollutant. The simulation reveals that, during all the diurnal cycle, the region of ground-level concentration higher than $5 \mu\text{g}/\text{m}^3$ is small. When an identical sulphur dioxide source is added on the south coast, the results show that there is no interaction at low levels between the pollutants from both plants, and that the main urban sites located in the south bay of the island remain unaffected.

Again, the convergence zones intercept the transport of the new plume towards the north, but in this case the plume can progress much further inland and this progression continues during the night after the decay of the sea breeze. Vertical diffusion proves to be the main factor in the ground-level concentration intensity during the day. However, after the decay of the breeze, fumigation to ground stops and the downward air motion related to a slight land breeze becomes the process most responsible for the ground-level concentration at the beginning of the next cycle. In this sense, the impact of the new power plant seems to be more important, since practically the entire eastern part of the island is affected by the pollutant sinking.

The derived daily rainfall patterns for Mediterranean Spain confirm that the extent of region and the exposure-sheltering systems induced by the complex topography are sufficiently important as to produce a clear regionalization of the rainfalls. It is interesting to note that the spatial patterns obtained for both significant and torrential rainfalls are basically equivalent. Distinct seasonal distributions have been observed, though. For rainfalls in general, the western Andalucía patterns show a clear preference for the winter months, followed almost indistinctly by spring and autumn, and are infrequent in summer, whereas for the torrential limit, winter and autumn are similarly important and the spring season becomes unimportant. In regard to the eastern patterns, for the general case they tend to be similarly frequent in spring and autumn, showing additional peak values in winter the Balearic and southern Valencia patterns and in summer the northern Valencia and Catalan patterns, whereas for torrential events, all of them have a clear predilection for the autumn season.

The results obtained for the heavy precipitation cases show that mesoscale models, with appropriate parametrizations for convection, can be used successfully to study and forecast the heavy rainfalls of the western Mediterranean area. The SALSA model gave results that approximated very well the observed spatial distribution of precipitation over land. However, the forecast of amount of precipitation for the Catalonia and Tarragona events was not so good because the model underestimated the rainfall. In contrast, the quantitative forecast in the Piedmont region was excellent due to the dominant contribution of the large-scale precipitation in that case. The effect of the orography was decisive in the spatial structure of precipitation over land for two of the events. For the Catalonia event, the orography was responsible for localizing the precipitation within the coastal zone. For the Piedmont event, the substantial upslope component provided by the Alps and surrounding mountains was correctly forecast by the model, explaining the good precipitation forecast. However, the most decisive factor for the Tarragona event was the synergism orography/evaporation, explaining the coastal maxima. The redistribution of the surface pressure and temperature fields induced by the topography (notably a shallow low and warm air tongue in the lee of the Atlas over the Mediterranean, and the blocking action of the Pyrenees) played also an important role for Catalonia and Tarragona events. Finally, it is shown that the inclusion of parameterized convection has beneficial effects on the forecast fields. In principle, the Kain-Fritsch scheme performed better than the Emanuel scheme. In particular, the former seems to be more sensitive to the presence of the coastal topography, focusing convection on that area in agreement with observations.

CONTENTS

CHAPTER 1. INTRODUCTION	1
1.1 General aspects	1
1.2 Sea breeze in Mallorca	2
1.3 Heavy precipitations in the western Mediterranean region	5
1.4 Objectives	13
CHAPTER 2. MODEL DESCRIPTION	16
2.1 Dynamical equations	17
2.2 Thermodynamical equations	18
2.3 Microphysical equations	19
2.4 Diffusion terms and TKE equation	24
2.5 Surface submodel	26
2.6 Radiation parameterization	31
2.7 Boundary conditions	32
2.8 Numerical aspects	33
CHAPTER 3. TRANSPORT AND DIFFUSION OF COASTAL POLLUTANTS DURING THE BREEZE CYCLE IN MALLORCA	35
3.1 Initialization and sulphur dioxide sources	36
3.1.1 The atmosphere	36
3.1.2 The surface	37
3.1.3 Sulphur dioxide sources	38
3.2 Meteorological aspects	38
3.2.1 Development and structure of the sea breeze	38
3.2.2 Verification of results	44
3.2.3 Influence of the orography and soil dryness	45
3.3 Concentration of sulphur dioxide	51
3.3.1 Ground-level concentration	51
3.3.2 Vertical cross sections	55
3.3.3 Comparison against sampler data	57
3.3.4 Impact of dry deposition and second cycle	57
3.4 Conclusions	60

CHAPTER 4. DAILY RAINFALL PATTERNS IN THE SPANISH MEDITERRANEAN AREA	62
4.1 Data base construction	62
4.2 Methodology	64
4.3 Emergent patterns and discussion	66
4.3.1 Significant days	66
4.3.2 Torrential days	72
4.4 Conclusions	75
 CHAPTER 5. CATALONIA AND PIEDMONT HEAVY PRECIPITATION EVENTS	 78
5.1 Model developments	79
5.1.1 Surface submodel	79
5.1.2 Cumulus convection parameterizations	79
5.1.3 Initialization and boundary conditions	82
5.2 Catalonia event	83
5.2.1 Synoptic overview	83
5.2.2 Description of the experiments	86
5.2.3 Results of the full experiment	88
5.2.4 Effects of the orography and evaporation from the sea	92
5.3 Piedmont event	96
5.3.1 Synoptic overview	96
5.3.2 Description of the experiments	100
5.3.3 Results of the full experiment	101
5.3.4 Effects of the orography and evaporation from the sea	103
5.3.5 Effects of cumulus convection parameterization	106
5.4 Conclusions	111

CHAPTER 6. TARRAGONA HEAVY PRECIPITATION EVENT	116
6.1 Synoptic overview	116
6.2 Diagnostic study	121
6.2.1 Synoptic diagnosis	121
6.2.2 Subsynoptic study	127
6.3 Description of the experiments	130
6.4 Results for 9 October	131
6.5 Results for 10 October	140
6.6 Conclusions	142
CHAPTER 7. CONCLUSIONS AND PERSPECTIVES	147
APPENDIX	151
REFERENCES	153

Chapter 1

INTRODUCTION

1.1 General aspects

The atmosphere manifests a wide range of motion scales, i.e, many processes with different characteristic wavelengths and periods. The classical division of that spectra, which extends from ultra-long waves of climatological scale to little eddies produced by roughness in the scale of centimetres and fractions of second, is given by the classification of macro, meso and micro-scales. The macroscale is basically quasi-geostrophic and hydrostatic. The mesoscale is non-geostrophic and hydrostatic, and the microscale is non-geostrophic, non-hydrostatic and turbulent. Spectral analysis of many meteorological observations suggest a minimum of energy density for the mesoscale, whereas both microscale and macroscale represent a maxim (Atkinson 1981). Nevertheless, mesoscale circulations are very important as a vital link in the atmospheric energy cascade from very large to very small scales (Robinson 1967).

Mesoscale can be descriptively defined to include the motion systems that have horizontal scales in the range of about 10-1000 km, that is, smaller than the conventional rawinsonde network, but significantly larger than individual cumulus clouds. It includes circulations ranging from thunderstorms and internal gravity waves at the small end of the scale to fronts and hurricanes at the large end. Very importantly, mesoscale circulations become very relevant to human lives virtually anywhere in the world. Most severe weather is associated with mesoscale motion systems, and air pollution is largely influenced by mesoscale wind systems such as the breeze circulation. Thus, understanding of the mesoscale phenomena is of both scientific and practical importance. Theory, experimental design and observational systems have all contributed to improve that understanding. With the advent of efficient computational capabilities during the last decades, mesoscale numerical models have been also applied massively, becoming essential in the great development experienced by mesoscale meteorology.

Within the operational context, successful forecast of mesoscale meteorological processes and phenomena is a permanent challenge to meteorologists. Any effort directed to the identification and study of the physical mechanisms controlling the development of hazardous phenomena, such as flash floods, has the potential to improve forecasts and

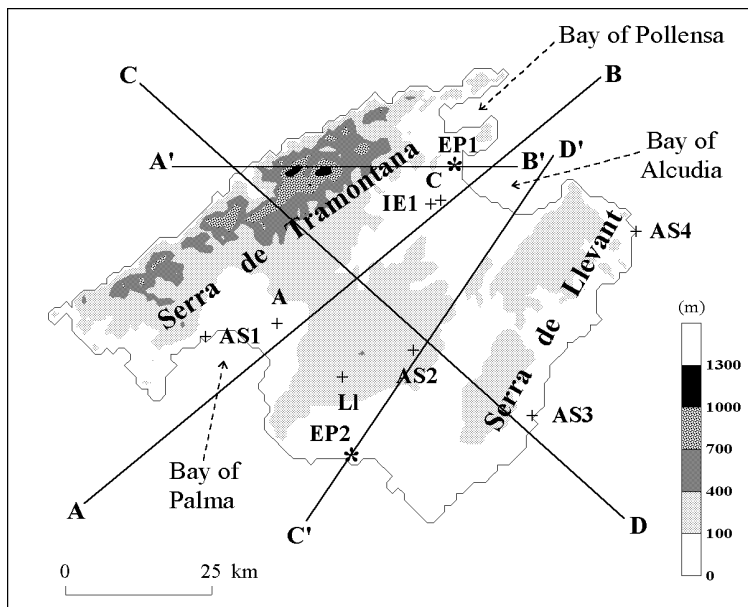


Figure 1.1: The island of Mallorca. Orography and the sites referred to in the text are indicated. Symbolized with +, ASn represent the location of the automatic weather stations, A represents the airport observatory, C the climatological station and Ll the town of Lluçmajor. Symbolized with *, EP1 and EP2 represent the electric power plants, whereas IE1 is the pollutant concentration measurement site. AB, CD, A'B', and C'D' indicate the cross-sections analysed in the text.

warnings to the public. On the other hand, numerical models have been widely used for ambient air quality studies. Since they contain realistic mathematical representations of decisive physical and chemical processes that operate in the atmosphere, such as transport over complex terrain, turbulence, stability-dependent diffusion or transformations by chemical reactions, they can be a practical tool for determining the impact of extant or hypothetical pollutant sources.

In this work, we have considered two mesoscale processes that are particularly relevant in our area: the sea breeze in the island of Mallorca and its impact on the air pollution; and for a larger spatial context, the problem of heavy precipitations in the western Mediterranean region.

1.2 Sea breeze in Mallorca

The island of Mallorca is located in the centre of the Western Mediterranean (between 39° and 40° N and 2.5° and 3.5° E; Figures 1.5 and 1.6). It measures approximately $100 \times 80 \text{ km}^2$ and possesses three major relief units: the high relief of the Serra de Tramontana in the west and northwest, with the highest point of 1440 m at Puig Major; a central lowland plateau; and the eastern uplands of the Serra de Llevant, reaching up to 500 m above sea level. Two big bays are situated in the northeast and the southwest (see Figure 1.1). The coast is smooth except in the northwest where there are sharp cliffs. A long beach is found along the south coast of the island.

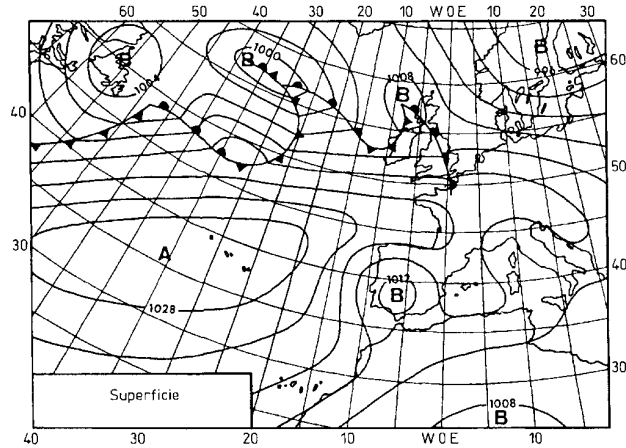


Figure 1.2: Typical synoptic situation during summer in central and western Europe. A and B represent high and low pressure, respectively (after Font 1983).

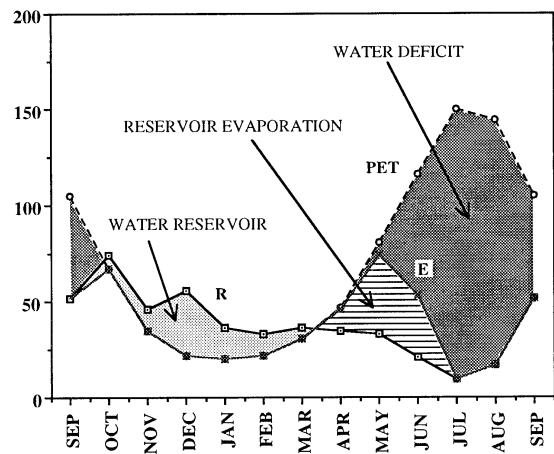


Figure 1.3: Thornthwaite climatologic hydric balance in Lluçmajor (see Figure 1.1 for location). R=rainfall, E=evaporation, PET=potential evapotranspiration.

The meteorological conditions during the summer over the Western Mediterranean are normally very favourable for the development of breeze circulation. In fact, the synoptic scale over this area is dominated by the Azores anticyclone which even extends its influence to central Europe. As a consequence of the thermal low-pressure developed over the Iberian peninsula, the anticyclonic circulation, and therefore the stability, become reinforced over the Western Mediterranean (Figure 1.2) favouring sunshine and fair weather.

Another favourable condition to produce thermal differential heating is that the total heat flux from the surface over land results displaced toward the sensible heat in detriment of the latent heat. In fact, most of the island of Mallorca is very dry during summer and soil water deficit is present after the beginning of June. As an example, Figure 1.3 represents the Thornthwaite hydric balance in Lluçmajor, a town on the south of the island (see Figure 1.1), and shows that the water deficit exceeds 140 mm in July.

These climatological features result in the development of the sea breeze in Mallorca,

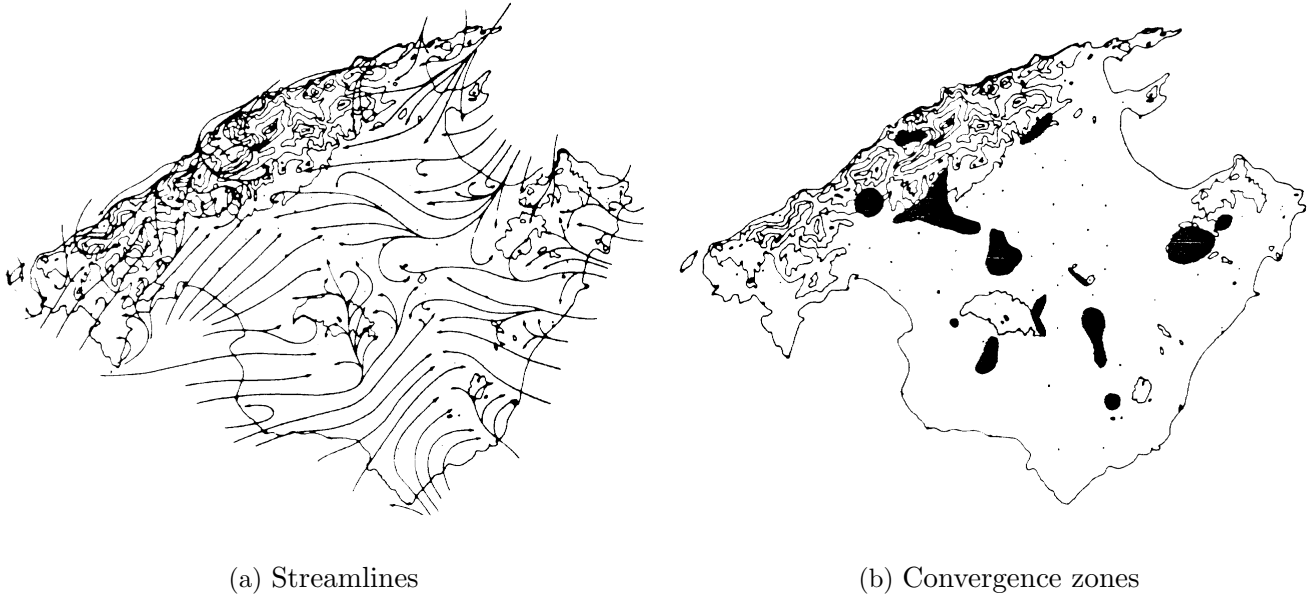


Figure 1.4: (a) Streamlines of the mature sea breeze in Mallorca, and (b) Convergence zones. (after Jansà and Jaume 1946; reproduced by permission of Rev. de Geofísica).

often from April to October and almost every day during July and August. In fact, at the airport, close to the Bay of Palma (see Figure 1.1), the frequency of the apparition of the sea breeze at 1200 UTC is 80% of the days in July and 76% in August. In spite of this high frequency, there are only a few studies about it: Jansà and Jaume (1946) published a paper showing some details from an inquiry made among farmers and fishermen. Ramis and Alonso (1988) showed a satellite observation of the clouds formed by the circulation and Ramis et al. (1990) presented a numerical simulation using a very simple one-level model.

Figure 1.4, from Jansà and Jaume (1946), shows the main features of the sea breeze in its mature state. The main structure is the convergence line, located at the centre of the island, and formed by the flux from the two bays. Other convergence zones can be identified, specially in the northeast and the west. On the northwest side of the island the mountain range blocks the current. This scheme also shows that the eastern slope of that mountain range could participate in the final structure of the full developed circulation as a consequence of the slope winds generated in the morning.

Of course, there is special interest in studying the environmental impact during the frequent breeze episodes, since the air pollutants released over the coast, where the main urban and industrial centres are located, are easily dragged inland by the current.

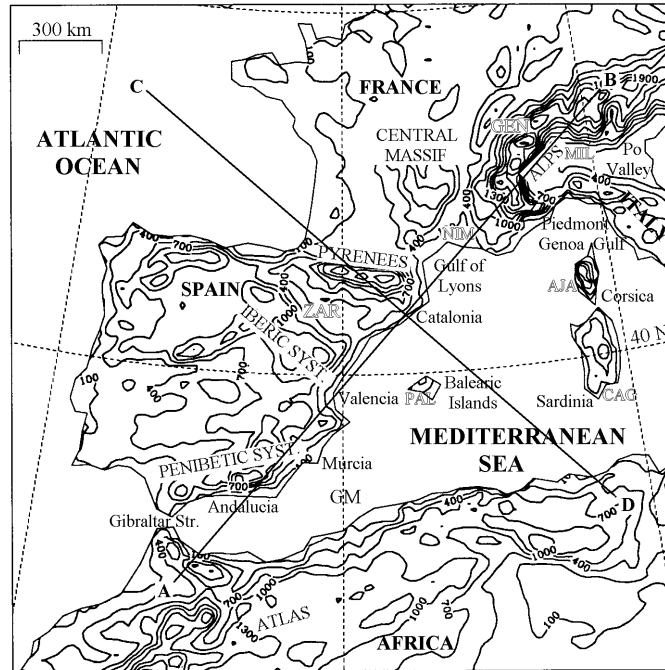


Figure 1.5: The western Mediterranean region and its smoothed orography (contour interval is 300 m starting at 100 m). The sites mentioned in the text are indicated. AB and CD indicate the cross-sections analysed in chapter 5.

1.3 Heavy precipitations in the western Mediterranean region

The western Mediterranean region is defined as the portion of the Mediterranean Sea enclosed by Spain, France, Corsica, Sardinia and north Africa, and the surrounding lands (Meteorol. Office 1962). That part of the Mediterranean Sea is surrounded by important mountain ranges with notable foothills reaching the coast line. Figure 1.5 shows a smoothed orography of the region. The most relevant and known ranges are the Atlas mountains in north Africa, Penibetic and Iberic Systems in Spain, Pyrenees between Spain and France, Central Massif in France, and Alps between France and Italy. Even the islands, regardless of their small size, emerge abruptly from the sea (Balearic Islands, Corsica, Sardinia, Figure 1.5). That topography configures the western Mediterranean as a closed basin isolated from other regions except through the valleys and narrow straits; for example the Gulf of Lyons area, where Atlantic flows can be channelled, or the Gibraltar Strait, that opens the Mediterranean Sea toward the Atlantic Ocean (Figure 1.5). Topographic variability is specially accentuated in the Mediterranean subdomain composed by the Spanish Mediterranean regions (Catalonia, Valencia, Murcia, Andalusía and Balearic Islands, see Figure 1.5). Figure 1.6 shows that area and the names of some relevant geographical units. The region measures approximately 1000 km along N-S and E-W directions. In some areas of the Pyrenees and Penibetic System, not too far from the sea, terrain height exceeds 3000 m.

Of course, the complex topography of the western Mediterranean becomes decisive for

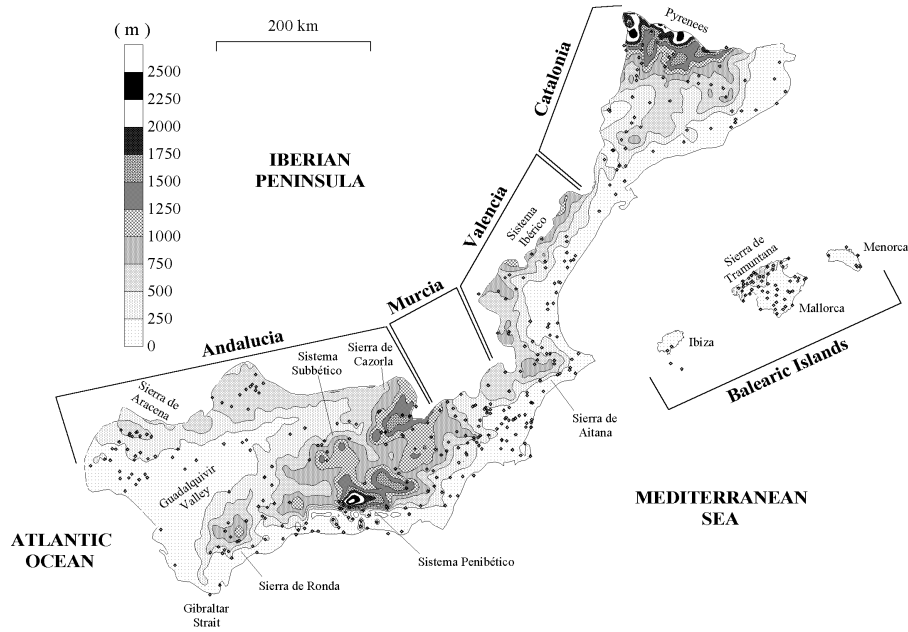
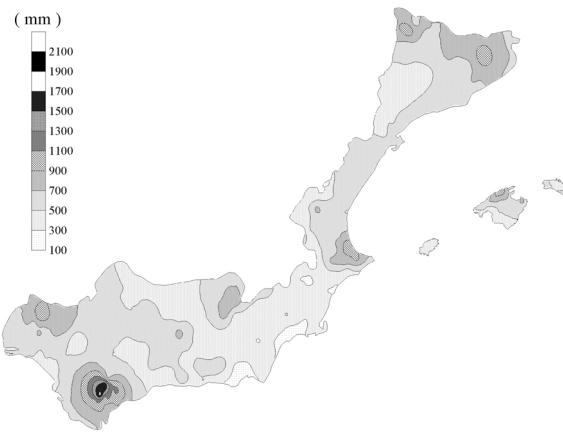


Figure 1.6: The Spanish Mediterranean area, formed by the administrative regions: Catalonia, Valencia, Murcia, Andalucía, and Balearic Islands. (see Figure 1.5). It includes a smoothed version of its orography, the position of the 410 rain gauge stations of the daily rainfall data base, and some geographical references mentioned in the text. The two stations adjacent to Ibiza belong to the small island of Formentera, which is not represented.

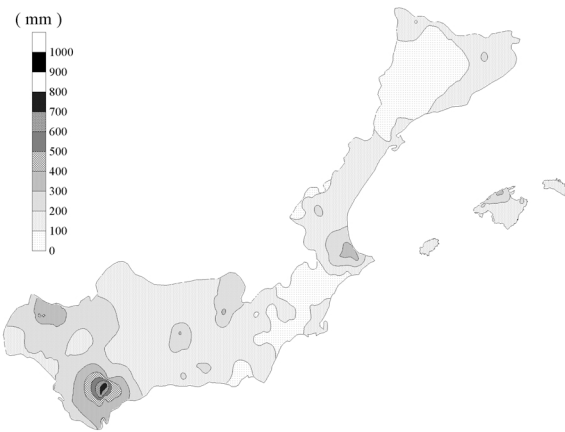
the pluviometry of the region. At the local scale, it assists the development of clouds at fixed zones or to enhance precipitation from preexisting cloud systems, leading to accentuated rainfall differences between uplands and lowlands, or between slopes with different exposures to the maritime winds. At larger scales, it acts to transform the atmospheric disturbances that approach from the Atlantic, frequently generating secondary cyclones over the Mediterranean, mainly in the lee of the Atlas, Pyrenees and Alps (Reiter 1975). In fact, the western Mediterranean is the world's region with highest density of cyclogenesis (Petterssen 1956). Synoptic and mesoscale flows can be generated or redirected, focusing rainfall in favorably exposed areas and suppressing it in other more sheltered areas. Observe the large spatial contrasts of mean precipitation registered in Mediterranean Spain (Figure 1.7a).

The latitude of the region (between 36° and 44° N), imposes extreme contrasts between warm and cold seasons. During the warm season, the region is persistently affected by the Azores anticyclone (Font 1983) and the weather is hot and very dry, although mid-afternoon convection usually occurs in mountainous areas as well as in convergence zones produced by local sea breezes or by the typical thermal low of the Iberian peninsula (Alonso et al. 1994). During the cold season, however, travelling disturbances associated with the mid-latitude westerlies can easily reach those latitudes and the weather becomes temperate and moderately wet. Figure 1.7 illustrates these seasonal contrasts for Mediterranean Spain.

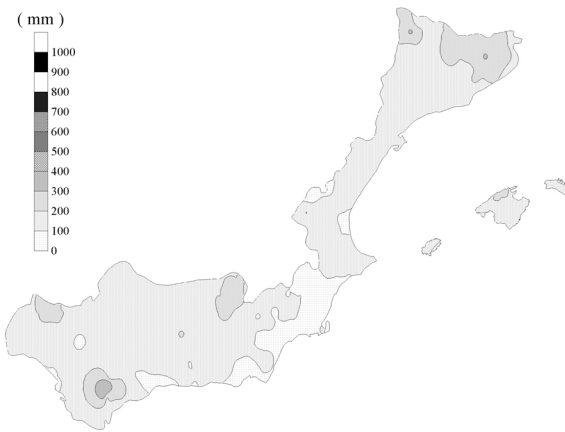
On the other hand, the closed characteristic of the Mediterranean sea and the high



(a) Yearly



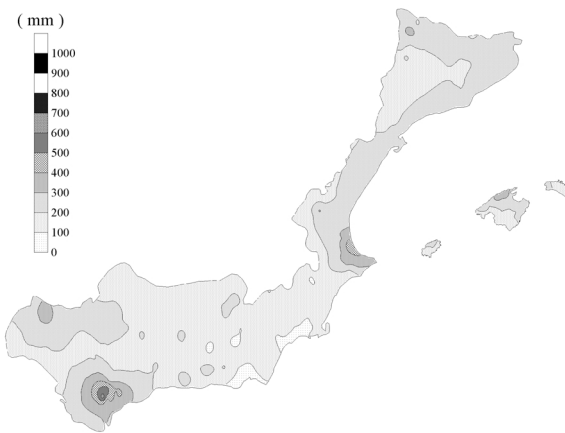
(b) Winter



(c) Spring



(d) Summer



(e) Autumn

Figure 1.7: Mean precipitation in the Spanish Mediterranean area (depicted in Figure 1.6), for (a) years, (b) winters, (c) springs, (d) summers, and (e) autumns, of 1984-93. Note the different scale of (a) and the other maps. Winter is composed by December, January and February months; Spring by March, April and May; Summer by June, July and August; and Autumn by September, October and November.

insolation received during the summer lead to high sea surface temperatures during the summer and autumn. This aspect ensures strong water vapour availability in the Mediterranean environment and during that period the Mediterranean air masses present frequently convective instability (Meteorol. Office 1962; Ramis 1995). This is premonitory of the torrential character of rainfalls during the late summer and autumn when, under favorable synoptic conditions, that instability is released over the coastal areas, sometimes causing local flooding. Riosalido (1990) has shown that most of the heavy rainfall events are produced by quasistationary Mesoscale Convective Systems (MCS), although they typically are relatively small in size and practically never fulfill the criteria for a Mesoscale Convective Complex (MCC) given by Maddox (1980). Figure 1.8 displays the mean amount of daily rainfalls in Mediterranean Spain. Observe that the greatest values are registered in the coastal zones, clearly associated with the coastal mountains. Comparison of Figures 1.8a, b, c and d shows that the highest rates are obtained in the autumn season. Most of the extreme precipitation events occur during that season (Figure 1.9), especially in the eastern part of the region.

Therefore, the occurrence of damaging flash floods is a problem of major concern in the western Mediterranean region and particularly in Mediterranean Spain. Several episodes of devastating rainfalls occur every year in coastal regions of Spain, France and Italy, especially during the autumn, causing many casualties and material losses. Three of such events (referred to as Catalonia, Piedmont and Tarragona events) will serve as case studies for the numerical modelling research developed in this work.

For the Catalonia event, there was heavy rainfall during the evening and early night of 12 November 1988 in that coastal region of north-eastern Spain (Figure 1.10). Floods occurred as a consequence of some rivers overflowing. Eleven people lost their lives and damage was calculated at around 20 million ECUs (European Currency Units).

The Piedmont event is quite interesting, because an important part of the rainfall in inland areas appears to be predominantly non-convective (Lionetti 1996; Buzzi and Tartaglione 1996). Although rainfall was not limited to northwestern Italy, the majority of damage and casualties (6400 billion lira (4 billion US dollars) and about 65 deaths, according to Lionetti 1996) occurred there, in what is known as the Piedmont region (Figure 1.5). Maximum daily rainfall amounts on 5 November 1994 (Figure 1.11) exceeded 200 mm in the northwestern portion of the area, close to the Alps. Another maximum in observed precipitation can be seen near the Italian coast. The Piedmont event has suscited several international studies, as demonstrates the fact that this event has been included among the case studies of the european projects ANOMALIA (“Anomalies induced by mountains and sea in rainfall over land in the western Mediterranean area”) and MAP (“Mesoscale Alpine Programme”).

The Tarragona case represents the episode of 9 and 10 October 1994, in which the heavy rain affected the eastern and north-eastern regions of Spain, from south Valencia to Catalonia (Figure 1.5). The most important rainfall occurred in the Alforja town of south Catalonia (Tarragona region), where 450 mm fell (240 mm in an interval of about 2.5 hours, between 0500 and 0730 UTC on 10 October). In addition, very high amounts were also registered in many locations close to the coast as can be seen in Fig. 1.12. Floods were very important in Catalonia, producing damage on houses, farms, routs and railways. Moreover, 8 people lost their lives. This heavy rain episode is considered as the

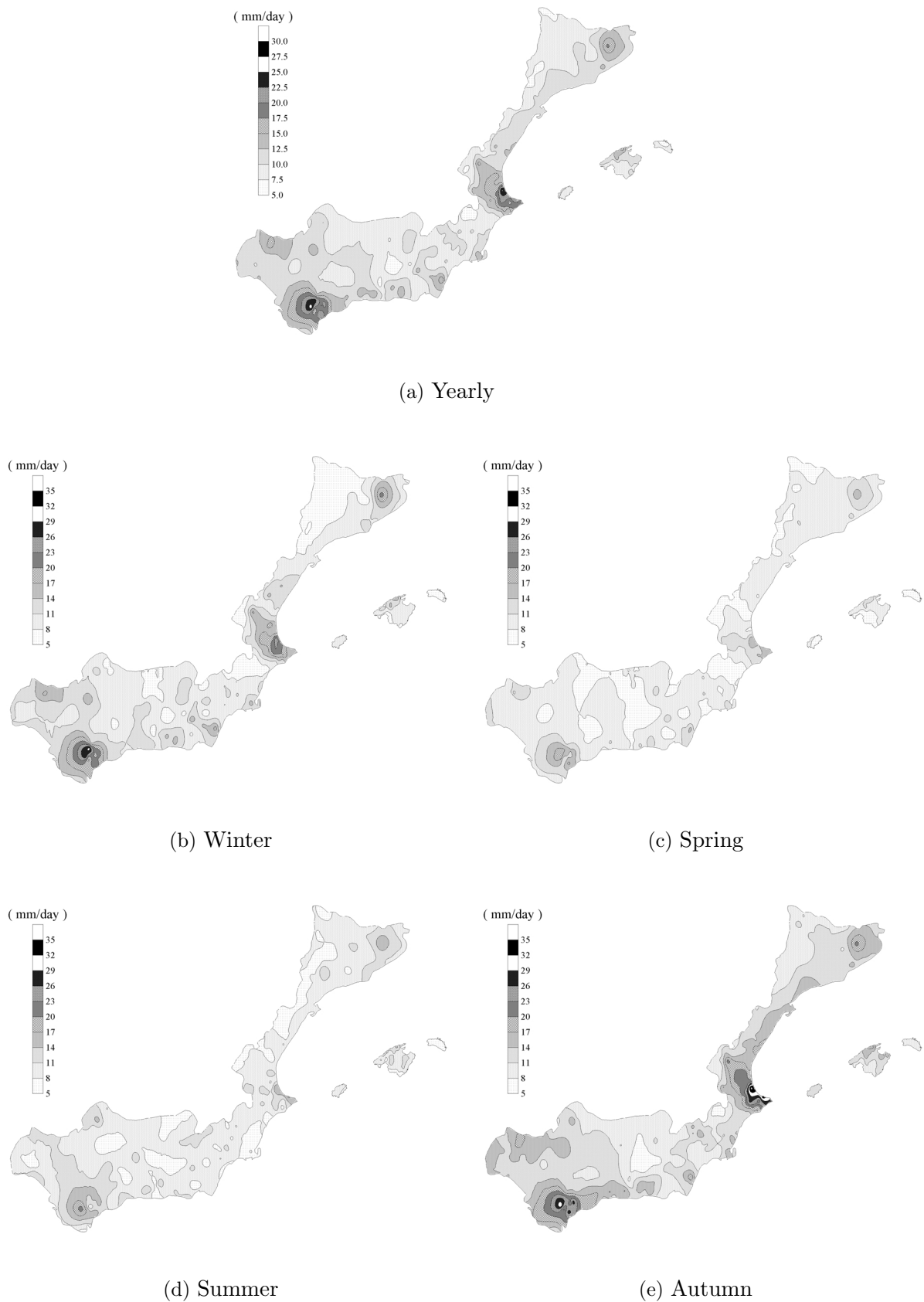


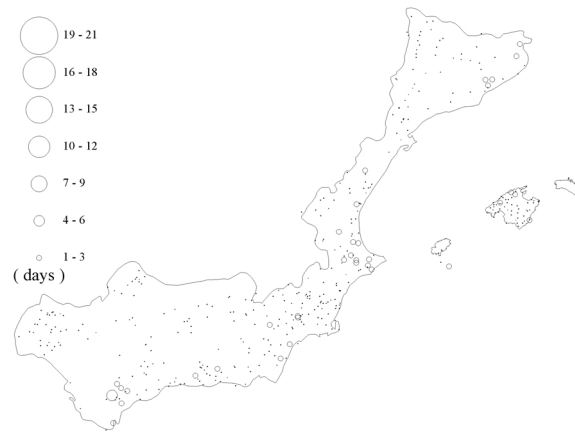
Figure 1.8: Mean rates of daily rainfalls in the Spanish Mediterranean area (depicted in Figure 1.6), for (a) years, (b) winters, (c) springs, (d) summers, and (e) autumns, of 1984-93. Note the different scale of (a) and the other maps.



(a) Yearly



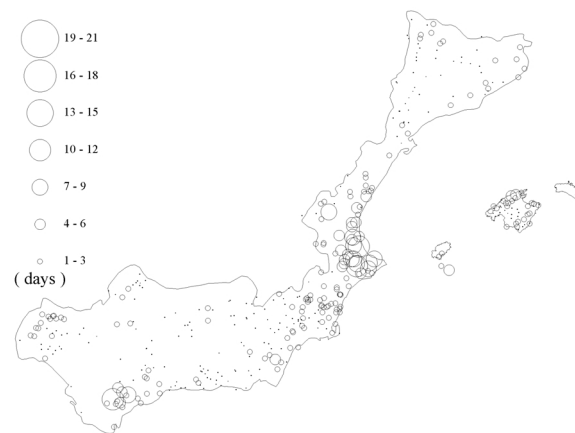
(b) Winter



(c) Spring



(d) Summer



(e) Autumn

Figure 1.9: Days with extreme rainfalls (≥ 100 mm) in the stations shown in Figure 1.6, for (a) years, (b) winters, (c) springs, (d) summers, and (e) autumns, of 1984-93. Note the different scale of (a) and the other maps. The dots represent the position of the stations where extreme events were not registered.

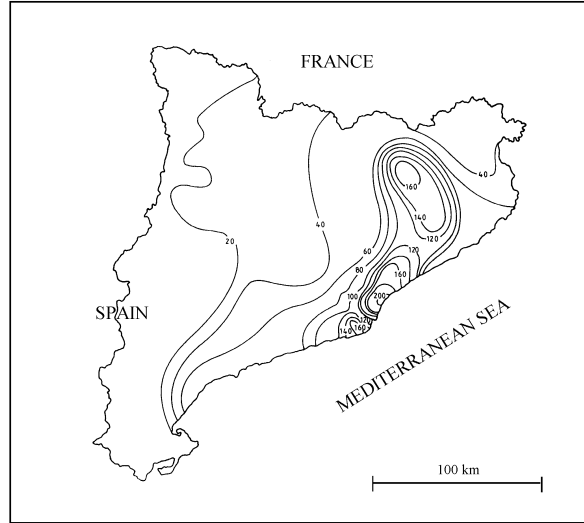


Figure 1.10: Accumulated precipitation (mm) in Catalonia (Figure 1.6), for the period 07 UTC 12 November - 07 UTC 13 November.

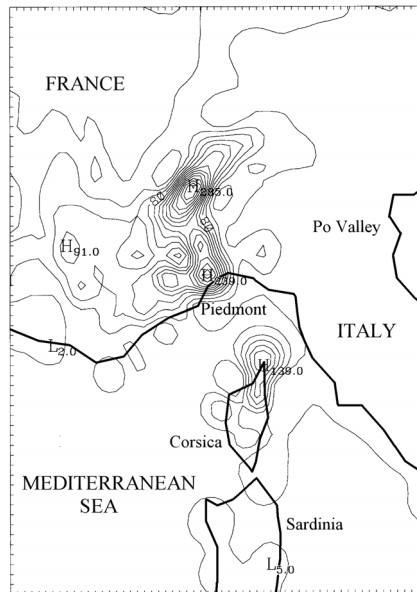


Figure 1.11: Analysis of the accumulated precipitation (mm) in the Piedmont area, Corsica and Sardinia (Figure 1.5), from 00 UTC to 24 UTC 5 November 1994. Contour interval is 20 mm starting at 20 mm. (Courtesy of A. Buzzi).

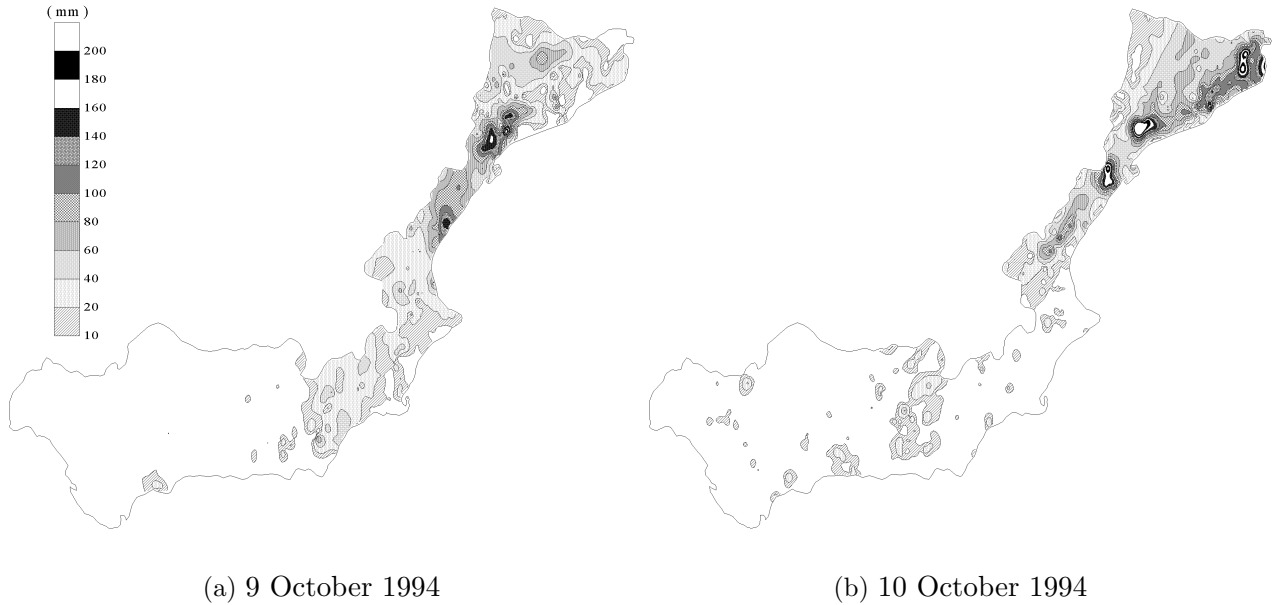


Figure 1.12: Accumulated precipitation (mm) in eastern and southern Spain. (a) from 07 UTC 9 October to 07 UTC 10 October 1994, (b) from 07 UTC 10 October to 07 UTC 11 October 1994.

most devastating in Catalonia during the last 10 years.

There are several studies devoted to the diagnosis of extreme rainfall episodes in the western Mediterranean (e.g., Doswell et al. 1998 and the references therein). These studies focus on identifying the synoptic and mesoscale mechanisms responsible for the flash floods. They apply an “ingredients-based” methodology (Doswell et al. 1996), and try to derive a useful collection of diagnostic techniques that best describe those ingredients. These studies have shown that most of the flash flood events are characterized by synoptic scenarios favorable for convection development and its maintenance: moisture convergence in the lowest 1500 metres, upward quasi-geostrophic forcing at 850 hPa, convective instability in the 500-1000 hPa layer, and high values and/or sharp gradients of Convective Available Potential Energy (CAPE). Using observations and conceptual models, the mesoscale triggering mechanisms have been normally attributed to the interaction of the low-level flow with the terrain features, or to the existence of outflow boundaries produced by previous convection.

However, only a few numerical simulations of flash flood events have been done for the western Mediterranean during the past, in spite of the advantage that numerical simulation provides in developing improved understanding. The feasibility of numerical simulations for this kind of event has been already demonstrated by, among others, Paccagnella et al. (1992) for a heavy rain event in the Po valley, and Fernández et al. (1995) for a case occurred in Valencia.

1.4 Objectives

The general motivation of our research is the development of new understanding about those environmental problems of our region that were described in sections 1.2 and 1.3: Impact of coastal pollutants during the breeze cycle in the island of Mallorca, and the occurrence of heavy precipitations in the western Mediterranean region. Both problems have a quite different nature. However, the basic approach followed in both cases is the numerical modelling, since we apply a mesoscale numerical model (the SALSA model) to assess the role of some relevant physical processes in each case. Next, we explain in more detail our specific objectives:

The first objective is to apply the SALSA model to study the transport and diffusion during the breeze of non-reactive sulphur dioxide emitted from a power plant located in the north bay of Mallorca (EP1 in Figure 1.1), paying special attention to the physical mechanisms responsible of the ground-level concentration. The impacts that would result from a potential change in location or magnitude of emissions also can be usefully studied by numerical models (e.g. McVehil 1989, in Alberta, Canada; Hearn 1989, in Latrobe Valley, Australia). The planned study, therefore, is also extended to a hypothetical scenario to consider a similar power plant on the south coast (EP2 in Figure 1.1).

For reasons of simplicity, Eulerian models have often been implemented with a two-step process separating the meteorological background and the pollutant transport model. As the first step, direct specification or diagnosis from observations of the wind field over the region of interest is required, as well as quantitative information about diffusive activity. The diffusive activity can be found, for example, by specifying certain stability classes (Pasquill 1974; Gifford 1968) which determine the eddy coefficients. In the second step, the meteorological fields are used to solve the conservation relation for the pollutants species (e.g., Davis et al. 1984). Using such an approach, simulations of pollutant transport over small and large areas, including complex terrain, have given reasonable results when compared with data of intensive field experiments (King and Bunker 1984). Other dispersion models use the meteorological fields already predicted by an operational weather forecasting model and therefore their computation times are low. With such methods, reasonable accuracy has been obtained in cases of large scale atmospheric dispersion of pollutants, as in the case derived from the Chernobyl release (Piedelievre et al. 1990). However, owing to the structure and diurnal variability of the sea-land breeze (not resolvable by large scale models), plumes from coastal industries and power plants present a complicated behaviour under the influence of this kind of mesoscale circulations. For example, the plume may be swept inland during the sea breeze, rise vertically in the convergence zone and return to the coast transported by the return flow at greater heights (Lyons 1975), or the plume can drift offshore at night and return to land when the sea breeze develops the next morning. The phenomenon of fumigation in the coastal environment due to strong vertical mixing in the boundary layer also has been recognized as an important agent of ground-level concentration (Hewson and Olsson 1967). In absence of sufficiently dense (in space and time) meteorological measurements, as it occurs in Mallorca, such complicated behaviour is best treated by means of three-dimensional prognostic models which are able to account for the short-period meteorological variability (e.g., Yamada et al. 1992; Uliasz 1993; Ferretti et al. 1993). Obviously, the cost is

the large amount of computation time required.

As emphasized in section 1.3, the particular topographical configuration and the strong seasonal contrasts in the western Mediterranean area, contribute to define this region as an independent climatic entity, very interesting for mesoclimatological studies on spatial and temporal variability of rainfall, and where the torrential component plays a key role. As a contribution to the pluviometric characterization of Mediterranean Spain (shown in Figure 1.6), the second objective of our research is to find (using cluster analysis) the principal spatial patterns under which significant and torrential daily rainfalls tend to occur in that region. From our regional experience, and from the previous results obtained in Romero et al. (1998b), it can be anticipated that the resulting rainfall patterns will be strongly linked to the topography of the region, and that distinctive seasonal distributions will characterize them. Objective classifications of rainfall patterns have been applied for different regions of the world: Po valley in Italy (Cacciamani et al. 1994), New Zealand (Kidson 1994), Wales (Sumner 1996), Mallorca (Summer et al. 1995a) etc., but similar studies have not been done for the considered area. Although the spatial patterns we are seeking constitute, of course, a simplification of the complex reality, they can be useful as additional objective elements for regional forecasters. That practicality may be largely increased once the atmospheric circulation patterns associated with the typical rainfall distributions are determined.

In the third part of our work, we concentrate the numerical modelling efforts on the Catalonia, Piedmont and Tarragona heavy precipitation cases presented in section 1.3, with a special emphasis on the spatial distribution of the rainfall produced by the SALSA simulations. First, we wish to study the feasibility of mesoscale numerical simulations for this kind of event in the western Mediterranean area. Significant reduction of the hazards to human life associated with heavy precipitation is possible if its occurrence can be forecast reliably, although the short time scales often mean that property losses from flash floods are difficult to mitigate. We will show that some superficial synoptic-scale similarities exist among the three events. That is, on the day of the event, all of the cases had a strong synoptic-scale trough or closed cyclone at upper levels, to the west of the threat area. Along with this common structure aloft, moist air is being advected upslope in each case at low levels. These common features might be interpreted to suggest that forecasting heavy rainfalls in the western Mediterranean region ought to be easy. However, the details of when and where the heavy rain is expected within the broad synoptic pattern, as well as the intensity of the rainfall, appear to be challenging problems for operational synoptic-scale numerical prediction models.

It was noted earlier that both the orography and the evaporation from the warm sea seem to exert an important influence on the development of heavy rainfalls in the western Mediterranean. In previous subjective studies (e.g. García-Dana et al. 1982; Miró-Granada 1974; Ramis et al. 1986), both factors were considered as being the most important in this kind of event. By means of numerical simulations, in this work we will also study the effect of these factors explicitly. Any investigation of the processes by which heavy precipitation occurs can be of value to weather forecasters, provided the study focuses on the physical processes giving rise to the intense precipitation.

Prior to the presentation of the simulations, it is possible to anticipate that the strong topographic influence provides a real opportunity for successful application of mesoscale

models for operational forecasting of heavy precipitations in our region. For that purpose, however, the sensitivity of model forecasts to different physical parameterizations (in their sophistication or in their closure assumptions) is a problem that must be addressed. Our work tries to do a contribution to this aspect, since we also investigate the performance of two cumulus convection parameterizations (Emanuel 1991; Kain and Fritsch 1990) for the Piedmont case study.

Following this introduction, in chapter 2 we provide a description of the SALSA model. The numerical study on the transport and diffusion of coastal pollutants in Mallorca under the breeze circulation is presented in chapter 3. Chapter 4 presents the classification of the daily rainfall patterns in the Spanish Mediterranean area. The numerical studies of the Catalonia and Piedmont events are contained in chapter 5, whereas that of the Tarragona event is presented in chapter 6. Finally, chapter 7 contains the general conclusions of our research and some potential aspects to be developed in future research.

Chapter 2

MODEL DESCRIPTION

The numerical model used for our research (known as SALSA model), is the primitive-equation meso- β scale model initially described by Nickerson and Magaziner (1976). A more complete version was presented in Nickerson et al. (1986). The model is hydrostatic and its equations are expressed in a terrain-following coordinate system (see Figure 2.1), where the vertical coordinate ν is related to the classical σ pressure coordinate ($\sigma = (P - P_t)/(P_s - P_t) = (P - P_t)/\pi$) by the expression

$$\sigma = (4\nu - \nu^4)/3,$$

where ν and σ take values from 0 (upper boundary of pressure P_t) to 1 (ground). The vertical coordinate also satisfies the condition that $d\sigma/d\nu$ must be finite over the entire domain and must be equal to zero at the lower boundary to assure second order accuracy in the discretization scheme (De Rivas 1972). The ν coordinate has the advantage of allowing for a high resolution of the planetary boundary layer (PBL) in spite of working with an uniform computational grid.

Terrain-following coordinates are very convenient in domains with complex terrain. They facilitate the treatment of the lower boundary since the ground is a surface of constant vertical coordinate. Furthermore, the parameterizations included in the model of short and longwave radiation, surface fluxes, warm microphysics and PBL turbulence allow to study the effect of diurnal cycle, air moisture and surface characteristics. In fact, the model has been used in previous works to simulate a wide range of mesoscale phenomena such as orographic enhancement of rain and clouds (Nickerson 1979; Richard et al. 1986), mesoscale flows induced by vegetation or soil moisture inhomogeneities (Mahfouf et al. 1987a; Pinty et al. 1989), downslope windstorms (Richard et al. 1989), mountain waves (Nickerson et al. 1986; Richard et al. 1985; Romero et al. 1995), or the breeze circulation (in Florida, Mahfouf et al. 1987b; in Mallorca, Ramis and Romero 1995). The SALSA model has been applied also to study air pollution problems (e.g., Chaumerliac et al. 1987; Chaumerliac et al. 1992).

The governing equations and physical parameterizations initially included in the SALSA model are presented in next sections (see the Appendix for symbols). Descriptions of new developments and adaptations of the model, necessary for our particular objectives, are reserved for the corresponding chapters.

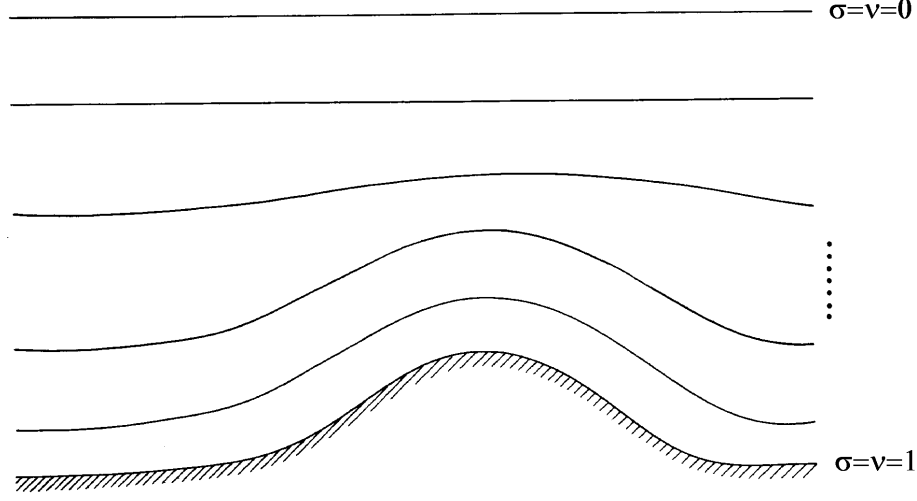


Figure 2.1: Illustration of the terrain-following coordinate system.

2.1 Dynamical equations

The prognostic equations for the horizontal momentum variables (u, v) have the form:

$$\begin{aligned} \frac{\partial \pi u}{\partial t} = & -m^2 \frac{\partial(\pi u u / m)}{\partial x} - m^2 \frac{\partial(\pi u v / m)}{\partial y} - \frac{1}{\sigma'} \frac{\partial \sigma' \pi u \dot{\nu}}{\partial \nu} + f \pi v + \\ & m \left(\phi - \frac{R_v T^* \sigma \pi}{P} \right) \frac{\partial \pi}{\partial x} - m \frac{\partial \pi \phi}{\partial x} + F_{\pi u} + D_{\pi u} \end{aligned} \quad (2.1)$$

$$\begin{aligned} \frac{\partial \pi v}{\partial t} = & -m^2 \frac{\partial \pi v u / m}{\partial x} - m^2 \frac{\partial \pi v v / m}{\partial y} - \frac{1}{\sigma'} \frac{\partial \sigma' \pi v \dot{\nu}}{\partial \nu} - f \pi u + \\ & m \left(\phi - \frac{R_v T^* \sigma \pi}{P} \right) \frac{\partial \pi}{\partial y} - m \frac{\partial \pi \phi}{\partial y} + F_{\pi v} + D_{\pi v}. \end{aligned} \quad (2.2)$$

The map scale factor m must be introduced when the earth's sphere is transformed into the (x, y) plane. In the case of the polar stereographic projection (used in Chapters 5 and 6), m is:

$$m = \frac{1 + \sin \varphi_o}{1 + \sin \varphi},$$

where φ is the latitude, and the constant φ_o is the latitude where the projection is true (90°).

In addition, when that map projection is used, the wind components u and v are related with u_s and v_s (zonal and meridional wind components on the sphere respectively), through the rotations:

$$\begin{cases} u = -\sin(\lambda - \lambda_o) u_s - \cos(\lambda - \lambda_o) v_s \\ v = \cos(\lambda - \lambda_o) u_s - \sin(\lambda - \lambda_o) v_s \end{cases}$$

where λ is the longitude, and the constant λ_o is the meridian pointing in the x direction (90°).

In the (x, y, ν) coordinates the continuity equation is written

$$\frac{\partial \pi}{\partial t} = -m^2 \frac{\partial \pi u/m}{\partial x} - m^2 \frac{\partial \pi v/m}{\partial y} - \frac{1}{\sigma'} \frac{\partial \sigma' \pi \dot{\nu}}{\partial \nu}.$$

Since the boundary conditions on the vertical velocity $\dot{\nu}$ are:

1. At the surface: $\dot{\nu} = 0$ (the flow must be along the surface, i.e normal component zero).
2. Top of the domain: $\dot{\nu} = 0$ (this is a reasonable condition when the pressure at the upper boundary P_t is not greater than 100 hPa).

then the continuity equation can be vertically integrated over part of the atmosphere to give the vertical velocity $\dot{\nu}$:

$$\dot{\nu} = -\frac{1}{\pi \sigma'} \int_0^\nu \sigma' \left[\frac{\partial \pi}{\partial t} + m^2 \left(\frac{\partial \pi u/m}{\partial x} + \frac{\partial \pi v/m}{\partial y} \right) \right] d\nu, \quad (2.3)$$

or over the entire atmosphere to give the temporal evolution of the surface pressure:

$$\frac{\partial \pi}{\partial t} = -m^2 \int_0^1 \left(\frac{\partial \pi u/m}{\partial x} + \frac{\partial \pi v/m}{\partial y} \right) \sigma' d\nu. \quad (2.4)$$

Finally, the geopotential ϕ is calculated from the hydrostatic equation:

$$\frac{\partial \phi}{\partial \hat{P}} = -C_p \theta (1 + 0.61 q_v). \quad (2.5)$$

2.2 Thermodynamical equations

An entropy variable $S = \pi H$ is defined, where

$$H = \ln \left(\frac{T}{\hat{P}} \right) + \frac{L_v q_v}{C_p T}$$

apart from a small correction factor which is proportional to the mixing ratio of liquid water present in the model, is conserved during both dry and wet reversible adiabatic transformations (Dufour and Van Mieghem 1975). The present case consists of an open system in which the condensation products do not necessarily remain in the air if precipitation forms. However, the entropy variable is approximately conserved in this pseudoadiabatic, pseudoreversible system. Its predictive equation is:

$$\frac{\partial S}{\partial t} = -m^2 \frac{\partial (Su/m)}{\partial x} - m^2 \frac{\partial (Sv/m)}{\partial y} - \frac{1}{\sigma'} \frac{\partial \sigma' S \dot{\nu}}{\partial \nu} + F_S + D_S + S_S. \quad (2.6)$$

The other predicted thermodynamic variable is the moisture variable $W = \pi(q_v + q_{cw})$, in which transformation between mixing ratios of water vapour q_v and cloud water q_{cw} when saturation occurs is taken into account:

$$\frac{\partial W}{\partial t} = -m^2 \frac{\partial (Wu/m)}{\partial x} - m^2 \frac{\partial (Wv/m)}{\partial y} - \frac{1}{\sigma'} \frac{\partial \sigma' W \dot{\nu}}{\partial \nu} + F_W + D_W + S_W. \quad (2.7)$$

The source-sink terms S_S and S_W in Eqs. 2.6 and 2.7 will contain, respectively, radiative processes (short and long wave), and transformations between rainwater and the moisture variable W (loss by autoconversion and accretion, and production by evaporation). Parameterizations of these processes are explained in section 2.3 and 2.6.

Temperature and cloud water mixing ratio are not explicitly predicted by the model, but are diagnosed from the predicted values of S and W (Nickerson 1979). If the air is saturated, the mixing ratio is a known function of temperature, and the definition of S becomes a transcendental equation for the temperature T_s , corresponding to saturation with respect to liquid water. Excess vapour from the saturation value is converted into cloud water. If on the other hand the air is unsaturated, cloud water is zero, the vapour mixing ratio in the definition of S is replaced by W/π and the temperature is solved for directly, using the temperature at the previous time step to account for the temperature dependence of the latent heat.

In summary, T_s and q_{vs} , the saturation temperature and its corresponding vapour mixing ratio, are computed from the value of S using the Newton-Raphson technique. Temperature and mixing ratios of water vapour and cloud water are then arrived at in accordance with the following criteria:

$$\left. \begin{aligned} q_v &= q_{vs} \\ q_{cw} &= W/\pi - q_{vs} \\ T &= T_s \end{aligned} \right\} W > \pi q_{vs}$$

$$\left. \begin{aligned} q_v &= W/\pi \\ q_{cw} &= 0 \\ T &= T_{uns} \end{aligned} \right\} W \leq \pi q_{vs}$$

The saturation vapor pressure with respect to water, e_s , used to compute q_{vs} , is taken from Murray (1967):

$$e_s = 6.11 \exp[17.27(T - 273.16)/(T - 35.86)].$$

2.3 Microphysical equations

Apart from cloud water which wafts around with the air, liquid water in the model is present as rainwater, which falls through the air. Ice processes are not considered. Separate prognostic equations are written for both rainwater mixing ratio q_r and number of raindrops concentration N_r :

$$\frac{\partial \pi q_r}{\partial t} = -m^2 \frac{\partial \pi(q_r u/m)}{\partial x} - m^2 \frac{\partial \pi(q_r v/m)}{\partial y} - \frac{1}{\sigma'} \frac{\partial \sigma' \pi q_r \dot{\nu}}{\partial \nu} + F_{\pi q_r} + D_{\pi q_r} + S_{\pi q_r} \quad (2.8)$$

$$\frac{\partial \pi N_r}{\partial t} = -m^2 \frac{\partial \pi(N_r u/m)}{\partial x} - m^2 \frac{\partial \pi(N_r v/m)}{\partial y} - \frac{1}{\sigma'} \frac{\partial \sigma' \pi N_r \dot{\nu}}{\partial \nu} + F_{\pi N_r} + D_{\pi N_r} + S_{\pi N_r}. \quad (2.9)$$

The terms $S_{\pi q_r}$ and $S_{\pi N_r}$ are related to autoconversion, selfcollection, accretion, evaporation and sedimentation processes. However, selfcollection affects only the concentration of raindrops whereas accretion affects only the rainwater mixing ratio:

$$S_{\pi q_r} = \pi \left. \frac{\partial q_r}{\partial t} \right|_{auto} + \pi \left. \frac{\partial q_r}{\partial t} \right|_{accr} + \pi \left. \frac{\partial q_r}{\partial t} \right|_{eva} + \pi \left. \frac{\partial q_r}{\partial t} \right|_{sed} \quad (2.10)$$

$$S_{\pi N_r} = \pi \left. \frac{\partial N_r}{\partial t} \right|_{auto} + \pi \left. \frac{\partial N_r}{\partial t} \right|_{self} + \pi \left. \frac{\partial N_r}{\partial t} \right|_{eva} + \pi \left. \frac{\partial N_r}{\partial t} \right|_{sed}. \quad (2.11)$$

Diffusional growth of raindrops is not included since the model does not permit supersaturation with respect to water. The parameterization of the above terms is based on the assumption that rainwater is lognormally distributed with diameter; that is,

$$dN_r = \frac{N_r}{(2\pi)^{1/2}\sigma_0 D} \exp\left[-\frac{1}{2\sigma_0^2} \ln^2\left(\frac{D}{D_0}\right)\right] dD \quad (2.12)$$

is the number of raindrops in the size range D to $D + dD$ and N_r is the total number of raindrops. Here σ_0 and D_0 are distribution parameters. The lognormal distribution adequately describes the average spectra for a number of rainfalls of several intensities (Markowitz 1976).

If the diameter D_0 is large enough so that cloud-size droplets contribute very little to the total number concentration, the integration of Eq. 2.12 over the entire spectrum of drops of mass $\pi\rho_l D^3/6$ yields the following expression for q_r , the rainwater mixing ratio:

$$q_r = \frac{N_r}{\rho} \left(\frac{\pi}{6} D_0^3 \rho_l\right) \exp\left(\frac{9}{2}\sigma_0^2\right),$$

where ρ and ρ_l represent the density of air and liquid water respectively. It is also convenient to define a mean drop diameter \bar{D}_r , which is the diameter the raindrops would have if they were all the same size. \bar{D}_r is related to the lognormal distribution parameters by

$$\bar{D}_r = D_0 \exp\left(\frac{3}{2}\sigma_0^2\right).$$

Since there are two independent distribution parameters σ_0 and D_0 , only one of which can be diagnosed given q_r and N_r , the microphysical system of equations is closed by assuming a constant value for σ_0 ($= 0.547$) and computing \bar{D}_r .

A detailed derivation of each contribution in Eqs. 2.10 and 2.11 making extensive use of the work of Berry and Reinhardt (1973), can be found in Nickerson et al. (1986). Only the final expressions (in mks units) to parameterize each source-sink term will be given in this summary.

a. Autoconversion

Autoconversion is the growth of cloud water to form rainwater. The tendency for rainwater mixing ratio is given by

$$\left. \frac{\partial q_r}{\partial t} \right|_{auto} = \alpha \rho q_{cw}^2,$$

and the corresponding expression for the number concentration of raindrops is

$$\left. \frac{\partial N_r}{\partial t} \right|_{auto} = 3.5 \times 10^9 \rho \left. \frac{\partial q_r}{\partial t} \right|_{auto},$$

where

$$\alpha = 0.067\{10^{16}x_{fcw}^{4/3}(varx)^{1/2} - 2.7\} \times \{10^4[x_{fcw}(varx)^{1/2}]^{1/3} - 1.2\}.$$

In the expression for α , x_{fcw} is the mean mass of the cloud droplets and $varx$ is a variance parameter. Both are related to the size distribution of the cloud water. It is assumed that the cloud droplets are also partitioned according to a lognormal distribution for which the distribution parameters σ_{0cw} and D_{0cw} remain constant.

$$\begin{aligned} varx &= \exp(9\sigma_{0cw}^2) - 1 \\ x_{fcw} &= \frac{\rho q_{cw}}{N_{cw}} = \pi \rho_l \bar{D}_{cw}^3 / 6, \end{aligned}$$

where the mean diameter of the cloud droplets \bar{D}_{cw} is

$$\bar{D}_{cw} = D_{0cw} \exp\left(\frac{3}{2}\sigma_{0cw}^2\right).$$

The chosen values $D_{0cw} = 32.5\mu\text{m}$ and $\sigma_{0cw} = 0.2203$ lead to a value of $\alpha = 4$.

b. Accretion

Accretion is the process whereby cloud droplets are collected by raindrops. Obviously, this process affects the rainwater mixing ratio but not the number of raindrops concentration:

$$\left. \frac{\partial q_r}{\partial t} \right|_{accr} = \frac{3\rho q_r q_{cw}}{2\rho_l D_{gr}} \gamma_c^2(D_{gr}, \bar{D}_{cw}) [v(D_{gr}) - v(\bar{D}_{cw})],$$

where D_{gr} is the diameter corresponding to the predominant mass relative to the rainwater spectrum,

$$D_{gr} = \left(\frac{6\rho q_r}{\pi \rho_l N_r} \right)^{1/3} \exp(3\sigma_0^2).$$

For evaluation of the collision efficiency γ_c , the following approximation based on Berry (1967) and Shafrir and Neiburger (1963) is adopted:

$$\gamma_c(r_l, p) = 1 + p + \frac{d}{p^f} + \frac{e}{(1-p)^g},$$

where $p = r_s/r_l$ is the ratio of the radius of the small drop to the radius of the collector drop, and

$$\begin{aligned} d &= -27/r_l^{1.65} \\ e &= -58/r_l^{1.9} \\ f &= (15/r_l)^4 + 1.13 \\ g &= (16.7/r_l)^8 + 0.004r_l + 1. \end{aligned}$$

with the radii expressed in micrometers.

Berry and Pranger (1974) have developed an empirical expression for the terminal velocity of the form

$$v(D) = \frac{\eta Re}{D\rho}, \quad (2.13)$$

where Re is the Reynolds number for the airflow around the drops, and η , the dynamic viscosity of the air, is given by the relation

$$\eta = 1.496286 \times 10^{-6} \frac{T^{1.5}}{T + 120}.$$

The expressions for Reynolds number are based on the data of Beard and Pruppacher (1969) and Gunn and Kinzer (1949):

$$Re = \begin{cases} 0.0412657y - 1.50074 \times 10^{-4}y^2 \\ + 7.58884 \times 10^{-7}y^3 - 1.68841 \times 10^{-9}y^4 & \text{when } 0 < y \leq 175.27 \\ \exp[-2.36534 + 0.767787 \ln y \\ + 0.00535826(\ln y)^2 - 7.63554 \times 10^{-4}(\ln y)^3] & \text{when } 175.27 < y \leq 10^7 \end{cases}$$

The parameter y is given by

$$y = \frac{4\rho\rho_l g}{3\eta^2} D^3.$$

c. Selfcollection

Selfcollection is the process by which collisions between raindrops produce larger drops. In contrast to the growth by accretion, the interacting drops are of the same size range. The expression is

$$\left. \frac{\partial N_r}{\partial t} \right|_{self} = -b_s(\tilde{D}, D^*) N_r \rho q_r,$$

where

$$b_s(D, D') = \frac{3D^2}{2\rho_l(D^3 + D'^3)} \gamma_c^2(D, D') [v(D) - v(D')].$$

In the parameterization $\tilde{D} = D_{gr}$ and $D^* = \bar{D}_r$, already defined.

d. Sedimentation

Sedimentation of N_r and q_r is given by the divergence of their fluxes (driven by the terminal fall velocity), through a unit horizontal surface:

$$\left. \frac{\partial N_r}{\partial t} \right|_{sed} = \frac{\partial S_n}{\partial z}$$

$$\left. \frac{\partial q_r}{\partial t} \right|_{sed} = \frac{\partial S_q}{\partial z}.$$

The fluxes are calculated as

$$S_n = \frac{N_r v(D_0)}{2^{1/2} \sigma_0 p} \exp \left[\frac{(k_2 - 1)^2}{4p^2} \right]$$

$$S_q = \frac{q_0 v(D_0)}{2^{1/2} \sigma_0 p} \exp \left[\frac{(k_2 + 2)^2}{4p^2} \right].$$

For the calculation of the terminal fall velocity in terms of Reynolds number and dynamic viscosity as expressed in 2.13, Berry and Pranger (1974) give the following expression for the Reynolds number:

$$Re(D) = \exp[c_1 + c_2(\ln y) + c_3(\ln y)^2].$$

The constants c_1 , c_2 and c_3 take the values -3.12611, 1.01338 and -0.0191182 respectively, and

$$y = \left(\frac{4\rho\rho_l g}{3\eta^2} \right) D^3 = aD^3.$$

The other constants which appear in the expressions of S_n and S_q are given by

$$p^2 = \left(\frac{1}{2\sigma_0^2} - 9c_3 \right)$$

$$k_2 = 3c_2 + 6c_3 \ln(aD_0^3)$$

$$q_0 = \frac{N_r m(D_0)}{\rho}.$$

e. Rain evaporation

The evaporation rate of rainfall is given by the expression

$$\left. \frac{\partial q_r}{\partial t} \right|_{eva} = \frac{\rho_l \pi}{\rho} AS N_r \left[0.572 D_O \exp\left(\frac{\sigma_0^2}{2}\right) + 5.31 \times 10^3 D_O^2 \exp(2\sigma_0^2) - 4.33 \times 10^5 D_O^3 \exp\left(\frac{9\sigma_0^2}{2}\right) \right]$$

which combines the ventilation effect, the undersaturation S given by the expression

$$S = \frac{q_v}{q_{vs} - 1},$$

and A , a thermodynamical function of pressure and temperature:

$$A = \frac{1}{1000(d_1 + d_2)}.$$

The parameters d_1 and d_2 are calculated with the expressions:

$$d_1 = \frac{R_v T P}{2.26 e_s \left(\frac{T}{T_0}\right)^{1.81}}$$

and

$$d_2 = \frac{L_v}{T(0.0243 + 8 \times 10^{15}(T - T_0))} \left(\frac{L_v}{R_v T} - 1 \right).$$

Finally, the number of raindrops which completely evaporate during one model time step is given by

$$N_{reva} = \frac{1}{\Delta t} \int_0^{D_{crit}} \frac{N_r}{(2\pi)^{1/2} \sigma_0 D} \exp\left(-\frac{1}{2\sigma_0^2} \ln^2 \frac{D}{D_0}\right) dD,$$

where

$$D_{crit} = (-2AS\Delta t)^{1/2}.$$

2.4 Diffusion terms and TKE equation

In the model equations 2.1, 2.2, 2.6, 2.7, 2.8, 2.9 and 2.15, the terms noted as D_{var} ($var = \pi u, \pi v, S, W, \pi q_r, \pi N_r, \pi e$) represent the horizontal diffusion, which acts on the ν -surfaces and is numerically introduced by a second order operator $D_2(var)$:

$$D_2(var) = K_H \left[\frac{\partial^2(var)}{\partial x^2} + \frac{\partial^2(var)}{\partial y^2} \right],$$

or alternatively by a fourth order operator $D_4(var)$:

$$D_4(var) = K_H \left[\frac{\partial^4(var)}{\partial x^4} + \frac{\partial^4(var)}{\partial y^4} \right],$$

where K_H is a constant coefficient.

The fourth order diffusion is more selective than the second order one, and therefore eliminates effectively short wavelength contributions that can lead to nonlinear instability (Pielke 1984, chapter 10), whereas preserves the meteorological modes of longer wavelengths much better. Table 2.1 illustrates the different behaviour of second and fourth order diffusion.

	$[K_H]$ (Second Order)					$[K_H]$ (Fourth Order)	
	0.25	0.10	0.05	0.01	0.001	-0.01	-0.001
$n = 2$	1	2	5	24	249	5	61
$n = 4$	1	4	9	49	499	24	249
$n = 6$	4	9	19	99	999	99	999
$n = 8$	6	17	33	170	1707	290	2913
$n = 10$	10	26	51	261	2618	684	6853
$n = 12$	14	37	74	373	3732	1392	13927
$n = 20$	40	102	203	1021	10215	10435	104363

Table 2.1: Number of time steps necessary to attenuate by e^{-1} a wave of wavelength $n\Delta x$ as function of the nondimensional diffusion coefficient $[K_H]$ for the second and fourth order diffusion operators (Richard et al. 1985). The nondimensional coefficients $[K_H]$ are defined as $K_H 2\Delta t / \Delta x^2$ and $K_H 2\Delta t / \Delta x^4$ for the second and fourth order respectively.

On the other hand, the F_{var} terms of the governing equations represent the vertical turbulent mixing. They are parameterized according to an eddy coefficient K_{ex} :

$$F_{var} = B \frac{\partial}{\partial \nu} \left(BK_{ex} \frac{\partial var}{\partial \nu} \right), \quad (2.14)$$

where

$$B = -\frac{gP}{\pi R_v T \sigma'}.$$

The exchange coefficients K_{ex} (K_m for the momentum, K_θ for the thermodynamic and microphysical variables and K_e for the mean turbulent kinetic energy TKE), are calculated as functions of the TKE (one and a half order closure) and the mixing length l_k following Therry and Lacarrère (1983) and Bougeault and Lacarrère (1989):

$$K_m = C_k l_k e^{1/2}$$

$$K_\theta = \alpha_T K_m$$

$$K_e = \alpha_e K_m.$$

The TKE (e) is predicted by the model through the equation:

$$\begin{aligned} \frac{\partial \pi e}{\partial t} = & -m^2 \frac{\partial(\pi e u/m)}{\partial x} - m^2 \frac{\partial(\pi e v/m)}{\partial y} - \frac{1}{\sigma'} \frac{\partial \sigma' \pi e \dot{\nu}}{\partial \nu} + \pi K_m \left[\left(B \frac{\partial u}{\partial \nu} \right)^2 + \left(B \frac{\partial v}{\partial \nu} \right)^2 \right] - \\ & \frac{g}{\theta_v} \pi K_\theta B \left(\frac{\partial \theta_v}{\partial \nu} - \gamma_{cg} \right) - C_\epsilon \pi \frac{e^{3/2}}{l_\epsilon} + F_{\pi e} + D_{\pi e}, \end{aligned} \quad (2.15)$$

where the first, second and third terms on the right-hand side are the advective terms, the fourth term is the shear-production term, the fifth is the bouyancy term and the sixth term represents the turbulence dissipation. The constant γ_{cg} is the so-called ‘‘countergradient’’ correction (Deardorff 1972), which applies only in the convective PBL, and allows for slightly stable stratification persinting with upward heat flux.

In the above relations, the inverse turbulent Prandtl numbers α_T and α_e are given the values $\alpha_T = \alpha_e = 1$. The numerical coefficients C_k and C_ϵ , once ajusted to experimentally determined values, take the values $C_k = 0.4$ and $C_\epsilon = 1/1.4$ (Bougeault and Lacarrère 1989).

Generalized specifications for the mixing length l_k and the dissipation length l_ϵ , based on the resistance to vertical displacements due to the static stability, are used by the model following Bougeault and Lacarrère (1989). This parameterization gives a good response outside the PBL and therefore is appropriate for orography-induced turbulence.

$$l_k = \min(l_{up}, l_{down})$$

$$l_\epsilon = (l_{up} l_{down})^{1/2}.$$

For each level Z in the atmosphere, l_{up} and l_{down} are the distances that a parcel originating from this level, and having an initial kinetic energy equal to the mean TKE of

the layer, can travel upward and downward respectively, before being stopped by buoyancy effects. More precisely, l_{up} and l_{down} are defined by

$$\int_Z^{Z+l_{up}} \beta(\theta(Z) - \theta(Z')) dZ' = e(Z)$$

$$\int_{Z-l_{down}}^Z \beta(\theta(Z') - \theta(Z)) dZ' = e(Z),$$

where β is the buoyancy coefficient ($\beta = g/T$).

2.5 Surface submodel

To apply the equation 2.14, which contains the expression for the vertical turbulent diffusion F_{var} in the boundary layer, it is necessary to know the turbulent fluxes $BK_{ex} \frac{\partial var}{\partial \nu}$ at the lower boundary ($\nu = \sigma = 1$). These are given by

$$BK_m \frac{\partial \pi u}{\partial \nu} = \pi Q_m \cos \alpha$$

$$BK_m \frac{\partial \pi v}{\partial \nu} = \pi Q_m \sin \alpha$$

$$BK_\theta \frac{\partial S}{\partial \nu} = \pi \left(\frac{Q_s \hat{P}}{T} + \frac{L_v Q_e}{C_p T} \right)$$

$$BK_\theta \frac{\partial W}{\partial \nu} = \pi Q_e,$$

where $\tan \alpha = V_h/U_h$, the ratio of the two wind components at the first grid point above the surface, and where Q_m , Q_s and Q_e represent the vertical eddy fluxes of momentum, sensible heat and water vapour at the surface:

$$Q_m = u_*^2$$

$$Q_s = -u_* \theta_*$$

$$Q_e = -u_* q_*,$$

where u_* , θ_* and q_* are scaling velocity, temperature and specific humidity.

The above turbulent fluxes are calculated in the model following the surface layer parameterization of Louis (1979). The scheme is based on the Monin-Obukhov similarity theory with bulk relations evaluated between the surface, with roughness length z_0 , and the lowest model level at a height z above the ground. In summary, defining the bulk Richardson number (a stability parameter) for the layer

$$Ri_B = \frac{gz\Delta\theta}{\bar{\theta}u^2},$$

the surface eddy fluxes are calculated as

$$u_*^2 = a^2 u^2 F_m \left(\frac{z}{z_0}, Ri_B \right)$$

$$u_*\theta_* = \frac{a^2}{R}u\Delta\theta F_h\left(\frac{z}{z_0}, Ri_B\right)$$

$$u_*q_* = \frac{a^2}{R}u\Delta q F_h\left(\frac{z}{z_0}, Ri_B\right),$$

where

$$a^2 = k^2 \left/ \left(\ln \frac{z}{z_0} \right) \right.$$

is the drag coefficient in neutral conditions (k is the Von Karman constant), and u refers here to the total wind, not to the x-component. The constant R , ratio of the drag coefficients for momentum and heat in the neutral limit, was estimated by Businger et al. (1971) to be 0.74. The universal functions F_m and F_h are adjusted for each of the following regimes:

1. In the unstable case ($Ri_B \leq 0$):

$$F = 1 - \frac{bRi_B}{1 + c|Ri_B|^{1/2}}.$$

2. In stable conditions ($Ri_B > 0$):

$$F = 1/(1 + b'Ri_B)^2,$$

where the factors b , b' and c are given by

$$b = 2b' = 9.4$$

$$c = C^*a^2b\left(\frac{z}{z_0}\right)^{1/2}.$$

$C^* = 7.4$ for momentum and 5.3 for the heat and moisture fluxes.

3. For free convection ($u \rightarrow 0$ and $Ri_B < 0$):

$$u_*\theta_* = -\frac{1}{5.3R_v}\left(\frac{gz_0}{\theta}\right)^{1/2}\Delta\theta^{3/2}$$

$$u_*q_* = -\frac{1}{5.3R_v}\left(\frac{gz_0}{\theta}\right)^{1/2}\Delta\theta^{1/2}\Delta q.$$

4. In the case $u \rightarrow 0$ and $Ri_B \geq 0$:

$$u_*\theta_* = u_*q_* = 0.$$

As can be seen in the above expressions, the surface eddy fluxes are directly dependent on the surface values of temperature and humidity. In particular, the necessary θ_{z_0} and q_{z_0} are calculated from the surface values θ_G and q_G with the expressions

$$\theta_{z_0} = \theta_G + 0.0962(\theta_*/k)(u_*z_0/\nu)^{0.45}$$

$$q_{z_0} = q_G + 0.0962(q_*/k)(u_*z_0/\nu)^{0.45},$$

where ν the kinematic viscosity of air.

Except over water masses as seas or lakes, where the surface temperature is assumed constant and the humidity is saturant, these parameters can vary significantly during the diurnal cycle. As a consequence, the surface sub-model is closed solving the energy and water budget equations at the air-soil interface to obtain the temperature and moisture at the surface. Diffusion equations for temperature and moisture content are solved in the soil, which is divided into several vertical levels. Such balances are significantly affected by the presence of vegetation, which modifies the partition and intensity of the surface turbulent fluxes. Its effect is modulated through the shielding factor, defined as the fractional coverage on a grid area by a dense vegetation canopy.

For convenience, we distinguish between bare soil and vegetative surfaces. Only the main formulations applied by the surface sub-model are given. For more details and for a description of the numerical implementation of the scheme, see Mahfouf et al. (1987a), Pinty et al. (1989), McCumber and Pielke (1981) and Deardorff (1978).

a. Bare soil

The land surface temperature $(T_s)_G$ for a surface of emissivity ϵ and albedo α , is computed by a iterative solution to the energy balance equation

$$(1 - \alpha)R_S + \epsilon R_L - \epsilon\sigma(T_s)_G^4 + \rho L_v u_* q_* + \rho C_p u_* \theta_* - (H_s)_G = 0. \quad (2.16)$$

R_S and R_L in the first and second terms are the solar and downcoming longwave radiative fluxes respectively, and the third term the outgoing longwave radiation from the surface (σ is the Stefan-Boltzman constant). Therefore, the three terms combined form the net radiation at the surface. The fourth, fifth and sixth terms are the latent, sensible and soil heat fluxes.

On the other hand, the moisture at the surface is obtained by solving the water budget equation

$$\rho u_* q_* + P - (W_s)_G = 0,$$

where P is the precipitation rate and $(W_s)_G$ the soil moisture flux at the surface.

The ground heat flux, H_s , and soil moisture flux, W_s , are written as

$$H_s = -\lambda \frac{\partial T_s}{\partial Z}$$

$$W_s = -\rho_w K_\eta \frac{(\psi + Z)}{\partial Z},$$

where ρ_w is the liquid water density, ψ the moisture potential, K_η the hydraulic conductivity of the soil and λ its thermal conductivity.

These fluxes are obtained by solving for several levels in the first meter of soil, diffusion equations for the temperature, T_s , and the volumetric moisture content, η :

$$\rho c \frac{\partial T_s}{\partial t} = \frac{\partial}{\partial Z} \left(\lambda \frac{\partial T_s}{\partial Z} \right)$$

$$\frac{\partial \eta}{\partial t} = \frac{\partial}{\partial Z} \left(D_\eta \frac{\partial \eta}{\partial Z} \right) + \frac{\partial K_\eta}{\partial Z},$$

where ρc is the specific heat capacity of the soil and D_η its hydraulic diffusivity. A set of equations relate the variables ψ , K_η , D_η , ρc and λ as functions of the soil moisture:

$$\begin{aligned} \psi &= \psi_s \left(\frac{\eta_s}{\eta} \right)^b \\ K_\eta &= K_{\eta_s} \left(\frac{\eta}{\eta_s} \right)^{2b+3} \\ D_\eta &= -\frac{bK_{\eta_s}\psi_s}{\eta} \left(\frac{\eta}{\eta_s} \right)^{b+3} \\ \rho c &= (1 - \eta_s)\rho_i c_i + \eta\rho_w c_w \\ \lambda &= 0.167\eta + 0.1. \end{aligned}$$

In the above equations, the saturated values η_s , K_{η_s} , ψ_s , the volumetric heat capacity of dry soil $\rho_i c_i$, as well the exponent b , are functions of the soil texture. Here, $\rho_w c_w$ is the heat capacity of water.

The relative humidity at the surface is calculated as function of $(T_s)_G$ and the surface moisture potential ψ_G :

$$h = \exp \left(-\frac{g\psi_G}{R_w(T_s)_G} \right).$$

The surface specific humidity is then determined from

$$q_G = hq_s,$$

where q_s is the saturation value at the temperature $(T_s)_G$.

b. Vegetative surfaces

Based on Deardorff (1978), the surface scheme also allows for the inclusion of a single layer of vegetation which is assumed to have negligible heat capacity. A second energy budget is established for the foliage layer taking into account the exchanges above and below the canopy. The modified expressions for the sensible heat and the evapotranspiration fluxes (H_{sh} and E_h respectively) from the ground foliage system to the atmosphere are

$$H_{sh} = H_{sg} + H_{sf} = \rho C_p c_{Hg} u_{af} (T_g - T_{af}) + 1.1N \rho C_p c_{f} u_{af} (T_f - T_{af}), \quad (2.17)$$

$$E_h = E_g + E_f = \rho c_{Hg} u_{af} (q_g - q_{af}) + N \rho c_{f} u_{af} [q_{sat}(T_f) - q_{af}] r''. \quad (2.18)$$

The first term of the sensible heat flux (H_{sg}) is the generalization of the sensible heat flux at the ground surface, and the second term (H_{sf}) the expression for the net sensible heat flux from the foliage to the surrounding air. Similarly, the first term of the evapotranspiration rate (E_g) denotes the evaporation at the ground surface, and the second

term (E_f) the net foliage evaporation and/or transpiration rate per unit horizontal ground area.

In Eqs. 2.17 and 2.18, c_{Hg} is the heat and moisture transfer coefficient applicable to the ground surface underneath a canopy. It is given by interpolation between that applicable to bare ground c_{H0} , and that applicable to the top of a dense canopy c_{Hh} :

$$c_{Hg} = (1 - \sigma_f)c_{H0} + \sigma_f c_{Hh},$$

where σ_f represents the shielding factor.

T_g and T_f (and q_g and q_f), refer to ground surface and foliage surface values respectively. The mean properties of the air within the foliage, T_{af} and q_{af} , are assumed to be intermediate between above-canopy air properties at $z = z_a$ (first atmospheric level of the model), foliage surface properties, and ground surface properties:

$$T_{af} = (1 - \sigma_f)T_a + \sigma_f(0.3T_a + 0.6T_f + 0.1T_g),$$

$$q_{af} = (1 - \sigma_f)q_a + \sigma_f(0.3q_a + 0.6q_f + 0.1q_g).$$

For the mean wind, the following expression is used

$$u_{af} = 0.83\sigma_f c_{Hh}^{1/2} u_a + (1 - \sigma_f)u_a.$$

The dimensionless heat transfer coefficient c_f which appears in Eqs. 2.17 and 2.18 is assumed to be given by

$$c_f = 0.01(1 + 0.3/u_{af}).$$

N , the net leaf area index, is defined as the total one-sided leaf area of the foliage relative to the ground area. As explained in Deardorff (1978), the fraction of potential evaporation from the foliage r'' is function of the liquid water retained on the foliage (predicted in response to precipitation and evaporation or condensation from or onto the leaves), the atmospheric resistance $(c_f u_{af})^{-1}$, and the stomatal resistance r_{st} , calculated with the expression

$$r_{st} = r_{st_{min}} S_{st} M_{st},$$

where $r_{st_{min}}$ is the minimum stomatal resistance (function of the vegetation type), S_{st} is the solar radiation factor and M_{st} is a factor limiting the transpiration when the soil becomes very dry or when the atmospheric demand is too strong (Pinty et al. 1989).

A gross energy budget for the foliage layer must be established in order to estimate T_f . The values at the top of the canopy being denoted by subscript h , those at the ground by subscript g , and the direction of radiative fluxes by arrows, the assumption of no canopy heat storage leads to

$$R_{Sh} \downarrow + R_{Lh} \downarrow - R_{Sh} \uparrow - R_{Lh} \uparrow - (R_{Sg} \downarrow + R_{Lg} \downarrow - R_{Sg} \uparrow - R_{Lg} \uparrow) = H_{sf} + L_v E_f,$$

where as in Eq. 2.16, R_S is the shortwave and R_L the longwave flux. The fluxes $R_{Sh} \downarrow$ and $R_{Lh} \downarrow$ are given by the radiation scheme. By definition of the shielding factor σ_f , $R_{Sg} \downarrow$ is given by

$$R_{Sg} \downarrow = (1 - \sigma_f) R_{Sh} \downarrow.$$

Given the ground albedo α_g , the reflected flux $R_{Sg} \uparrow$ is given by

$$R_{Sg} \uparrow = \alpha_g(1 - \sigma_f)R_{Sh} \downarrow.$$

The upward longwave flux just above the ground, $R_{Lg} \uparrow$, is obtained by interpolating with σ_f between the expression applicable above bare soil and that applicable just above soil overlain with a dense canopy:

$$R_{Lg} \uparrow = (1 - \sigma_f)[\epsilon_g \sigma T_g^4 + (1 - \epsilon_g)R_{Lh} \downarrow] + \sigma_f[\epsilon_g \sigma T_g^4 + (1 - \epsilon_g)\epsilon_f \sigma T_f^4]/(\epsilon_f + \epsilon_g - \epsilon_f \epsilon_g).$$

For $\sigma_f = 1$ this expression for $R_{Lg} \uparrow$ reverts to that for the radiative flux between two parallel surfaces of emissivities ϵ_g and ϵ_f . For $\sigma_f = 0$ the expression similarly accounts for the upward reflection of $R_{Lh} \downarrow$ from the ground when $\epsilon_g < 1$. The three remaining radiative fluxes are similarly obtained:

$$R_{Sh} \uparrow = \alpha_g(1 - \sigma_f)R_{Sh} \downarrow + \alpha_f \sigma_f R_{Sh} \downarrow,$$

$$R_{Lh} \uparrow = (1 - \sigma_f)[\epsilon_g \sigma T_g^4 + (1 - \epsilon_g)R_{Lh} \downarrow] + \sigma_f[\epsilon_f \sigma T_f^4 + (1 - \epsilon_f)R_{Lh} \downarrow],$$

$$R_{Lg} \downarrow = (1 - \sigma_f)R_{Lh} \downarrow + \sigma_f[\epsilon_f \sigma T_f^4 + (1 - \epsilon_f)\epsilon_g \sigma T_g^4]/(\epsilon_f + \epsilon_g - \epsilon_f \epsilon_g).$$

At the ground surface, the balance equations written for bare soil are maintained, but the fluxes are now represented by $R_{Sg} \downarrow$, $R_{Lg} \uparrow$, $R_{Lg} \downarrow$, H_{sg} , E_g , etc.

2.6 Radiation parameterization

Calculations of solar radiation R_S and downcoming longwave radiation R_L are necessary to solve the surface energy balances presented in section 2.5. The radiation scheme, based on Mahrer and Pielke (1977), determines the evolving radiative fluxes in the atmosphere. Therefore, it allows the calculation of R_S and R_L at the ground, and the solar radiative heating and longwave cooling rates for each atmospheric layer through the flux divergence. Both rates combine to give the source-sink term S_S in the thermodynamical equation 2.6.

Scattering and absorption of solar radiation by permanent gases such as oxygen, ozone and carbon dioxide is included in the scheme. Absorption and longwave emission by the atmospheric water constituents (water vapor and clouds) is also considered. For a detailed description of the radiation scheme, the reader can find the parameterized form of the shortwave transmissivity functions and longwave emissivities in Mahrer and Pielke (1977) and Pielke (1984, chapter 8). Only the formulation of the modified surface fluxes to account for the terrain slope is here given explicitly:

Denoting \bar{R}_S and \bar{R}_L as the solar and longwave fluxes for a horizontal surface, for a slant surface the solar and infrared radiation will be modified to

$$R_S = \bar{R}_S \frac{\cos i}{\cos Z},$$

$$R_L = \bar{R}_L \cos \alpha.$$

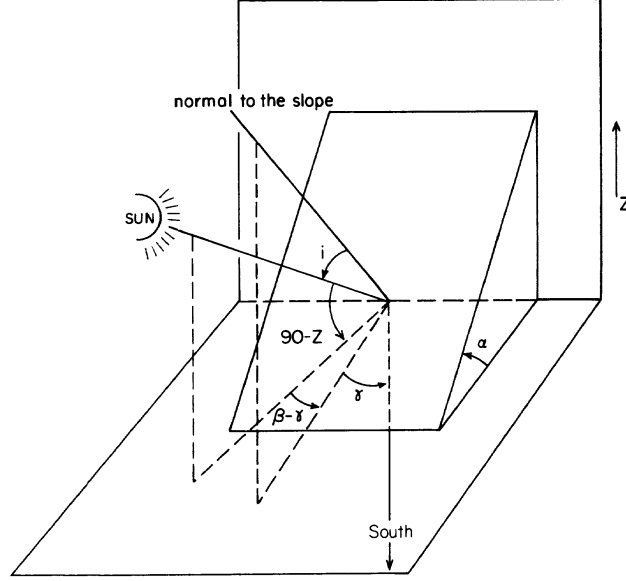


Figure 2.2: Angles considered to derive the radiative fluxes for slant surfaces.

The slope angle α is calculated from the terrain height z_G with the expression

$$\alpha = \tan^{-1} \left[\left(\frac{\partial z_G}{\partial x} \right)^2 + \left(\frac{\partial z_G}{\partial y} \right)^2 \right]^{1/2}.$$

The solar zenith angle Z obeys $\cos Z = \sin \varphi \sin \delta + \cos \varphi \cos \delta \cos \psi$, where φ is the latitude, δ the solar declination and ψ the solar hour angle (see Figure 2.2). Finally, i is the angle of incidence of solar rays on the inclined surface, where

$$\cos i = \cos \alpha \cos Z + \sin \alpha \sin Z \cos(\beta - \gamma).$$

Requiring that south has zero azimuth, the solar and slope azimuths β and γ are given by:

$$\beta = \sin^{-1} \left(\frac{\cos \delta \sin \psi}{\sin Z} \right),$$

$$\gamma = \tan^{-1} \left(\frac{\partial z_G}{\partial y} / \frac{\partial z_G}{\partial x} \right) - \frac{\pi}{2}.$$

2.7 Boundary conditions

At the top of the model domain, the vertical velocity $\dot{\nu}$ is set to zero. However, especially for the case of flows over mountains, vertical transport of momentum may be very important and reach high altitudes, inducing reflection from the uppermost level with such boundary condition. To minimize reflection from the upper boundary, an absorbing layer containing several computational levels is included. In the absorbing layer, the

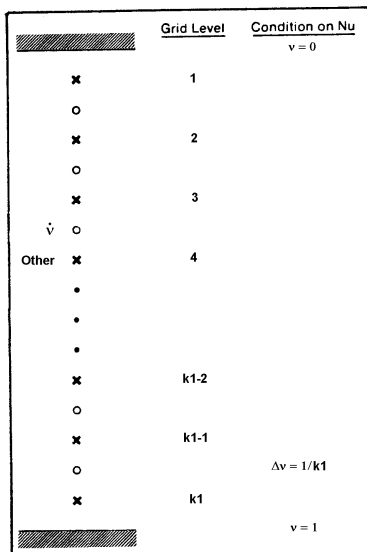


Figure 2.3: Vertical grid of the numerical model.

background diffusion (imposed by a second order operator in this layer), is progressively increased, reaching its maximum value at the top level (Nickerson et al. 1986):

$$K_{H2} = K_{H2}^* + K_{H2}^{abs} \left(\sin \frac{\pi}{2} \frac{\sigma_{kabs} - \sigma_k}{\sigma_{kabs}} \right)^2 \text{ for } k < kabs.$$

In this expression, $kabs$ is the number of vertical levels composing the absorbing layer. The second-order diffusion constant K_{H2} has the maximum value $K_{H2}^* + K_{H2}^{abs}$ at the top where $\sigma_1 = 0$, and equals the background value K_{H2}^* at level $k = kabs$

At the lateral boundaries, the values of the fields are prescribed externally. To avoid reflection, the prognostic variables are subjected to a forcing in the marginal zone (4 interior points from the boundary) that constrains them to relax towards the externally specified field on a time scale that varies with distance from the lateral boundary (Davies 1976).

2.8 Numerical aspects

For the integration of the governing equations, a staggered vertical grid (Figure 2.3) is used. With reference to the figure, variable $\dot{\nu}$ is defined at the circled levels, and all other variables are defined at the crosses.

The horizontal grid (Figure 2.4) is also staggered to reduce the truncation errors on the level ν surfaces (Anthes and Warner 1974). The dynamical variables u and v are defined at the crosses, while all thermodynamic variables are defined at the dots. The variable $\dot{\nu}$ is not defined on this horizontal level but at distances $\Delta\nu/2$ above or below this level and at positions corresponding to the dots.

Centered differences are used to represent the time and space derivatives. That is, the terms of the equations are evaluated with centered spatial differences at the middle

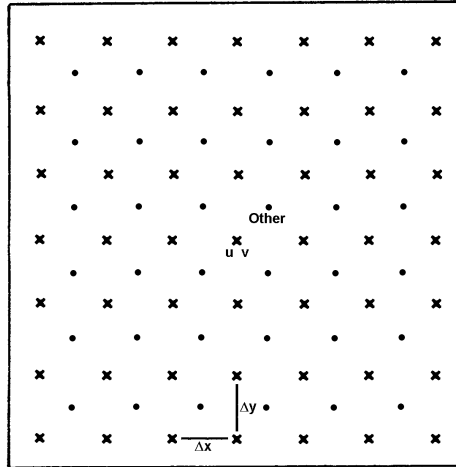


Figure 2.4: Horizontal grid of the numerical model.

time level and used to advance the integration between $t - \Delta t$ and $t + \Delta t$ in a single step (leapfrog scheme). However, for reasons of stability the horizontal diffusion term is evaluated at $t - \Delta t$. The vertical diffusion is treated implicitly.

An Asselin filter is applied to connect odd and even time steps. The filtered value at the $t - 1$ time level $\tilde{\chi}^{t-1}$ is given by

$$\tilde{\chi}^{t-1} = \chi^t + \alpha(\chi^{t+1} - 2\chi^t + \chi^{t-1}),$$

where the coefficient α takes a value of 0.25 (Schlesinger et al. 1983).

Chapter 3

TRANSPORT AND DIFFUSION OF COASTAL POLLUTANTS DURING THE BREEZE CYCLE IN MALLORCA

In this chapter¹, the SALSA model is used to perform an Eulerian study of the distribution over Mallorca of a non-reactive pollutant (SO₂) emitted from the electric power plant operating on the north coast (EP1 in Figure 1.1). The study, referred to as experiment S1, is applied to the conditions of sea-land breeze development. As emphasized in section 1.2, this is a local circulation that dominates the flow during the summer and favours transporting pollutants from the coast toward the centre of the island. In order to assess the impact of a hypothetical scenario with a second power plant on the south coast of the island, a second experiment is designed. For this experiment, referred to as S2, the numerical simulation is carried out with the inclusion of a twin electric plant (EP2 in Figure 1.1).

Since wind and stability are highly variable throughout the breeze cycle, continuously affecting the advection and diffusion of the pollutant, meteorological fields and pollutant distribution are predicted simultaneously in order to capture such dependence better. We have adapted the SALSA model with the inclusion of a new prognostic equation, representing the transport and diffusion of a pollutant which is assumed not to be affected by chemical reactions (see the Appendix for a list of symbols):

$$\frac{\partial \pi C_i}{\partial t} = -\frac{\partial \pi C_i u}{\partial x} - \frac{\partial \pi C_i v}{\partial y} - \frac{1}{\sigma'} \frac{\partial \sigma' \pi C_i \dot{\nu}}{\partial \nu} + D_{\pi C_i} + F_{\pi C_i} + S_{\pi C_i}. \quad (3.1)$$

In this conservation relation, the term $S_{\pi C_i}$ represents the sources and sinks of the pollutant. Neglecting chemical transformations (a constraint that can be accepted for

¹The content of this chapter is based on the papers (i) Ramis, C., and R. Romero, 1995: A first numerical simulation of the development and structure of the sea breeze in the island of Mallorca. *Ann. Geophys.*, **13**, 981-994. (ii) Romero, R., and C. Ramis, 1996: A numerical study of the transport and diffusion of coastal pollutants during the breeze cycle in the island of Mallorca. *Ann. Geophys.*, **14**, 351-363.

sulphur dioxide released into a dry environment for local studies; see McVehil 1989) and dry deposition, that term becomes zero except at grid points identified as the contaminant sources.

$D_{\pi C_i}$ and $F_{\pi C_i}$ represent the diffusive terms. The horizontal diffusion $D_{\pi C_i}$ is described by a fourth-order operator. Vertical turbulent mixing $F_{\pi C_i}$ is expressed through an eddy-diffusivity assumption:

$$F_{\pi C_i} = B \frac{\partial}{\partial \nu} \left(BK_{ex} \frac{\partial \pi C_i}{\partial \nu} \right),$$

with

$$B = -\frac{gP}{\pi R_v T \sigma'}.$$

The exchange coefficient K_{ex} is space and time dependent, since it is calculated as a function of the turbulent kinetic energy e , which is predicted by the model, and of the mixing length scale l_k ,

$$K_{ex} = 0.4l_k e^{1/2},$$

following Therry and Lacarrère (1983) and Bougeault and Lacarrère (1989).

Prior to the presentation of the results, section 3.1 explains the initialization of the experiments and characteristics of the pollutant sources. Section 3.2 presents the meteorological aspects of the breeze cycle, which are fundamental to understand the physical mechanisms operating on the pollutant. Results of SO₂ concentration are discussed in section 3.3, and the possible impact of dry deposition and a second cycle of breeze is determined by means of a new simulation. Finally, section 3.4 contains the conclusions.

3.1 Initialization and sulphur dioxide sources

Both numerical simulations were run with identical meteorological background. The first simulation S1 includes a sulphur dioxide source that represents continuous emission from the presently working electric plant EP1 (see Figure 1.1 for location). In the second simulation S2, a twin electric plant is added at the point EP2 (see Figure 1.1). In both experiments the radiation parameters correspond to 15 July at a latitude of 40°N. The simulations begin at 0500 LST (on Mallorca, the local time practically matches UTC) and cover the diurnal cycle. The model domain is 150 x 150 km² with a horizontal grid length of 2.5 km.

3.1.1 The atmosphere

We used 30 vertical levels resulting in 9 computational levels in the lowest kilometer, the first of which was approximately 4.5 m above the ground. A high resolution of the PBL is important in this kind of simulation. The model was initialized with a single radiosonde, providing horizontally uniform fields at the beginning of the simulation. This radiosounding (Figure 3.1) corresponds to the mean vertical structure of the atmosphere over Mallorca for July at 0000 UTC (Ramis 1976). During summer, the Azores anticyclone affects the western Mediterranean. As a consequence of the thermal low-pressure developed over the Iberian peninsula, an anticyclonic circulation becomes reinforced in

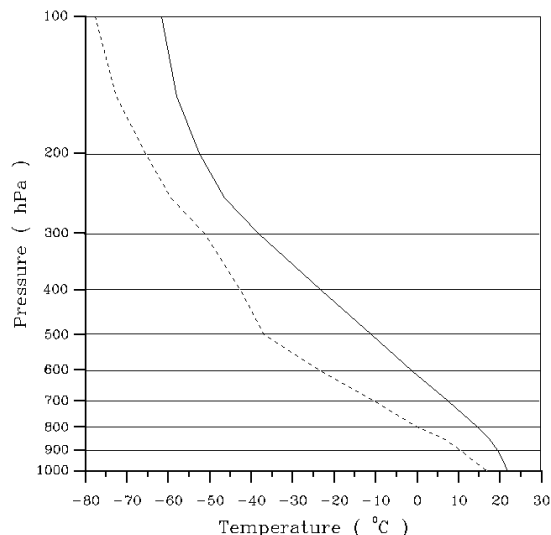


Figure 3.1: Mean vertical structure of the atmosphere over Mallorca for July at 0000 UTC (after Ramis 1976). Solid line represents temperature and dashed line represents dew point.

such a manner, that the pressure gradient, and therefore the synoptic forcing, is very weak over the western Mediterranean (Font 1983; Figure 1.2). For that reason, the wind was initialized as calm. During the simulation, all fields are relaxed toward their initial values at the lateral boundaries (Davies 1976).

3.1.2 The surface

Despite its small size, the island of Mallorca presents a complex distribution of vegetative covers and soil textures. This aspect could influence the structure of the breeze through the spatial and temporal distribution of surface fluxes and friction. For that reason, a detailed representation of vegetation covers and soil characteristics has been considered.

Figures 3.2a and b show the distribution of soil and vegetation types on the island used for the simulation. The maps are a coarse version of soil and vegetation charts of the region. Landsat images have been considered in addition to the charts information. Five representative textural classes and vegetative covers have been considered. The characteristic parameters required by the surface submodel described in section 2.5, have been approximated based on previous classifications (Tables 3.1 and 3.2). Areas of sparse vegetation are mixed with others of dense cover as can be seen in Figure 3.2c, which shows the shielding factor.

The sea surface temperature is 25°C. The initial temperature on the land surface corresponds to the distribution of the mean minimum temperature during July over the island (Guijarro 1986).

The soil, supposed to have a depth of 1 m, is divided into 13 vertical levels. Sub-surface measurements are not available at present. As a consequence, temperature and moisture profiles have been initialized in a simple way. The temperature profile is initially homogeneous, given by the value at the soil surface. Representing the soil state during

Soil type	η_s	K_{η_s} ($\cdot 10^{-6}$ m s $^{-1}$)	ψ_s (m)	$\rho_i c_i$ ($\cdot 10^6$ J m $^{-3}$ K $^{-1}$)	b	ε	a	z_0 (mm)
Sand	0.395	176.0	-0.121	1.463	4.05	0.99	0.25	5
Sandy Loam	0.410	156.0	-0.090	1.404	4.38	0.99	0.25	5
Silt Loam	0.430	25.0	-0.200	1.300	4.80	0.99	0.30	5
Clay Loam	0.460	3.0	-0.440	1.150	8.40	0.99	0.25	5
Clay	0.482	1.3	-0.405	1.089	11.40	0.99	0.35	5

Table 3.1: Soil parameters for five textural classes representative of Mallorca. The parameters have been computed combining those given in the classification of the U. S. Department of Agriculture (Clapp and Hornberger 1978; McCumber 1980): η_s (soil porosity), K_{η_s} (saturated hydraulic conductivity), ψ_s (saturated moisture potential), $\rho_i c_i$ (dry volumetric heat capacity) and b (dimensionless exponent). ε is the emissivity, a the albedo and z_0 the roughness length.

summer, which presents a strong water deficit (see Figure 1.3), the volumetric water content (see Table 3.3) is given as a function of the soil type but is very low at the surface and increases a little with the depth (Vadell, personal communication). However, the listed values are modified by a regional multiplicative factor in order to account for the heterogeneous mean pluviometry on the island. The spatial distribution of the multiplicative factor is shown in Figure 3.2d.

3.1.3 Sulphur dioxide sources

The thermal electric plant burns 2400 T/day of coal with a sulphur content of 0.6 %. The effluents are released into the atmosphere through a stack with a height of 144 m and a diameter of 3.3 m. The gases are released at a temperature of 155 °C and a vertical velocity of 30 m/s.

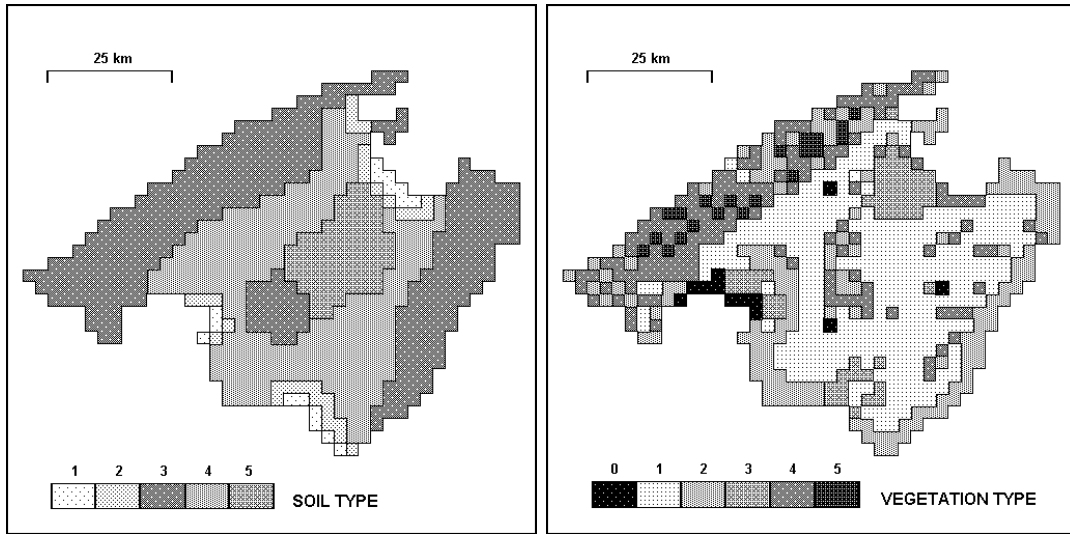
For a typical meteorological state during the breeze in Mallorca, those parameters result in an effective source height (Pasquill 1974) of approximately 500 m, which corresponds to the sixth atmospheric level of the computational grid. Also, the nearly constant consumption by the plant results in a continuous emission rate of 0.34 kg/s of SO₂, which is assumed to mix instantly with the environmental air within the source grid cell.

3.2 Meteorological aspects

3.2.1 Development and structure of the sea breeze

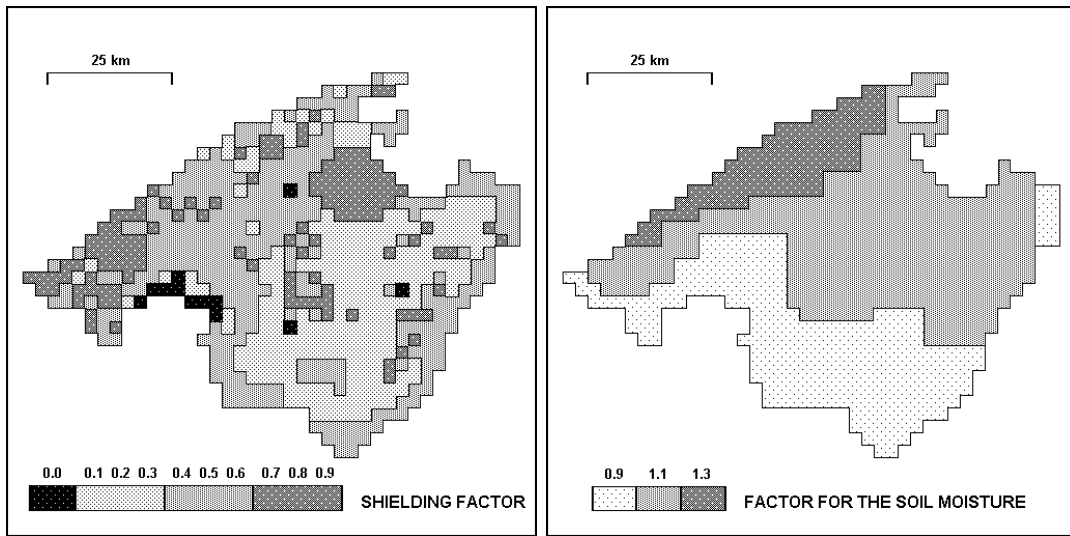
The wind distribution at different times over the island corresponding to the lowest level of the model (4.5 m above the ground) are presented in Figure 3.3.

At 0900 LST (Figure 3.3a) the breeze penetrates inland by only a few kilometers, except at the northwest coast where the wind is very weak. The breeze front is easily identified. The flux is stronger from the Bay of Palma. The influence of the eastern slope



(a) Soil

(b) Vegetation



(c) Shielding factor

(d) Moisture factor

Figure 3.2: (a) Soil distribution on Mallorca: 1=sand, 2=sandy loam, 3=silt loam, 4=clay loam and 5=clay; (b) Vegetation distribution: 0=bare, 1=grass, 2=shrub, 3=crop, 4=forest and 5=woodland; (c) Shielding factor; (d) Regional multiplicative factor used to compute the soil moisture on the island.



Figure 3.3: Diurnal evolution of the sea breeze. (a) 0900 LST; (b) 1500 LST; (c) 2100 LST and (d) 0500 LST. The arrow on the upper left corner represents 10 m s^{-1} . Orographic contours of 300 and 700 m are included.

Parameter	Vegetation type				
	Tall Grass	Shrub	Crop	Conifer Forest	Woodland
Height (m)	2.0	0.5	0.4	12.0	10.0
Displacement height (m)	1.50	0.37	0.30	9.00	7.50
Plant resistance (s)	8.10^9	10.10^9	6.10^9	8.10^9	8.10^9
Minimum stomatal resistance ($s\ m^{-1}$)	350	500	50	350	350
Critical leaf water potential (m)	-150	-150	-100	-150	-180
Green leaf area index	2.0	1.0	1.0	3.5	5.0
Dry leaf area index	2.0	2.0	0.1	0.7	1.0
Canopy emissivity	0.98	0.98	0.96	0.98	0.98
Canopy albedo	0.16	0.16	0.20	0.10	0.15
Roughness length (m)	0.17	0.04	0.03	1.00	0.83
Average rooting depth (m)	0.2	0.2	0.2	0.9	0.9

Table 3.2: Parameters of five representative types of vegetation of Mallorca. The values have been approximated using the HAPEX-MOBILHY data (Pinty et al. 1989).

of the Serra de Tramontana can be identified: the flux from the two bays is veering and backing, respectively, toward that warmer slope.

The circulation becomes developed after 1200 LST, with a clear appearance of the convergence line in the centre of the island. Figure 3.3b shows the wind distribution at 1500 LST and represents the fully developed state. It may be compared with Figure 1.4a. The convergence line formed between the breezes from the two bays is represented as well as other smaller convergence zones in the northeast, close to the coast, in the southeast as a continuation of the main convergence and over the eastern part of the main range mountain, in good correspondence with Figure 1.4b. Two small and very shallow cyclonic circulations have appeared in the simulation at this time. The first one, in the centre of the island, is a consequence of the shear between the main fluxes and the heat flux from the soil to the air. This cyclonic circulation can be considered as a small thermal low since its thermal structure, as we will show later, is similar, in a smaller scale, to that previously identified in such kinds of systems. The second is located over the west of the island, in the south of a notable mountain group. Much more than a lee development, it may be considered as a result of cape effect combined with the fact that the breeze is a shallow circulation.

The simulation shows that the breeze weakens very quickly after 1900 LST. At 2100 LST (Figure 3.3c) a weak cyclonic circulation remains around the island. However, the small cyclones still seem to maintain their influence on the breeze. In fact, that previously located in the centre has moved to the north and influences the wind in the northern part of the island. At the same time, the cyclonic circulation previously located over the west has moved to the east, being over the coast of the Bay of Palma and dominating the circulation in the bay and on south coasts.

Soil type	η_{up}	η_{down}
Sand	0.005	0.020
Sandy Loam	0.020	0.060
Silt Loam	0.030	0.090
Clay Loam	0.040	0.100
Clay	0.050	0.110

Table 3.3: Representative volumetric water content as a function of soil type for the case of Mallorca during July. η_{up} corresponds to the upper 10 cm layer and η_{down} to the 90 cm layer below.

The structure at the end of the simulated diurnal cycle (0500 LST) is presented in Figure 3.3d. Although some remaining winds can be appreciated to the north and south-west of the island, the circulation is very weak. A slight land breeze has developed at the same time over the coast of the south, east and northeast. The simulation with a second diurnal cycle shows that the circulation appears again with similar timing and characteristics.

The vertical structure of the circulation has been studied by means of cross sections along the lines AB, which includes the strongest winds at low levels, and CD, which includes the convergence line (see Figure 1.1).

The Figure 3.4a shows the vertical structure of the wind component along AB at 1500 LST. This section shows that the sea breeze, when fully developed, has a depth smaller than 1 km. The maximum winds occur over the coast, but the wind from the Bay of Alcudia reaches higher values. The convergence in the centre of the island is very strong, with large values for the acceleration of the currents. The counter-current also has a depth of approximately 1 km but with values less than those of the currents. The greater values of the counter-current are from the northeast and located over the Bay of Palma. The cross section along the convergence line CD (Figure 3.4b) shows that in this direction the sea breeze is shallower than along the AB direction. In the northwest of the island the breeze does not overcome the mountain range and becomes restricted over the sea, whereas on the eastern coast the wind can overcome the mountains, albeit with lower speeds with respect to the other direction. Although some evidence of convergence can be appreciated over the eastern part of the island, the central part of the section is entirely dominated by divergence in contrast with section AB, where convergence at low levels corresponds to divergence at upper levels.

The vertical velocity at 1500 LST along the cross section AB is shown in Figure 3.5. As a consequence of the convergence over the centre of the island, a region of strong and concentrated upward vertical motion is developed, with velocity values that exceed 35 cm s^{-1} . A secondary zone of upward velocity is produced by the southwest flux due to orographic lifting. The descending motion is very slow and spread out with values that do not exceed 10 cm s^{-1} .

The perturbation on the temperature field at 1500 LST along AB as a consequence

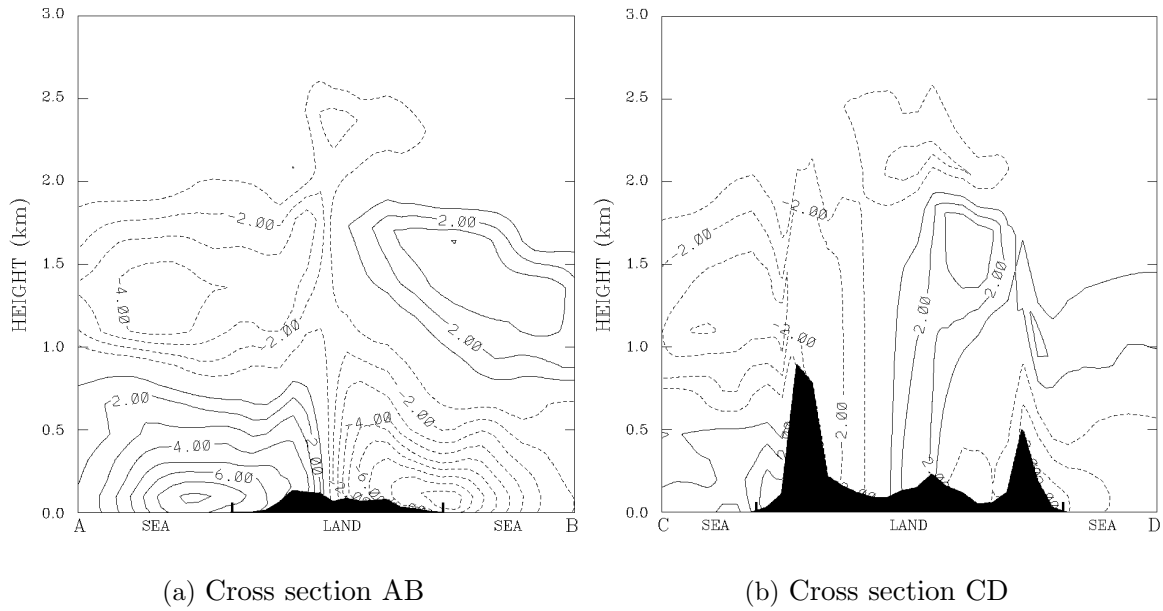


Figure 3.4: Vertical cross section (see Figure 1.1) showing the horizontal wind component (ms^{-1}) at 1500 LST: (a) along AB (positive values, in solid line, are from the southwest); (b) along CD (positive values from the northwest). Contour interval is 1 ms^{-1} and zero contour is not shown.

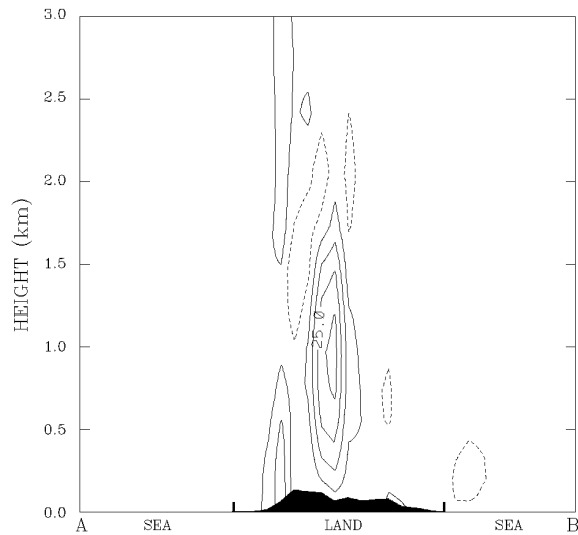


Figure 3.5: Vertical cross section along AB (Figure 1.1) showing the vertical velocity field (cms^{-1}) at 1500 LST. Contour interval is 10 cms^{-1} starting at 5 cms^{-1} for solid contour (ascending motion) and -5 cms^{-1} for dashed contour (descending motion).

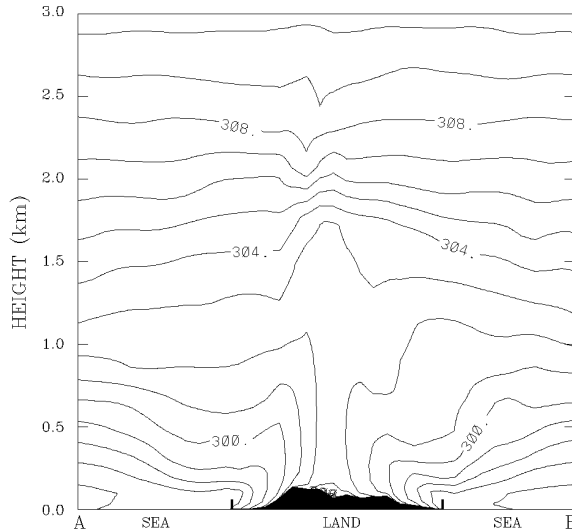


Figure 3.6: Vertical cross section along AB (Figure 1.1) showing the potential temperature (K) at 1500 LST. Contour interval is 1 K.

of the solar radiation is presented in Figure 3.6. The perturbation is limited to the lowest 3 km, but the most important feature occurs at low levels where the isentropes intercept the surface, determining a dome of superadiabatic lapse rate and therefore of absolute instability. The higher temperatures are reached in the centre of the island where the small cyclone appears. This thermal configuration, associated with the circulation, resembles, at a smaller scale, that observed over the Iberian peninsula when thermal low pressure develops during the summer (Alonso et al. 1994).

3.2.2 Verification of results

The model results have been compared against observations made at different points over the island during July 1993, in particular with the data from four automatic weather stations, the aeronautical observations at the airport and the data from a climatic observatory (see Figure 1.1 for location). In all the observatories, there are for different days, some differences in the breeze data as a consequence of the influence on the local circulation of the particular synoptic situation. For this reason the model results must be considered as an approximation to the mean aspects of the breeze, since the initialization process uses horizontally uniform atmospheric mean values and does not include background flux.

Figure 3.7 shows the comparison between the temporal sequence given by the model and observations at the automatic weather station AS1 (see Figure 1.1 for location). The wind direction (Figure 3.7a) matches very well with the observations, including the change observed at about 2000 LST. In the model, this change is produced by the displacement of the cyclonic circulation developed on the west side of the island toward the coast of the Bay of Palma. This result supports the development of such small circulation and explains the observed change in the wind direction. Figure 3.7b shows that the model overestimates the wind speed, especially during the central hours of the day, but also shows that it represents well the decrease and later increase of the wind speed associated

with the change in the wind direction. Despite the initialization of the atmospheric fields based on the mean sounding of July, and the crude initial soil profiles, the tendencies for the temperature and relative humidity given by the model close to the surface are again in agreement with those indicated by the observations (Figures 3.7c and d).

Figure 3.8 displays the model results and observations at AS2. Wind speed and direction are well represented by the model, except between 1400 and 1600 LST. During this interval the observed wind direction changes between northwest and northeast, despite the previous and later dominant direction being south-southwest. At the same time the wind speed decreases but afterwards increases to recover the tendency previously indicated. This abnormal structure at this particular day can be due to the local formation, south to the position given by the model, of the central cyclonic circulation. This is the only evidence of such development since this anomalous change is not observed on other days at AS2 and the model reproduces the wind data well.

The model underestimates the wind speed at AS3, as can be seen in Figure 3.9b, but reproduces the direction (Figure 3.9a) well, especially during the afternoon. This underestimation is observed during the majority of the days selected for verification.

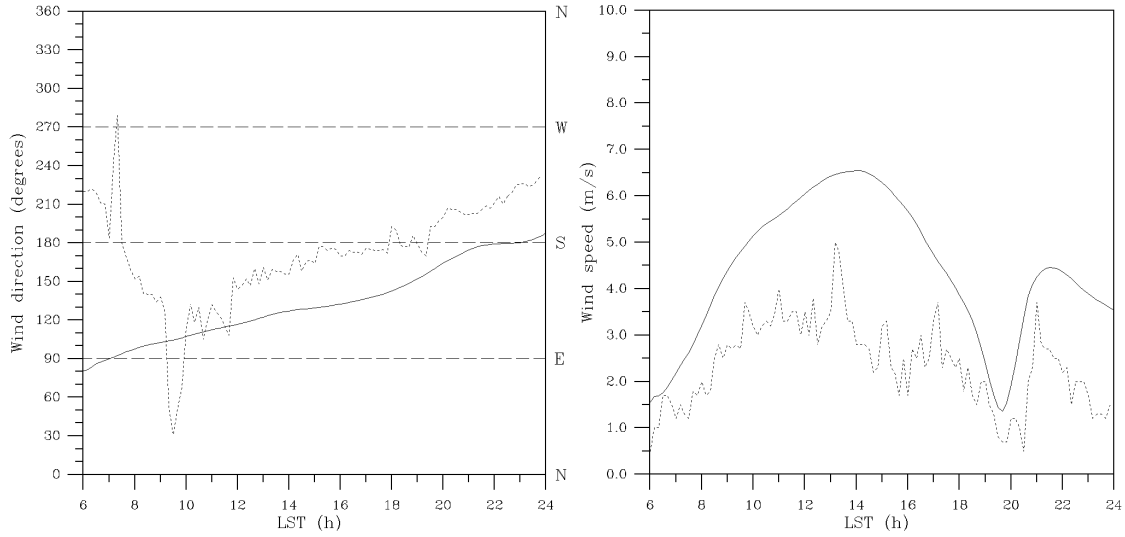
The agreement between observed data and model results is quite good at AS4 (Figure 3.10). A particular feature that appears at AS4 is that the wind maintains an appreciable value during the evening in contrast with the other stations where the wind decreases rapidly to very small values after 2100 LST. The model reproduces this behaviour at AS4.

The comparison between the aeronautical observations at the airport (A in Figure 1.1) and the model results (Figure 3.11) shows that the simulation is good in direction as well as in the speed of the wind. Although the climatological observations at C (see Figure 1.1) are limited to three values during the day, the model results match well with the data at these particular times.

3.2.3 Influence of the orography and soil dryness

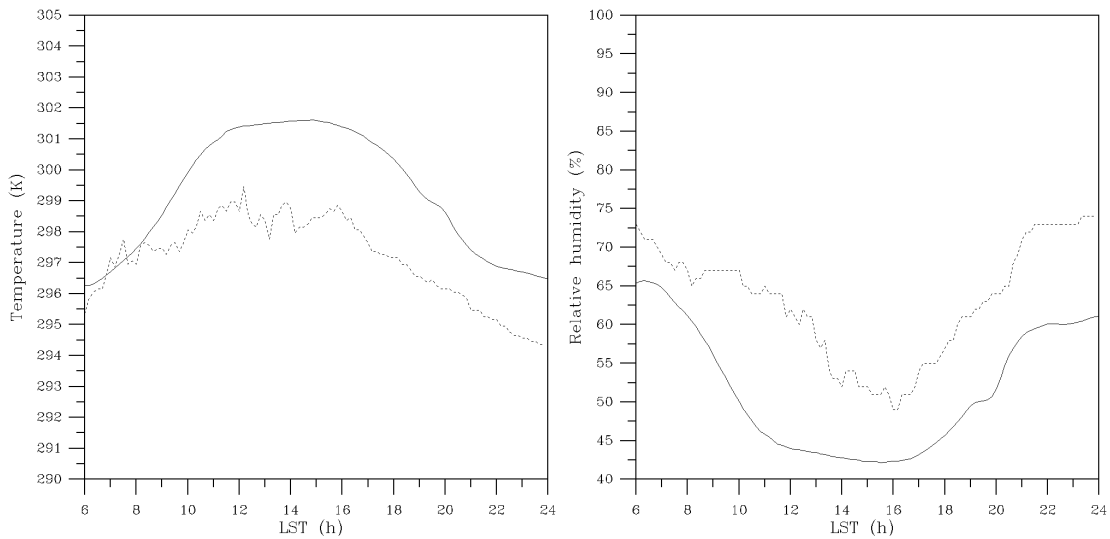
From the previous results, it seems that the orography and soil dryness of the island are decisive factors for determining the structure and intensity of the breeze. We have isolated the effects of these factors by means of numerical simulations, following the technique of Stein and Alpert (1993). An important principle of this technique is that when more than one factor is considered, it is not sufficient simply to compare a simulation done by removing some physical effect from the control simulation. That is, there is a contribution associated with the interaction of two (or more) factors that must be considered. In general, to isolate the effect of n factors, it is necessary to perform 2^n simulations. In our case, three more experiments have been necessary. Table 3.4 shows the characteristics of the whole set of experiments.

We identify as f_0 the experiment without orography and with saturated soil, f_1 represents the experiment with orography and saturated soil, f_2 without orography and with dry soil, and f_{12} is the complete experiment with orography and dry soil, already discussed in the previous sections. Except for these two factors the rest of parameters are initially the same for the four experiments. The contributions associated with both factors are determined by



(a) Wind direction

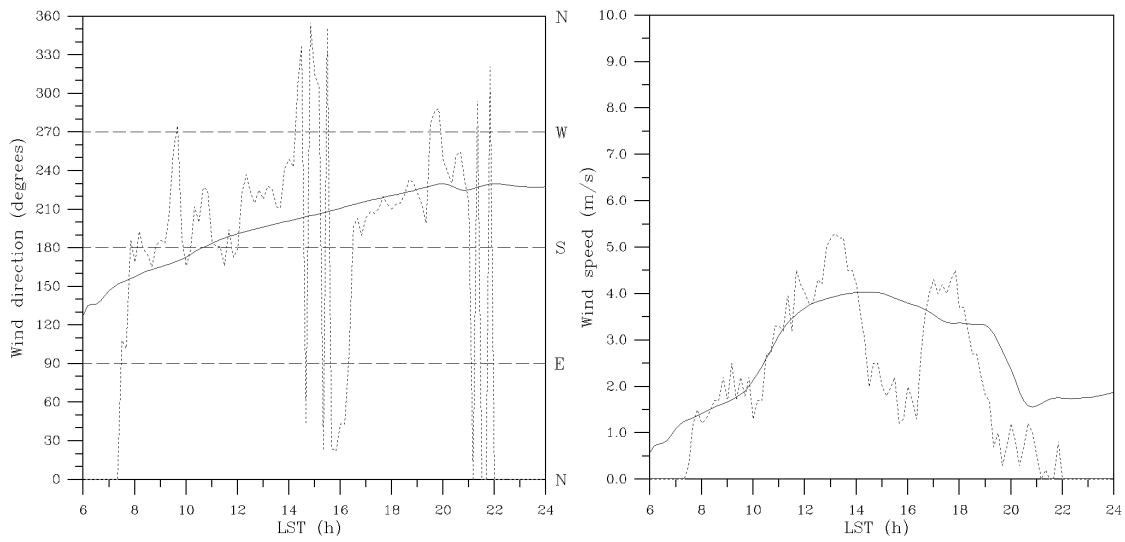
(b) Wind speed



(c) Temperature

(d) Relative humidity

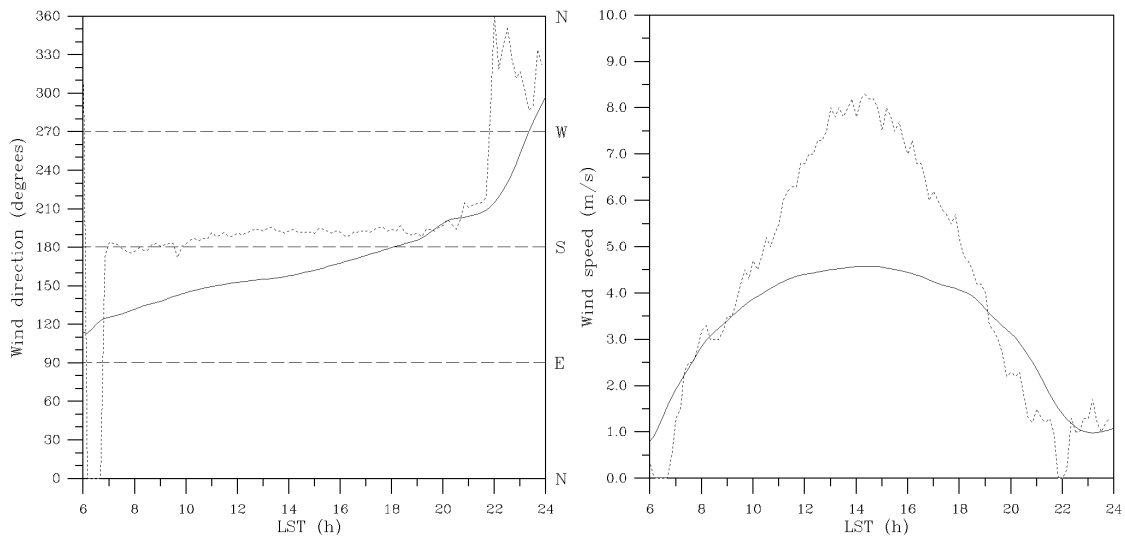
Figure 3.7: Model results (solid line) compared against observations on 22 July 1993 (dots) at AS1 (Figure 1.1): (a) wind direction; (b) wind speed; (c) temperature and (d) relative humidity.



(a) Wind direction

(b) Wind speed

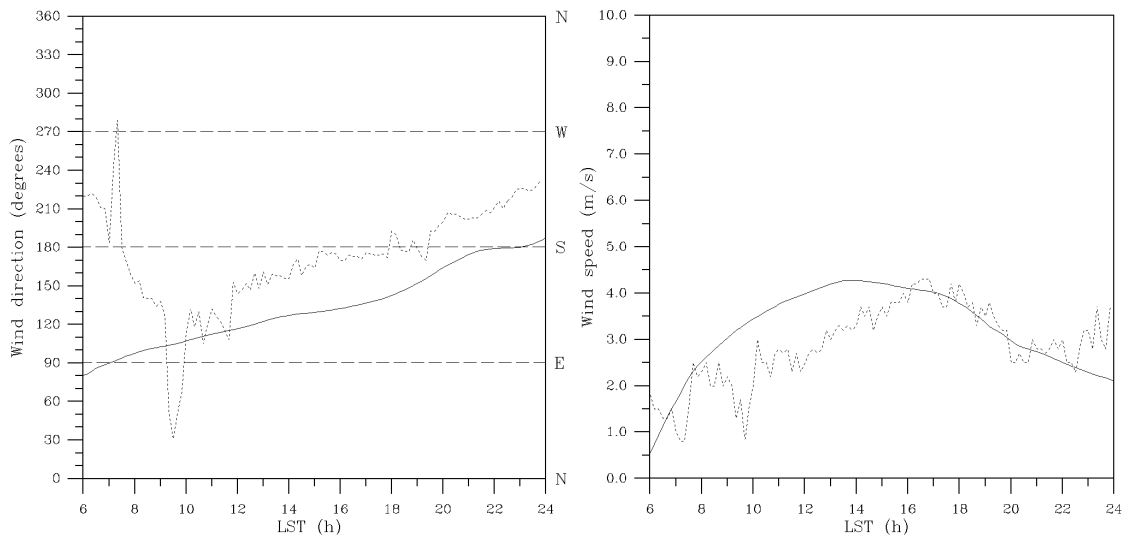
Figure 3.8: The same as in Figure 3.7 but at AS2 (Figure 1.1) for: (a) wind direction; (b) wind speed.



(a) Wind direction

(b) Wind speed

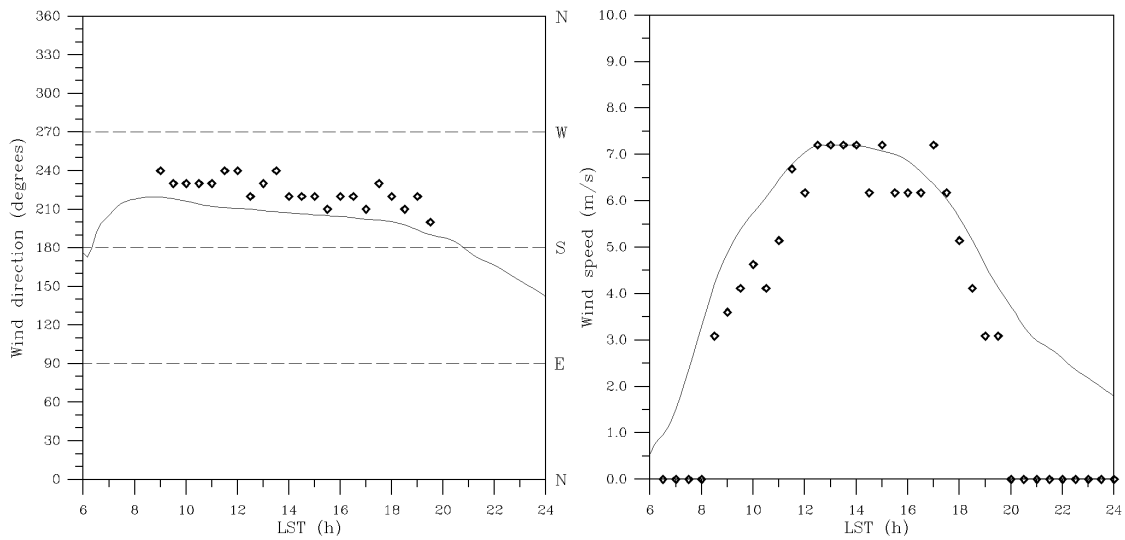
Figure 3.9: The same as in Figure 3.7 but at AS3 (Figure 1.1) for: (a) wind direction; (b) wind speed.



(a) Wind direction

(b) Wind speed

Figure 3.10: The same as in Figure 3.7 but at AS4 (Figure 1.1) for: (a) wind direction; (b) wind speed.



(a) Wind direction

(b) Wind speed

Figure 3.11: Model results (solid line) against observations on 22 July 1993 (rhombs) in A (Figure 1.1): (a) wind direction; b) wind speed.

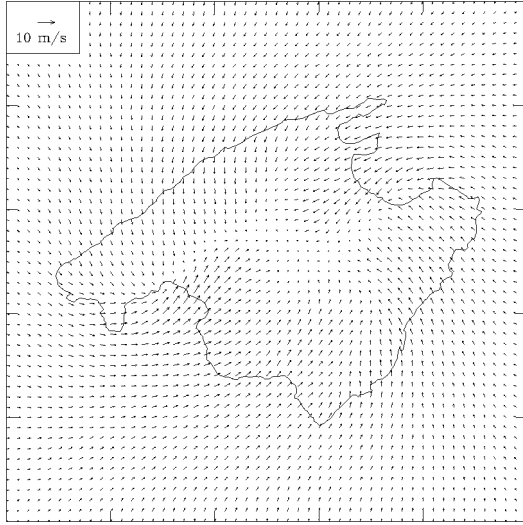
Experiment	Orography	Soil Dryness
f_0	NO	NO
f_1	YES	NO
f_2	NO	YES
f_{12}	YES	YES

Table 3.4: Summary of the numerical experiments performed in order to isolate the effect of the orography and soil dryness on the breeze circulation over Mallorca. f_{12} is the complete or actual case discussed in section 3.2.1.

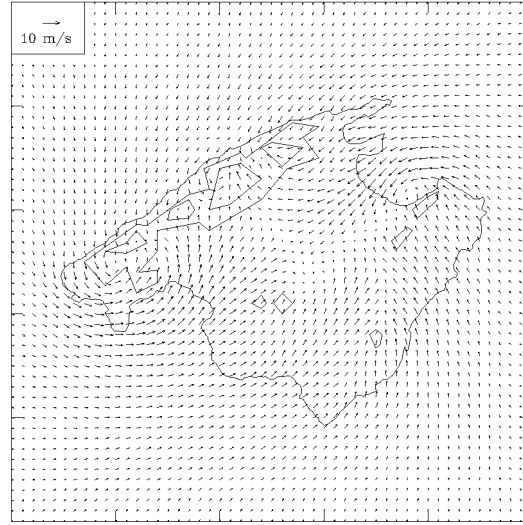
1. Effect of the orography $f_1^* = f_1 - f_0$
2. Effect of the soil dryness $f_2^* = f_2 - f_0$
3. Effect of the interaction
 orography - soil dryness $f_{12}^* = f_{12} - (f_1 + f_2) + f_0$

Results for experiments f_0 , f_1 and f_2 at 1500 LST are shown in Figure 3.12. For experiment f_0 , the absence of orography implies that the breeze developed along the northwest coast can progress inland. On the rest of the island, the wind field is similar to the complete case, but the circulation is weaker and not fully developed, in such way that the convergence line does not appear (Figure 3.12a). When the orography is included (experiment f_1), the structure is very similar to the complete case but the circulation and the convergence in the centre of the island are weaker. Moreover, the central cyclone is not identified (Figure 3.12b). Experiment f_2 shows that with dry soil and flat terrain, the breeze developed along the northwestern coast is able to progress much further inland than in experiment f_0 and can reach the Bay of Palma. In the same manner, the flux from the eastern coast can reach the Bay of Alcudia. The strongest fluxes are again those developed along the coasts of the main bays. The central cyclone is well marked in this experiment (Figure 3.12c).

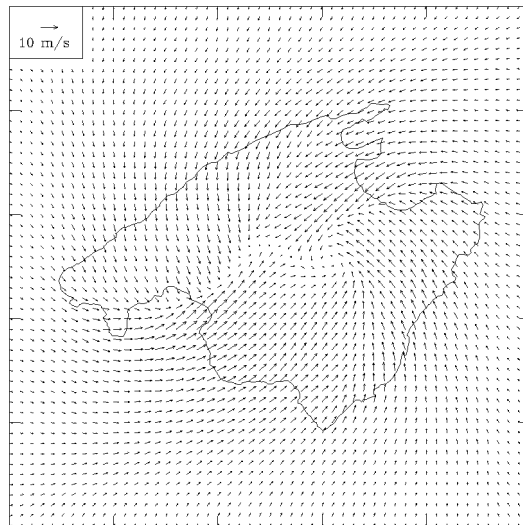
Figure 3.13 shows the effects of each factor on the mature breeze and the effect due to the interaction between orography and dryness. The action of the orography is presented in Figure 3.13a. This action is very strong over the east slope of the Serra de Tramontana. The presence of the strongest f_1^* winds towards the coast in this area shows that the block by the Serra de Tramontana on the sea breeze along the northwest coast is decisive to define the full structure of the circulation. From a direct examination of the results f_1 and f_0 (Figures 3.12b and a respectively), we can deduce that the veering of the breeze towards the main range is also due to the orography by the heating of the eastern slope. Although to a lesser extent, the Serra de Llevant also blocks the breeze from the eastern



(a) Experiment f_0



(b) Experiment f_1



(c) Experiment f_2

Figure 3.12: Results at 1500 LST for the experiments: (a) without orography and with saturated soil; (b) with orography and saturated soil; (c) without orography and with dry soil.

coast. The blocking action from both relief units can even be observed over the sea along the corresponding coast lines, since the f_1^* winds are outward from the island. Another important effect of the orography is the development of the cyclonic circulation over the west of the island. This structure is absolutely separated by the orographic factor. Moreover, another cyclonic circulation appears over the Bay of Alcudia. The contribution of the orography to the development of the cyclonic circulation in the centre of the island seems to be very weak.

Figure 3.13b shows the effect of the soil dryness. The main effect is to increase the wind over practically the whole island and to permit the fluxes from the two bays to form the convergence line in the centre. The cyclonic circulation in the centre becomes completely determined by this factor, which does not participate in the other cyclonic circulation that appears in the full structure. Curiously, close to the Bay of Palma the dryness effect f_2^* seems to be in opposition to the development of the breeze. This behaviour is associated, as we noted previously, with the fact that the breeze developed without orography along the northwestern coast is able to arrive at the Bay of Palma when the soil is dry but not when the soil is wet.

The effect of the interaction between dryness and orography is presented in Figure 3.13c. This contribution seems to work to compensate for the dryness effect. In fact, its action is strong over the same areas where the dryness acts appreciably, but is directed in the opposite sense. The strongest f_{12}^* winds are found again inland near the Bay of Palma. This fact could be associated with an enhancement of the slope winds, which are favoured in this area due to the shape and dimensions of the south basin (see Figure 1.1).

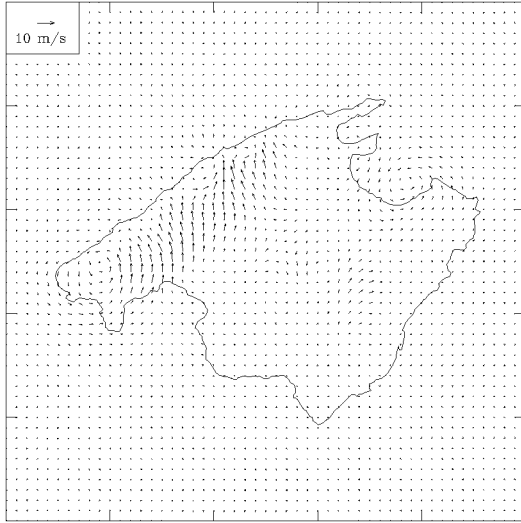
3.3 Concentration of sulphur dioxide

3.3.1 Ground-level concentration

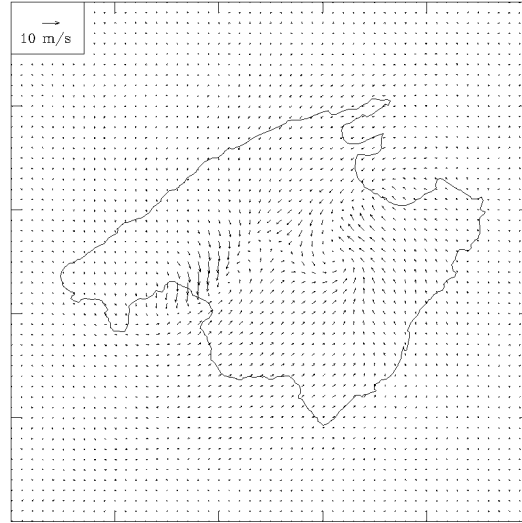
We have concluded from the experiments that the location of EP1 and EP2 (see Figure 1.1), is such that there appears to be no interaction at ground level between the pollutants released by both plants, at least for this kind of circulation. This means that only the results of experiment S2 are necessary to study the problem. Figure 3.14 shows the ground-level concentration of sulphur dioxide at the reference times (0900, 1500, 2100 and 0500 LST). The effect of each electric plant can be independently interpreted over the same figure.

The regions of concentrations higher than $5 \mu\text{g}/\text{m}^3$ are contoured. The main urban sites, located along the Bay of Palma, are not affected by the plant emissions. Independently of the values reached, the points of maximum concentration are always at least 5 km away from the sources. The effective height of EP1 and EP2 is widely sufficient to prevent the neighbouring areas from high values of SO_2 concentration.

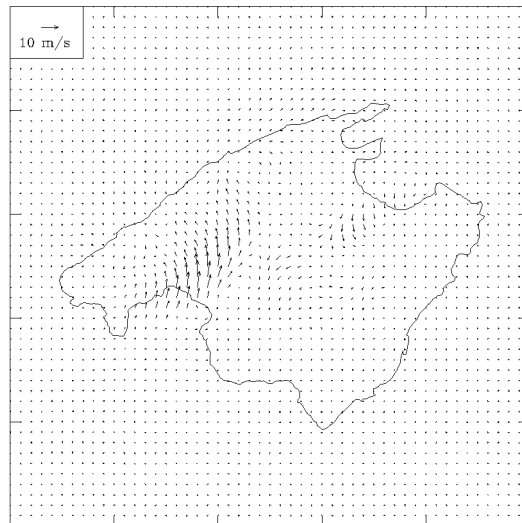
Analysis of the series of figures showing the temporal evolution of the sea breeze (Figure 3.3), shows that the diurnal variability in the circulation around EP1 has two tendencies. In a first stage, the wind initially from the east backs during the morning and becomes northeasterly about 1500 LST. In a second stage, the wind veers; with the arrival of the central cyclone the wind becomes easterly again and, subsequently, with the development of the land breeze, it is from south.



(a) Effect orography



(b) Effect soil dryness



(c) Effect interaction

Figure 3.13: Effects on the sea breeze circulation at 1500 LST by the factors: (a) orography; (b) soil dryness; (c) interaction between orography and soil dryness.

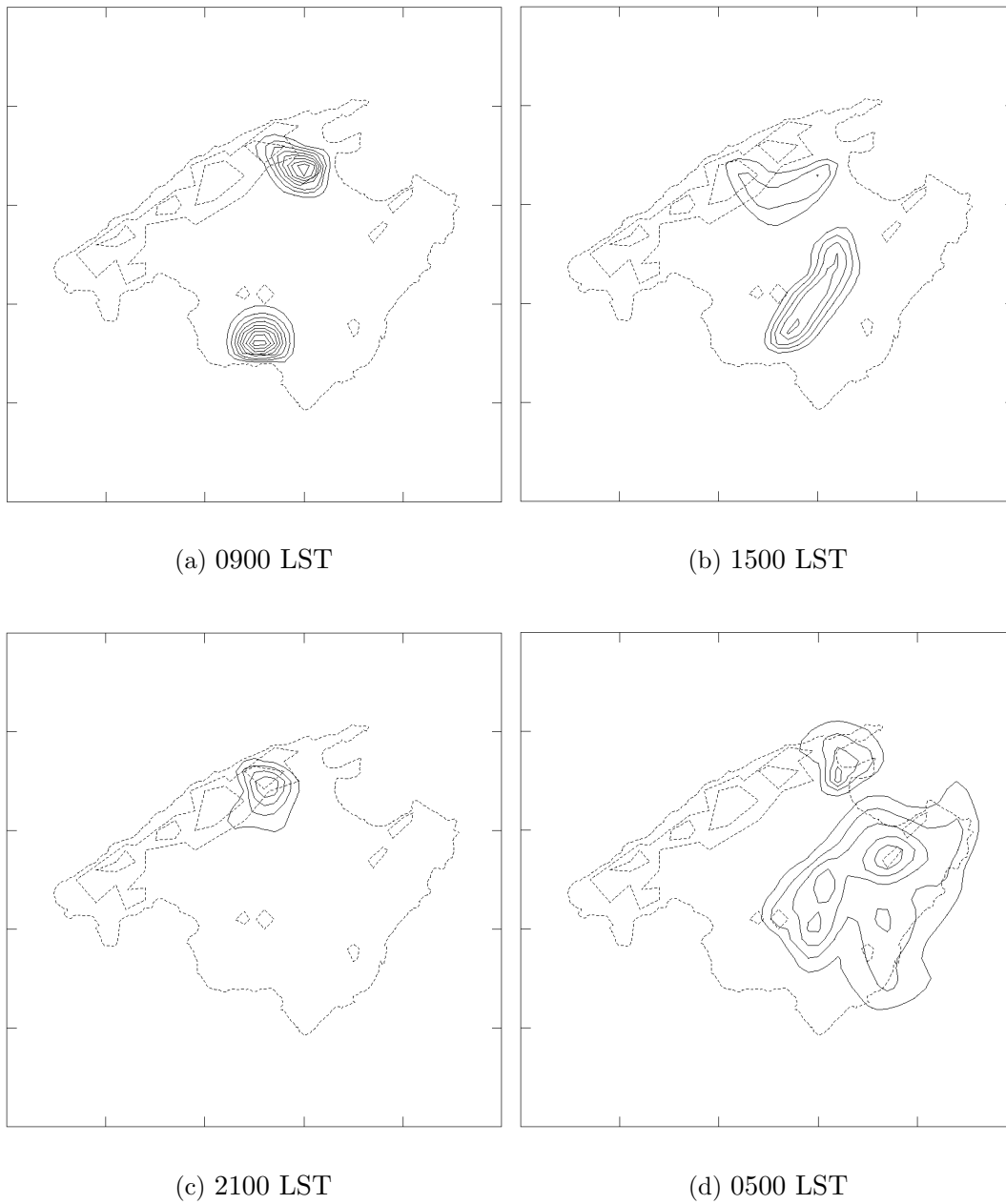


Figure 3.14: Results of SO_2 concentration at ground-level for the S2 experiment: (a) at 0900 LST; (b) at 1500 LST; (c) at 2100 LST and (d) at 0500 LST. Contour interval is $5 \mu\text{g}/\text{m}^3$ starting at $5 \mu\text{g}/\text{m}^3$ (solid line). Coast line and contours of 300 and 700 m are also included (dashed line).

This variability in the wind direction has implications in the transport of air pollutants from EP1. Indeed, the region of concentrations higher than $5 \mu\text{g}/\text{m}^3$ extends to the west of the electric plant toward the Serra de Tramontana at 0900 LST (Figure 3.14a). Later at 1500 LST (Figure 3.14b), that region's influence is extended towards the centre of the island, although the convergence line (see Figure 3.3b) limits its entrance and deflects the plume toward the mountain range. As the flow veers from northeast to south during the subsequent hours, the region affected by SO_2 moves along the Serra de Tramontana and ends up over the Bay of Pollensa (Figures 3.14c and d).

It must be noticed that the northern part of the Serra de Tramontana (a wild area), is continually affected by the pollutant as a consequence of its altitude and attraction of the flux from the Bay of Alcudia. From the model results, it seems that the role played by the breeze on the ground concentration of SO_2 emitted by EP1 is not to permit its expansion toward the centre and south of the island, but to restrict its influence on a limited region in the north, mainly mountainous and unpopulated.

In contrast, the behaviour of the wind field in the south around EP2 is simpler. The wind is predominantly southerly in the early hours and veers gradually during the day to become westerly at the decay of the sea breeze (see Figure 3.3). As a result, the pollutant extends north to EP2 at 0900 LST (Figure 3.14a), but later is transported toward the northeast (Figure 3.14b). In this case the pollutant can progress toward the centre and northeast of the island, although such progression is still limited at 1500 LST (Figure 3.14b) as a consequence of the convergence line of the eastern part of the island, which tends to deflect the plume toward the central region (see Figure 3.3b). However, as the convergence lines disappear and the central cyclonic circulation moves north, the transport toward the northeast continues.

The maximum SO_2 concentration at ground level also depends on the time, as the mixing layer and advection evolve. At 0900 LST the sea breeze front has not yet penetrated much inland and the winds are light, whereas the vertical diffusion is already appreciable as we will see in next section. As a result, the pollutant released in preceding hours that has not yet spread very much, undergoes appreciable vertical mixing and values higher than $40 \mu\text{g}/\text{m}^3$ for EP1 and $45 \mu\text{g}/\text{m}^3$ for EP2 occur at the ground (see Figure 3.14a).

At 1500 LST the breeze is in its mature state (wind speeds stronger than 8 m s^{-1} occur in the Bay of Alcudia). The flux reaches the centre of the island and a deep mixing layer develops there. Strong vertical mixing in a deeper and wider region leads to lower values of the concentration at the ground (Figure 3.14b).

From that time, the breeze and turbulent mixing weaken progressively but horizontal diffusion continues. As a result, ground concentrations derived from EP2 are smaller than $5 \mu\text{g}/\text{m}^3$ at 2100 LST. However, the pollutant from EP1 is blocked over the eastern slope of the Serra de Tramontana and values higher than $20 \mu\text{g}/\text{m}^3$ are given by the model at that time (Figure 3.14c).

During the day light hours, vertical diffusive mechanisms are the main factors in the ground-level concentration pattern. However, after sunset, vertical diffusion plays a secondary role, whereas the transport by downward air motion over the island associated with the land breeze becomes the dominant mechanism. A substantial increase of the sulphur dioxide at low levels is produced as a consequence of this transport process. That effect can be seen at 0500 LST (Figure 3.14d). The sulphur dioxide from EP1 maintains

its concentration over lowlands about the Bay of Pollensa. That released from EP2 which remained in upper levels has sunk spectacularly, and practically all the eastern side of the island has concentrations exceeding $10 \mu\text{g}/\text{m}^3$.

From the point of view of the regulated ambient air quality standards, the concentrations forecast by the model are appreciably smaller than those characteristic of a very polluted area. For example, the daily average value of $130 \mu\text{g}/\text{m}^3$, which is the upper limit established by the Spanish Government, is not exceeded at any point on the island according to the model results.

3.3.2 Vertical cross sections

A series of vertical cross sections have been included and discussed in order to support some results commented in last section. Vertical diffusion has been identified, apart from the night, as the main factor in the ground concentration intensity. During the early hours, when the winds are still light and restricted over the coastal areas, the vertical diffusion over land is already appreciable, although the mixing layer depth is moderated. That leads to fumigation and high values of ground-level concentration not too far from the coast. Later, as the cold air from the sea penetrates inland with a well-defined sea breeze, vertical turbulent diffusion diminishes near the coast but intensifies and extends vertically toward the centre of the island, where strong sensible heat flux occurs. Therefore, the fumigation moves inland, although the mixing acts in a deeper layer and lower values of the concentration are reached at the ground. This behaviour of the vertical diffusion is shown clearly in Figure 3.15, which represents the turbulent kinetic energy in a cross section along the Bays of Palma and Alcudia (section AB in Figure 1.1). At 0900 LST, turbulent diffusivity exceeding $1 \text{ m}^2/\text{s}^2$ is restricted to below a height of 1 km, but is very homogeneous over a great part of the island (Figure 3.15a). At 1500 LST, turbulent diffusivity has fallen by one half near the coasts, especially near the Bay of Alcudia, but has doubled over the centre of the island and occupies a height of 1.5 km (Figure 3.15b).

As was pointed out in the last section, as the incoming radiation decreases late in the day, the vertical diffusion loses its activity and low values of SO_2 occur at the ground (except around EP1 due to the blocking action of the Serra de Tramontana). This effect can be seen in Figure 3.16, which shows a cross section of the sulphur dioxide concentration at 2100 LST along the direction A'B' (indicated in Figure 1.1), for the experiment S1. The pollutant is confined against the eastern slope of the mountain range.

The interaction with the orography is not as important in the case of EP2 since the terrain is not as complex and elevated in the east of the island. The extensive impact of EP2 is well reflected in the cross sections contained in Figure 3.17, which corresponds to the sulphur dioxide concentration along the direction C'D' (indicated in Figure 1.1), for the experiment S2. At 0900 LST, concentrations higher than $5 \mu\text{g}/\text{m}^3$ exist only in the proximity of the coast below a height of 900 m (Figure 3.17a). However, with the mature breeze at 1500 LST, that region extends its influence almost to the opposite coast and has a vertical mixing depth of 2 km, producing smaller values at ground-level (Figure 3.17b). The dome observable in the centre of the figure could be attributed to the transport by the upward air motion over the convergence zone. On the other hand, the figure shows that the pollutant is also transported backward by the counter-current over the source

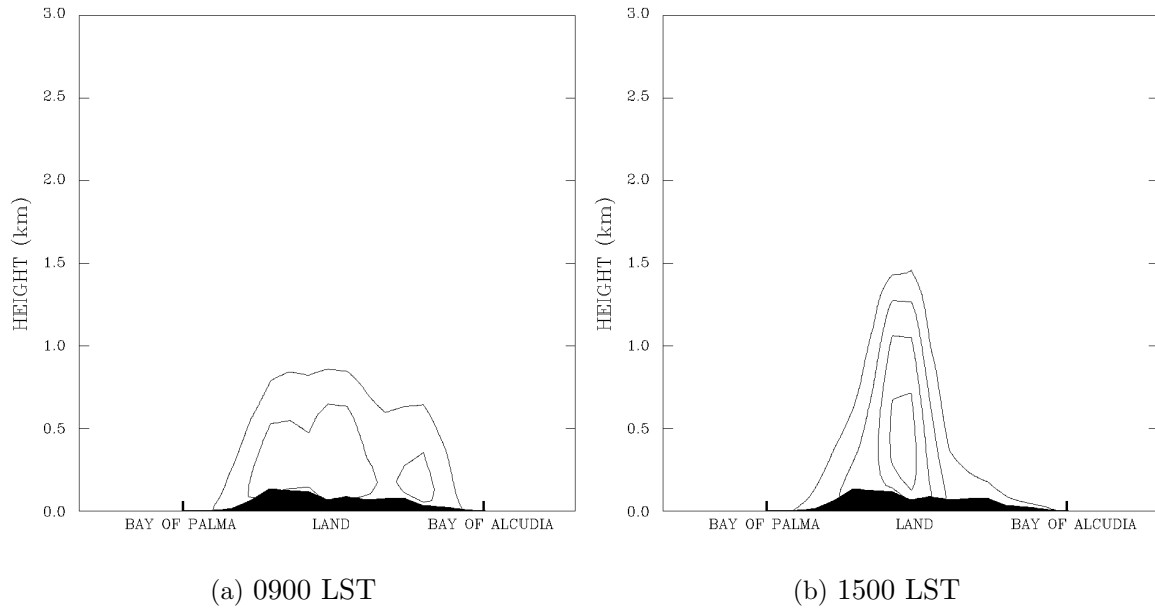


Figure 3.15: Vertical cross section across the bays of Palma and Alcudia (along direction AB in Figure 1.1) of the turbulent kinetic energy: (a) at 0900 LST; (b) at 1500 LST. Contour interval is $1 \text{ m}^2/\text{s}^2$ starting at $1 \text{ m}^2/\text{s}^2$.

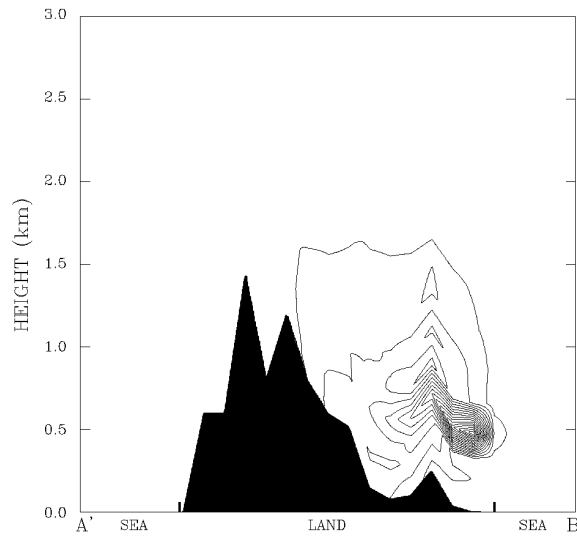


Figure 3.16: Vertical cross section along A'B' (Figure 1.1) showing the SO_2 concentration for the S1 experiment at 2100 LST. Contour interval is $10 \text{ }\mu\text{g}/\text{m}^3$ starting at $5 \text{ }\mu\text{g}/\text{m}^3$. Maximum concentration is $165 \text{ }\mu\text{g}/\text{m}^3$.

level. Figure 3.17c shows that, as mentioned in the last section, the pollutant remains at the source level approximately and does not affect the ground during the night. An examination of the wind field at source level during the nocturnal hours (not shown), reveals that a slight transport from C' to D' exists all this time. With the land breeze established during the early morning, the pollutant is forced to descend over the land as the air does, and the concentration at ground-level increases again, although affecting a larger region (see Figure 3.17d).

3.3.3 Comparison against sampler data

The availability of permanent SO₂ measurements in Mallorca is very limited and is not sufficient to permit a detailed comparison with the model results. The measurements also are affected by local features not resolvable by the model. Moreover, as a consequence of the initialization data, the meteorological fields given by the model presume an approximation to the mean structure of the breeze and not to the circulation of any particular day. Small differences in wind direction, for example, can produce a large difference in computed and measured concentration sufficiently downwind of a source (King and Bunker 1984).

Unfortunately, measurements in the region where the model indicates the highest concentrations of sulphur dioxide from EP1 do not exist at present. The available station IE1 (see Figure 1.1 for location) is located near the boundary of the area with appreciable pollutant concentration shown by the model (see Figure 3.14).

Figure 3.18 shows the graphical comparison at the station IE1 with observations on 27 and 28 July 1993, when a sea breeze developed. The order of magnitude of the concentration is well represented by the model throughout the diurnal cycle. Even the shape of the curves, dominated by the maximum between 0900 and 1300 LST, is well simulated by the model. A secondary maximum given by the model at 2300 LST, is also reflected in the data of one of the days.

3.3.4 Impact of dry deposition and second cycle

In the previous experiments, dry deposition was not considered. This sink process can be neglected for species that do not undergo chemical reaction at the surface or that are insoluble in water; for example carbon monoxide. However, SO₂ is highly water-soluble and therefore behaves similarly to water vapour, exhibiting deposition velocities of up to 1 cm s⁻¹ (Sehmel 1980).

Although the physical mechanisms governing the behaviour of the coastal pollutants seem clear from the previous simulations, it is worthwhile examining the modification of ground-level concentration when dry deposition of SO₂ is included in the model. For that purpose, we have repeated the experiment S2 (in this case covering two diurnal cycles), but with the deposition flux $v_d \pi C_i$ as the lower boundary condition in the conservation equation 3.1. See the Appendix for symbols.

The deposition velocity v_d is calculated in terms of a total resistance $r_a + r_{na}$ (Wesely and Hicks 1977):

$$v_d = (r_a + r_{na})^{-1}$$

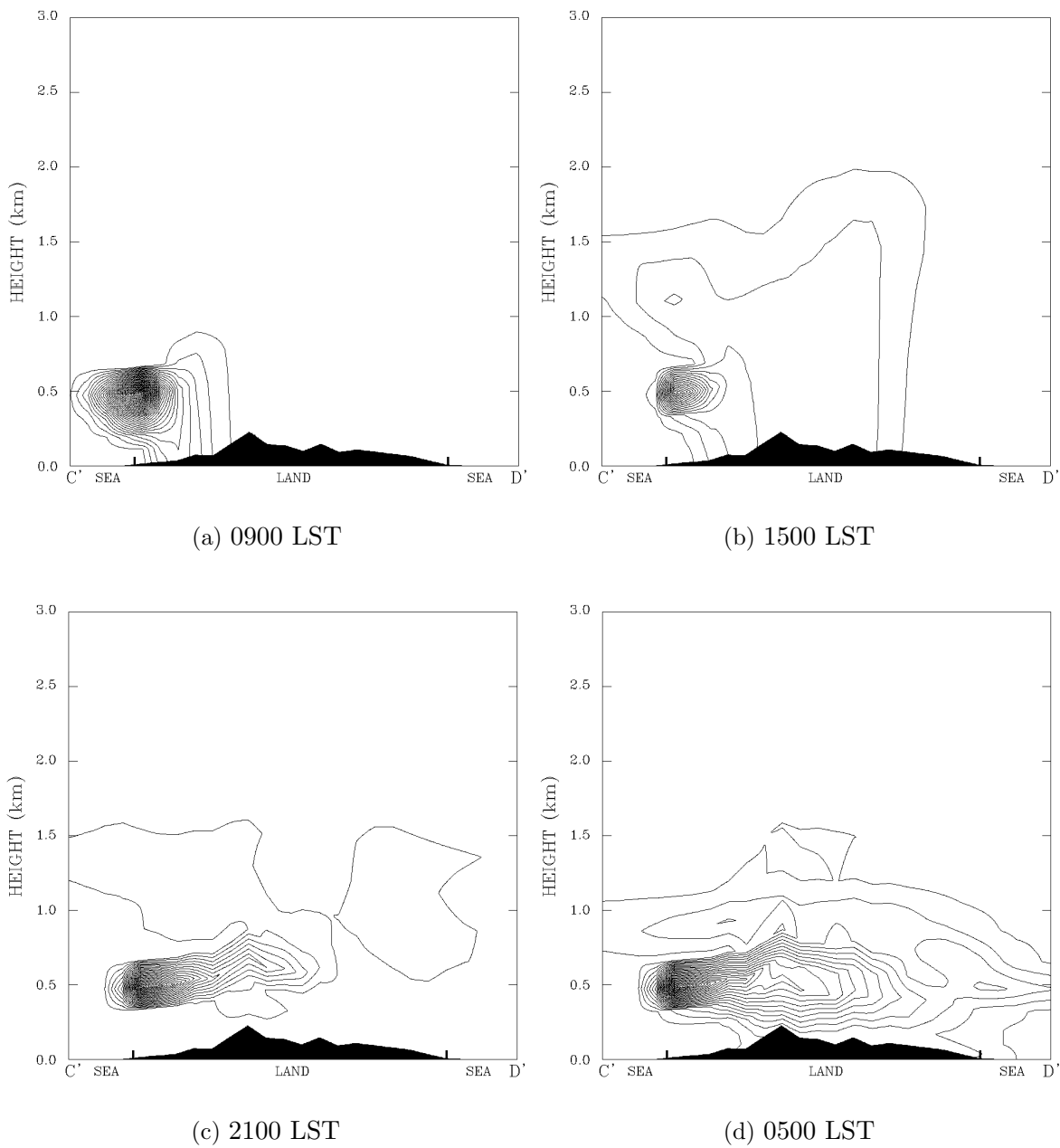


Figure 3.17: Vertical cross section along C'D' (Figure 1.1) showing the SO₂ concentration for the S2 experiment: (a) at 0900 LST, (b) at 1500 LST, (c) at 2100 LST and (d) at 0500 LST. Contour interval is 10 $\mu\text{g}/\text{m}^3$ starting at 5 $\mu\text{g}/\text{m}^3$. Maximum concentration is 250, 175, 230 and 235 $\mu\text{g}/\text{m}^3$ respectively.

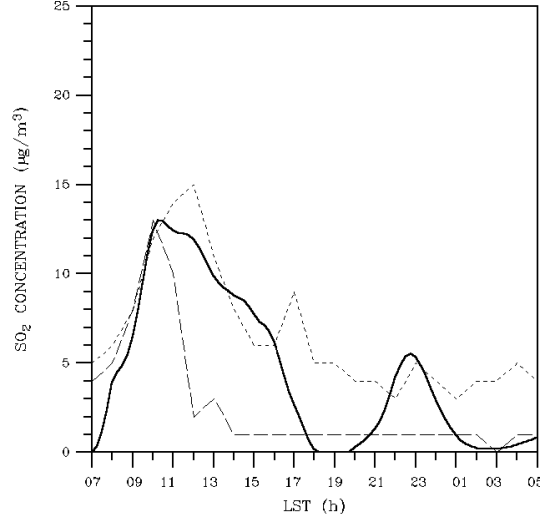


Figure 3.18: Model results (solid line) compared against measured SO_2 concentrations on 27 July 1993 (short dashes) and 28 July 1993 (long dashes) at IE1 (see Figure 1.1 for location).

The atmospheric resistance r_a is given as

$$r_a = (ku_*)^{-1} \left[\ln \left(\frac{z_s}{z_0} \right) - \Psi \right]$$

where k is the Von Karman constant, u_* the friction velocity, z_s the reference height and z_0 the roughness length. Ψ is the stability correction factor, which is approximated as

$$\Psi = \begin{cases} \exp[0.598 + 0.39 \ln(-z_s/L) - 0.09 \ln^2(-z_s/L)], & -1 < z_s/L < 0 \\ 0, & z_s/L = 0 \\ -5z_s/L, & 0 < z_s/L < 1 \end{cases}$$

where L is the Monin-Obukhov length.

Over the sea, the nonatmospheric resistance r_{na} for SO_2 is approximated by $1/u$ (Slinn et al. 1978), where u is the mean surface wind predicted by the model. Over land areas, r_{na} is composed by the deposition layer resistance (r_d) and the canopy/vegetation resistance (r_c). Following Wesely and Hicks (1977), r_d is given by the expression

$$r_d = 2.5/ku_*$$

For gases such as SO_2 , the canopy resistance r_c is dominated by the stomatal resistance which is calculated by the surface sub-model as function of the vegetation type (minimum values are given in Table 3.2).

The results for the first diurnal cycle reveal that the effect of dry deposition on ground-level values can be only clearly discerned at 1500 LST, with reductions of up to $5 \mu\text{g}/\text{m}^3$ in some areas (compare Figure 3.19 against Figure 3.14b). This fact is consistent with the highest deposition velocities reached at that time over the centre of the island where the thermal stability is weak.

An important issue is the effect of a second cycle of breeze on the pollutant distribution. The results of the second cycle practically reproduce the patterns found in the first diurnal

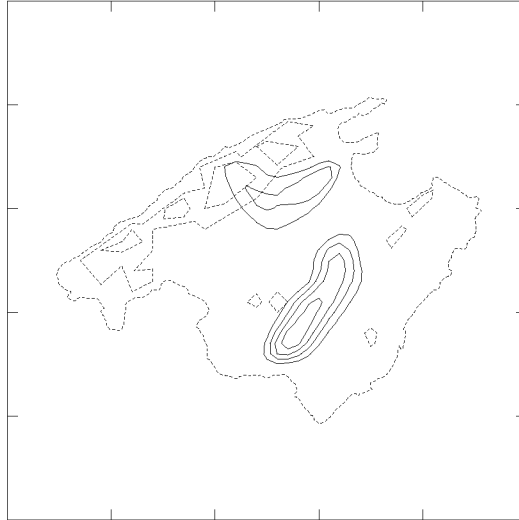


Figure 3.19: Result of SO_2 concentration at ground-level for the S2 experiment when dry deposition is included. The result corresponds to the first diurnal period at 1500 LST. Contour interval is $5 \mu\text{g}/\text{m}^3$ starting at $5 \mu\text{g}/\text{m}^3$ (solid line). Coastal line and orographic contours of 300 and 700 m are also included (dashed line).

period except at 0900 LST. At that time (Figure 3.20), the SO_2 transported downward during the night is still present at low levels while a new fumigation process has started. With such conditions, much of the centre of the island is affected by the pollutant and there is interaction between the pollutants released from EP1 and EP2 (compare Figure 3.20 against Figure 3.14a).

It should be noted, however, that the absence of chemical transformations becomes more critical as the simulation time increases. Furthermore, the accumulation of pollutants in the island environment is a direct consequence of the initial and boundary conditions, which are somewhat artificial since the slight transport associated with the synoptic winds (typically weak during summer as was indicated in section 3.1) has been totally suppressed in the initialization process. The simulated meteorological fields must be only considered as the mean circulation of the breeze. Really, when the synoptic flow is important enough, the actual breeze can be enhanced, reduced or modified significantly.

3.4 Conclusions

A numerical study of the pollutant transport and diffusion over the island of Mallorca based on two numerical simulations has been presented. The study has focused on a particular meteorological situation, very common during the summer season, and the most favourable for capturing the pollutants emitted by coastal sources over the island. Such circulation is the land-sea breeze cycle, which has been reasonably well reproduced by the SALSA model, and hence the simulated meteorological fields are suitable for environmental applications.

In the first experiment, the effluence of non-reactive sulfur dioxide from a real power plant located in the north bay of the island is considered. The convergence line along the

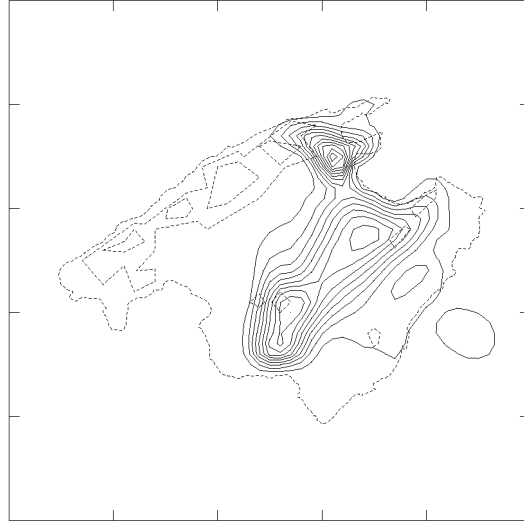


Figure 3.20: As in Figure 3.19 except at 0900 LST of the second diurnal cycle.

centre of the island limits the plume expansion toward the south and deflects its transport toward the Serra de Tramuntana (the major wild area of the island), which acts to block the pollutant. During the night, the plume moves along the Serra de Tramuntana and finally concentrates around the shore when a new sea breeze begins its development. The simulation reveals that, during all the diurnal cycle, the region of ground-level concentration higher than $5 \mu\text{g}/\text{m}^3$ is small. Such a region is not covered by the current measurements and therefore the model accuracy cannot be entirely validated.

A second simulation is performed in order to assess the impact of a hypothetical power plant system for the island. Thus, an identical sulphur dioxide source has been added on the south coast. The results show that there is no interaction at low levels between the pollutants from both plants, and that the main urban sites located in the south bay of the island remain unaffected. Again, the convergence zones intercept the transport of the new plume towards the north, but in this case the plume can progress much further inland and this progression continues during the night after the decay of the sea breeze. Vertical diffusion proves to be the main factor in the ground-level concentration intensity during the day, leading to high values in the morning due to appreciable diffusion over the whole island, and lower values in the afternoon as the mixing layer weakens near the coast but intensifies in the centre of the island. However, after the decay of the breeze, fumigation to ground stops and the downward air motion related to a slight land breeze becomes the process most responsible for the ground-level concentration at the beginning of the next cycle. In this sense, the impact of the new power plant seems to be more important, since practically the entire eastern part of the island is affected by the pollutant sinking. An additional simulation including the dry deposition flux reveals that this process is not important to define the intensity of the ground-level concentration, except during the central part of the day.

Chapter 4

DAILY RAINFALL PATTERNS IN THE SPANISH MEDITERRANEAN AREA

In this chapter¹, the main spatial patterns controlling significant and torrential daily rainfalls in the Spanish Mediterranean region are derived. This is done by applying cluster analysis on the most relevant principal directions extracted from a principal components analysis of the between-day correlation matrix.

To accomplish that objective, we have created an homogeneous and complete daily rainfall data base, with an appropriate density to effectively capture spatial variabilities. The data base contains 30 years of data (1964-1993), at 410 sites of Mediterranean Spain (Figure 1.6).

The structure of the chapter starts with a description of the data base construction (section 4.1), and the details of the methodology employed to derive the rainfall patterns (section 4.2). In section 4.3, the emergent rainfall patterns are presented and discussed. Finally, section 4.4 is dedicated to the conclusions.

4.1 Data base construction

The raw data consisted of the 3366 available daily precipitation records from the Spanish Mediterranean regions during some period between 1951 and 1995, provided by the Instituto Nacional de Meteorología (INM). A first selection was made to consider only stations with a minimum of 1000 data values (almost three years), which yielded a set of 2842 raingauges.

The inventory of the data showed a great variety of record lengths, with only 5 stations with no missing data. Then, a search was performed to choose the longest subperiod of 1951-95 having the highest number of stations with tolerable completion. The final

¹The content of this chapter is based on the papers (i) Romero, R., J. A. Guijarro, C. Ramis, and S. Alonso, 1998: A 30 year (1964-1993) daily rainfall data base for the Spanish mediterranean regions: First exploratory study., *Int. J. Climatol.*, (in press). (ii) Romero, R., C. Ramis, and J. A. Guijarro, 1998: Daily rainfall patterns in the Spanish mediterranean area: An objective classification. *Int. J. Climatol.*, (in press).

decision was to keep all stations with 90% of data available during 1964-93 (30 years). As a consequence, the final number of stations in the data base was reduced to 410, for the period 1964-93. Its spatial distribution is shown in Figure 1.6. As can be observed, the resulting coverage is globally satisfactory (exceptional in Mallorca), although it is poor within the Guadalquivir valley, in mountainous areas of Andalucía, north of Valencia, and some areas of Catalonia.

The following task was to check the quality of the data, as well as to fill the missing data by interpolation from the surrounding stations. The need of a suitable method for data homogenization and quality control has been a constant concern by investigators dealing with climatological data (e.g., Shearman 1975; De Ruffray et al. 1981; Spackman and Singleton 1982; Baker et al. 1995). The average between-site distance for the 410 stations is 15 km, whereas that distance reduces to only 7 km when all the 2842 stations are considered. It seems, therefore, that although our requisite of minimum completion is only reached by 410 stations, there is still very useful information in the remaining stations that can be used for the interpolation task. We considered opportune, then, to use all this information. We developed an iterative method:

First of all, a new complete record p_i^{*n} (i : station, n : day) was calculated for each of the 2842 stations for the whole period 1951-95:

$$p_i^{*n} = \frac{\sum_{j=1}^J \alpha_{ij} (p_i^m)_j}{\sum_{j=1}^J \alpha_{ij}} \quad (4.1)$$

Here, p_i^{*n} is a weighted average of the J estimated values at position i , noted as $(p_i^m)_j$. The J reference stations are all stations which, lying within a radius of 0.5 degrees around the target station i , have a common observing period of at least 1000 daily values with station i , and have no missing data on the target day n . The radius for acceptance was chosen large enough as to yield several stations even in areas with small raingauge density.

The estimated values $(p_i^m)_j$ in equation 4.1 are formulated as

$$(p_i^m)_j = p_j^n q_{ij}, \quad (4.2)$$

where p_j^n is the observed precipitation at reference site j , and q_{ij} is the ratio between accumulated rainfalls at stations i and j :

$$q_{ij} = \frac{\sum_{k=1}^K p_i^k}{\sum_{k=1}^K p_j^k}, \quad (4.3)$$

which is evaluated over the common observing period of K days. As implied by the previous arbitrary threshold, K is never less than 1000, ensuring the statistical significance of q_{ij} .

The criterion expressed by equation 4.2 is based on the idea of interpolating normal ratio precipitations rather than absolute data, which was used by Paulhus and Kohler (1952) to eliminate the influence of orographically enhanced precipitation. But we cannot compute homogeneous station normals until the precipitation series have been completed. Therefore, we use ratios of precipitation totals for the common observing period for each pair of stations. We are then applying a simplified form of regression in which the independent term has been removed, and the regression coefficient can then be calculated as

the ratio between the accumulated data of the dependent and independent variables (p_i and p_j respectively). This simpler regression form has the advantage of being more robust as it is less influenced by outliers, and it is, in fact, the ratio method proposed by Conrad and Pollack (1962) to reduce precipitation averages to a common observing period. We applied the same technique but for the estimation of individual data.

Much discussion has been raised with respect to the functional form of the weighting factors (α_{ij} in equation 4.1). Some authors perform the weighting as an inverse function of the distance, while others prefer a function of the correlation coefficient. When looking to a plot of correlation coefficients versus distance or to mapped correlation fields (e.g. Sumner et al. 1995b), it is clear that for close stations any of the methods may be applied with good results. For longer distances, however, pairs of stations separated by similar distances may have a wide range of correlation coefficients, and stations related with similar correlations may be separated by quite different distances. Moreover, while the correlation coefficient has the ability to account for geographically induced anisotropies, the distance may introduce more consistency in the analysis of highly variable fields such as the daily precipitation. We have adopted a compromise between both methods:

$$\alpha_{ij} = \frac{r_{ij}^2}{d_{ij}^2}, \quad (4.4)$$

where the correlation coefficient r_{ij} and distance d_{ij} between stations i and j are squared to enhance the preeminence of the closer stations (both in spatial and correlation terms). This is especially useful in areas with a high density of stations, where close reference data could otherwise be masked by many farther stations.

More sophisticated interpolation techniques as multiple correlation, optimal interpolation, kriging, or spline-surface fitting have been proposed (Gandin 1963; Creutin and Obled 1982; Young 1992). Their estimations were sometimes better when compared with simpler methods, but with the cost of a higher bias and reduction of variance.

Once the precipitation series p_i^{*n} were calculated, relative deviations (original datum minus calculated one, divided by the mean yearly calculated precipitation) were computed for each of the 2842 stations, and used to test the original data. Relative deviations series showed high variances and very leptokurtic frequency distributions. Only original data with relative deviations beyond seven times the standard deviation of its series were rejected and substituted by the calculated value. This process was performed iteratively, starting each new cycle at equation 4.1, until no rejections were given. Ten iterations were needed, and less than 0.07% of the original data were rejected as a result of the whole process. Finally, the precipitation series calculated in the last iteration were used to fill the holes present in the records of the 410 selected stations.

4.2 Methodology

A large proportion of the 10958 days contained in the 30 years of data are absolutely dry in most of the stations, and therefore a restrictive criterium must be imposed to keep only those days characterized by significant rainfall over the area. We decided to keep those days in which at least 5% of the stations registered more than 5 mm, yielding a total

of 3941 days. Of course, such thresholds are arbitrary. Other values were tested (15% - 5 mm, 30% - 5 mm, etc.) and quite similar rainfall patterns were obtained. However, since 3941 days represent a considerable population, we judged the 5% - 5 mm limit opportune for statistical reasons. In addition, the 5% threshold implies 20 stations, which are sufficient to represent the main topographic units and adjacent lands that we aim to resolve (see Figure 1.6). Of the 3941 selected days, 30.0% occurred in winter (December, January, February), 29.6% in spring (March, April, May), 26.8% in autumn (September, October, November), and only 13.6% in summer (June, July, August).

As torrential days, we decided to filter days with rainfalls exceeding 50 mm in at least 2% of stations (8 stations). This criterium yielded 449 days (15 per year on the average, normally grouped in a few episodes), and was considered the most appropriate compromise for three reasons: 8 stations is an adequate number to represent the main torrential centres (Sierra de Aracena, Sierra de Ronda, Sierra de Aitana, Sierra de Tramuntana, coastal domains; Figures 1.8 and 1.9), and ensures that very localized events are not included; other more restrictive criteriums reduce strongly the number of filtered days (for example, 2% - 60 mm gives only 226 days, and 5% - 50 mm, 124); finally, we could verify that well-known case studies appeared in the literature (e.g. Fernández et al. 1995, Ramis et al. 1994, Romero et al. 1997, 1998a) were effectively captured by the selected criterium. It is interesting to note that all the 449 torrential days were also significant days. In this case, 44.8% belong to the autumn season, 35.2% to winter, 14.9% to spring, and 5.1% to summer. Clearly, there is a preeminence of the fall season, as we expected.

As in Sumner et al. (1995a), the approach followed to derive the typical precipitation patterns consists in subjecting the T-mode (day-by-day) correlation matrix to principal components analysis (PCA), and carrying out cluster analysis (CA) on the most important extracted components. That is, days participating with similar loadings on the extracted components will be clustered together. This approach is aimed to join days with similar precipitation distributions, irrespectively of the precipitation amounts. The method is the analogue to that applied in regionalization studies, where the S-mode (site by site) correlation matrix is used instead (e.g. White et al. 1991, Bonell and Sumner 1992, Sumner et al. 1993, Gong and Richman 1995).

The PCA is designed not merely as a data reduction technique, but as a method to achieve that only the fundamental modes of variation of the data are considered for the clustering process. Several criteria have been suggested for deciding how many PCs to retain in order to separate “signal” from “noise” (e.g. Jolliffe 1986, Barring 1987, Preisendorfer 1988), but a clear-cut number of PCs is certainly rare. We adopted the simple scree test of Cattell (1966). Figure 4.1 shows the scree plot obtained from the analysis of significant and torrential data sets. Several breaks of the slope are present in both cases. We retained 17 PCs for significant days, which account for 49% of the total variance (Figure 4.1a); and 15 PCs for torrential days, which account for 68.5% of the total variance (Figure 4.1b).

Some authors promulgate the use of rotated PCs and have demonstrated its benefit in spatial contexts, in which the S-mode decomposition is used (e.g. Richman 1986, White et al. 1991). We experienced with obliquely rotated PCs, which produced moderate simple structures (see Richman 1986). The obtained precipitation patterns were similar to those based on unrotated PCs. However, we found the latter classification superior

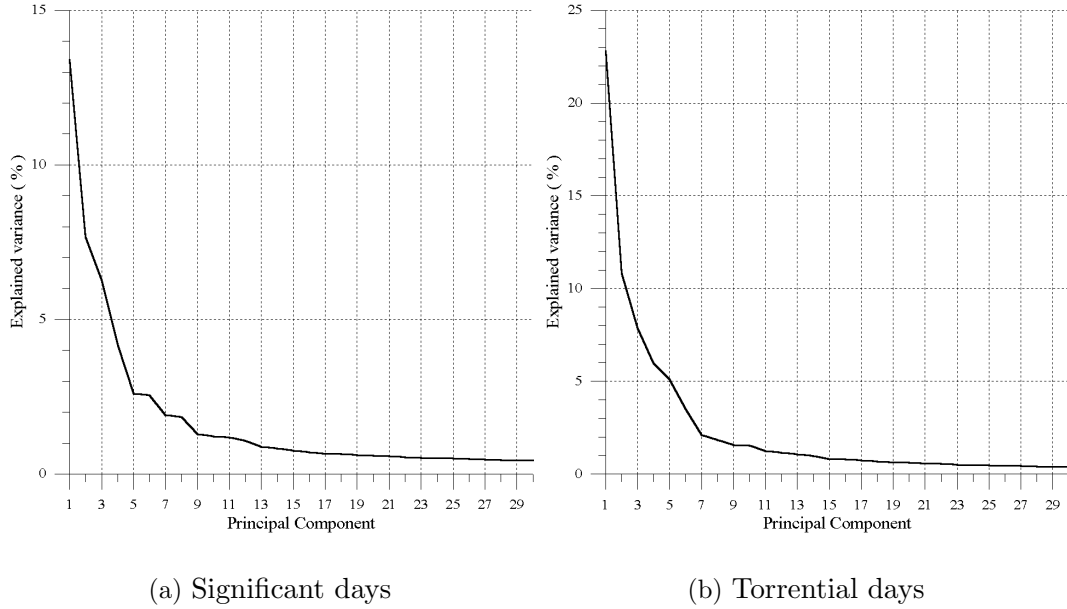


Figure 4.1: Principal components scree plot for (a) significant days, and (b) torrential days. Only the first 30 PCs of the resulting 409 PCs are shown.

after noting that some randomly selected maps had been allocated in better agreement with our subjective criteria. Therefore, the solution based on unrotated PCs was finally selected.

For the cluster analysis, the nonhierarchical k -means method (Anderberg 1973), as implemented in the *STATISTICA* utility (1994), was used. The euclidean distance was taken as the similarity index. Gong and Richman (1995) showed that nonhierarchical methods as the one used outperformed hierarchical techniques. Nevertheless, hierarchical tree plots generated by Ward’s method (Ward 1963) were also considered as reference for deciding how many clusters to create. The final decision on the proper number of clusters is still an unresolved problem (Everitt 1979; Gong and Richman 1995), prone to subjectivity and most of the times dictated by the researcher’s experience. We judged satisfactory the solution of 11 typical patterns for significant rainfalls, and 8 patterns for torrential rainfalls. These patterns are presented and discussed in next section (consider Figure 1.6 for locations mentioned therein).

4.3 Emergent patterns and discussion

4.3.1 Significant days

Figure 4.2 shows rainfall composites for the 11 clusters (referred to as pattern groups, PGs), which are summarized in Table 4.1. The considered area is large enough as to yield a clear separation of the PGs, in the sense that each of the patterns tends to highlight distinct localities and their areas of influence do not overlap exceedingly. All the PGs appear clearly associated with the topographic entities of the region (Figure 1.6).

The relative position of these entities and the main rain-bearing atmospheric systems will determine the occurrence of these idealized patterns. Although the attribution of meteorological causes to the rainfall patterns is not the objective of this work, we made a visual inspection of a sample of meteorological maps for each cluster (as given by ECMWF gridded analyses), in order to better interpret each PG.

S1 represents rainfalls almost exclusive of western Andalucía, especially in its western-most part. The maximums are found, therefore, in the mountains of Sierra de Aracena. A secondary maximum is found about Sierra de Ronda, which also participates actively in other PGs. As emphasized in Romero et al. (1998b), Sierra de Ronda is a peculiar zone, favorably exposed to a wide range of flows, and as a consequence presenting the maximum yearly rainfalls of the whole region (see Figure 1.7a). Pattern S1 is principally associated with Atlantic depressions west of the Iberian peninsula inducing southerly to westerly humid winds over western Andalucía.

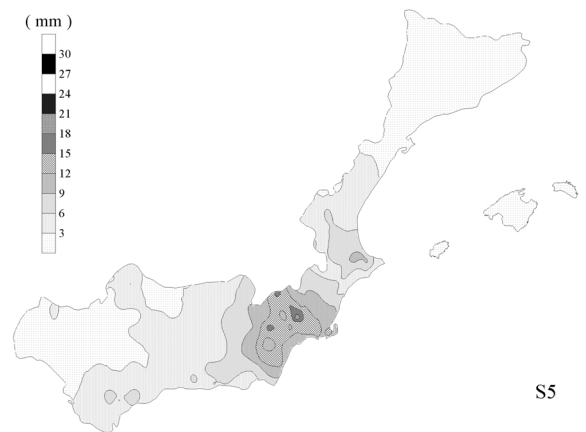
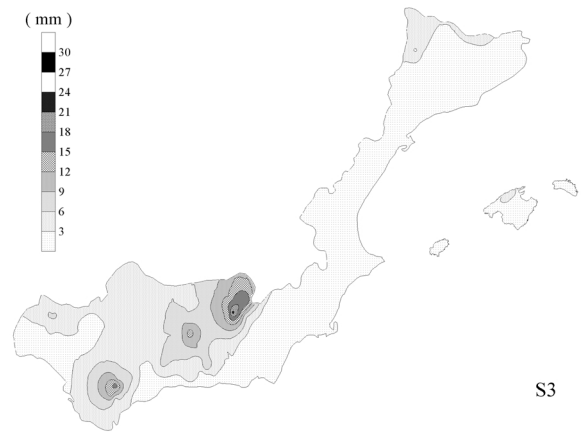
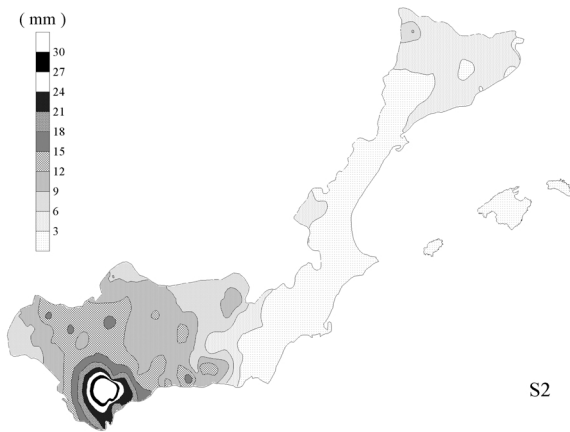
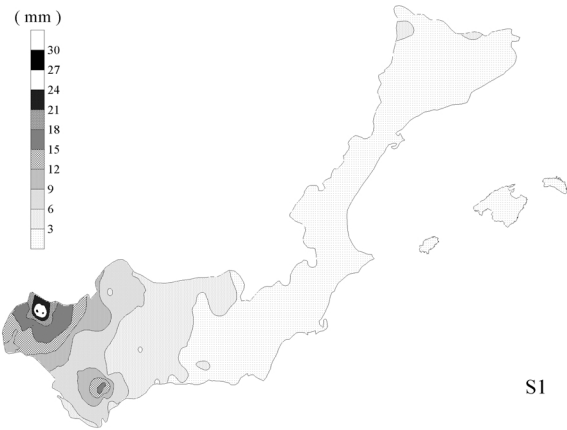
S2 characterizes quite substantial rainfalls about the Gibraltar area (maximum in Sierra de Ronda), but affecting in general the bulk of Andalucía except its eastern part. This is a very extensive pattern that may be also reflected in Catalonia region, especially in the Pyrenees mountains. As S1, this pattern is a logical result of upper levels troughs close to the Atlantic coasts with the associated low-pressure systems at low levels providing southwesterly-westerly flows over Andalucía. The teleconnection between this area and Pyrenees mountains is explained by large depressions lying about western Spain, which provide the aforementioned flows and also warm and moistened southerly flows over the Pyrenees mountains. Atlantic depressions are hardly effective for the remainder areas, which become strongly sheltered (especially the Southeast). As a result, this PG is characterized by little rain in these areas.

S3 is characterized by rainfalls in the mountainous interior of central and western Andalucía, away from the coast except in the Gibraltar area. In this case, the main centre is Sierra de Cazorla, and secondary maximums are found in Sistema Subbético, Sierra de Ronda and Sierra de Aracena. Pyrenees mountains, and even Sierra de Tramuntana mountains of Mallorca, can sporadically participate of this PG. S3 pattern is principally related to the pass of cold fronts over the Iberian Peninsula, which are associated with mid-latitude disturbances.

S4 is a particular PG of Andalucía, especially of its central part, and is maximized over the south-southeast facing slopes close to the coast. Probably the signal over the Sistema Penético is too weak due to the poor coverage of stations in these mountains (see Figure 1.6). This PG is associated with troughs about southern Spain, frequently presenting cut-off low characteristics. There is not a clear preference for specific surface flows in this case, but Mediterranean warm flows tend to be present most of the cases.

S5 represents the rainfalls in the Southeast, which is the most arid zone of Spain (see Figure 1.7). Logically, this PG relies principally on easterly-southeasterly flows over the area, most of the times associated with well marked troughs or lows at upper levels along western Spain. For easterly flow regimes, other adjacent areas are also favorably exposed. As a consequence this PG is rather extensive, and exhibits two secondary maximums about Sierra de Ronda and Sierra de Aitana. We also observed that S5 sometimes occurs with very weak flows at low levels, but with cold air aloft over eastern Spain.

Pattern S6 represents the rainfalls that affect southern Valencia and Murcia, exhibiting



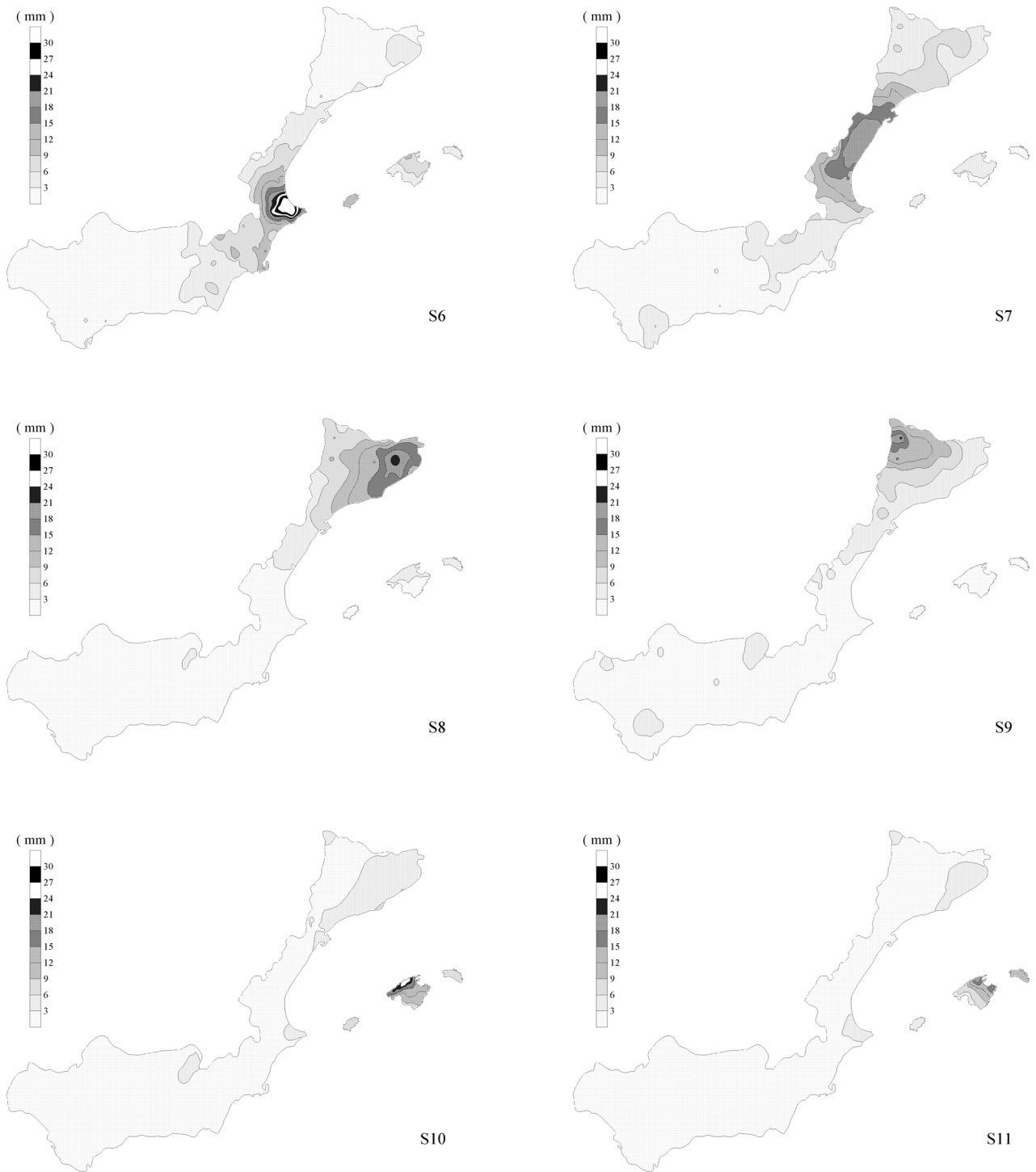


Figure 4.2: Daily rainfall composites for the 11 PGs obtained in the classification of significant events.

a strong maximum in the Sierra de Aitana area. The Sierra de Aitana area, and also Sierra de Ronda, are characterized by the most abundant daily rainfalls of the whole region (see Figure 1.8). It is reasonable to conclude that this PG is mainly the result of depressions located in the southern part of the western Mediterranean region, but in this case providing rather easterly-northeasterly winds over the Sierra de Aitana area. Indeed, this is what we generally observed from the ECMWF fields. A notable aspect of this PG is that the nearby island of Ibiza and the mountainous north of Mallorca may participate appreciably of these situations.

S7 is characterized by rainfalls in the generality of Valencia and south of Catalonia, but in this case the main centre is not Sierra de Aitana area but shifts to the north adopting an elongated shape along the Gulf of Valencia, parallel to the coastal mountains. In this case, easterly-southeasterly flows over the Gulf of Valencia benefit this pattern. This PG is quite extensive, since any sector of the eastern regions may be favoured by these airflows.

Pattern S8 is very local and characterizes those rainfalls of Catalonia concentrated close to the coast. This PG exhibits a marked suppressing gradient from the coast toward the interior of Catalonia (one of the driest zones of the studied area; Figure 1.7). The maximum is found in the northeastern sector, over the prelitoral foothills of the Pyrenees mountains. Southerly-southeasterly onshore flows, cold fronts from the north, and also easterly to northerly flows induced by frequent depressions in the north of the Mediterranean basin (also reflected in northern Mallorca and Menorca), assist to explain this pattern. Warm season convection forced in the slopes of the Pyrenees mountains may also contribute to this PG.

S9 is the complementary pattern of S8 over Catalonia. It represents rainfalls in its western side with maximum values found along the Pyrenees range. Apart from the typical mid-afternoon convection of the warm season, the main contributors to this pattern are the Atlantic fronts during its circulation over northern Spain.

S10 and S11 conform two particular patterns of the Balearic Islands. Such degree of detail for a comparatively small territory could have been motivated by the large number of stations available over Mallorca (see Figure 1.6). Both PGs were already isolated as the most important precipitation structures in the work by Sumner et al. (1995a). S10 closely resembles the mean annual rainfall of Mallorca (compare with Figure 1.7a). It clearly reflects the rainfall enhancement produced by the uplands of this island (notably, Sierra de Tramuntana mountains) for a wide variety of flows (Sumner et al. 1995a). S11 represents a wetting gradient toward northeastern Mallorca and Menorca, being this PG principally linked to northerly airflows associated with a low to the east of the islands, and with cold fronts linked to higher latitude disturbances (Sumner et al. 1995a).

Of the 11 PGs (see Table 4.1), the most frequent are S1 and S2. This is what we expected, since these patterns are essentially linked to the Atlantic dynamics that quasi-periodically influences the Spanish latitudes during the cold season. Consequently, S3 also exhibits an important frequency. PGs S8, S9 and S10 (and its variant S11) could be included in a second group. This group is also contributed to by Atlantic disturbances circulating at higher latitudes, and is also influenced by secondary cyclones generated frequently over the northern part of the Mediterranean basin (e.g. the well studied Genoa Gulf cyclone, Reiter 1975). Those PGs which more frequently rely on the Mediterranean

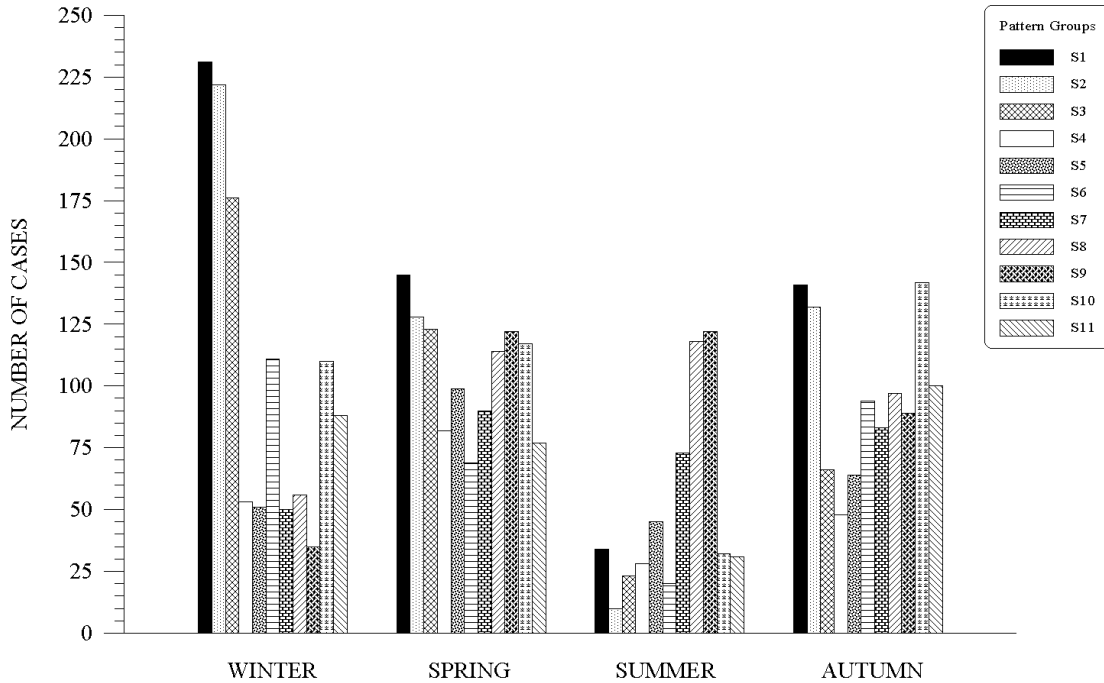


Figure 4.3: Seasonal distribution for the 11 PGs of significant daily rainfall.

dynamics (S4, S5, S6 and S7), present the lowest frequencies.

The seasonal distribution (Figure 4.3) also shows distinct behaviours among the PGs. Some PGs maximize their occurrences during winter (S1, S2, S3, and less strongly S6); other reveal peak values in spring (S4, S5 and S7); S10 and S11 during autumn, although with similar frequencies in winter and spring; and the Catalan patterns S8 and S9 exhibit their maximum occurrences in summer, closely followed by spring.

In comparative terms, Figure 4.3 shows that the Andalusian patterns S1, S2 and S3 clearly dominate during the winter months, since Atlantic depressions tend to affect directly the western part of Andalucía during that period. S6 and the Balearic patterns S10 and S11 are also comparatively frequent during that season. During spring, there are not so large differences among the patterns occurrence. Nevertheless, S1, S2 and S3 exhibit again the highest frequencies (sensibly smaller than in winter, however), followed very closely by S8, S9 and S10. For all PGs except for S7, S8 and S9, the lowest frequencies occur during summer. The important summer contribution to PGs S7, S8 and S9 (representative of the northern peninsular sector) is also noted in Figure 1.7d, and reflects the relevant weight of the typical mid-afternoon convection in the interior north of Valencia and north of Catalonia during summer. That convective activity is triggered over Sistema Ibérico and Pyrenees mountains with the support of the Iberian thermal low (Alonso et al. 1994). During autumn, the most frequent PG is S10. As in winter and spring, S1 and S2 are very frequent, but not S3 in this case.

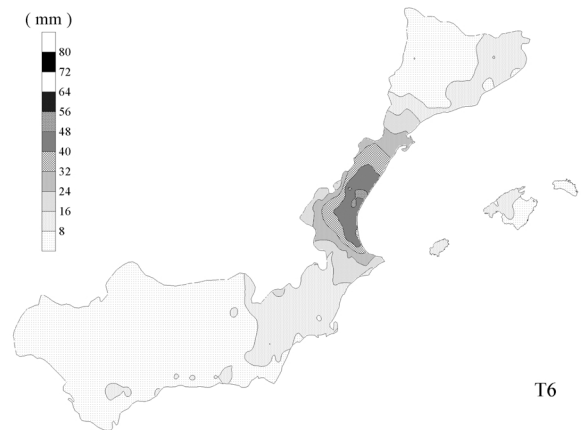
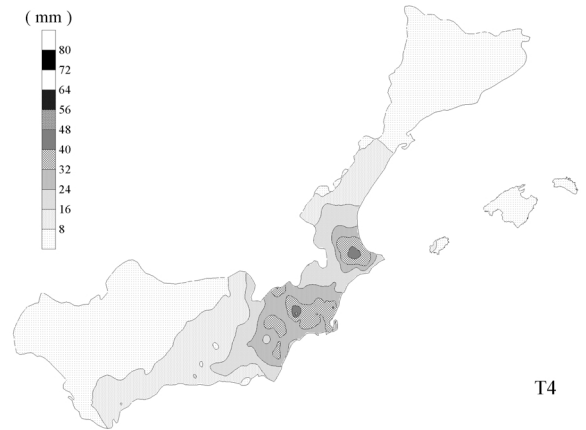
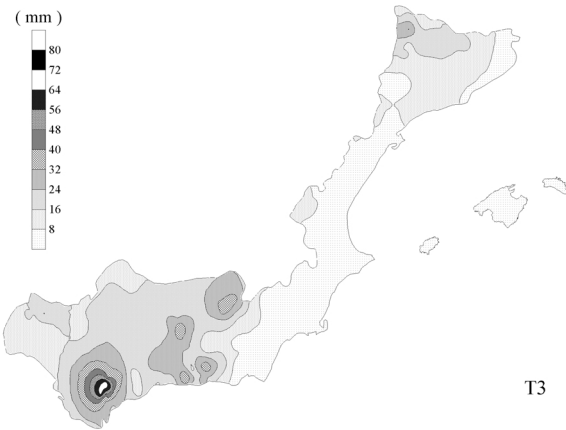
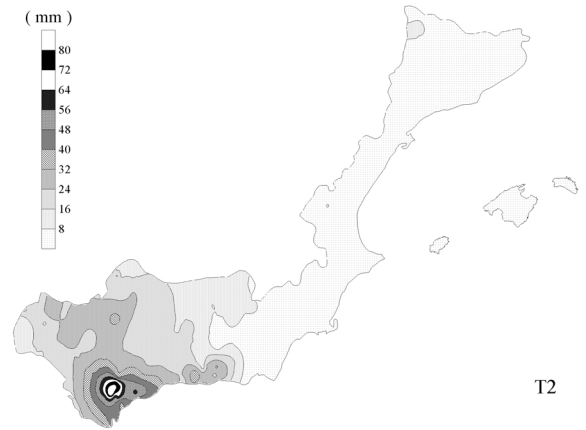
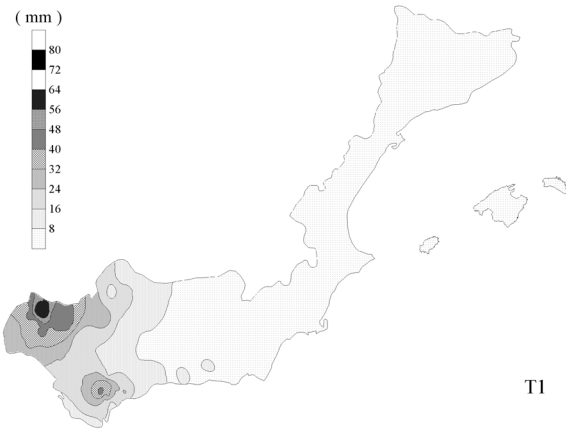
4.3.2 Torrential days

Figure 4.4 shows the 8 PGs obtained in this case. A summary of their main characteristics is provided in Table 4.2. Although much more intense, they resemble the patterns obtained in last section (Figure 4.2). This fact evidences the leading action of the topography for the spatial organization of rainfall, and states that both weak/moderate and torrential events are produced by the same basic synoptic patterns, with the particularity that these patterns become very effective for the latter case. Nevertheless, there are some structural differences between both solutions that we proved to be independent on the number of clusters considered, since they were also present for 9, 10 and 11 clusters solutions: a single PG appears for torrential rainfalls in the Balearic Islands (T8); the Pyrenees cluster S9 does not appear as an independent cluster in the torrential case, rather these mountains play their role as part of clusters T3 and T7; S4 does not have its counterpart in Figure 4.4, but in contrast, the southern coasts of Andalucía play a major role in T3 than in S3.

Figure 4.4 clearly depicts the preference of heavy precipitations for coastal areas and interior mountainous zones. PG T1 represents substantial rainfalls in western Andalucía with maximums in Sierra de Aracena and Sierra de Ronda. PG T2 is representative of heavy precipitations in the Gibraltar area that can extend inland or along the southern coasts of Andalucía. PG T3 represents a broad band connecting central Andalucía with Pyrenees mountains, with maximum values in the peaks and slopes of Sierra de Ronda, Sistema Subbético, Sistema Penético, Sierra de Cazorla and Pyrenees. PG T4 represents heavy precipitations in the Southeast, and T5 is a more local PG representative of heavy rainfalls forced by Sierra de Aitana mountains. PG T6 is characteristic of rainfalls along the coastal band of eastern Spain, most pronounced along the Gulf of Valencia. The Catalan pattern T7 focuses its main action on litoral and prelitoral areas; and T8 is characteristic of important rainfalls in the Balearics, with the maximums usually found in Sierra de Tramuntana.

As seen in Table 4.2, T2 pattern is significantly more frequent than the remainder PGs, and is followed by the Mallorca pattern T8. The least numerous group is T3, that relies importantly on interior zones. Note that the lowest probability obtained in last section for significant rainfalls in eastern Andalucía, Murcia and Valencia (S4 to S7; Table 4.1), is not observed for torrential rainfalls (Table 4.2).

The seasonal distribution of the PGs (Figure 4.5) confirms a different scenario for the occurrence of heavy precipitations that for general rainfalls (Figure 4.3). An accentuated maximum is observed in this case during the autumn season. In this period, synoptic disturbances become very effective by the strong interaction between large amounts of water vapour released from the warm Mediterranean and coastal terrain features (Doswell et al. 1998, Romero et al. 1997, Romero et al. 1998a). This is the most substantial season for all PGs except for the Andalusian patterns T1, T2 and T3, which tend to manifest higher frequencies in winter (but not so clearly as in the general case, Figure 4.3). The spring season loses its relative importance in this case, and torrential events are rarely observed during June, July and August (none of T3 and T5 events were produced in 30 years).



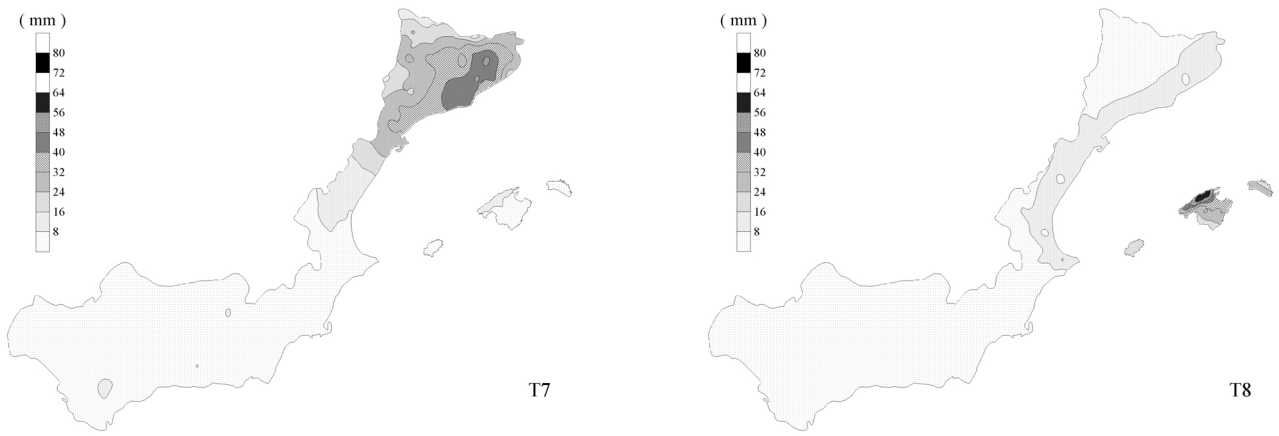


Figure 4.4: Daily rainfall composites for the 8 PGs obtained in the classification of torrential events.

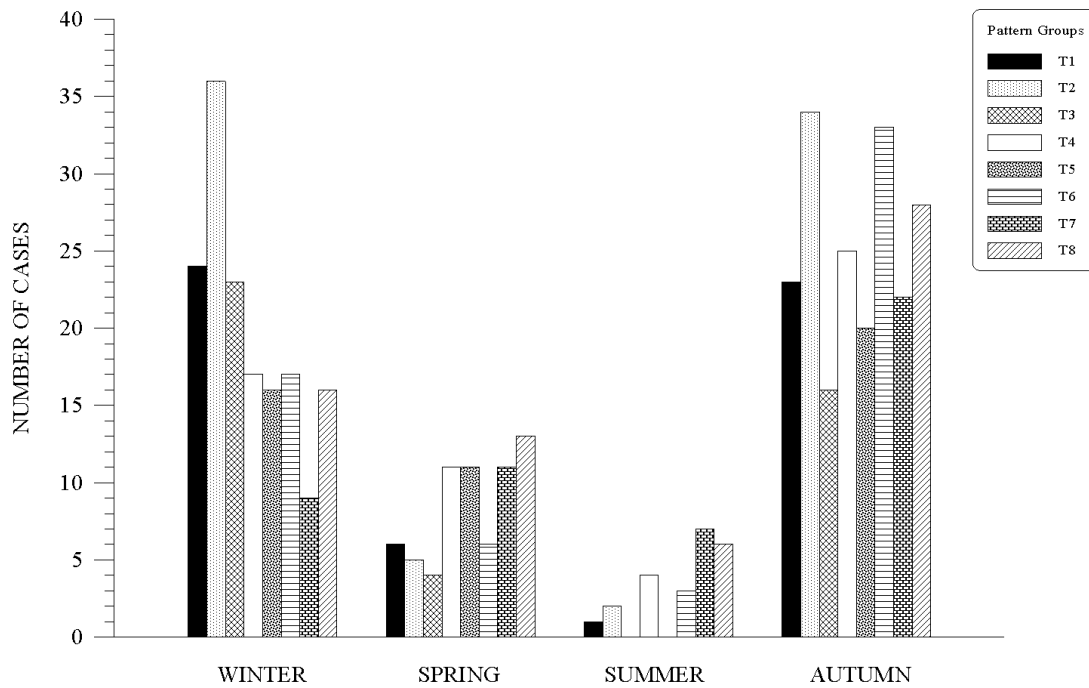


Figure 4.5: Seasonal distribution for the 8 PGs of torrential daily rainfall.

4.4 Conclusions

A daily rainfall data base for the 1964-1993 period has been compiled for the Mediterranean regions of Spain, based on 410 regularly distributed raingauge stations. The coverage was found to be suitable to permit studies on rainfall spatial and temporal variability.

In this chapter we have focused our attention on the spatial distribution of rainfalls in that area. Considering daily rainfalls of enough significance on one hand (3941; during 1964-1993), and only heavy rainfalls on the other hand (449; for the same period), our particular objective has been to derive a simplified collection of spatial patterns governing those events. This task has been accomplished by means of cluster analysis, forcing all individual days to become classified in nonoverlapping clusters, or pattern groups (PGs). As a result, 11 and 8 PGs have been produced for significant and torrential rainfalls respectively (Figures 4.2 and 4.4).

A visual inspection of those PGs confirms that the extent of region and the exposure-sheltering systems induced by the complex topography are sufficiently important as to produce a clear regionalization of the rainfalls. In a broad sense, three main scenarios can be easily conceived: the first one, characteristic of rainfalls in the bulk of Andalucía except its eastern part, and occasionally including the Pyrenees mountains; the second one, representing wet events along the east-facing lands of eastern Andalucía, Murcia and Valencia, and sometimes the Balearics and coastal Catalonia; and the third one, comprising rainfalls in definite zones of the northern part of the Spanish Mediterranean (Pyrenees mountains, eastern Catalonia-northern Valencia, or the Balearic Islands). However, the resulting PGs complete that oversimplified model with additional details, and have permitted to perform a quantitative analysis of the patterns frequency and interseasonal variability.

It is interesting to note that the spatial patterns obtained for both types of rainfalls are basically equivalent. The patterns reflect in both cases the dominant role exerted by the topography for the spatial distribution of rainfalls. Distinct seasonal distributions have been observed, though. For rainfalls in general, the western Andalucía patterns show a clear preference for the winter months, followed almost indistinctly by spring and autumn, and are infrequent in summer, whereas for the torrential limit, winter and autumn are similarly important and the spring season becomes unimportant. In regard to the eastern patterns, for the general case they tend to be similarly frequent in spring and autumn, showing additional peak values in winter the Balearic and southern Valencia PGs and in summer the northern Valencia and Catalan patterns, whereas for torrential events, all of them have a clear predilection for the autumn season.

SIGNIFICANT RAINFALLS

Pattern Group	Days Included	General Area (Maximums)
S1	551	Western Andalucía (Sierra de Aracena, Sierra de Ronda)
S2	492	Central-Western Andalucía and Pyrenees mountains (Gibraltar Strait area)
S3	388	Interior Andalucía, Gibraltar area and Pyrenees (Sierra de Cazorla, Sistema Subbético, Sierra de Ronda)
S4	211	Central Andalucía (Sistema Penibético and south coast)
S5	259	Southeast area (east-facing slopes and coastal areas)
S6	294	Southern Valencia, east Murcia, Ibiza and northern Mallorca (Sierra de Aitana area)
S7	296	Northern Valencia and south Catalonia (Gulf of Valencia)
S8	385	East of Catalonia (coastal zones)
S9	368	Pyrenees mountains and interior Catalonia (western Pyrenees)
S10	401	Mallorca (Sierra de Tramuntana)
S11	296	Mallorca and Menorca (northeastern mountains of Mallorca)
	3941	

Table 4.1: Summary of the 11 pattern groups obtained for significant daily rainfalls (see Figure 1.6 for locations).

TORRENTIAL RAINFALLS

Pattern Group	Days Included	General Area (Maximums)
T1	54	Western Andalucía (Sierra de Aracena, Sierra de Ronda)
T2	77	Central-Western Andalucía (Gibraltar area)
T3	43	Central Andalucía and Pyrenees (Sierra de Ronda, Sistema Subbético, Sierra de Cazorla, south coast and western Pyrenees)
T4	57	Southeast region (east-facing slopes, Sierra de Aitana and coastal zones)
T5	47	Sierra de Aitana zone, Ibiza and northern Mallorca (Sierra de Aitana area)
T6	59	Northern Valencia (coastal areas)
T7	49	Catalonia (coastal areas)
T8	63	Mallorca and Menorca (Sierra de Tramuntana)
	449	

Table 4.2: Summary of the 8 pattern groups obtained for torrential daily rainfalls (see Figure 1.6 for locations).

Chapter 5

CATALONIA AND PIEDMONT HEAVY PRECIPITATION EVENTS

In this chapter¹, we study the extreme precipitation events of Catalonia (12 November 1988) and Piedmont (5 November 1994), presented in section 1.3. Using the SALSA model, we present a numerical study of both events, focusing our attention on the precipitation and surface wind fields. First, we wish to study the feasibility of numerical simulations for this kind of event in the Mediterranean area, and secondly to study the effect of orography and evaporation from the sea on both episodes. This we accomplish following the methodology of Stein and Alpert (1993) and Alpert et al. (1995).

In third place, with additional simulations we compare the performance of two recent parameterization schemes of moist convection (Emanuel 1991; Kain and Fritsch 1990), that have been incorporated in the SALSA model. This task is done for the Piedmont case only, since the latter scheme was not still implemented in the model for the study of the Catalonia case. Moreover, since the relevance of the physical processes involved in the formulation of the convection vary complexely in space and time for a real event, its isolation being very difficult, our analysis overpass this point and it is essentially practical: the results are compared and evaluated using observed precipitation and thermodynamic vertical profiles, and also information from satellite images.

In section 5.1 we describe the new parameterizations and the initialization process that were included in the SALSA model to accomplish our objectives. The study of the Catalonia and Piedmont events is presented in sections 5.2 and 5.3, respectively. Section 5.4 contains the conclusions.

¹The content of this chapter is based on the papers (i) Romero, R., C. Ramis, and S. Alonso, 1997: Numerical simulation of an extreme rainfall event in Catalonia: Role of orography and evaporation from the sea. *Quart. J. Roy. Meteor. Soc.*, **123**, 537-559. (ii) Doswell, C. A. III, C. Ramis, R. Romero, and S. Alonso, 1998: A diagnostic study of three heavy precipitation episodes in the western Mediterranean region. *Wea. Forecasting*, (in press). (iii) Romero, R., C. Ramis, S. Alonso, C. A. Doswell III, and Stensrud, D. J., 1998: Mesoscale model simulations of three heavy precipitation events in the western Mediterranean region. *Mon. Wea. Rev.*, (in press). (iv) Romero, R., C. Ramis, and S. Alonso, 1998: Performance of two cumulus convection parameterizations for two heavy precipitation events in the western Mediterranean. *Meteorol. Atmos. Phys.*, (in press).

5.1 Model developments

5.1.1 Surface submodel

The use of the complex surface physical package described in section 2.5 requires the specification of temperature and moisture profiles within the soil, and a large number of surface parameters related with soil and vegetation properties (see Tables 3.1 and 3.2). When spatial distributions of all these parameters can not be easily obtained, it is preferable to use simpler surface schemes.

For our simulations of heavy precipitation events in the western Mediterranean, we have included in the SALSA model a two-layer force-restore method (Bhumralkar 1975; Blackadar 1976) to account for the surface temperature variation. In this method, the ground surface temperature T_G is predicted by the equation:

$$\frac{\partial T_G}{\partial t} = \frac{c_1}{k\tau_d^{1/2}}(H_s)_G - \frac{c_2}{\tau_d}(T_G - T_D) \quad (5.1)$$

where $c_1=2\pi^{1/2}$, $c_2=2\pi$, k is the thermal inertia and τ_d the diurnal period.

On the right-hand side of equation 5.1, the first term represents the forcing by the ground heat flux $(H_s)_G$, and the second term is a restoring term which contains the deep soil temperature T_D . $(H_s)_G$ is obtained through the energy balance equation 2.16, which in turn depends on surface albedo, emissivity, roughness and available moisture for evaporation. The deep soil temperature T_D can be treated as a constant for short-range simulations (Deardorff 1978).

In the above surface model, only five surface properties are necessary: albedo, emissivity, roughness, thermal inertia and available moisture. As in Benjamin and Carlson (1986), all these properties have been specified by the same surface index under the assumption that they appear related for natural surfaces. Based on NOAA-AVHRR mosaics and other information, six types of land have been considered for the western Mediterranean region (Table 5.1). The surface types, depicted in Figure 5.1, show a transition from dry surfaces, characteristic of Africa and the major part of Spain, to the more humid zones of western Europe and the northern part of the Mediterranean basin.

Although simple, the force-restore method is able to represent the effect of surface heterogeneities on atmospheric circulations (Benjamin and Carlson 1986), and seems sufficient given the lack of a flexible data-base of surface parameters specified for the purpose of running a more complete surface package.

5.1.2 Cumulus convection parameterizations

Since the type of event being studied is influenced or dominated by deep convection, moist convective processes must be represented adequately in the numerical model. At the resolutions of our mesoscale simulations (20 km), the use of some type of convective parameterization scheme is still necessary since moist convective processes in the atmosphere occur almost exclusively on spatial scales smaller than those explicitly resolved. Based on different assumptions, several techniques for estimating the rate of subgrid scale convective precipitation and the redistribution of heat, moisture and momentum produced by the ensembles of convective clouds have been developed to be used in numerical

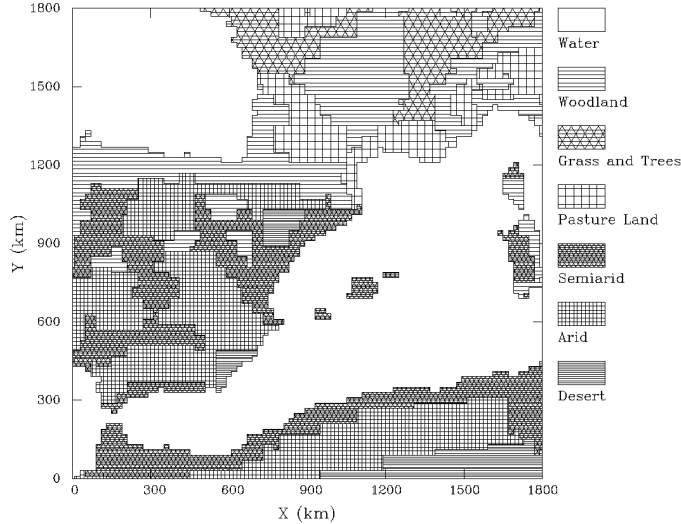


Figure 5.1: Distribution of surface types in the western Mediterranean region.

Type of surface	Albedo (%)	Available Moisture	Thermal inertia (Jul m ⁻² s ^{-0.5} K ⁻¹)	Emissivity	Roughness (cm)
Woodland	10	0.75	2926	0.95	50.0
Grass and Trees	12	0.60	2508	0.92	30.0
Pasture Land	15	0.30	2090	0.90	20.0
Semiarid	20	0.10	1672	0.85	10.0
Arid	25	0.05	1254	0.80	5.0
Desert	30	0.02	836	0.75	1.0

Table 5.1: Characteristics of the six land types derived for the western Mediterranean (from Benjamin and Carlson 1986).

models (Frank 1983). We have included two of the most recent parameterization schemes in the SALSA model: the scheme of Emanuel (1991), hereinafter referred to as EM, and the scheme of Kain and Fritsch (1990), referred to as KF.

The EM scheme is based on the dynamics and microphysics of convection as revealed by aircraft observations. The fundamental entities for moist convective transports are the subcloud-scale drafts rather than the clouds themselves. As opposed to other schemes based on bulk-entraining plumes (e.g. Fritsch and Chappell 1980; Arakawa and Schubert 1974), the convective transports are idealized based on reversible ascent of the subcloud-scale entities, mixing, and buoyancy sorting (Raymond and Blyth 1986). That is, air from the subcloud layer is lifted to each level i between cloud base and the level of neutral buoyancy for undilute air; a fraction of the condensed water is then converted to precipitation, which falls and partially or completely evaporates in an unsaturated downdraft; the remaining cloudy air is then assumed to form a uniform spectrum of

mixtures with environmental air at that level, that ascend or descend according to their buoyancy. A detailed formulation of this episodic mixing model can be found in Emanuel (1991).

The essential idea of EM is the quasi-equilibrium assumption used to determine the updraft mass fluxes M^i of undilute boundary-layer air to each level i . M^i , that must be known to close the system, are represented as vertical velocities w^i determined by the amount of Convective Available Potential Energy (CAPE) for undilute ascent to level i , multiplied by fractional areas σ^i . These fractional areas are in turn determined in such a way as to drive the mass fluxes toward a state of quasi-equilibrium with the large-scale (explicitly resolved) forcing. In summary:

$$M^i = \rho^i \sigma^i w^i,$$

where ρ^i is the air density, $w^i = (2CAPE^i)^{1/2}$, and σ^i is adjusted at each time step according to

$$\delta\sigma^i = \begin{cases} \alpha\delta w^i + \beta, & w^i > 0 \\ \alpha\delta w^i - \beta, & w^i = 0, \end{cases}$$

where δ represents the change between two consecutive time steps, and α , β are two external parameters controlling the evolution of the mass flux.

The quasi-equilibrium criterium for calculating the convective mass fluxes is supported by the observed behaviour of the cloud ensembles (as a collective) in maritime tropical atmospheres. Since the air masses over the Mediterranean present frequently convective instability (Meteorol. Office 1962, Ramis 1995), it seems that such type of scheme could be appropriate for the considered area.

Alternatively, other authors suggest that the magnitude of convective heating and drying effects on scales less than 50 km (typical resolutions of mesoscale models) is much more strongly correlated with local CAPE than with the large-scale rate of destabilization or moisture convergence (Fritsch et al. 1976; Kreitzberg and Perkey 1976). Built in basis of this argument, the KF convective scheme assumes that moist convection only occurs when potential buoyant energy (PBE \equiv CAPE) becomes available (ABE), which means that any negative buoyancy experienced by a parcel to rise to its level of free convection has been eliminated or overcome. With this philosophy, convection responds not only to the rate at which the large scale is generating buoyant energy, but also to the buoyant energy generated and stored prior to the onset of deep convection. Processes as low-level convergence, air mass overrunning, or when low-level heating and mixing remove any stable layers drive the atmosphere to the release of convection (PBE becomes ABE). The amount of convection is determined by expanding the stabilization rate (destruction of ABE) over a characteristic short time (30 min - 1 h) (Fritsch and Chappell 1980). This is expressed as

$$ABE = \int_{L\hat{F}C}^{E\hat{T}L} g \left[\frac{\hat{T}_U(z) - \hat{T}(z)}{\hat{T}(z)} \right] dz \rightarrow 0,$$

where the hat symbol indicates values after the adjustment process. In particular, $\hat{T}_U(z)$ is the vertical distribution of temperature in the updraft that results from lifting the convectively modified air, $\hat{T}(z)$. $L\hat{F}C$ is the new level of free convection and $E\hat{T}L$ the new equilibrium temperature level.

In KF, the changes in temperature and mixing ratio in the atmospheric column are the sum of the effects of compensating subsidence in the environment plus the effect of area-weighting the cloud updraft, downdraft and environment. The interaction between cloudy parcels and their environment is formulated using a one-dimensional entraining/detraining plume model (see Kain and Fritsch (1990) for a detailed description). In addition to heat and humidity, momentum is also vertically exchanged in the KF parameterization.

5.1.3 Initialization and boundary conditions

Numerical experiments of the breeze circulation in Mallorca (chapter 3), could be initialized in a very simple manner, using a single radiosounding and assuming horizontally uniform fields and calm wind. For the purpose of running simulations of real events in regions as large as the western Mediterranean, however, the atmosphere must be initialized with balanced three-dimensional fields based on observations, and lateral boundary conditions must represent appropriately the time-varying external forcing. Therefore, we adapted the SALSA model to use large-scale meteorological fields in the form of uninitialized gridded analyses on standard pressure levels. Analyses from the limited area model (LAM) of the INM of Spain were used for the Catalonia case, and analyses from the ECMWF were used for the Piedmont case and Tarragona case (next chapter). These analyses are given on regular latitude-longitude grids with grid intervals of 0.91 and 0.75 degrees, respectively.

First of all, the SALSA model regular grid is defined, where a polar-stereographic projection is used to map the region of interest. The orographic data-base (NGDC/NOAA Orography, with resolution of 5 minutes), is then interpolated linearly to the model grid points. The short wavelength components of the interpolated orography are filtered to avoid excessive grid-length scale orographic forcing (Shapiro 1970).

The large-scale meteorological fields comprise temperature, relative humidity, geopotential and wind components. In the case of temperature and humidity, the fields are analysed at the model grid points on the pressure surfaces by a univariate method of successive corrections (Pedder 1993).

For the wind and geopotential fields, a mass-wind balance is imposed in which the geopotential is made to adjust to the “observed” wind field -a process which is applied in two steps. In the first step, the stream function and wind (including a divergent component) are analysed for each isobaric surface, applying the statistical technique of Pedder (1989) on the wind data. This technique avoids the need for the empirical specification of external boundary conditions for the stream function and velocity potential, which is necessary in those other methods where the wind components are derived from estimated values of vorticity and divergence. In the second step, we follow Warner et al. (1978) and calculate the geopotential, ϕ , from the stream function, ψ , by solving the balance equation

$$\nabla^2\phi = f(\psi_{xx} + \psi_{yy}) - 2m^2(\psi_{xy}^2 - \psi_{xx}\psi_{yy}) + f_y\psi_y + f_x\psi_x$$

where m is the map factor, f the Coriolis parameter, and subscripts indicate derivatives. The boundary values of ϕ are given by direct analysis of geopotential data.

Sea-level data are extrapolated from the 1000 hPa level, assuming a standard temperature lapse rate and constant relative humidity. The pressure is found hydrostatically

and the wind is set to zero.

The analysed fields are then vertically interpolated at the ν -levels of the mesoscale model. But as a consequence of the analysis and interpolation process, some unbalances of the fields could arise that could induce a degradation of the forecast. In order to reduce this effect, a hydrostatic adjustment is applied through a variational method, correcting the profiles of geopotential and temperature for each grid point. And the wind, which is interpolated linearly with the already-corrected values of geopotential to preserve the mass-wind balance, is also slightly modified after applying a variational adjustment that minimizes the vertical integral of the horizontal divergence (Pinty 1984). The aim of this dynamic adjustment is to filter out the fast gravity waves.

One-way nesting of the mesoscale model allows assimilation of the external forcing, which is given by time-dependent prescribed values of the fields at the lateral boundaries. At any given time, the fields at the boundaries are determined by linear interpolation between the values corresponding to the available analysis times (00 and 12 UTC for LAM analyses; and 00, 06, 12 and 18 UTC for ECMWF analyses).

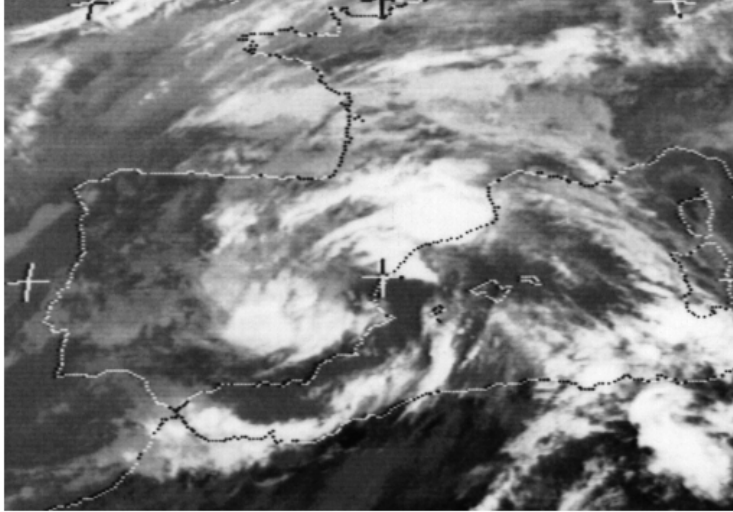
5.2 Catalonia event

5.2.1 Synoptic overview

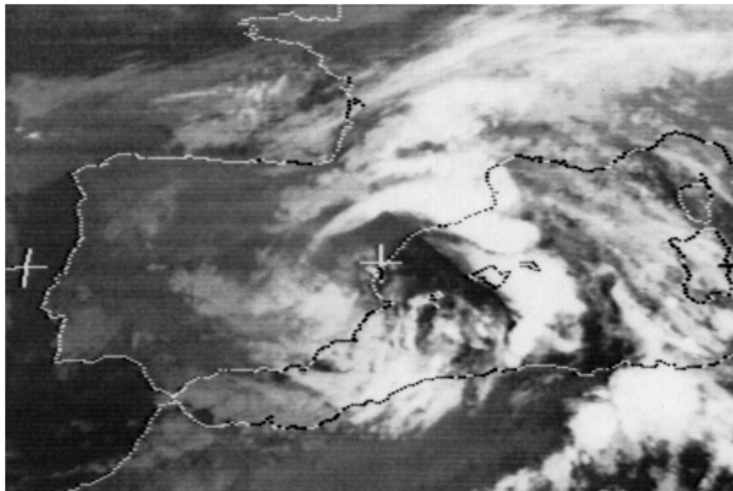
The synoptic pattern at low levels for this event was dominated by an anticyclone located on the European continent, stretching as far as the western Mediterranean and producing a south-easterly flow towards the Catalan coast. A baroclinic shortwave trough, reflected as a low pressure centre with an associated frontal system, moved towards the east from Gibraltar and was located over south-east Spain. This low-pressure centre, combined with the anticyclone, created a strong pressure gradient over the Mediterranean, with winds blowing directly towards the Catalan coast, so favouring the advection of warm humid air towards the northern part of the western Mediterranean. In Figures 5.2a and b, which show the meteorological situation at 1000 and 850 hPa at 12 UTC on 12 November 1988, these features are clearly visible.

At upper levels, the wave exhibited a closed circulation with a cold core over south-eastern Spain (see Figure 5.2c), the trough having a slightly negative tilt and low cyclonic vorticity. From an inspection of Figures 5.2a, b and c and the 300 hPa chart (not shown) it seems that the vertical axis of the wave tended to tilt slightly to the south-east with height. The satellite picture at that time (Figure 5.3a) shows clouds over Catalonia and the Mediterranean area, with a frontal band over the African coast. Convection cannot easily be observed within the general structure of the clouds but it did occur over Catalonia (as indicated by the SYNOP information).

A synoptic-scale objective diagnosis of the event was done by Ramis et al. (1995) who calculated the factors favourable for convective development at that scale (Barnes 1985; Barnes and Newton 1986). They summarized the diagnostic information by means of a composite chart in which were plotted the zero contours of quasi-geostrophic forcing at 850 hPa, the difference of θ_e between 500 and 1000 hPa, and the vapour convergence in the 1000-850 hPa layer. The area where the three favourable processes overlap represents a zone where, as a consequence of the synoptic structure, mesoscale lifting mechanisms



(a) 12 UTC 12 November



(b) 00 UTC 13 November

Figure 5.3: Infrared Meteosat image for (a) 12 UTC 12 November 1988, (b) 00 UTC 13 November 1988.

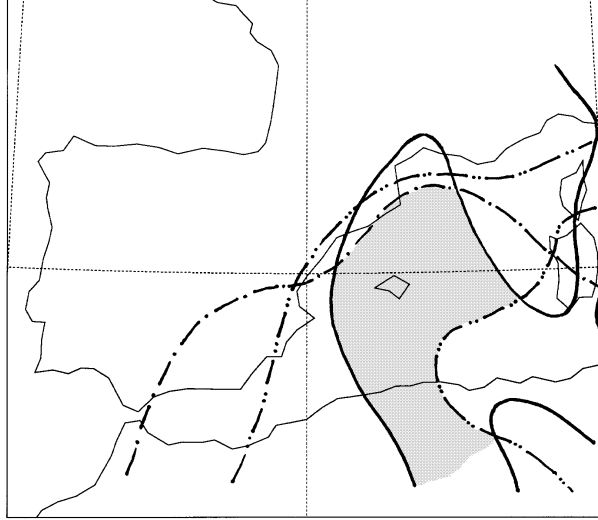


Figure 5.4: Composite chart for 12 UTC 12 November 1988 (after Ramis et al. 1995). Continuous line, zero contour of quasi-geostrophic forcing, FQ , at 850 hPa. Dot-dashed line, zero contour of equivalent potential temperature difference, $\Delta\theta_e$, between 500 and 1000 hPa. Dot-dot-dashed line, zero contour of moisture convergence, F_q , in the 1000-850 hPa layer. The shaded zone denotes existence of the three forcing mechanisms ($FQ > 0$, $\Delta\theta_e < 0$, $F_q > 0$).

have greater facility for the development of convection. Figure 5.4 contains the composite chart for 12 UTC 12 November 1988. It shows that the area of overlap for the favourable mechanisms extended over the western Mediterranean as far as the Catalan coast. Satellite pictures show that convection developed during the afternoon south of the Balearic Islands and progressed to the north (see Figure 5.3).

The synoptic pattern evolved in the hours following with a displacement of the low to the north, the displacement in the upper levels being much more distinct than in the lower levels. The composite chart of favourable synoptic-scale parameters for 00 UTC 13 November 1988 showed the intersection zone situated over the Mediterranean and reaching as far as the south of France. The satellite picture for that time (Figure 5.3b) shows the cold front and the convection over the Mediterranean and Catalonia.

The total rainfall in Catalonia for the period from 07 UTC 12 November to 07 UTC 13 November was very high (see Figure 1.10). According to the classification derived in chapter 4, this pattern closely corresponds to a T7 pattern (compare with Figure 4.4). Most of the precipitation fell during the evening of the 12th. It can be seen that more than 200 mm fell close to Barcelona, with a tongue of high precipitation extending to the north. The greatest quantity was collected on the coast and pre-coastal zone where there exists important orography (see Figure 1.6). It seems quite possible, therefore, that the orography played an important part in focusing the convection.

5.2.2 Description of the experiments

Although the total rainfall, shown in Figure 1.10, corresponds to a 24-hour period, most of it was registered during the late afternoon and early night. In which case, there-

fore, we considered those meteorological LAM analyses available for 12 UTC 12 November and 00 UTC 13 November and have extended the simulations for a 12-hour period between these times.

Figure 5.5 shows the mesoscale model domain. It is centred in the south of Catalonia at position 1°E , 41°N and measures $1800 \times 1800 \text{ km}^2$. That region is wide enough to incorporate the major Spanish orographic systems and also those formed by the western part of the Alps (see Figure 1.5). North Africa, with its important orography, is also included in this area, since the influence of the Atlas range under low level southerly flow regimes is suspected of having an important influence on the meteorological systems that develop over the southern part of the western Mediterranean (Reiter 1975). The numerical experiments have a horizontal grid-length of 20 km (91x91 points), and 30 vertical levels. The first atmospheric level is at a height of about 4.5 m above the ground and the lowest 2 km are covered by 12 computational levels. The EM convective scheme has been used for the simulations.

The roughness length, which is a function of soil type (Table 5.1), has been explicitly increased to 1 m in areas of elevated terrain to better represent the subgrid mountain drag (Georgelin et al. 1994). In addition, owing to the season in which the event occurred, the available soil moisture listed in Table 5.1, has been increased by a fraction of 0.1 for all soil types. Sea surface temperature (SST) and subsoil temperature (both constant during the simulation) correspond to the November mean values of SST and surface air temperature, respectively (Robinson et al. 1979, WMO Unesco 1970).

As in section 3.2.3, we apply the factor separation technique of Stein and Alpert (1993) to isolate the effect of orography and evaporation from the sea. Therefore, four experiments are considered necessary for our purposes. We identify as f_0 the experiment without orography and without evaporation from the sea, f_1 represents the simulation with orography but without evaporation, f_2 without orography but with evaporation from the sea allowed, and f_{12} is the full experiment with both orography and sea evaporation present; these experiments are summarized in Table 5.2.

Experiment	Orography	Sea evaporation
f_0	NO	NO
f_1	YES	NO
f_2	NO	YES
f_{12}	YES	YES

Table 5.2: Experiments designed to isolate the effect of orography and evaporation from the sea for the case studies.

The contributions associated with each factor can be written:

1. Effect of the orography $f_1^* = f_1 - f_0$
2. Effect of the sea evaporation $f_2^* = f_2 - f_0$
3. Effect of the interaction
orography - sea evaporation $f_{12}^* = f_{12} - (f_1 + f_2) + f_0$

Apart from the orography and latent-heat flux at the sea surface, which are either included, or omitted (see Table 5.2), the rest of the parameters are initially the same for all four experiments. It should be noted that the initial fields in experiments f_0 and f_2 are not entirely free of orographic influence, since they are based on observations which, of necessity, contain orographic effects.

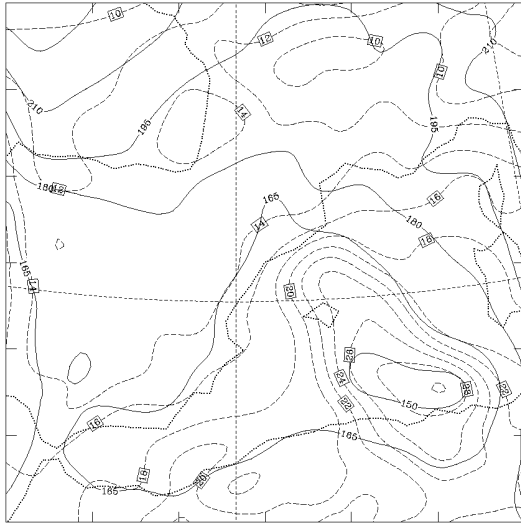
5.2.3 Results of the full experiment

In spite of the simulation being short, the spin-up process seems not to be crucial for the results, partly because of the initialization procedure applied. Twenty minutes after the simulation has started, the initial imbalances have practically disappeared. In addition, precipitation (both convective and large scale) was already occurring at the same time.

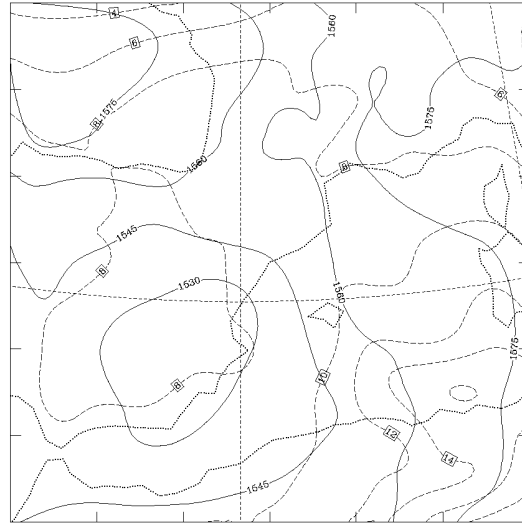
Model results at the end of the f_{12} simulation (00 UTC on 13 November) show that at 1000 hPa (Figure 5.5a), a low has developed over the sea close to the Algerian coast and there is very warm air over the Mediterranean. The distribution of isotherms over the sea shows clearly a “warm/cold” frontal structure, and the warm temperature advection seems to be large close to the Catalan coast. The isohypse distribution at 850 hPa (Figure 5.5b) shows the low over south-east Spain, but the associated flow over the Atlas mountains is from the south, which shows that the shallow low at 1000 hPa is an orographic effect. In addition, isotherms a foehn effect in the lee of the Atlas mountains and warm advection over the Mediterranean towards the Catalan coast.

At the 500 and 300 hPa levels (Figures 5.5c and d), a low is located on the eastern coast of Spain. At the 500 hPa level the low exhibits a cold core and the closed isohypses look like a cut-off. At level 300 hPa, the thermal structure shows clearly the descent of the tropopause, especially over south-eastern Spain.

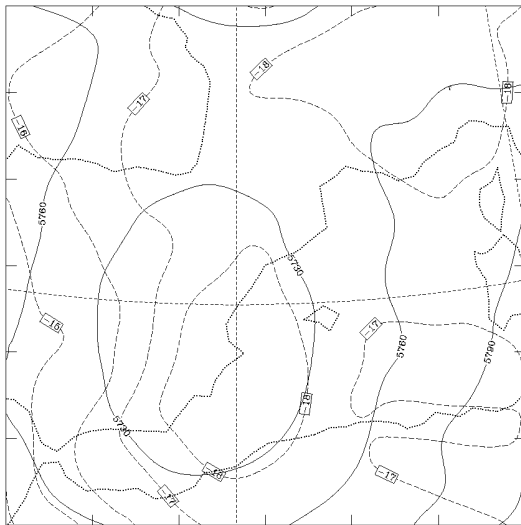
Figure 5.6 shows a subjective surface mesoscale analysis for 00 UTC 13 November. It should be noted that the analysis was rendered difficult in consequence of the lack of data from over the sea. When doing subjective analysis in data-sparse regions like the oceanic areas of the western Mediterranean, it is useful to apply conceptual models to help supplement the analysis. To this end we have applied models of pressure distribution around a thunderstorm (Schofield and Purdom 1986), and pressure dipole structures (high pressure in the windward side and low in the lee) such as are developed by a mountain range when wind blows normal to it, particularly in the case of southerly flows over the Alps (Vergeiner et al. 1982), the Pyrenees (Bessemoulin et al. 1993) and the Atlas mountains (Jansá et al. 1986). Although the data are certainly not available to validate some of the analysed structures, nevertheless we have tried to ensure that the analysis is consistent with the observations to the maximum extent possible. Thus, we believe that



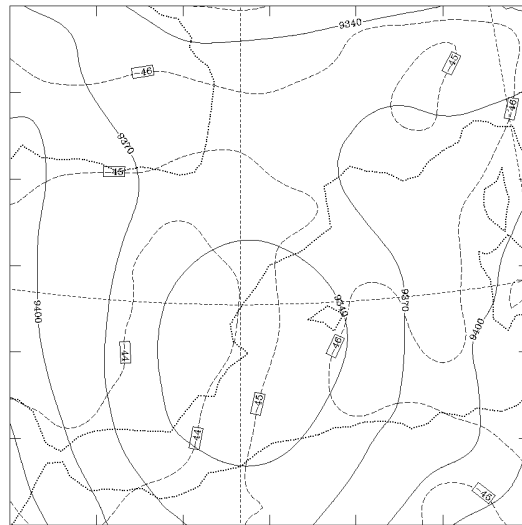
(a) 1000 hPa



(b) 850 hPa



(c) 500 hPa



(d) 300 hPa

Figure 5.5: Forecast fields on 00 UTC 13 November for experiment f_{12} of the Catalonia case, showing height (gpm, continuous line) and temperature ($^{\circ}$ C, dashed line): (a) 1000 hPa; (b) 850 hPa; (c) 500 hPa; (d) 300 hPa.

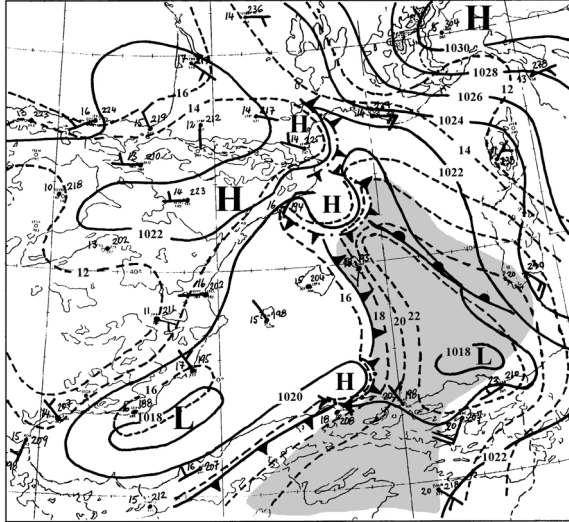


Figure 5.6: Subjective surface mesoscale analysis on 00 UTC 13 November 1988. Continuous lines represent isobars, dashed lines isotherms and the shaded area represents the zone with dew point higher than 16°C . Available pressure, temperature and wind observations are plotted.

our subjective analysis is, at least, a plausible hypothesis about the subsynoptic-scale structure and that it is not inconsistent with the observations (including the satellite imagery shown in Figure 5.3b, and the standard synoptic data). The most salient features shown in Figure 5.6 are the high pressure windward of the Alps and the low in the lee of the Atlas mountains, the cold front on the Mediterranean and a tongue of warm moist air extending from Africa to Catalonia. A mesoscale high produced by convection close to Catalonia provides the low-level lifting mechanism for maintaining the convection over the same area. Figure 5.6 may be compared with the satellite image (Figure 5.3b). The model result at 1000 hPa (Figure 5.5a) also shows the low in the lee of the Atlas mountains and warm air over the Mediterranean; the frontal structure is also well defined. The temperatures given by the model over the Mediterranean are higher than those that can be deduced from the data used in the subjective analysis.

The forecast precipitation field is shown in Figure 5.7. Figure 5.7a displays the total rainfall predicted by the model after 12 hours of simulation (00 UTC on 13 November). It can be seen that the precipitation is concentrated close to the coast and over Catalonia, and also to the east of the Balearic Islands. This figure may be compared with Figure 1.10; the correspondence between the spatial distribution of rainfall over land as predicted by the model and the precipitation registered seems rather good. In particular, the observed coastal maximum is given correctly by the model. On the other hand, the model has underestimated the total precipitation.

Figure 5.7b, which displays the convective part of the precipitation field, shows that the precipitation over the sea and most of the rainfall over the Catalan coast in Figure 5.7a, are given by the EM convective scheme.

A cross-section along direction AB in Figure 1.5 (Figure 5.8a), deduced from the 12-hour model forecast, shows that at low levels the warmest air is located close to Catalonia, while at middle tropospheric levels it is located slightly to the north-east. The equivalent

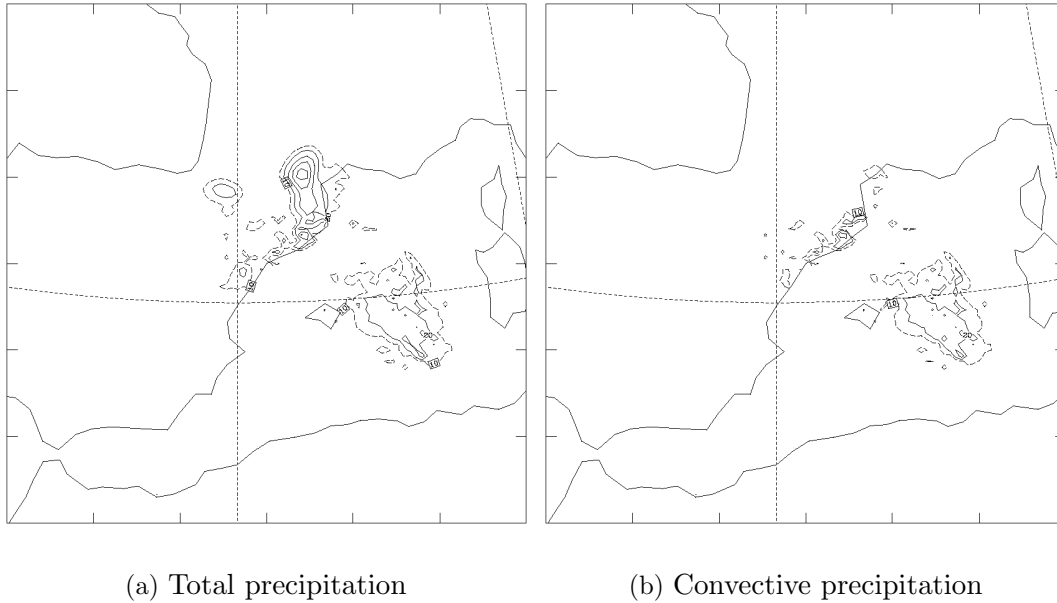


Figure 5.7: (a) Forecast total precipitation from 12 UTC 12 November to 00 UTC 13 November, for experiment f_{12} of the Catalonia case. (b) As for 5.7a, but for the convective contribution. Contour interval is 20 mm starting at 20 mm (continuous line). Dashed contour represents 10 mm.

potential temperature field shows that the warm air at low levels is also very humid, since there is potential instability to the south-west of, and aloft over, Catalonia up to a height of 3000 m, while at low levels over Catalonia, and to the north-east, the air is potentially stable.

Cross section CD (Figure 5.8b) shows also that warm air is located over the sea, to the south-east of Catalonia, where the dry static stability is very weak. In addition, isotherms of equivalent potential temperature show that the warm air is very humid at low levels, since the potential instability close to the Catalan coast is strong from surface up to 4000 m. Therefore, the conditions for convection are found over the sea, but in close proximity to the Catalan coast.

Figure 5.9 shows the predicted wind field at 00 UTC at the first level (approximately 4.5 m above the ground). The strongest winds are found in the northern Mediterranean, showing strong convergence close to the north Catalan coast. Two important convergence lines appear over the sea. When they are examined in conjunction with the thermal structure at 1000 hPa (Figure 5.5a), these are identified clearly as being associated with the frontal zones. A very small and intense cyclonic circulation appears over the Catalan coast with another (of larger diameter) between Catalonia and the Balearic Islands. The wind over Catalonia is very weak, except in the coastal zone where it is from the north and north-east. A qualitative comparison of the winds given by the model against those observed at some WMO observatories (Figure 5.6) is satisfactory, and shows that along the Catalan coast, where the synoptic analysis from the LAM of the INM (not shown) gives a south-easterly wind, the model has forecasted the observed north-easterly wind

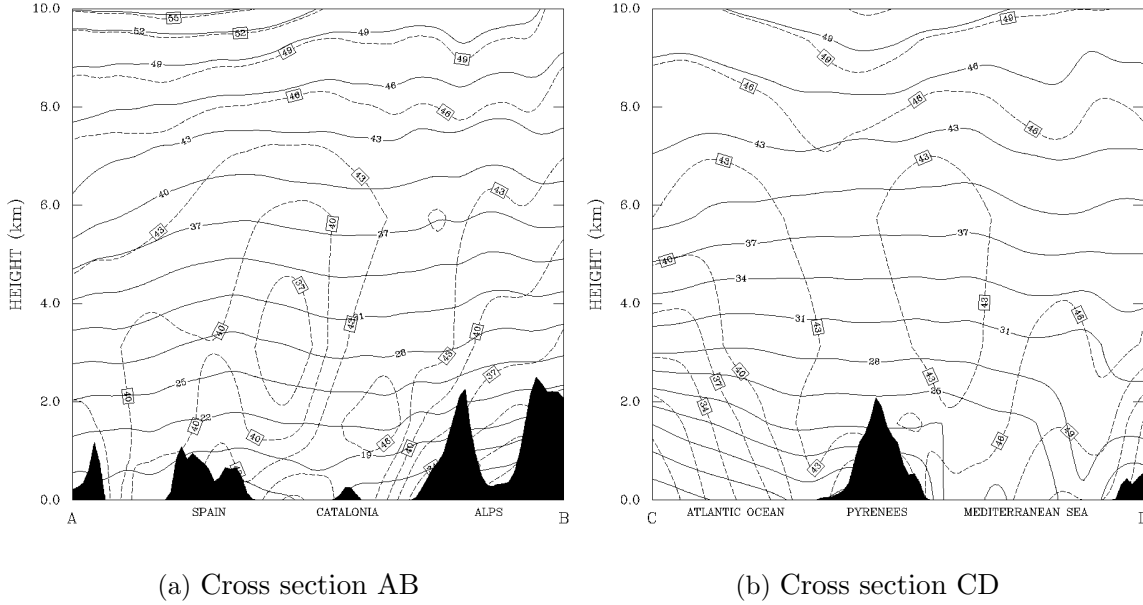


Figure 5.8: Thermodynamic fields given by experiment f_{12} of the Catalonia case on 00 UTC 13 November: (a) along vertical cross section AB; (b) along vertical cross section CD (see Figure 1.5 for cross sections). Continuous contours represent the field of dry potential temperature ($^{\circ}\text{C}$), and dashed contours of equivalent potential temperature ($^{\circ}\text{C}$).

well.

The latent-heat flux at the surface seems to be, a priori, an important factor in events of this kind, since the sea is still warm during the autumn season. Figure 5.10 shows the latent heat flux over the sea at 00 UTC as given by the model. Two well-defined areas of important evaporation are present. The first is located close to the Algerian coast, where the wind is appreciable and where the air is very warm and dry as a consequence of the Atlas-induced foehn. The second evaporation area is located in the northern Mediterranean, close to the French coast and coincides, again, with strong dry winds coming from the European continent.

5.2.4 Effects of the orography and evaporation from the sea

As was indicated in section 5.2.2, in the basic experiment, f_0 , both the orography and latent-heat flux from the sea are omitted. The forecast precipitation field at 00 UTC is given in Figure 5.11a. It can be seen that the precipitation over the sea is similar to that obtained in the full experiment, f_{12} (Figure 5.7a). The centre of maximum precipitation to the east of the Balearic Islands appears, but the precipitation over land is quite different.

Figure 5.11b displays the precipitation-field forecast for experiment f_1 , in which the orography was included but not the evaporation. The spatial structure of the precipitation resembles that of the full experiment f_{12} , both over sea and over land. The centre of heavy precipitation over the Catalan coast is now apparent in addition to the extension of the precipitation field inland. The isolated effect of the orography (f_1^*) is shown in Figure

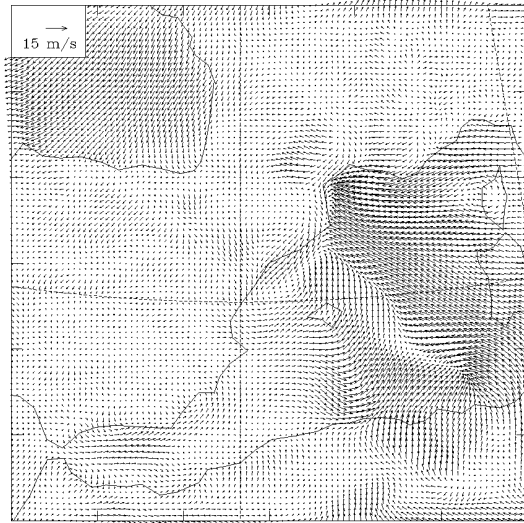


Figure 5.9: Forecast surface wind field on 00 UTC 13 November for experiment f_{12} of the Catalonia case. The arrow on the upper left-hand corner represents 15 m s^{-1} .

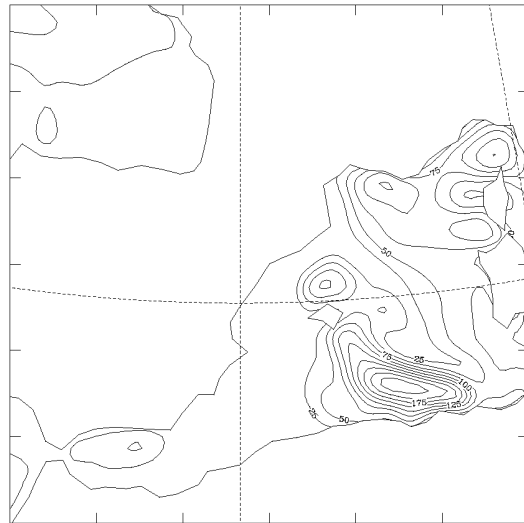


Figure 5.10: Latent heat flux from the sea on 00 UTC 13 November for experiment f_{12} of the Catalonia case. Contour interval is 25 W m^{-2} starting at 25 W m^{-2} .

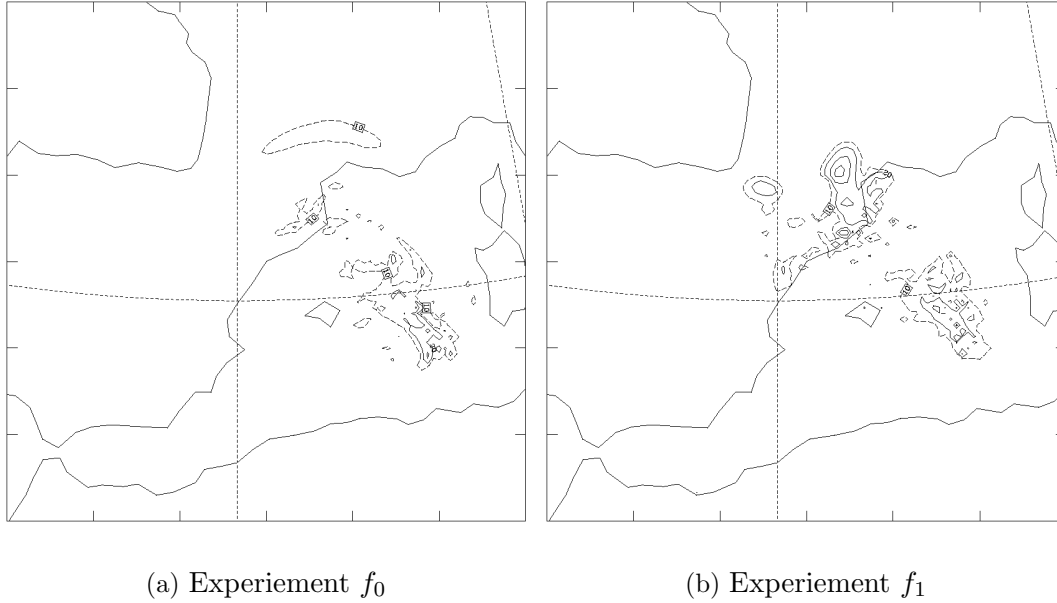
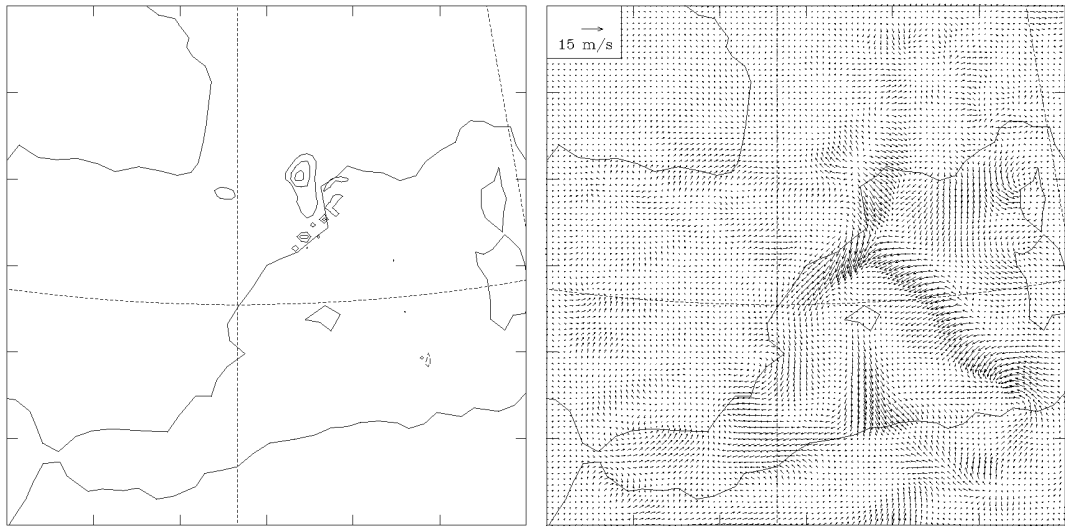


Figure 5.11: Forecast total precipitation from 12 UTC 12 November to 00 UTC 13 November: (a) for experiment f_0 of the Catalonia case; (b) for experiment f_1 of the Catalonia case. Contour interval is 20 mm starting at 20 mm (continuous line). Dashed contour represents 10 mm.

5.12a. The main effect on the precipitation has been to focus it on the Catalan coast and to extend it inland. Negative contributions are noticeable only over the sea, to the east of the Balearic Islands. The effect of the orography on the wind field is shown in Figure 5.12b. The most important action appears to take place over the sea. Close to the Catalan coast the effect is very strong in the sense that it produces a backing of the wind. Close to the Algerian coast, on the eastern side of the domain, a cyclonic circulation is clearly defined extending towards the Catalan coast. Another effect can be identified close to the French coast, in the sense that the wind increases where the flow from the Gulf of Genoa but ends but decreases over the coast. Similarly, the wind increases in the lee of the Pyrenees. The effect of Corsica and Sardinia is also evident; they produce in their lee, as a consequence of their shape and the atmospheric stability, circulations opposed to the general flow.

Experiment f_2 includes latent-heat flux from the sea, but not orography. The spatial distribution of precipitation obtained for the 12-hour forecast (not shown) is very similar to that obtained for experiment f_0 (Figure 5.11a). In the $f_2 - f_0$ precipitation field (Figure 5.13a), only small differences appear to the east of the Balearic Islands and close to the Catalan coast. Both areas correspond to the limit of zones where evaporation and moisture advection are strong. We can conclude that evaporation may be important in such events, but not for periods as short as this simulation, for which the atmosphere already contains significant moisture at low levels. Similarly, the effect of evaporation on the wind field is considered to be negligible (Figure 5.13b).

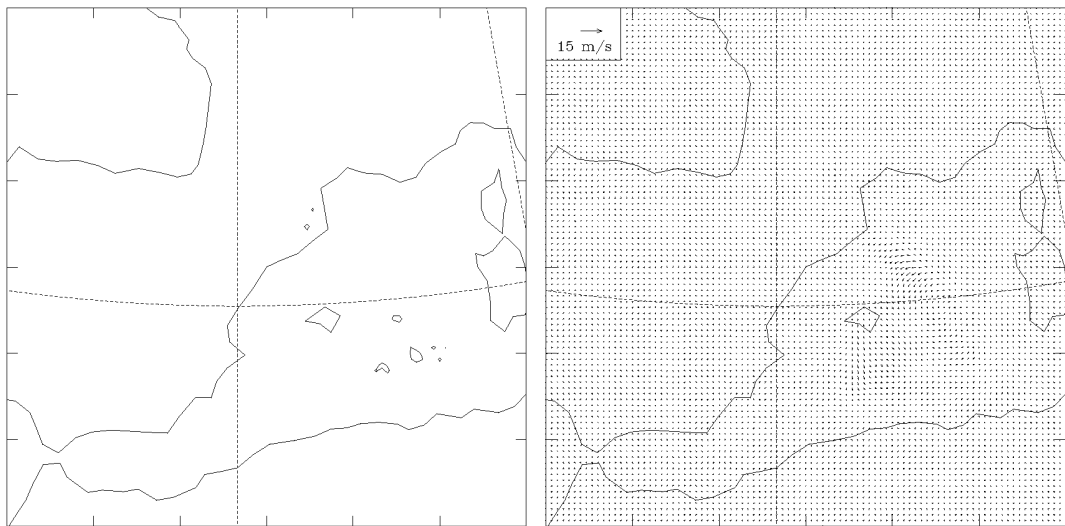
The effect of the interaction between orography and evaporation from the sea on the precipitation field (Figure 5.14a) is also weak. The largest positive effects in precipitation



(a) Total precipitation

(b) Surface wind field

Figure 5.12: Effect of the orography on 00 UTC 13 November for the Catalonia case: (a) on the total precipitation (contour interval is 20 mm starting at 20 mm, continuous line, and at -20 mm, dashed line); (b) on the surface wind field.



(a) Total precipitation

(b) Surface wind field

Figure 5.13: Effect of the evaporation on 00 UTC 13 November for the Catalonia case: (a) on the total precipitation (contour interval is 20 mm starting at 20 mm, continuous line, and at -20 mm, dashed line); (b) on the surface wind field.

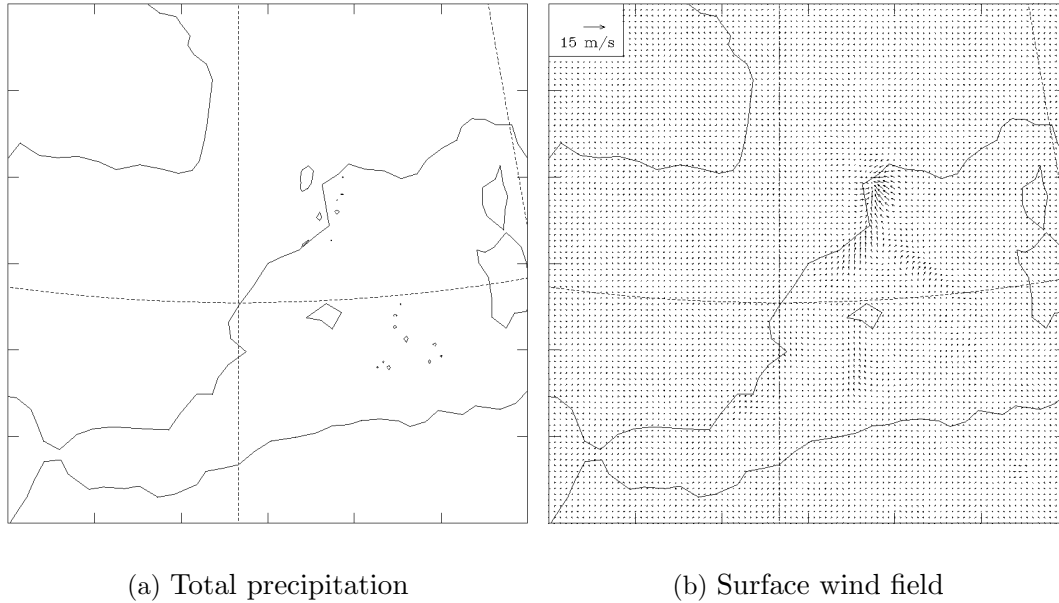


Figure 5.14: Effect of the interaction orography-evaporation on 00 UTC 13 November for the Catalonia case: (a) on the total precipitation (contour interval is 20 mm starting at 20 mm, continuous line, and at -20 mm, dashed line); (b) on the surface wind field.

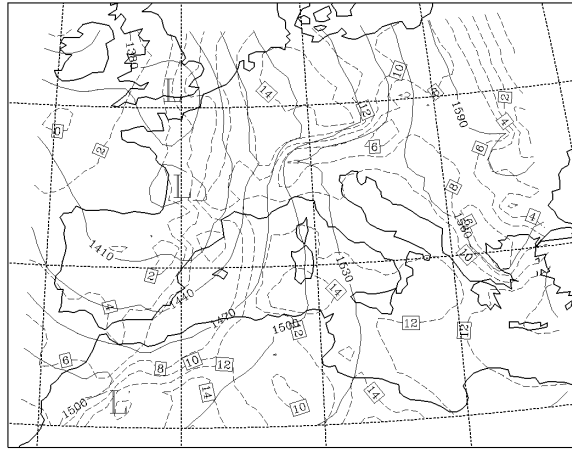
appear over the Catalan coast. They reveal some spatial redistribution, but they are not very significant. The effect on the wind field is also very weak, except over the sea close to the Catalan coast (Figure 5.14b). This effect seems to act in the opposite sense to the orographic effect, and the major outcome is a small cyclonic circulation that appears on the western side of the Gulf of Lyons.

5.3 Piedmont event

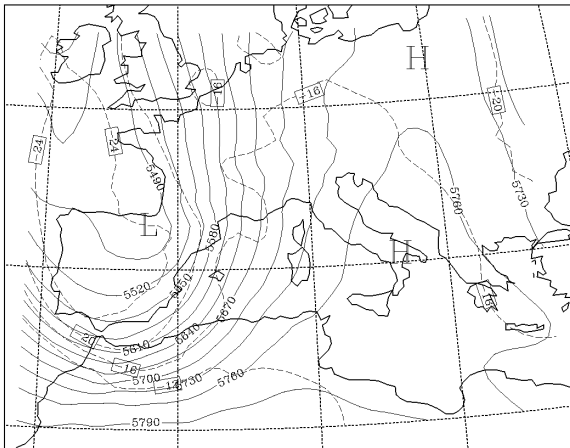
5.3.1 Synoptic overview

This event is quite interesting, because an important part of the rainfall over the Piedmont area (Figure 1.11) appears to be predominantly non-convective. However, convection affected the coastal area and dominated over wide areas of the western Mediterranean sea, and in Corsica and Sardinia.

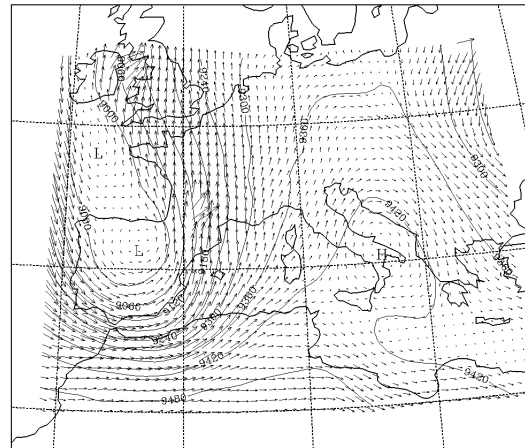
A mid-tropospheric, synoptic-scale trough is present upstream from the precipitation area (Figure 5.15). A cold front can be seen clearly at 850 hPa just to the east of the Balearic Islands at 00 UTC on 5 November (Figure 5.15a). The evolution of the synoptic situation is illustrated by the changes over 24 h from 00 UTC on 5 November to 00 UTC on 6 November (Figure 5.16). Frontal movement is relatively slow, such that by 00 UTC 6 November, the front is just east of the islands of Sardinia and Corsica (Figure 5.16a). During this period, a strong jet streak moves through the base of the trough and the trough overall is lifting out to the east-northeast (Figure 5.16c).



(a) 850 hPa

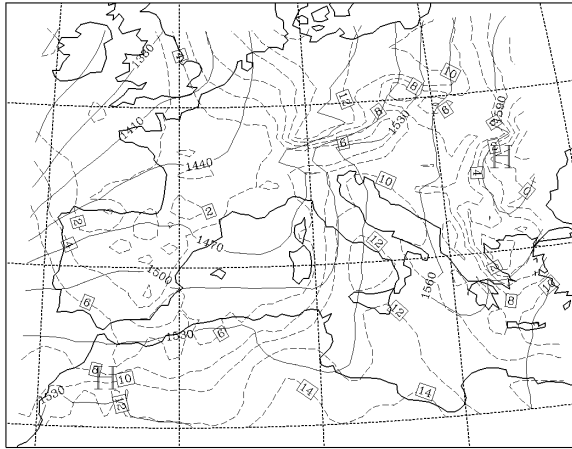


(b) 500 hPa

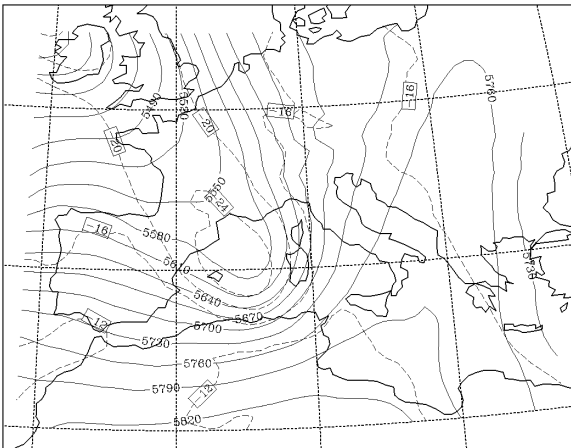


(c) 300 hPa

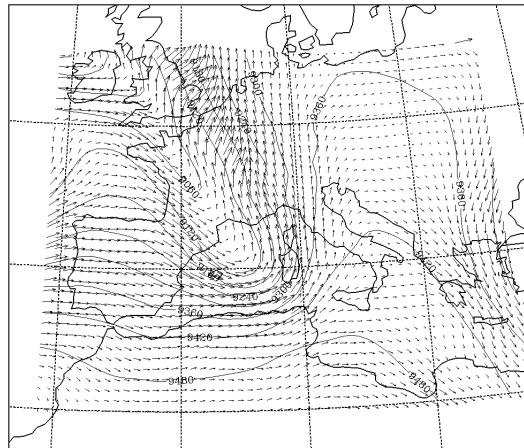
Figure 5.15: Synoptic situation on 00 UTC 5 November 1994 from ECMWF data: (a) 850 hPa, (b) 500 hPa, (c) 300 hPa. Height (gpm, continuous line) and temperature (⁰C, dashed line) for (a) and (b); height and wind vectors for (c). Arrow in the upper-right corner of (c) represents 50 m s⁻¹.



(a) 850 hPa



(b) 500 hPa



(c) 300 hPa

Figure 5.16: Synoptic situation on 00 UTC 6 November 1994 from ECMWF data: (a) 850 hPa, (b) 500 hPa, (c) 300 hPa. Height (gpm, continuous line) and temperature (⁰C, dashed line) for (a) and (b); height and wind vectors for (c). Arrow in the upper-right corner of (c) represents 50 m s⁻¹.

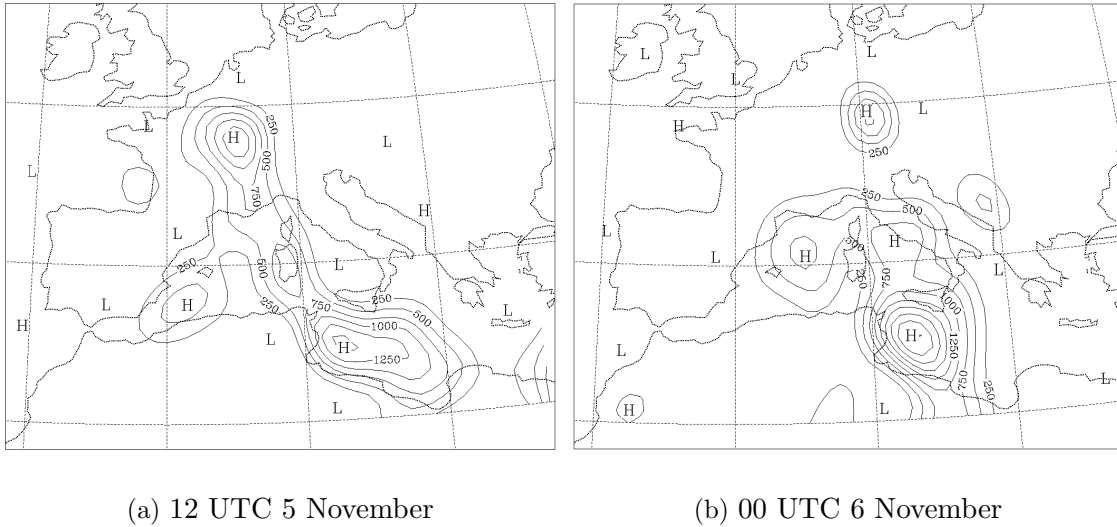


Figure 5.17: Spatial distribution of CAPE, calculated using ECMWF data: (a) on 12 UTC 5 November 1994; (b) on 00 UTC 6 November 1994. Isopleth interval is 250 J kg^{-1} , starting at 250 J kg^{-1} .

The cold front is the western boundary of a region of moderate CAPE (Figure 5.17), but the region of instability is primarily over the Mediterranean Sea and France. The zone of synoptic scale forcing in the middle and upper troposphere (see Figure 5.18 for 500 hPa) is well upstream of the Piedmont region during the day of 5 November, still only approaching the coastline by 00 UTC on 6 November, at which time the heavy rainfalls are essentially over.

Rather than explosive convective developments over the Piedmont region, the satellite images (Figure 5.19) indicate a large, indistinct cloud mass moving over northwestern Italy, connected to what are more obviously convective storms over the Italian coastline and extending over Corsica and Sardinia. There is a secondary convective band to the east the Balearic Islands. The low-level flow to the east of the boundary over Corsica and Sardinia is essentially southerly (Figures 5.15a and 5.16a), providing a substantial upslope component over the foothills of the Alps in the Piedmont area. Thus, it appears that much of the rainfall is associated with upslope flow of weakly stable, moist air. The characteristic Froude number in the Piedmont area is 0.90, suggesting there might be some tendency for the upslope flow to be blocked by the terrain rather than going over it (Smith 1989). However, for a saturated layer, the effective stability may be somewhat less than for unsaturated conditions; the satellite imagery showing considerable cloudiness (Figure 5.19) suggest a nearly saturated environment. The low-level moisture values in the moist air impinging on the Alps are significant, even if the CAPE is modest (recall Figure 5.17). Hence, the vertical motion associated with upslope flow appears to have been sufficient to produce significant rainfall in spite of the relative stability of the moist air. The quasi-geostrophic forcing fields derived from the synoptic charts (Figure 5.18) apparently are associated with the convective bands, rather than with the heavy rainfall inland. Heavy precipitation did not fall within a time span of a few hours, as is typical

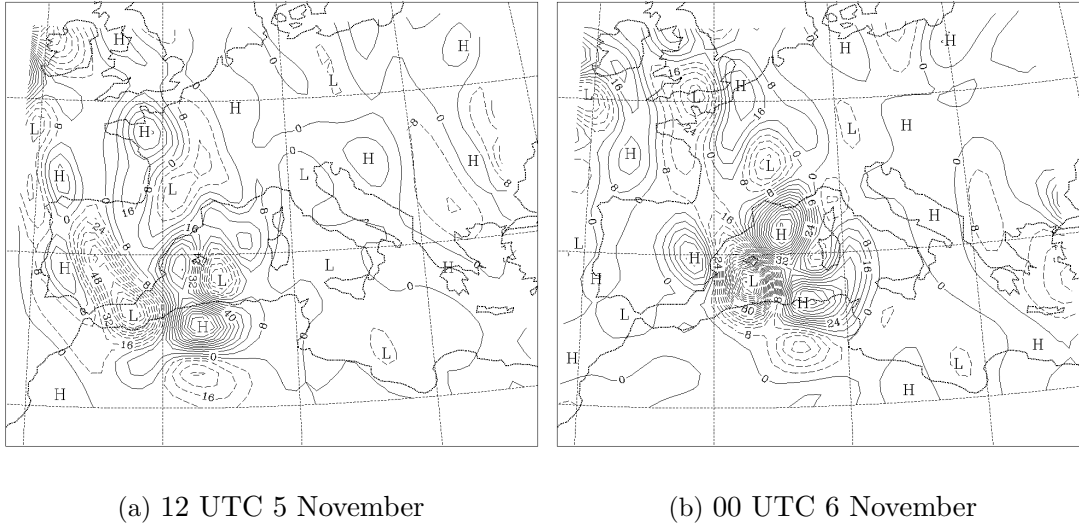


Figure 5.18: Quasigeostrophic vertical forcing (continuous lines upward, dashed lines downward), calculated using ECMWF data: (a) on 12 UTC 5 November 1994; (b) on 00 UTC 6 November 1994. Isoleth interval is $8 \cdot 10^{-8} \text{ m kg}^{-1} \text{ s}^{-1}$.

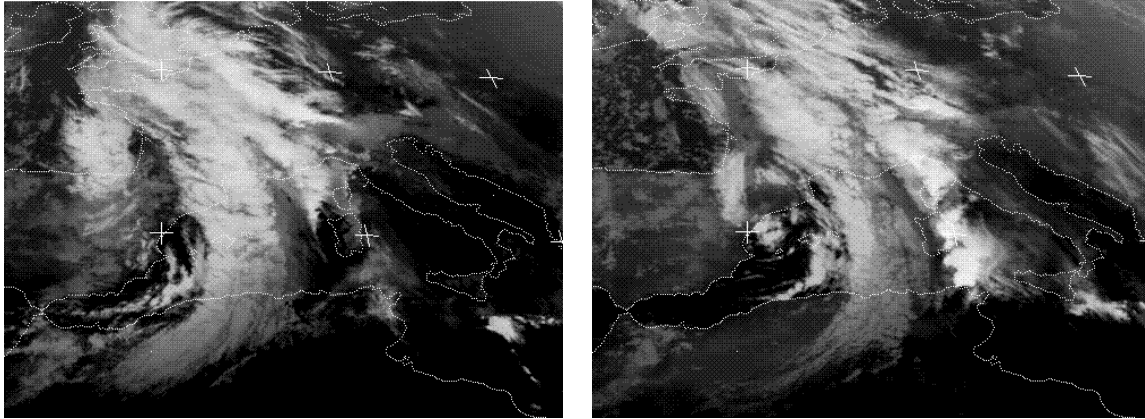
with a convective event. Rather, the rainfall persisted much of the day on 5 November, with average rates of perhaps $10\text{-}20 \text{ mm h}^{-1}$ (Lionetti 1996), also indicating the likelihood of a predominantly non-convective nature for this event.

5.3.2 Description of the experiments

The Italian and French rainfall data used to assess the model results (Figure 1.11), correspond to the 24-hour period of 5 November. Accordingly, in this case the simulations extend between 18 UTC 4 November and 00 UTC 6 November (30 hours). Starting the simulations 6 hours in advance gives the model considerable “spin-up” time before we evaluate the forecast precipitation.

For this case we used ECMWF analyses. Mesoscale grid dimensions and resolutions are identical to those used for the Catalonia case, but the model domain was centred at position 8°E , 43°N (Figure 5.20) to minimize the effect of lateral boundaries in the area of greatest interest. Another exception is that SST was initialized using the ECMWF surface data.

Using the EM convective scheme, the same experiments of Table 5.2 were performed to study the effects of orography and evaporation from the sea on this event. Results of the full experiment f_{12} are discussed in section 5.3.3, and the effects are presented in section 5.3.4. For the purpose of evaluating the possible improvements on the forecasts derived from the use of the convective schemes, additional simulations were performed: we repeated experiment f_{12} (referred to as f_{12}/EM), but using the KF convective scheme (f_{12}/KF), and without inclusion in the model of parameterized convection (f_{12}/NC). These three experiments are compared in section 5.3.5.



(a) 10 UTC

(b) 18 UTC

Figure 5.19: Infrared Meteosat image for (a) 10 UTC 5 November 1994, (b) 18 UTC 5 November 1994.

5.3.3 Results of the full experiment

The observed precipitation (Figure 1.11) has a tongue of significant rainfall (up to 250 mm in 24 h) extending from the Mediterranean Sea coast roughly toward the north in the Piedmont region of northwestern Italy. As Figure 5.20a shows, the model has simulated both the pattern and the amounts quite well, although the model has overpredicted the rainfall in southern France. Topography seems to be playing a dominant role. The pattern over land corresponds to the orography of the region (recall Figure 1.5). The heaviest rainfall is simulated along the important barrier of the Alps, and the sharp topographic gradient of the topography of the eastern slopes toward the Po Valley is associated with a comparable gradient in the precipitation, both observed (Figure 1.11) and simulated (Figure 5.20a). The model forecast surface flow (Figure 5.21), rich in moisture due to a long fetch over the Mediterranean Sea (Figure 5.22), is being forced over the terrain by the synoptic-scale processes.

Over the sea, the two bands of precipitation in Figure 5.20a are associated with the front as it passes over the western Mediterranean from west to east. Although we have no data to validate the precipitation predicted by the model over the sea, Figure 5.19 seems to confirm the timing (Figures 5.20a, b) and the shape of the precipitation bands (broad east of the Balearic Islands and narrow over Corsica and Sardinia). At 1000 UTC, a single broad cloud band with a north-south orientation and some convection can be seen just east of the Balearics (Figure 5.19a); at 1800 UTC, this band is weakening as another, narrow band with clear evidence of deep convection is present over Corsica and Sardinia (Figure 5.19b).

Of some significance in this case is that the model simulation (Figure 5.23) and the actual observations indicate that most of the rainfall associated with this system over land fell as non-convective precipitation. Deep convection did develop but apparently stayed mostly over the sea or very near the coast. The non-convective nature of the precipitation is perhaps one explanation for the excellent simulation in this case. The numerical model

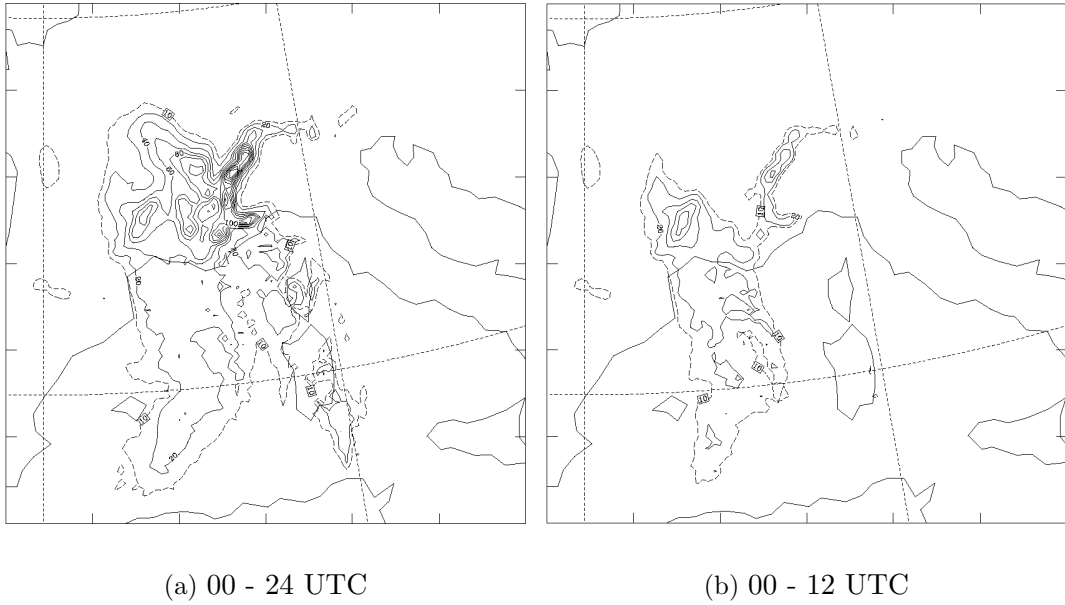


Figure 5.20: (a) Forecast total precipitation from 00 UTC 5 November to 00 UTC 6 November, for experiment f_{12} of the Piedmont case. (b) As for 5.20a, but from 00 UTC 5 November to 12 UTC 5 November. Contour interval is 20 mm starting at 20 mm (continuous line). Dashed contour represents 10 mm.

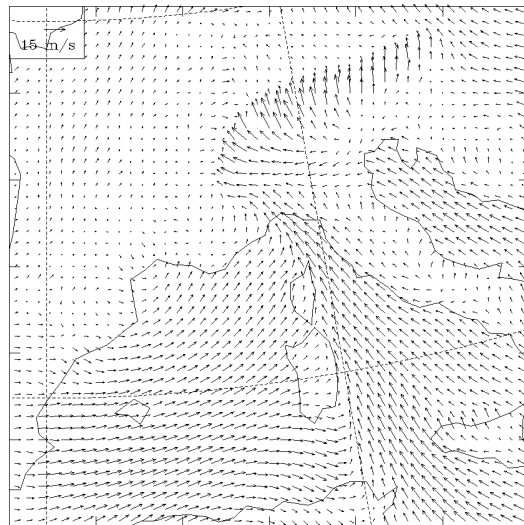


Figure 5.21: Forecast surface wind field on 00 UTC 6 November for experiment f_{12} of the Piedmont case. The arrow on the upper left-hand corner represents 15 m s^{-1} .

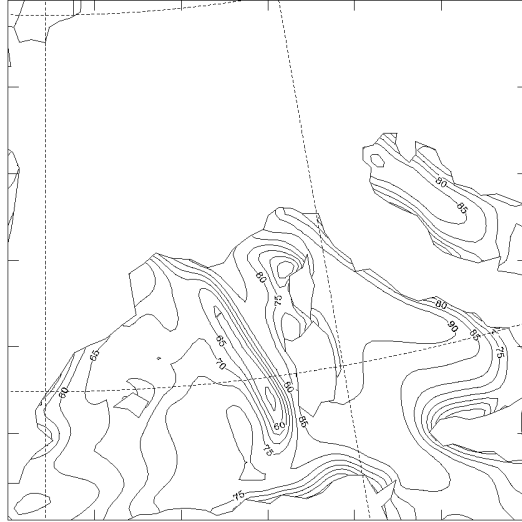


Figure 5.22: Forecast 1000-hPa relative humidity on 12 UTC 5 November, for experiment f_{12} of the Piedmont case. Contour interval is 5 %.

has a good chance of getting many of the quantitative details forecast correctly. What is needed is a reasonably accurate forecast of the low-level flow relative to the orography. This is what the model, in fact, managed to provide (see Figure 5.24; and observe its good correspondence with Figure 5.20).

5.3.4 Effects of the orography and evaporation from the sea

The observed precipitation and the mesoscale model's forecast of precipitation certainly suggest an important role for orography in this event. As for the Catalonia event, it is possible to argue that evaporation from the Mediterranean was not important in this case. The moisture content of the air flowing northward toward the Alps, between the Italian peninsula and the islands of Corsica and Sardinia, is very high (see Figure 5.22), while the evaporation in the same area is modest (Figure 5.25). Thus, the atmosphere apparently already contains considerable moisture at low levels and any additional contribution from sea surfaces fluxes is not likely to be important in this case.

Orographic effects on the low-level wind at the end of the simulation (Figure 5.26) shows two different aspects. First, the blocking action of the Alps on the windward side, stronger in the central part of the Alps than elsewhere, increases the wind along the Po valley toward the Piedmont region. Further, there are strong downslope winds in the lee of the Alps. Second, the orographic influence on the front in the Mediterranean appears to be significant; in the f_0 experiment, the front is farther east than when orography is included, indicating that Corsica and Sardinia are acting to delay the passage of the front.

Figure 5.27 shows the total precipitation forecast by experiment f_0 . As expected, the orographic influence on the precipitation field is decisive. It is evident that regardless of the synoptic and front scale dynamical forcing, an excellent forecast (Figure 5.20a) can become a worthless one (Figure 5.27) by solely eliminating the orographic forcing. The orographic influence on precipitation during the first half of the simulation (Figure 5.28a)

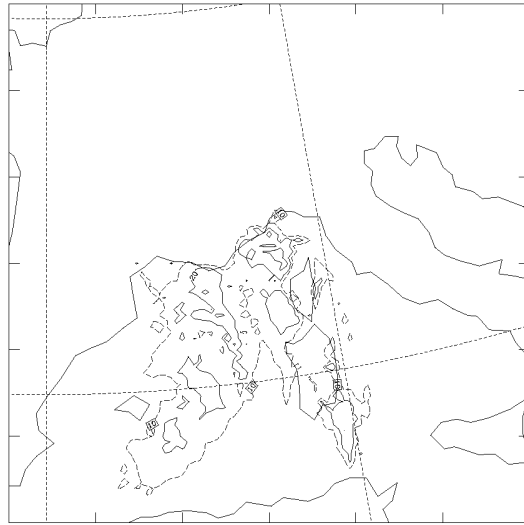


Figure 5.23: Forecast convective precipitation from 00 UTC 5 November to 00 UTC 6 November, for experiment f_{12} of the Piedmont case. Contour interval is 20 mm starting at 20 mm (continuous line). Dashed contour represents 10 mm.

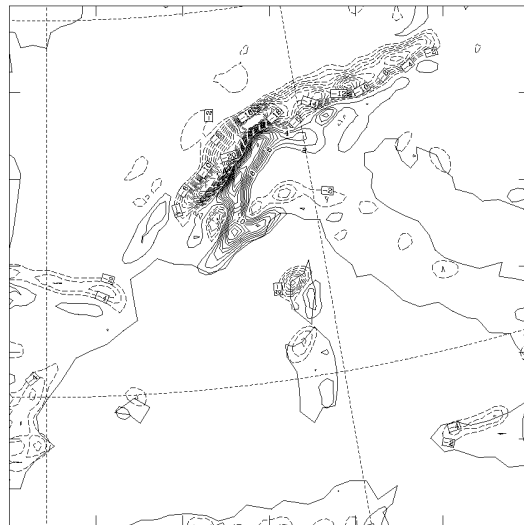


Figure 5.24: Forecast upslope flow ($= \vec{V}_s \cdot \vec{\nabla} h$, \vec{V}_s surface wind, h orography) on 12 UTC 5 November, for experiment f_{12} of the Piedmont case. Solid and dashed lines indicate upward and downward motion respectively. Contour interval is 2 cm s^{-1} starting at 2 and -2 cm s^{-1} .

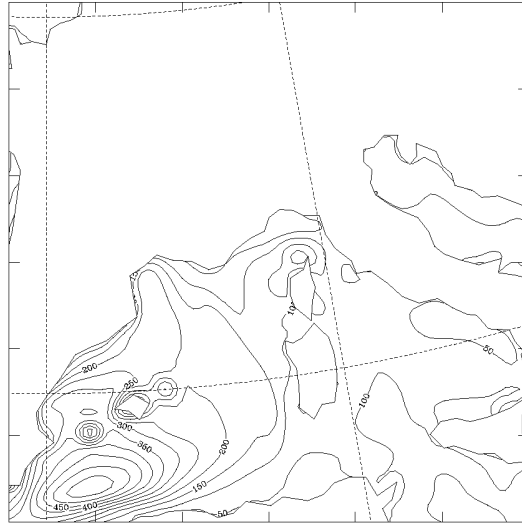


Figure 5.25: Latent heat flux from the sea on 12 UTC 5 November for experiment f_{12} of the Piedmont case. Contour interval is 50 W m^{-2} starting at 50 W m^{-2} .

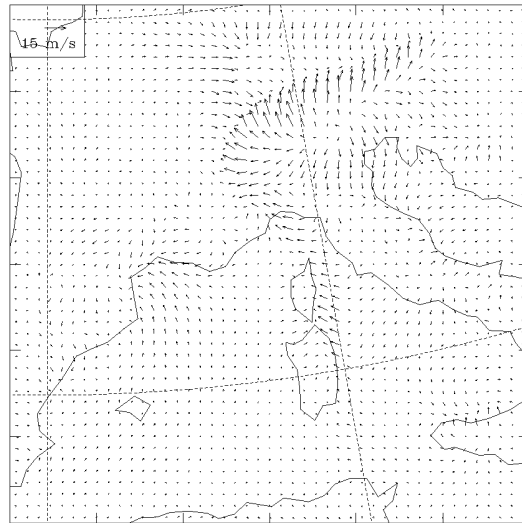


Figure 5.26: Effect of the orography on the surface wind field on 00 UTC 6 November for the Piedmont case. The arrow on the upper left-hand corner represents 15 m s^{-1} .

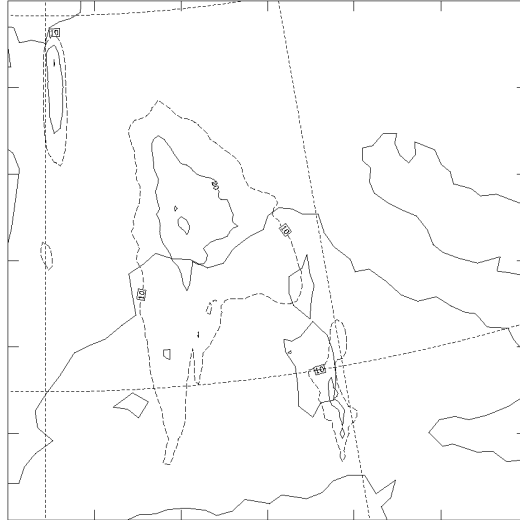


Figure 5.27: Forecast total precipitation from 00 UTC 5 November to 00 UTC 6 November, for experiment f_0 of the Piedmont case. Contour interval is 20 mm starting at 20 mm (continuous line). Dashed contour represents 10 mm.

is most apparent over the Central Massif (recall Figure 1.5) in France, and over the Alps by the end of the simulation (Figure 5.28b). The latter closely matches the precipitation pattern for the Piedmont event (compare with Figure 1.11).

As anticipated, the impact of evaporation from the sea on the precipitation is small through the end of the simulation in the Piedmont area (Figure 5.29); the effect is positive but is mostly restricted to the Central Massif in France and the open sea between Corsica and Sardinia and the Balearic Islands. The interaction's importance is also positive and substantial over the Central Massif (5.30). There are both positive and negative contributions to precipitation from the interaction over the western slopes of the Alps, albeit somewhat smaller than to the west (over the Central Massif), implying a complex redistribution of rainfall. Unlike other events, where the interaction is critical (e.g. next chapter; Romero et al. 1998a), the Piedmont case shows the interaction to be relevant primarily over France's Central Massif, not in the region where the event was most intense.

5.3.5 Effects of cumulus convection parameterization

From the previous results, it seems that the use of some type of convective parameterization has a secondary importance for the forecast in the Piedmont region, because the precipitation over that area (especially inland) is essentially stratiform. Forecast total precipitation by experiments f_{12}/EM , f_{12}/KF and f_{12}/NC is shown in figures 5.20a, 5.31a and 5.32 respectively. The observed rainfall pattern in the Piedmont area (Figure 1.11) is very well predicted in all experiments, both spatially and quantitatively. Figures 5.23 and 5.31b display the secondary role played by the convective contribution over that area, although the KF scheme contributes much more than the EM scheme (notably in the coastal zone). That convective activity, focused in the coastal zone, is in agreement with satellite information and previous studies (Buzzi and Tartaglione 1996). The same ten-



(a) 00 - 12 UTC

(b) 00 - 24 UTC

Figure 5.28: Effect of the orography on the total precipitation for the Piedmont case: (a) from 00 UTC 5 November to 12 UTC 5 November; (b) from 00 UTC 5 November to 00 UTC 6 November. Contour interval is 20 mm starting at 20 mm, continuous line, and at -20 mm, dashed line.

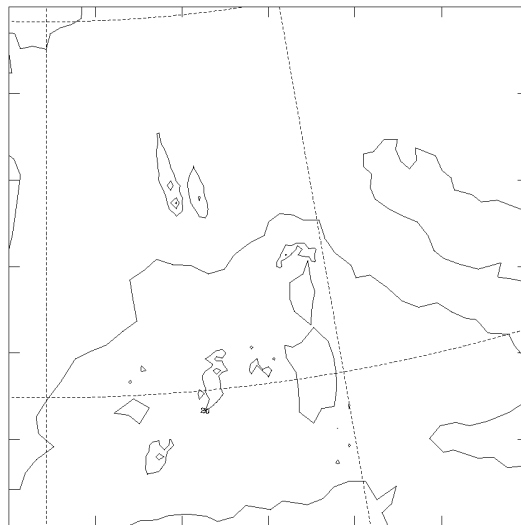


Figure 5.29: Effect of the evaporation on the total precipitation from 00 UTC 5 November to 00 UTC 6 November for the Piedmont case. Contour interval is 20 mm starting at 20 mm, continuous line, and at -20 mm, dashed line.

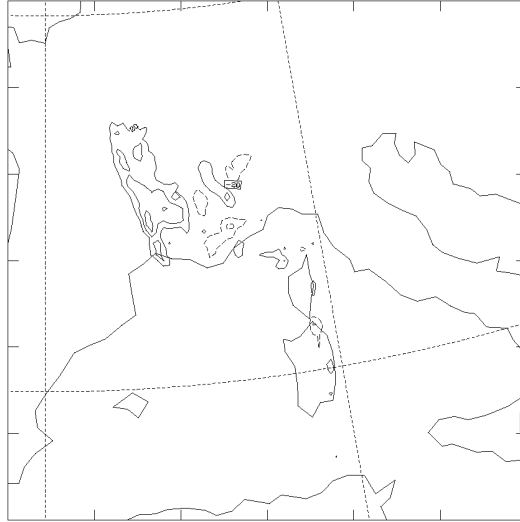
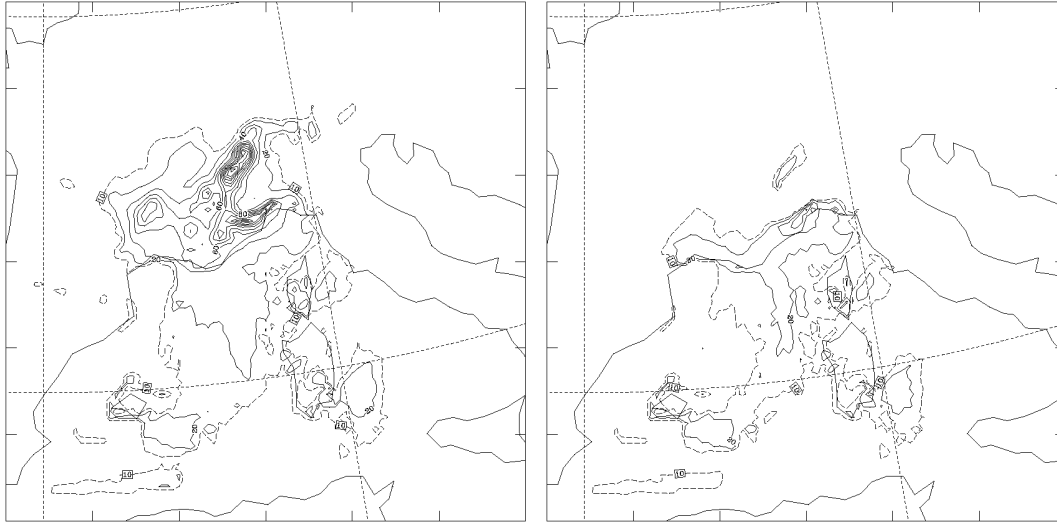


Figure 5.30: Effect of the interaction orography-evaporation on the total precipitation from 00 UTC 5 November to 00 UTC 6 November for the Piedmont case. Contour interval is 20 mm starting at 20 mm, continuous line, and at -20 mm, dashed line.

endency of the KF scheme to develop convection in coastal areas was obtained for another ANOMALIA case (Romero et al. 1998a). These results show that ascending motion associated with coastal upslope flow and with low level convergence in the sea-land transition are important mechanisms to initiate the convection in the KF scheme.

The major differences among the three experiments are related with the two precipitation bands over the western Mediterranean sea. In the case of the f_{12}/EM and f_{12}/KF simulations, these bands (essentially convective) take a spread shape, whereas for the f_{12}/NC simulation they are very intense and definite. The former structure seems more reasonable in basis of what satellite images show (Figure 5.19), and agrees with observed precipitation over Corsica and Sardinia (Figure 1.11). The compact bands given by f_{12}/NC (Figure 5.32) seem to be the result of explicit convection: in the absence of parameterized convection that could act stabilizing and drying the atmosphere over wide areas, the high water vapour content condenses vigorously in localized frontal zones. In such zones, the low-level convergence can force appreciable upward velocity due to the low static stability of the air. Some soundings analysed at the end of this section support this scenario.

Figure 5.33, that corresponds to 00 UTC 6 November, shows one of these convergence lines along Corsica and Sardinia. It is responsible, probably supported by the prominent topography of the islands, for the narrow band of heavy precipitation given by experiment f_{12}/NC over that area (Figure 5.32). Experiments f_{12}/EM and f_{12}/KF also give that convergence line (Figures 5.21 and 5.34), but it is appreciably smoother than in Figure 5.33 and it is displaced farther eastward, especially for f_{12}/KF (about 150 km). Such more advanced position is responsible for the convective rainfall present eastward of Sardinia and Corsica in Figures 5.20a and 5.31a (especially in the latter), and it is coherent with the satellite picture at 18 UTC (5.19b), which shows how convection is already occurring between the islands axis and the Italian peninsula, and southeast of Sardinia. It seems,



(a) Total precipitation

(b) Convective precipitation

Figure 5.31: (a) Forecast total precipitation from 00 UTC 5 November to 00 UTC 6 November, for experiment f_{12}/KF of the Piedmont case. (b) As for 5.30a, but for the convective contribution. Contour interval is 20 mm starting at 20 mm (continuous line). Dashed contour represents 10 mm.

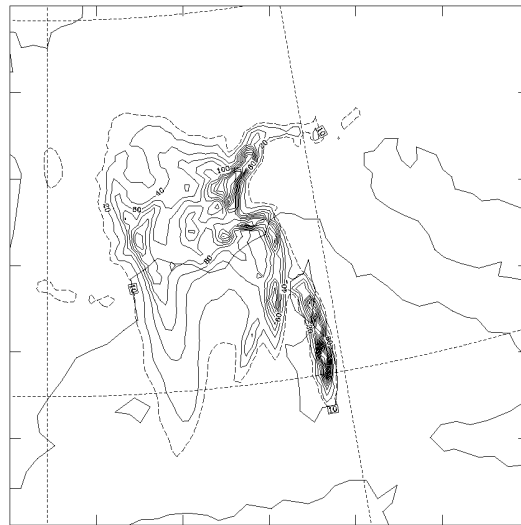


Figure 5.32: Forecast total precipitation from 00 UTC 5 November to 00 UTC 6 November, for experiment f_{12}/NC of the Piedmont case. Contour interval is 20 mm starting at 20 mm (continuous line). Dashed contour represents 10 mm.

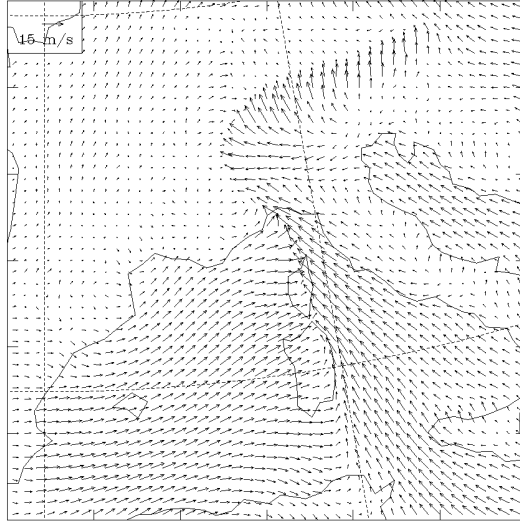


Figure 5.33: Forecast surface wind field on 00 UTC 6 November for experiment f_{12}/NC of the Piedmont case. The arrow on the upper left-hand corner represents 15 m s^{-1} .

therefore, that the inclusion of convective parameterizations has also important consequences on the forecast wind patterns, avoiding exaggerated developments of convergence lines as that shown in Figure 5.33.

The ability of each experiment to forecast the convectively transformed air masses was quantified by comparing the observed temperature and humidity profiles with the simulated ones. We have selected some points directly affected by convection or being downstream of regions where convection occurred: PAL, NIM, GEN, MIL, AJA and CAG (see Figure 1.5 for locations). As observations, we take the same ECMWF analyses used to nest the model (in Doswell et al. 1998, these fields were compared satisfactorily against real soundings). Note that the selected points are far enough from the lateral boundaries, so that the simulated structures are basically produced by the physics of the inner domain and little affected by the relaxation process toward the boundary “exact” fields.

Comparison of forecast heating and drying profiles with observed values involves considerable uncertainty because the time and space scales of the physical processes responsible are often highly disparate (recall, for instance, the “random” nature of convection). In addition, owing to their coarser resolution, ECMWF analysis can not resolve small mesoscale structures that are possible in the mesoscale simulations. To reduce these problems, although the comparison is done at fixed times, the soundings to be compared (both simulated and “analyzed”) are calculated as spatial averages on a $200 \times 200 \text{ km}^2$ square (11 x 11 grid points), for each standard pressure level between 300 and 1000 hPa. The comparisons are done after 6, 18, and 30 hours of simulation time. At each time and location, we have quantified the degree of correspondence by computing the root mean square (rms) of the temperature and specific humidity errors throughout the atmospheric column.

A global measure of the performance of each experiment can be obtained by comparing the number of times it performs the best (minimum rms) against the number of times it performs the worst (maximum rms). Tables 5.3 and 5.4 show the results of this test

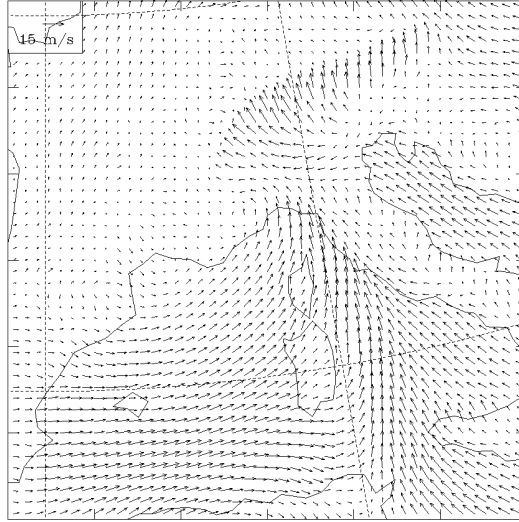


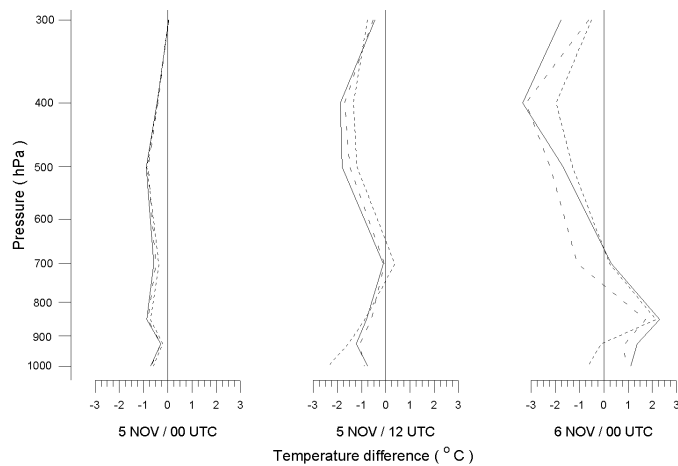
Figure 5.34: Forecast surface wind field on 00 UTC 6 November for experiment f_{12}/KF of the Piedmont case. The arrow on the upper left-hand corner represents 15 m s^{-1} .

for each considered location. Globally, f_{12}/EM and f_{12}/KF , with scores 5/2 and 11/6 respectively, perform appreciably better than f_{12}/NC for temperature (Table 5.3). For humidity (Table 5.4), f_{12}/KF is clearly superior, whereas f_{12}/EM and f_{12}/NC offer similar results (6/8 and 3/5 respectively). A similar test for another convective event (Romero et al. 1998a) revealed also the major performance of the KF scheme.

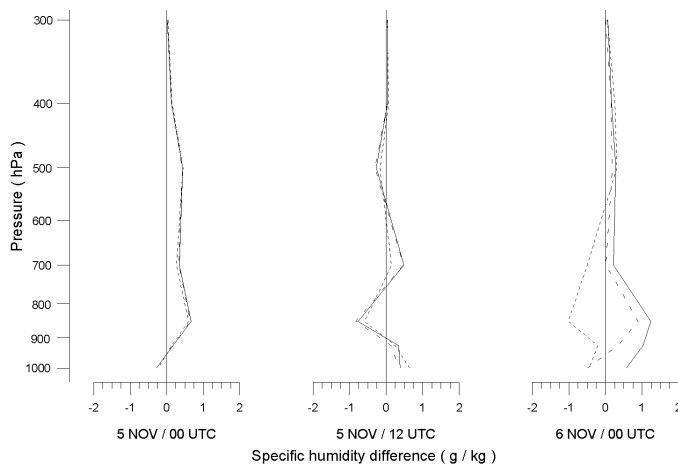
A general behaviour found in the selected soundings, are drier atmospheres at low levels and stabler lapse rates when a deep convection scheme has been included. This behaviour is more pronounced for f_{12}/KF than for f_{12}/EM . Figures 5.35 and 5.36 show the profiles at AJA and CAG respectively. These locations are in Corsica and Sardinia (Figure 1.5), and their atmospheric structures are especially sensitive because significant convection associated with the eastward-moving cold front occurs over the western Mediterranean. In both places, and particularly at 00 UTC on 6 November, the simulated atmosphere by f_{12}/KF and f_{12}/EM is colder at low levels and warmer at upper levels than for f_{12}/NC experiment (Figures 5.35a and 5.36a). Nevertheless, the observed lapse rates are still smaller. The atmosphere is also drier for the experiments including implicit convection (Figures 5.35b and 5.36b), even exceeding the observed values at some layers.

5.4 Conclusions

The results obtained show that mesoscale models, with appropriate parametrizations for convection, can be used successfully to study and forecast the heavy rainfalls of the western Mediterranean area. The SALSA model gave results that approximated very well the observed spatial distribution of precipitation over land. However, the forecast of amount of precipitation for the Catalonia event was not so good because the model underestimated the rainfall. In contrast, the quantitative forecast in the Piedmont region was excellent due to the dominant contribution of the large-scale precipitation in that

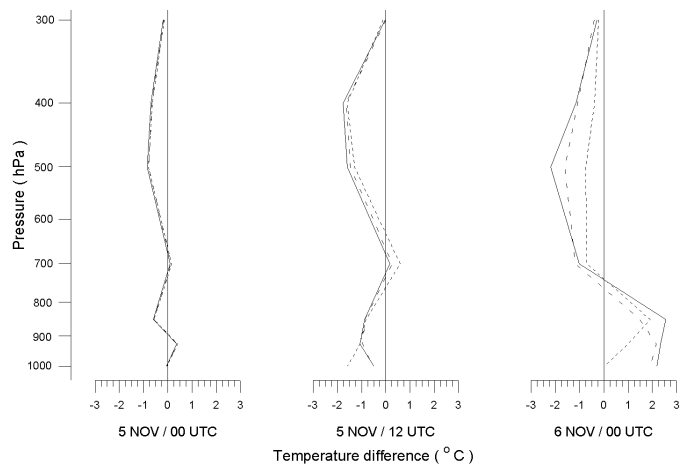


(a) Temperature

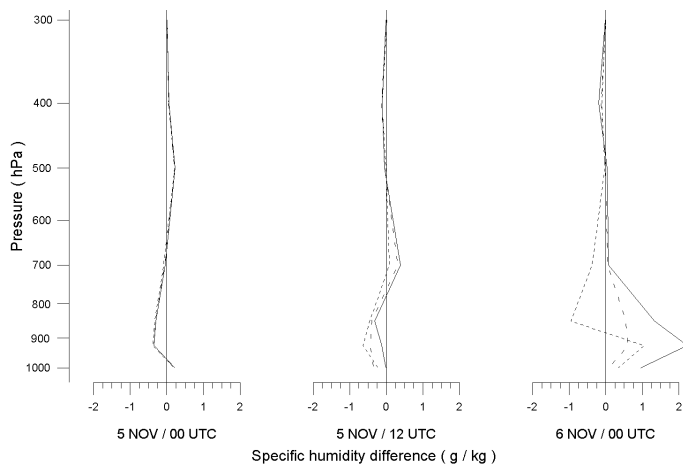


(b) Specific humidity

Figure 5.35: Difference profiles (forecast minus observed) at AJA (see Figure 1.5), for experiments f_{12}/NC (continuous line), f_{12}/EM (long dashed), and f_{12}/KF (short dashed): (a) Temperature, (b) Specific humidity.



(a) Temperature



(b) Specific humidity

Figure 5.36: Difference profiles (forecast minus observed) at CAG (see Figure 1.5), for experiments f_{12}/NC (continuous line), f_{12}/EM (long dashed), and f_{12}/KF (short dashed): (a) Temperature, (b) Specific humidity.

Temperature Piedmont

	f_{12}/\mathbf{NC}	f_{12}/\mathbf{EM}	f_{12}/\mathbf{KF}
PAL	2 / 0	0 / 1	1 / 2
NIM	0 / 2	1 / 0	2 / 1
GEN	0 / 2	0 / 1	3 / 0
MIL	0 / 2	1 / 0	2 / 1
AJA	0 / 2	1 / 0	2 / 1
CAG	0 / 2	2 / 0	1 / 1
Total	2 / 10	5 / 2	11 / 6

Table 5.3: Summary of the rms test of temperature error for the Piedmont case. In the pairs nf / nl , nf indicates number of times with the first position (minimum rms), and nl number of times with the last position (maximum rms).

case.

A qualitative comparison between the model results and the wind observations showed good correlation. The simulation of the Catalonia case also displayed some of the observed mesoscale structures, such as, in particular, the Algerian low in the lee of the Atlas mountains, which help to deflect the flow at low levels towards Catalonia and so localize convection over that area.

The study of the effects of orography and evaporation from the sea showed that the effect of the former appears to be decisive in the spatial structure of precipitation over land. For the Catalonia event, the orography was responsible for localizing the precipitation within the coastal zone. For the Piedmont event, the substantial upslope component provided by the Alps and surrounding mountains was correctly forecast by the model, explaining the good precipitation forecast. The effect of the orography on the wind field at low levels is also significant. For the Catalonia case, the formation of the shallow cyclonic circulation over the sea, close to the Algerian coast, and the strong modification of the wind field close to Catalonia is due to the orography. Both these zones are connected by a convergence line which also is associated with the orography. For the Piedmont case, the most important action is associated with the Alps, which act reconducting and converging the flow in the Piedmont region.

For both case studies, the effects of the evaporation from the sea and the synergistic factor seem to be weak on both precipitation and wind fields in the regions of interest. These factors are potentially important for this kind of event, but apparently the atmosphere was charged of sufficient moisture at the beginning of the simulations. In next chapter, these factors turn to be very important for the Tarragona heavy precipitation

Specific Humidity Piedmont

	f_{12}/\mathbf{NC}	f_{12}/\mathbf{EM}	f_{12}/\mathbf{KF}
PAL	0 / 2	1 / 1	2 / 0
NIM	0 / 1	0 / 2	3 / 0
GEN	1 / 1	0 / 1	2 / 1
MIL	3 / 0	0 / 1	0 / 2
AJA	0 / 3	1 / 0	2 / 0
CAG	2 / 1	1 / 0	0 / 2
Total	6 / 8	3 / 5	9 / 5

Table 5.4: Summary of the rms test of specific humidity error for the Piedmont case. In the pairs nf / nl , nf indicates number of times with the first position (minimum rms), and nl number of times with the last position (maximum rms).

event.

We have shown, for the Piedmont case and another ANOMALIA event not included here (see Romero et al. 1998a), that the inclusion of parameterized convection has beneficial effects on the forecast fields. A simple statistics has been carried out demonstrating that more realistic temperature and humidity profiles are obtained when using a cumulus convection parameterization. This fact becomes determinant for precipitation and surface wind forecasts as a consequence of a feedback process (presumably more remarkable as the simulation extends longer). In particular, due to the stabilization and drying rates produced by convection (preferentially over oceanic areas), artificial and intense rainfall patterns are prevented downstream where the flow is forced to ascend by topography or frontal convergence lines. In principle, the Kain-Fritsch scheme performed better than the Emanuel scheme. In particular, the former seems to be more sensitive to the presence of the coastal topography, focusing convection on that area in agreement with observations. Nevertheless, extraction of general conclusions needs the simulation of more cases, and the sensitivity of each scheme to some internal adjustable parameters can not be obviated.

Chapter 6

TARRAGONA HEAVY PRECIPITATION EVENT

In this chapter¹, we study the Tarragona event (9 and 10 October 1994), presented in section 1.3. Previous to the performance of the numerical simulations, we provide a detailed diagnosis of the event in order to make the study self contained. The diagnostic study is based on the analysis of the necessary synoptic and subsynoptic ingredients for the development of the heavy rain. As in the previous chapter, we design a set of numerical simulations with the SALSA model to test the capabilities of mesoscale models to forecast this type of event. Likewise, we apply the factor separation technique of Stein and Alpert (1993) to isolate the physical actions associated with the orography and sea surface water vapor flux. In addition, the numerical simulations become fundamental to support, or to complement, important arguments extracted from the diagnostic study.

The synoptic overview of the event as well as its evolution is provided in section 6.1. Section 6.2 presents the diagnostic study. Section 6.3 describes the characteristics of the numerical experiments. Results of the simulations for 9 and 10 October 1994 are presented in sections 6.4 and 6.5, respectively. Finally, section 6.6 contains the conclusions for this event.

6.1 Synoptic overview

For shortness, we present only the meteorological situation at 12 UTC 9 October 1994 and at 06 UTC 10 October 1994. Analyses come from ECMWF. On 9 October, the synoptic pattern at low levels (Figure 6.1a) was characterised by an anticyclone located north of Italy and extending towards north Africa. A low is located to the southwest of Spain. Over the western Mediterranean the flux is from the southeast as a consequence of a trough over the Algerian coast developed as the flux overcomes the Atlas (this will be shown in section 6.4). The wind is blowing and advecting warm air towards the Valencia and Murcia coasts since the edge of a warm tongue coming from Africa is located over the

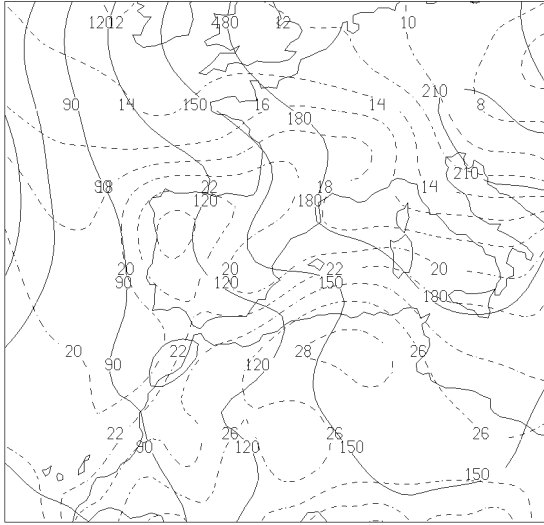
¹The content of this chapter is based on the paper: Ramis, C., R. Romero, V. Homar, S. Alonso, and M. Alarcón, 1998: Diagnosis and numerical simulation of a torrential precipitation event in Catalonia (Spain). *Meteorol. Atmos. Phys.*, (submitted).

south of the western Mediterranean. The same pattern can be identified at 850 hPa (Figure 6.1b), but an important feature is a southerly low-level jet (LLJ) that points directly towards the Valencia and Murcia regions. At middle levels, (Figure 6.1c), a trough, with a cold core, is located to the southwest of the Iberian peninsula producing south-southwest flux over the Spanish Mediterranean coast and northern Africa, in particular over the Atlas. A negatively tilted ridge is located over the western Mediterranean extending towards the British Isles. At upper levels (Figure 6.1d), the pattern is very similar to 500 hPa but there is a jet streak from the southwest over Spain. It is interesting to note that warm air is present in all the troposphere over the western Mediterranean.

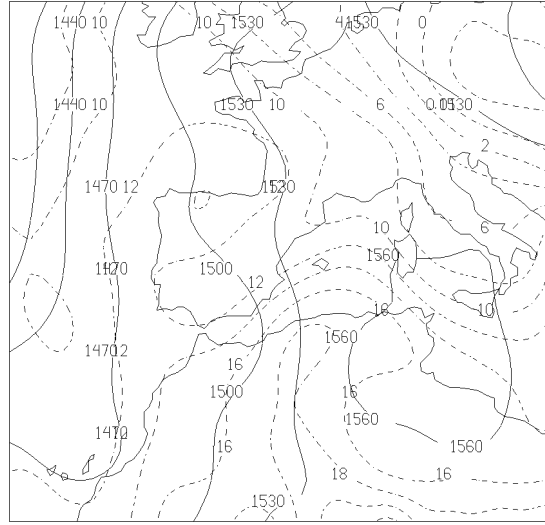
The synoptic situation evolved very slowly in the subsequent 18 hours. On 06 UTC 10 October, the low-levels charts (Figures 6.2a and b), show that the European high pressure centre has reinforced slightly but remains stationary. The flux over the western Mediterranean is still from the east-southeast, but the low-levels winds point towards the Catalonia and north Valencia regions. The LLJ at 850 hPa is also directed towards Catalonia at this time. Strong warm advection towards Catalonia can be easily identified. At middle levels (Figure 6.2c), the trough has moved towards the Mediterranean, this trough being now negatively tilted. The ridge over the western Mediterranean only experiences a small displacement towards the east from its situation 18 hours before. At upper levels (Figure 6.2d) the situation is very similar to 500 hPa and the strongest winds are over eastern Spain. At this time warm air is also identified over the western Mediterranean at all levels of the troposphere.

Meteosat image at 12 UTC 9 October (Figure 6.3a), shows a band of clouds over the eastern coast of Spain within which embedded convection can be identified over and south of the Valencia region. During the evening, convection over the Valencia region became deeper as shown by Figure 6.3b, and moved slowly towards the northeast following the coast line, reaching Catalonia during the night. Deep and stationary convection affected south Catalonia early in the morning during several hours (Figure 6.3c), and further moved northwards towards northeastern Catalonia (Figure 6.3d). As a consequence, high amounts of rainfall were registered in coastal areas of Valencia and Catalonia (Figure 1.12). Peak values of 450 mm during the whole episode occurred in the Alforja town (Tarragona province), where the convective system remained quasistationary. Observe that also in this case, it is relatively simple to include the observed rainfall patterns (Figure 1.12) within the model of typical patterns for Mediterranean Spain derived in chapter 4 (Figure 4.4). The rainfall distribution for 9 October (Figure 1.12a) resembles a T6 pattern, and the distribution for 10 October (Figure 1.12b) clearly corresponds to a T7 pattern.

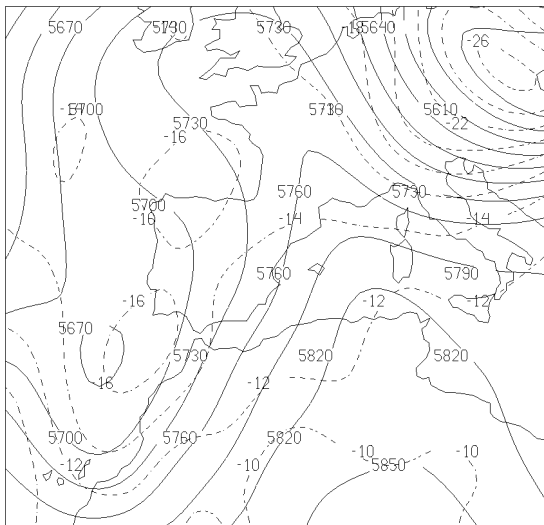
From the synoptic charts and satellite images, it can be seen that deep convection did not develop close to the trough of middle and upper levels, where vorticity advection is appreciable, but in between the trough and the ridge axes close to the ridge, where no appreciable vorticity centres can be easily identified on ECMWF charts. The clouds associated with the major trough are visible to the south of the deep convection, at the bottom portion of Figures 6.3c and d. A similar scenario was observed previously for another convective heavy rain event in Catalonia in October 1987 (Ramis et al. 1994).



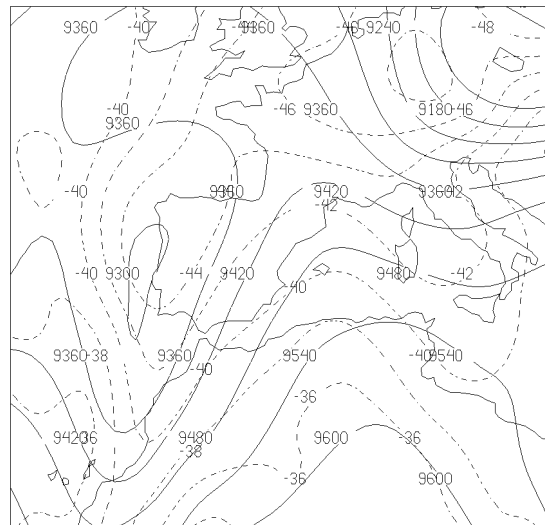
(a) 1000 hPa



(b) 850 hPa

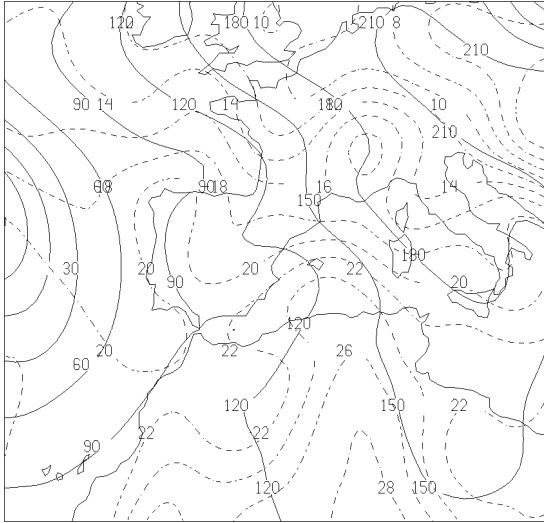


(c) 500 hPa

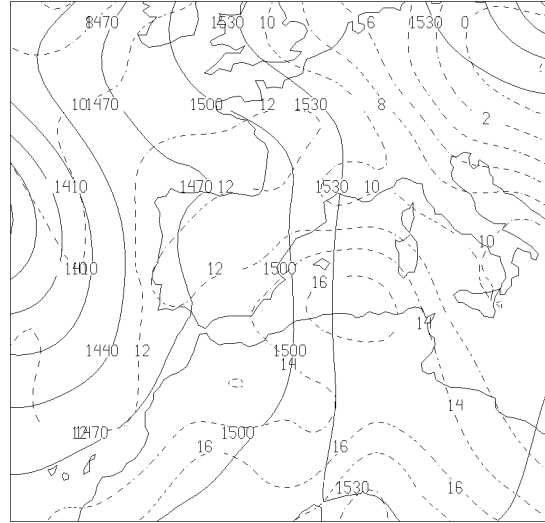


(d) 300 hPa

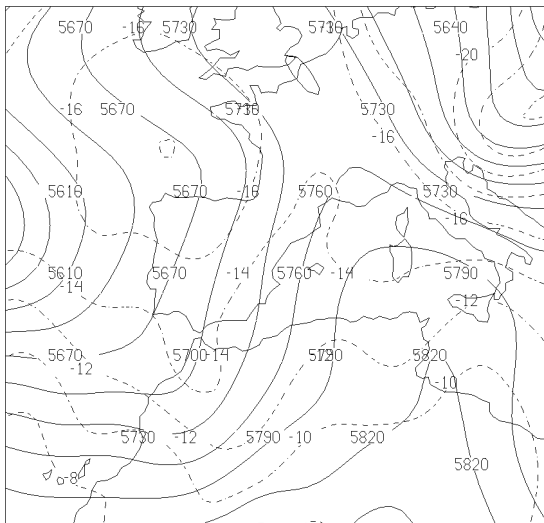
Figure 6.1: Synoptic situation at 12 UTC 9 October 1994, showing height (gpm, continuous line) and temperature ($^{\circ}$ C, dashed line). (a) 1000 hPa, (b) 850 hPa, (c) 500 hPa, (d) 300 hPa.



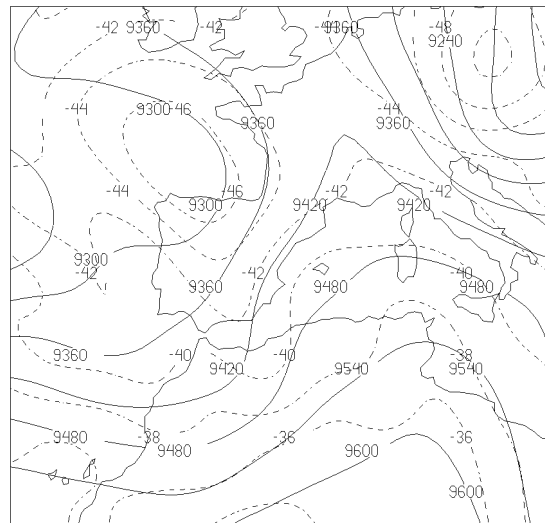
(a) 1000 hPa



(b) 850 hPa

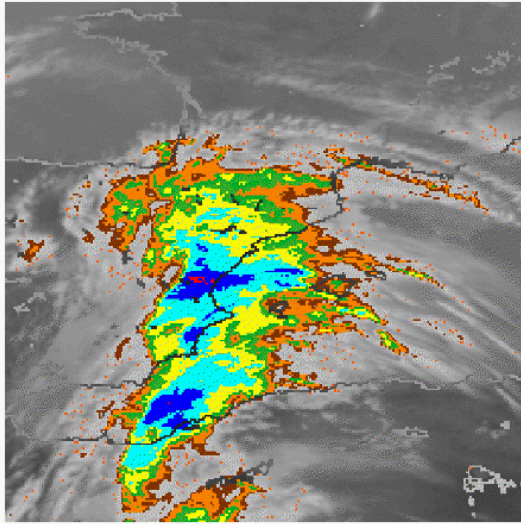


(c) 500 hPa

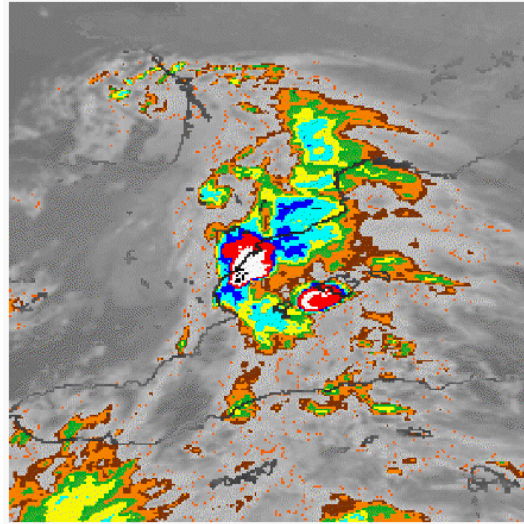


(d) 300 hPa

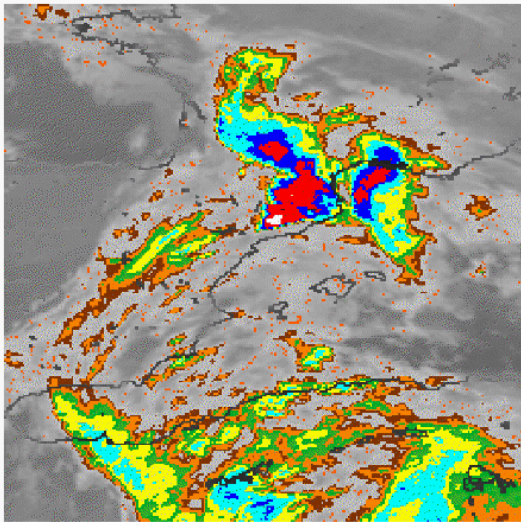
Figure 6.2: Synoptic situation at 06 UTC 10 October 1994, showing height (gpm, continuous line) and temperature ($^{\circ}$ C, dashed line). (a) 1000 hPa, (b) 850 hPa, (c) 500 hPa, (d) 300 hPa.



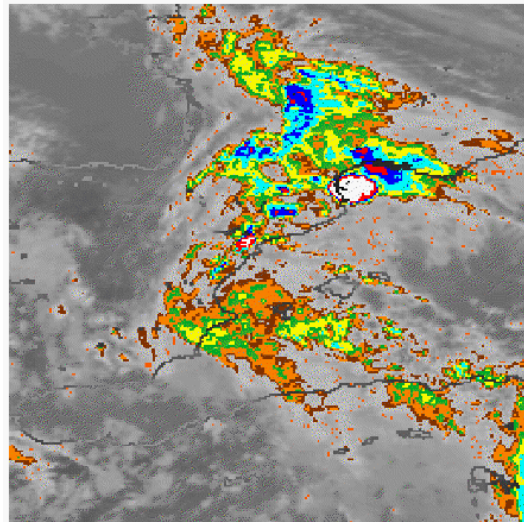
(a) 12 UTC 9 October



(b) 21 UTC 9 October



(c) 06 UTC 10 October



(d) 15 UTC 10 October

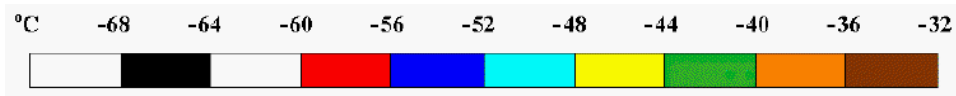


Figure 6.3: Infrared Meteosat image for (a) 12 UTC 9 October 1994, (b) 21 UTC 9 October 1994, (c) 06 UTC 10 October 1994, (d) 15 UTC 10 October 1994.

6.2 Diagnostic study

Forecasting and/or diagnosing deep convection producing heavy rain includes an evaluation of different ingredients and their possible contribution and interactions. These ingredients go from synoptic scale, which has to produce the favourable environment, to mesoscale, which provides the lifting mechanisms for low-level parcels (Doswell 1987). Although convection develops in environments with large spatial and temporal variability (Brooks et al. 1994), ingredients from synoptic scale can be evaluated from gridded numerical analysis or forecasts at that scale. Upward vertical motion, water vapour convergence at low levels, high water vapour content in a deep atmospheric column, and potential or latent instability, have been identified as favourable mechanisms (Maddox et al. 1979; Doswell 1987; McNulty 1995). Quasigeostrophic theory can be used to determine vertical motion (Holton 1993; Hoskins and Pedder 1980). Water vapour convergence can be calculated from the flux of specific humidity. Water vapour content can be represented by the precipitable water (PW). Potential instability for the low troposphere can be determined by means of the difference of equivalent potential temperature between two levels (e.g. 500 and 1000 hPa), and latent instability can be determined by means of the CAPE. A more detailed study on the vertical stability of the air masses to complement the gridded data analysis can be obtained through the analysis of radiosounding data.

The area where quasigeostrophic upward forcing, water vapour convergence between 1000 and 850 hPa, and convective instability between 1000 and 500 hPa overlap, has been found to be favourable for convective developments in the western Mediterranean (Ramis et al. 1994; Ramis et al. 1995; chapter 5).

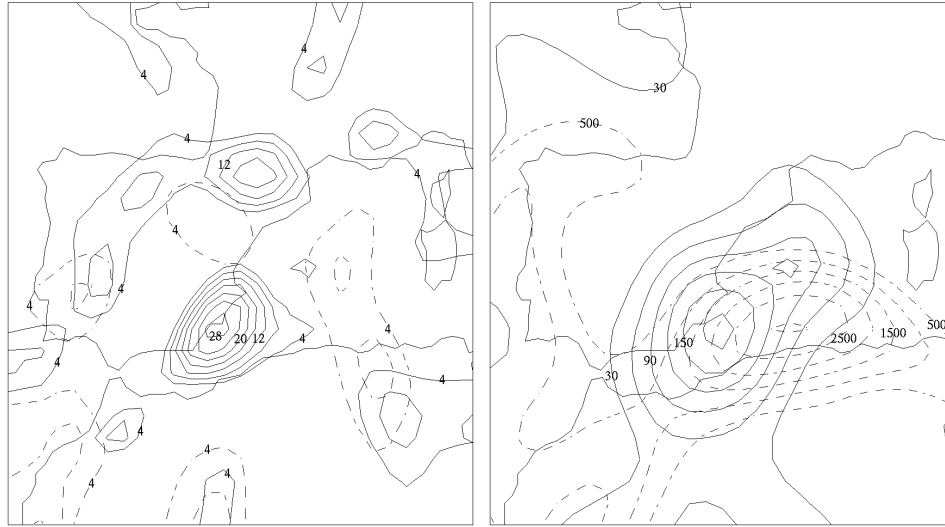
Mesoscale mechanisms are much more complex. They can go from physical effects (orographically induced convection), kinematic effects (convergence lines), mixed orographic-kinematic effects (Ramis et al. 1994), or dynamic effects [ageostrophic motion associated with short wave troughs or jet streaks at upper levels (Rockwood and Maddox 1988), interaction between two upper jet streaks (Hakim and Uccellini 1992), gravity waves (Uccellini 1975), conditional symmetric instability (Emanuel 1983) or coupling of upper and lower jet streaks (Uccellini and Johnson 1979)].

In this sense, deep convection can be considered as a typical example of interaction between scales. Large scale provides the appropriate environment, and mesoscale mechanisms determine when and where convection will develop.

6.2.1 Synoptic diagnosis

Diagnosis products have been calculated using gridded analysis from the ECMWF (0.75 degrees of latitude/longitude resolution). Large scale upward forcing for vertical motion, calculated from the divergence of the Q vector (Hoskins and Pedder 1980), is shown in Figure 6.4a for 12 UTC 9 October. At low levels, an upward maximum centre is located over southeastern Spain, and less values are found over northeastern Spain. The maximum over southeastern Spain is related to the warm advection that is identified over the synoptic charts. At medium levels, the upward forcing is weak and it is found in the areas where there is positive vorticity advection.

The location of the temperature advection in the low troposphere is represented by



(a) Upward forcing

(b) Positive helicity and CAPE

Figure 6.4: For 12 UTC 9 October 1994: (a) Upward quasigeostrophic forcing at 925 hPa (continuous line) and at 500 hPa (dashed line) (contour interval is $4 \cdot 10^{-8} \text{ m kg}^{-1} \text{ s}^{-1}$ starting at $4 \cdot 10^{-8} \text{ m kg}^{-1} \text{ s}^{-1}$); (b) Positive helicity (continuous line; contour interval is $30 \text{ m}^2 \text{ s}^{-2}$ starting at $30 \text{ m}^2 \text{ s}^{-2}$) and CAPE (dashed line; contour interval is 500 Jul kg^{-1} starting at 500 Jul kg^{-1}).

the helicity (Davies-Jones et al. 1990) between 1000 and 700 hPa (Figure 6.4b), since the helicity can be considered as a measurement of the integrated temperature advection between the considered levels (Tudurí and Ramis 1997). It can be observed that the zone with maximum values of helicity corresponds to the area with the strongest upward forcing at low levels (Figure 6.4a). Spatial distribution of CAPE (Figure 6.4b) shows that the greatest values appear over the south of the western Mediterranean, but that appreciable CAPE values occur also over Murcia and south Valencia.

Analyses of the radiosonde data at the same time from Palma, Murcia and Zaragoza (see Figure 1.5 for locations) show that ECMWF analyses give a good representation of the actual latent instability of the environment in the area of interest. In fact, over Palma (Figure 6.5a), although a LID (Farrel and Carlson 1989) structure is present, CAPE is 850 J kg^{-1} and the energy that inhibits convection is 36 J kg^{-1} . In addition, stability indices (see Tudurí and Ramis 1997 for a summary) indicate a high probability of convection, since the Lifted index (LI) is -1, the K index (KI) 31, and the Total Total's index (TT) 48. The humidity is very high in all the troposphere leading to a PW of 40 mm. Winds are from the east at low levels, veering to the southwest at 700 hPa (helicity is $83 \text{ m}^2 \text{ s}^{-2}$), but no evidence of LLJ exists at that time. The launched balloon over Murcia only attained 700 hPa and then very few information can be obtained. However the available data show strong southerly winds in the layer 800-700 hPa, suggesting the existence of a LLJ. The wind also veers from the east to the south indicating the presence of warm advection. Over Zaragoza (Figure 6.5b), the atmosphere is quite stable as a consequence of a strong inversion close to the ground. Stability indices do not exhibit high probability

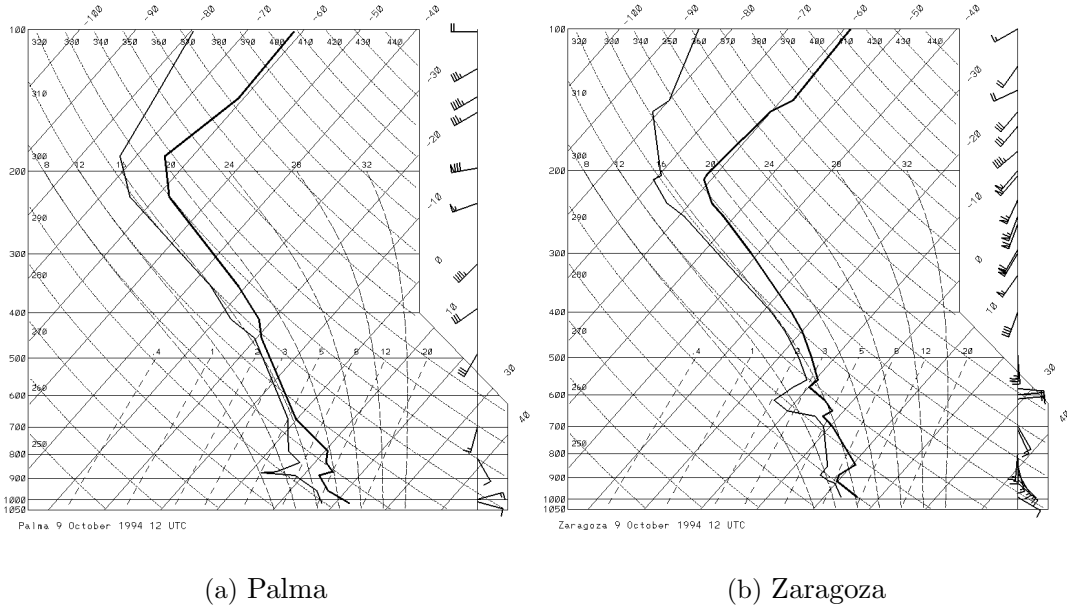


Figure 6.5: Radiosoundings on 12 UTC 9 October 1994: (a) at Palma (PAL in Figure 1.5), (b) at Zaragoza (ZAR in Figure 1.5).

of convection since $LI=6$ and $TT=45$. The PW is 30 mm. The wind is weak at low levels but also indicates warm advection with an helicity of $50 \text{ m}^2 \text{ s}^{-2}$.

At the considered time (12 UTC 9 October) there is water vapour convergence over southeast Spain and south of the Mediterranean, as well as convective instability as measured by the difference of equivalent potential temperature between 1000 and 500 hPa (not shown). A composite chart showing where quasigeostrophic upward forcing at 850 hPa, water vapour convergence in the layer 1000-850 hPa and convective instability between 1000 and 500 hPa overlap, is shown in Figure 6.6. Southeast Spain is then an area where the favorable synoptic mechanisms for convective developments are all present.

Another diagnosis for vertical motion can be deduced from the wind fields by looking for convergence zones at low levels and taking in mind the continuity equation. For a more graphical view of the convergence fields, the ageostrophic wind, deduced from the ECMWF analyses, has been split into its irrotational and solenoidal components following the Endlich (1967) method. Figure 6.7 shows the ageostrophic irrotational wind field and relative humidity at low levels. It can be seen that there is convergence over eastern Spain precisely where relative humidity is very high. The ageostrophic wind is probably associated with the isallobaric wind generated as a consequence of a deep pressure fall ($2.5 \text{ hPa}/3\text{h}$) observed in the Murcia coast.

Orographic forcing can be quantified by means of the upslope component, calculated using the orography, h , and the surface wind, \vec{V}_s , as $\vec{V}_s \cdot \vec{\nabla}h$. Figure 6.8 shows this orographic forcing at the ECMWF data resolution. Upslope motion exists along the Spanish Mediterranean coast, and hence the orography also represents a lifting mechanism for the parcels reaching the coast from the maritime zone.

In summary, on 12 UTC 9 October, the necessary ingredients for deep convection,

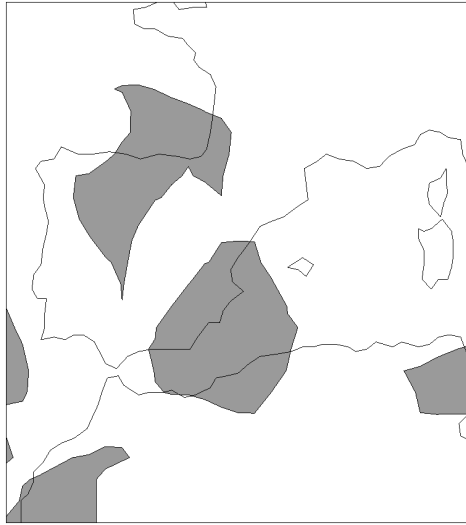


Figure 6.6: Composite chart for 12 UTC 9 October 1994. The shaded zones denote the existence of upward quasigeostrophic forcing at 850 hPa, potential instability between 500 and 1000 hPa and moisture convergence in the 1000-850 hPa layer.

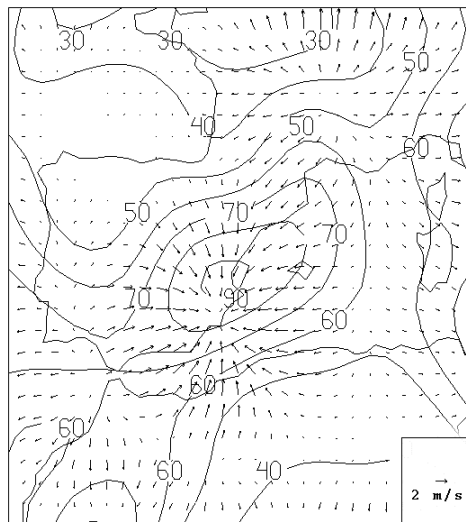


Figure 6.7: Irrotational component of the ageostrophic wind and relative humidity (in %) at 925 hPa on 12 UTC 9 October 1994.

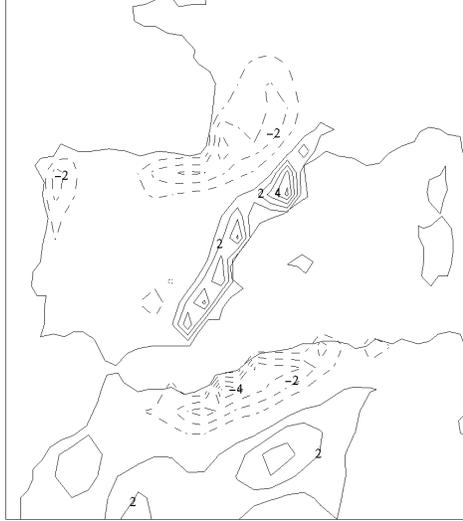


Figure 6.8: Upslope flow on 12 UTC 9 October 1994. Contour interval is 1 cm s^{-1} starting at 1 cm s^{-1} (continuous line) and at -1 cm s^{-1} (dashed line).

deduced from dynamical mechanisms (Figure 6.6), seem to be present over eastern and southeastern Spain and south of the western Mediterranean. In addition, these ingredients are supplemented by important orographic forcing and convergence of moist air over eastern Spain. Therefore, the diagnosis at synoptic scale suggests that the deepest convection is more likely in that area. This is consistent with Meteosat image at 12 UTC 9 October (Figure 6.3a), which shows that the deepest convection is occurring over the Valencia region.

Similar diagnostic products have been obtained for successive times (6 hours interval) during the episode. The changes observed in the spatial distribution of the dynamic mechanisms indicate a displacement of the zone favourable for convection towards the north following the Spanish Mediterranean coast. In fact, the composite chart for 06 UTC 10 October (Figure 6.9) displays that the favourable area comprises coastal Catalonia. Figure 6.10 shows positive helicity and CAPE at that time. The helicity field reflects that the strongest warm advection is now located over Catalonia. CAPE has also increased over the same area. Figure 6.11 illustrates that the orographic forcing has its strongest signal also there.

Radiosonde data from Palma at 00 UTC 10 October is not available. At 12 UTC (Figure 6.12), the LID structure is clear although the inversion is weak. This sounding yields a CAPE of 2900 J kg^{-1} , an inhibition energy of 6 J kg^{-1} , a LI of -4, a TT of 44, and very high humidity in all the troposphere resulting in 41 mm of PW. Comparing with Figure 6.5a, it is notable the appreciable warming of the lowest levels, this warming being the principal factor to explain the observed increase of the CAPE. Winds at low levels are from the southeast veering to the south, and a clear LLJ can be identified at 700 hPa. Over Murcia at 00 UTC 10 October (sounding not shown) the CAPE is 470 J kg^{-1} , the inhibition energy 90 J kg^{-1} , the LI is -1, the TT is 45 and the PW 37 mm. The atmosphere is very humid at low levels but there is a dry layer between 600 and 300 hPa. No evidence of LLJ appears at that time, although warm advection continues since helicity is 40 m^2

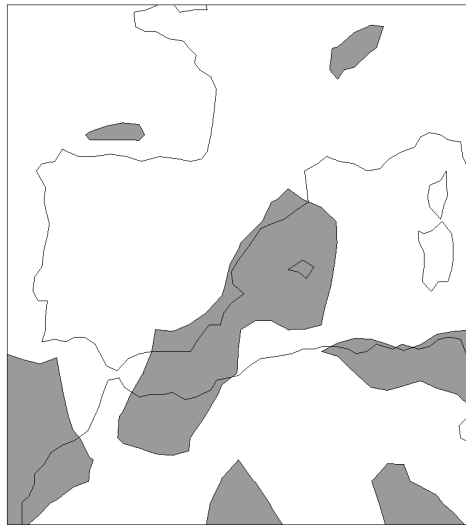


Figure 6.9: Composite chart for 06 UTC 10 October 1994. The shaded zones denote the existence of upward quasigeostrophic forcing at 850 hPa, potential instability between 500 and 1000 hPa and moisture convergence in the 1000-850 hPa layer.

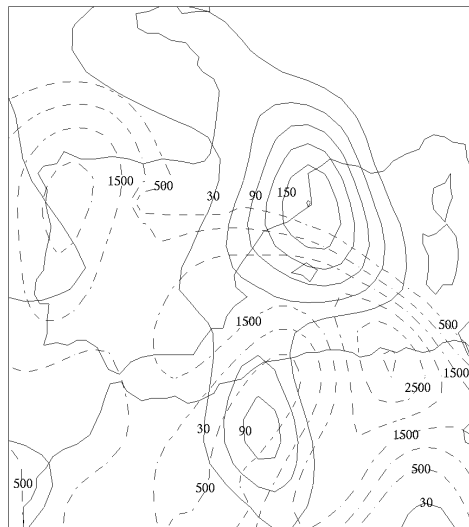


Figure 6.10: Positive helicity (continuous line; contour interval is $30 \text{ m}^2 \text{ s}^{-2}$ starting at $30 \text{ m}^2 \text{ s}^{-2}$) and CAPE (dashed line; contour interval is 500 Jul kg^{-1} starting at 500 Jul kg^{-1}), on 06 UTC 10 October 1994.

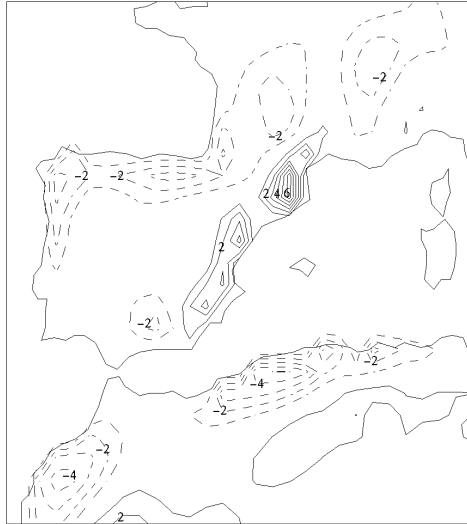


Figure 6.11: Upslope flow on 06 UTC 10 October 1994. Contour interval is 1 cm s^{-1} starting at 1 cm s^{-1} (continuous line) and at -1 cm s^{-1} (dashed line).

s^{-2} . Over Zaragoza at 00 UTC 10 October (sounding not shown) the atmosphere is very stable (CAPE=0), with a strong inversion at low levels as a consequence of the warm advection (helicity is $214 \text{ m}^2 \text{ s}^{-2}$) over the surface cold air.

In summary, on 10 October between 00 and 12 UTC, in which time interval the heaviest precipitation occurred in Catalonia, the synoptic ingredients for heavy rain have reached Catalonia, where orographic forcing is also maximized. The analysis of the radiosonde data from Palma, Murcia and Zaragoza reveals that the air mass over the Balearic Islands is the most representative of the environment in which convection developed. The wind at low levels (see Figures 6.2a and b) is advecting this air mass towards Catalonia, where the important orographic forcing would facilitate the breaking of the LID and the release of the instability. The high stability over Zaragoza indicates the presence of a sharp boundary between the Mediterranean air mass supporting the convection, and that over inland Spain (see Figures 6.3b and c).

6.2.2 Subsynoptic study

Surface subsynoptic analyses have been constructed by using all the available information over the area of interest. When doing the analyses, we have taken into account the effects induced by the Atlas and the Pyrenees on the pressure field. That is, since the flux at medium and upper levels blows almost normal to these mountain ranges, a pressure dipole structure (cyclone in the lee and anticyclone in the windward) develops (Besse-moulin et al. 1993). In addition, Meteosat images and conceptual models of pressure distribution around a thunderstorm (Schofield and Purdom 1986) have been considered. This is useful to mitigate the problem of the sparsity of the data.

Figure 6.13 shows the surface analysis at different times of the event. It can be observed that at the beginning of the event the low in the lee of the Atlas produces a strong and humid flux toward the Murcia and Valencia regions. Progressively, as the low

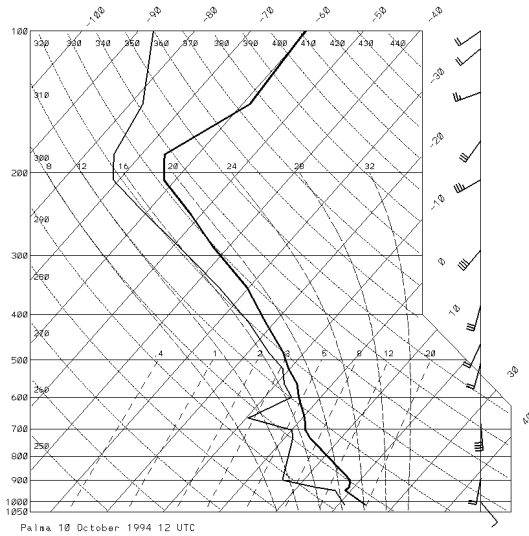


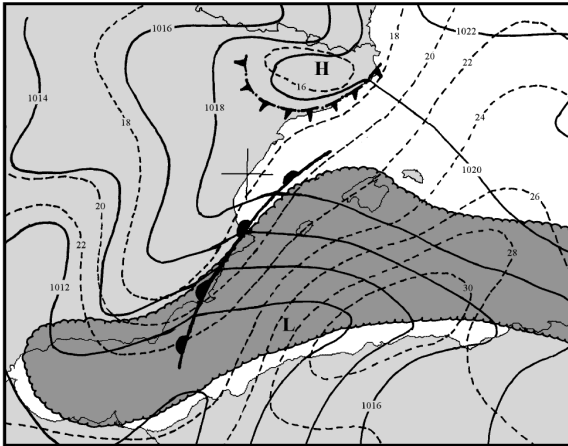
Figure 6.12: Radiosounding on 12 UTC 10 October 1994 at Palma (PAL in Figure 1.5).

moves northwards, the strongest flux focuses towards Catalonia. At the same time the humid air also displaces northwards. Figure 6.14 shows a reanalysis of the 500 hPa surface on 00 UTC 10 October. Available data and the Meteosat image at that time suggest the presence of a secondary trough over northeastern Spain. In the ECMWF analyses, this trough is weaker and located downstream over southwest France.

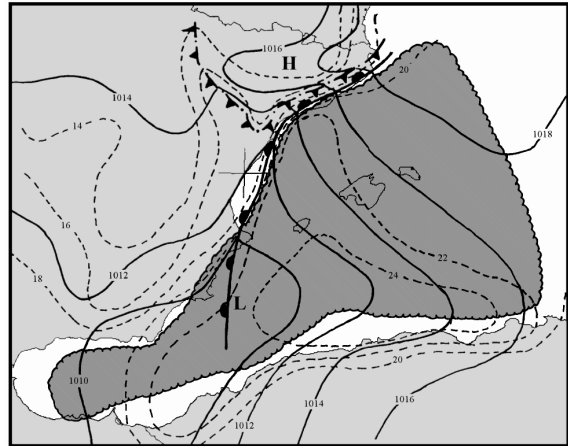
Considering these analysis and the satellite images, it is deduced that the most important convection developed by interaction of the humid flux with the coastal mountains, and ahead of the secondary trough at upper levels. Although orographic forcing is general over coastal Spain (Figures 6.8 and 6.11), convection only progresses northwards as the humid air does, in connection with the displacement of the surface low. However, the convection was almost stationary during several hours over south Catalonia where the centres of maximum precipitation occurred. This fact can be related to the convergence between the eastern general flow and the outflow from the high pressure developed in the windward of the Pyrenees. As the isotherms distribution reveals (Figure 6.13b), the high pressure limits define a true cold front.

The previous scenario matches in many aspects the situation described by Maddox et al. (1979) as a “mesohigh event” for flash floods in USA. In fact, the event occurred near the ridge axis and far from the large scale trough that appears on the 500 hPa analysis. Warm and humid surface air is advected towards the mesohigh and convergence exists in the boundary of this mesohigh. At 850 hPa the LLJ also feeds the convection with moist air. At medium levels, a secondary trough favours the vertical motion over the area with convergence at low levels. And the humidity is very high in all the troposphere, so favouring the precipitation efficiency.

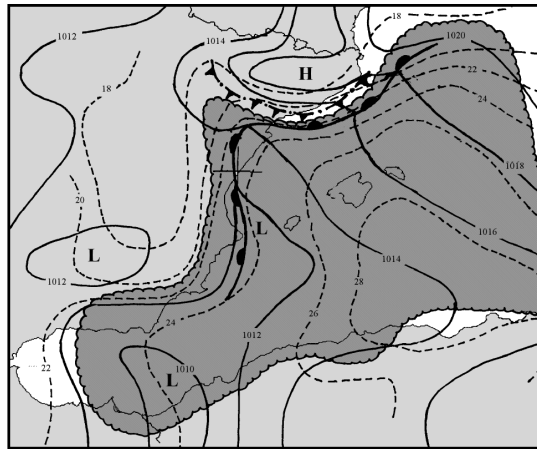
The major difference between our scenario and that described by Maddox et al. (1979) is that the mesohigh is not produced by previous thunderstorms, but by the Pyrenees, which creates an anticyclone in the windward side relative to the large scale flux at medium and high levels. The temperature and humidity at surface demonstrate that there is a true cold front around the mesohigh, which plays the same role as the front produced by



(a) 12 UTC 9 October



(b) 06 UTC 10 October



(c) 12 UTC 10 October

Figure 6.13: Subjective surface mesoscale analysis: (a) on 12 UTC 9 October 1994, (b) on 06 UTC 10 October 1994, (c) on 12 UTC 10 October 1994. Continuous lines represent isobars, dashed lines isotherms and the dark shaded area represents the zone with dew point higher than 18 °C.

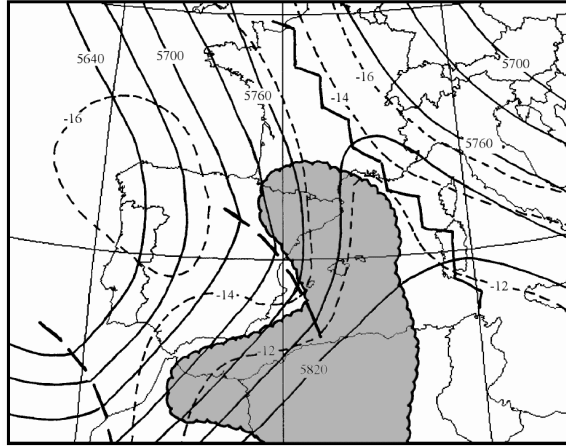


Figure 6.14: Subjective 500 hPa surface reanalysis on 00 UTC 10 October 1994. Continuous lines represent height, dashed lines isotherms and the dark shaded area represents the zone with relative humidity greater than 80%.

thunderstorm downdrafts. In addition, the low producing the warm and humid advection towards Catalonia is, at least during the first stage, a consequence of the interaction of the Atlas mountains with the synoptic flux. Finally, a particular aspect in our case is that the orographic lifting forced by the coastal mountains of Catalonia enhances the lifting produced by the convergence along the mesohigh boundary, and helps to trigger and maintain the convection. A scheme of this scenario is presented in Figure 6.15.

6.3 Description of the experiments

A set of mesoscale numerical simulations has been carried out for 9 and 10 October 1994 to test the capability of the model to forecast the event, to quantify the main physical processes that controlled the occurrence of the coastal heavy precipitation, and to help supplement the diagnostic study of the previous section. Four experiments have been performed for each day, with the characteristics summarized in Table 5.2. Implicitly, we are considering again the coastal topography and the latent heat flux from the warm Mediterranean sea as key factors responsible for the focalization of the heavy rainfall in the coastal areas of eastern Spain. Using the technique of Stein and Alpert (1993), the outputs of the experiments are algebraically combined to yield the effects of the orography, evaporation from the sea, and their synergism (see section 5.2.2).

Following the methodology described in section 5.1.3, the initialization and boundary conditions for the SALSA model have been obtained from the uninitialised ECMWF analyses. For this event, subsoil temperature has been approximated by the October climatological mean value, and as for the Piedmont case, the sea surface temperature is provided by the ECMWF surface data (Figure 6.16). Grid dimensions and resolutions are the same as in the last chapter. That is, the model domain (Figure 6.16), which is centered at (1°E,41°N), covers 1800 x 1800 km² (91x91 grid points with an horizontal grid length of 20 km), and 30 levels are defined in the vertical. Guided by the conclusions of

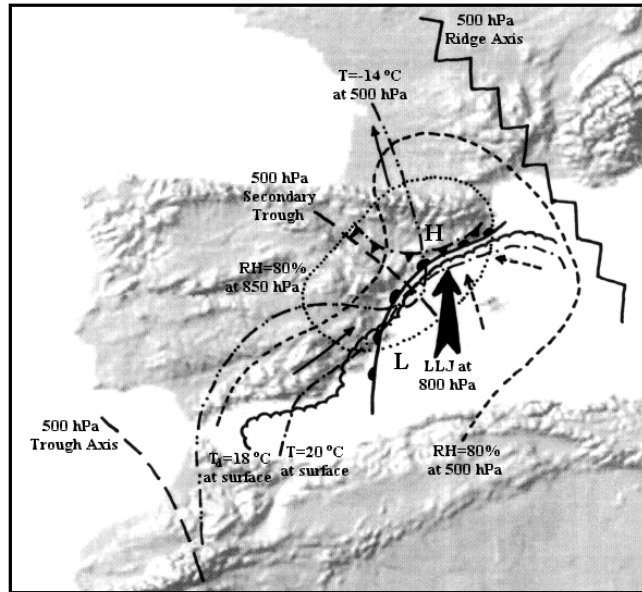


Figure 6.15: Scheme representing the meteorological scenario at 06 UTC 10 October 1994. H and L represent the position of the mesohigh and the mesolow at surface. Dashed arrows represent the flux at surface and continuous arrows the flux at 500 hPa.

section 5.3.5, for these experiments we have used the Kain and Fritsch (1990) convective scheme.

For each day, the simulations extend 30 h, from 00 UTC till 06 UTC (next day). This time interval is appropriate, since we intend to compare the forecast rainfall for the last 24 h (“free” of model spinup influences), with the observed rainfall which is valid for 07-07 UTC (Figure 1.12).

6.4 Results for 9 October

Forecast fields at 18 UTC (after 18 hours of simulation) show that at low levels (Figure 6.17a) a very well marked trough is located over the Algerian coast in the lee of the Atlas range. It is also remarkable the strong warm anomaly over the same area. Both aspects combine to produce warm advection over the south of the Valencia region. An anticyclonic circulation is present over northeastern Spain as a feature of the pressure dipole across the Pyrenees. Such pressure distribution produces an easterly flux over the Mediterranean, impinging almost perpendicular to the Spanish coast. This is especially notable over the Valencia coast where the upslope flow is strong and where convection is identified over the Meteosat picture (see Figures 6.3a and b). At 850 hPa (Figure 6.17b) the flux is from the south, with the strongest winds, 15 ms^{-1} , found over southeastern Spain, where well marked warm advection is identified. The pressure and thermal dipoles across the Pyrenees are also detected at this level. At upper levels, 500 and 300 hPa (Figures 6.17c and d), the flux is from the south-southwest over the Mediterranean and eastern Spain, with warm advection also occurring at these levels. A ridge is clearly depicted in the eastern part of the domain. No jet streak structures appear in the simulation.

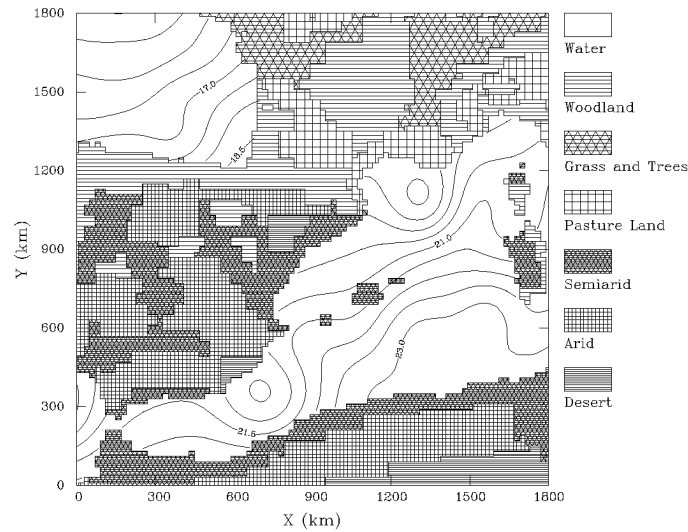
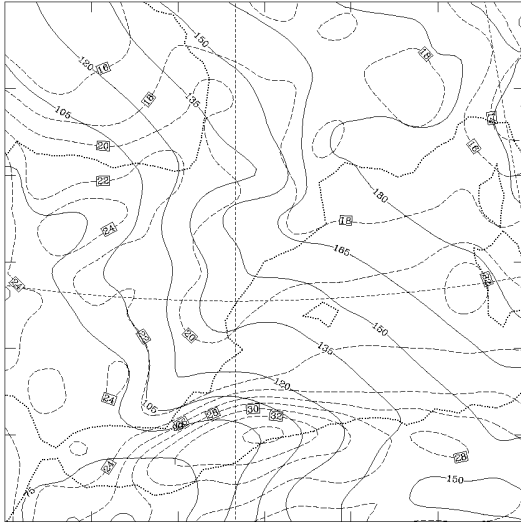


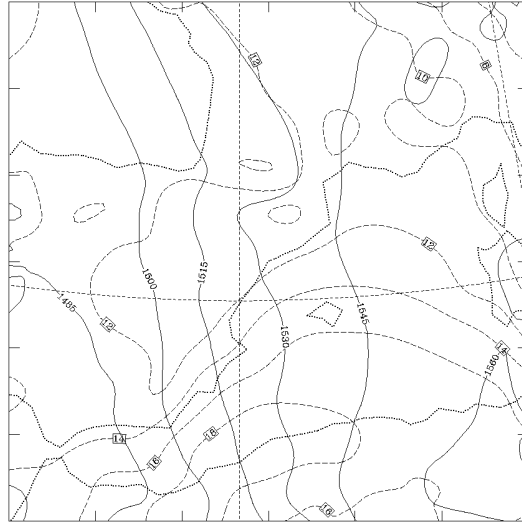
Figure 6.16: Distribution of surface types in the model domain and sea surface temperature ($^{\circ}\text{C}$) for the numerical simulations.

Forecast fields at 06 UTC 10 October (after 30 hours of simulation) show that at 1000 hPa (Figure 6.18a) the low has moved to the north along the Mediterranean coast. A strong geopotential gradient appears to the northeast of the low (over the Balearic Islands), producing a easterly flow towards north Valencia and south Catalonia. The pressure dipole in the Pyrenees continues in spite of the general pressure decrease in the domain. The warm anomaly has moved also to the north, producing a very well marked thermal boundary along the Valencia-Catalonia coast. At 850 hPa (Figure 6.18b) the geopotential structure is very similar to that of Figure 6.17b but displaced towards the east. The flux is from the south over the Mediterranean with a band of maximum winds from the Algerian coast to Catalonia. As a consequence of these winds, there is notable warm advection towards Catalonia. At upper levels (Figures 6.18c and d) the flux continues from the south-southwest over the Mediterranean and eastern Spain, but stronger cyclonic circulation appears at the west of the domain. The ridge continues over the eastern part of the domain. Again, no jet streak signatures are evident over eastern Spain and the Mediterranean. The thermal ridge remains over these zones.

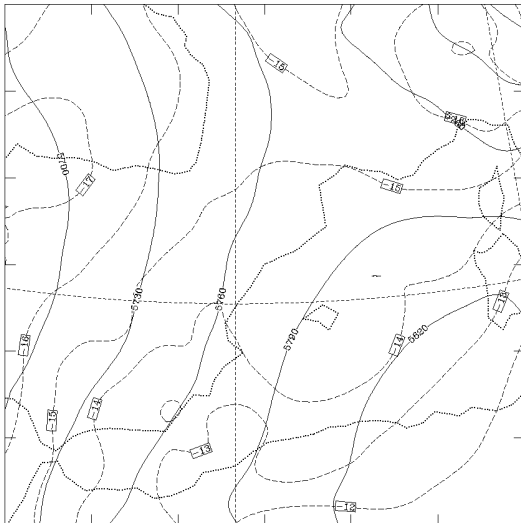
As an illustration of the pressure changes at surface, Figure 6.19a shows negative values of geopotential tendency at 1000 hPa given by the model between 06 UTC and 18 UTC 9 October, and between 18 UTC 9 October and 06 UTC 10 October. In the first case, the maximum values are located along the Algerian coast, so inducing a strong increase of the geopotential gradient to the southeast of Spain. This explains why the wind increased strongly in this area, and consequently the warm advection towards Spain. During the second time interval the greatest negative tendency occurs close to the Valencia coast. This structure implies an intensification of the geopotential gradient over the Balearic Islands, so enhancing the onshore flow towards Catalonia. Also interesting is the tendency field at 850 hPa (Figure 6.19b). The most significant feature is found between 18 UTC 9 October and 06 UTC 10 October. A large increase of the geopotential gradient is forced between Algeria and Catalonia, so favouring the strengthening of the LLJ.



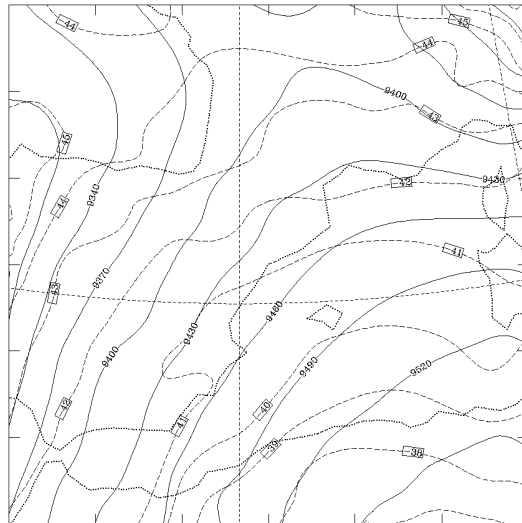
(a) 1000 hPa



(b) 850 hPa

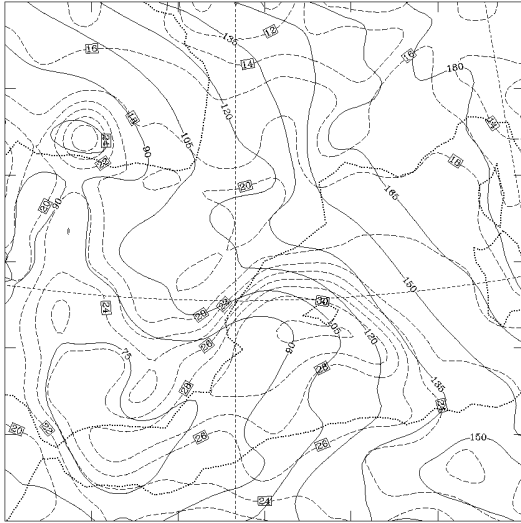


(c) 500 hPa

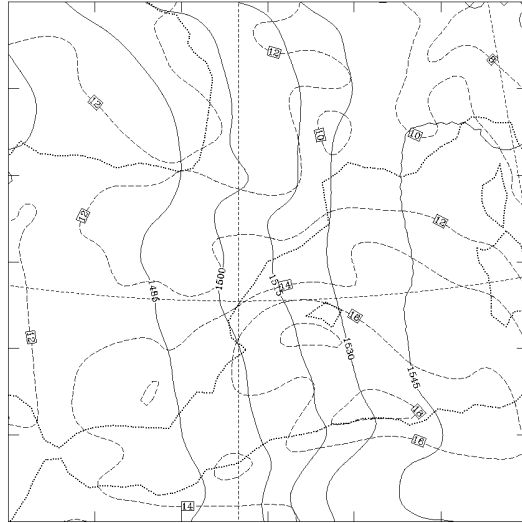


(d) 300 hPa

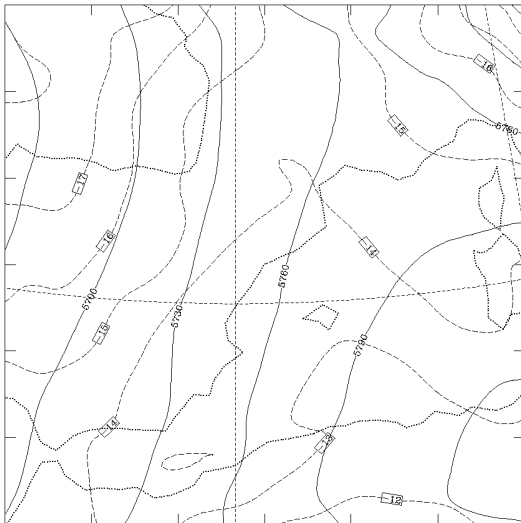
Figure 6.17: Forecast fields at 18 UTC 9 October 1994, showing height (gpm, continuous line) and temperature ($^{\circ}\text{C}$, dashed line): (a) 1000 hPa, (b) 850 hPa, (c) 500 hPa, (d) 300 hPa.



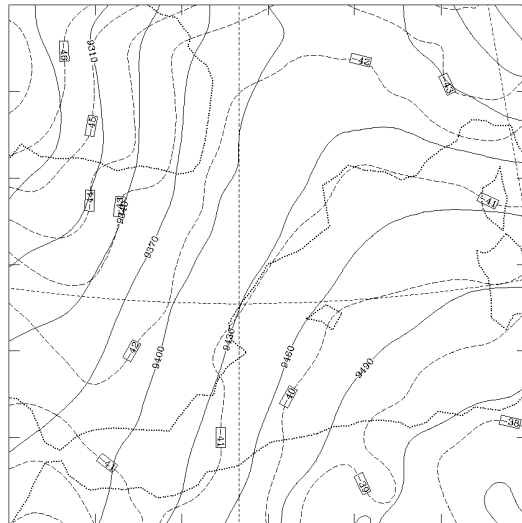
(a) 1000 hPa



(b) 850 hPa



(c) 500 hPa



(d) 300 hPa

Figure 6.18: Forecast fields at 06 UTC 10 October 1994, showing height (gpm, continuous line) and temperature ($^{\circ}\text{C}$, dashed line): (a) 1000 hPa, (b) 850 hPa, (c) 500 hPa, (d) 300 hPa.

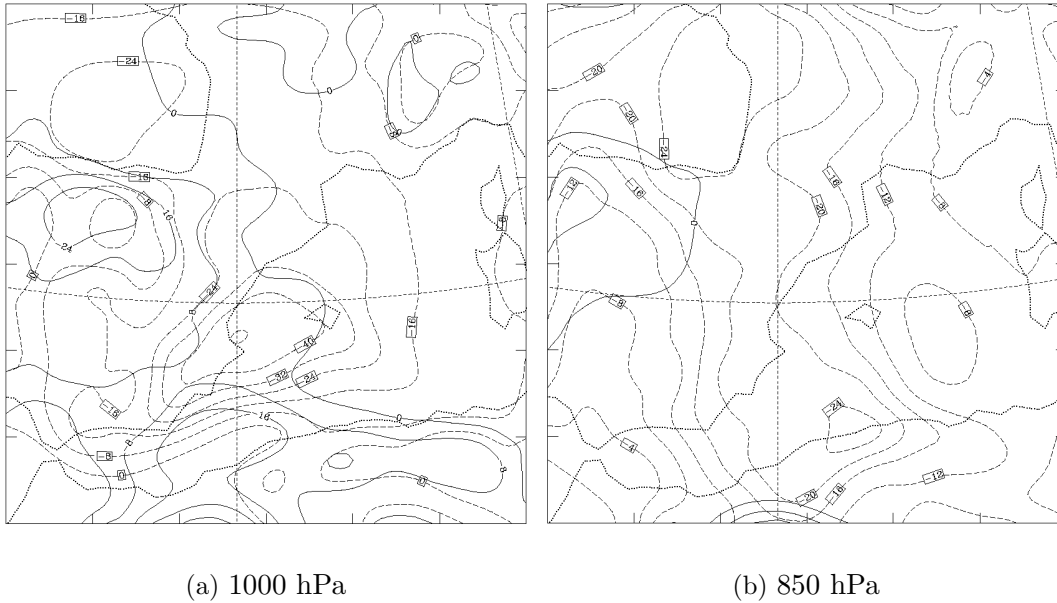


Figure 6.19: Model predicted geopotential negative tendency between 06 UTC and 18 UTC 9 October 1994 (continuous line) and between 18 UTC 9 October 1994 and 06 UTC 10 October 1994 (dashed line): (a) at 1000 hPa, (b) at 850 hPa.

Forecast rainfall for this day is shown in Figure 6.20a. In general terms, it compares favourably with the observed precipitation over eastern Spain (Figure 1.12a): it reproduces the elongated coastal maximum of northern Valencia, another structure parallel to the Pyrenees and important quantities also over Murcia. However, as usually occurs in meso- β scale simulations of convective events, the model clearly underestimates the records (only in northern Valencia 60 mm are slightly exceeded). In addition, the model gives an unobserved pattern over the Mediterranean coastal fringe of Andalucía, and underestimates and locates slightly southwards the most important maximum present in the southern extreme of Catalonia (see Figure 1.12a).

If only the convective contribution is considered (Figure 6.20b), it is concluded that, except in the area of the Pyrenees, the forecast rainfall shown in Figure 6.20a is essentially convective. By inspection of the forecast rainfall at previous times, it seems that the timing of the event produced by the model is in agreement with the activity displayed by Meteosat images (Figures 6.3a and b): convection started to develop in southeastern Spain about midday and progressed northwards, strengthening over northern Valencia and southern Catalonia during the night.

Although the forecast rainfall is somewhat deficient over Catalonia, we can consider the result of Figure 6.20a as a good guidance for forecasters. It is in these conditions, when the control simulation can be regarded of sufficient quality, that the factor separation technique of Stein and Alpert (1993) has its authentic utility. Next, we present the most important results of our factor separation study.

If simply the basic experiment is considered (f_0 in Table 5.2), then the forecast rainfall is quite deficient as shown in Figure 6.21. Significant rainfall is only obtained in inland

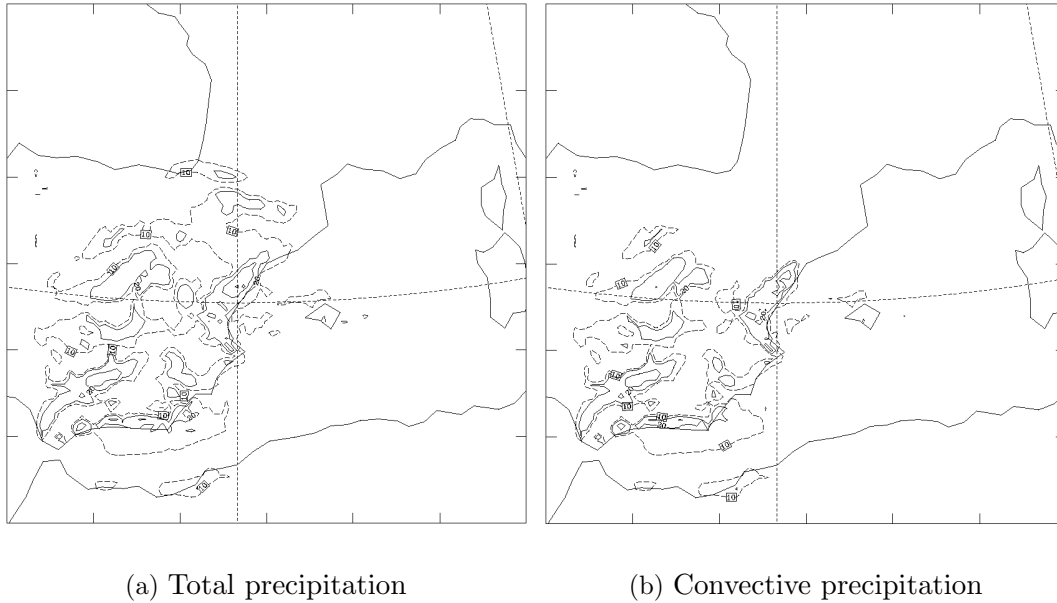


Figure 6.20: Forecast precipitation from 06 UTC 9 October 1994 to 06 UTC 10 October 1994: (a) Total precipitation, (b) Convective precipitation. Contour interval is 20 mm starting at 20 mm (continuous line). Dashed contour represents 10 mm.

areas, and less than 10 mm are given by the model over all the eastern coast of Spain. This result is in agreement with the results obtained for Catalonia and Piedmont events (chapter 5), and clearly confirms that only dynamic forcing is not sufficient to focalize the coastal rainfall maxima observed in these convective events. Rather, the synoptic scale is responsible for the creation of the appropriate conditions for convection development or for localised strong condensation and its maintenance during several hours, but it is the mesoscale, through the action of the topography, as we will show later, which ultimately determines where these processes will occur.

The effect of the orography on the 1000 hPa geopotential field at 06 UTC 10 October is shown in Figure 6.22a. This picture confirms that the trough developed over the Mediterranean, in the lee of the Atlas, has a topographic cause. Similarly the pressure dipole produced by the Pyrenees is clearly isolated. It is notable that the windward positive tendency extends its influence toward central Spain. On the low-level wind field the orographic effect is quite substantial. Particularly at the end of the simulation, (Figure 6.22b), this effect is very strong about the coasts of Catalonia and Valencia, in the sense of a backing and deceleration of the wind. This contribution is attributed to the blocking action of the Pyrenees and coastal ridges of eastern Spain, as well as to the suction effect of the low developed over the Mediterranean. The orographic effect is also very important from the African coast northwards, between Balearic Islands and Corsica and Sardinia. This contribution is approximately directed in the same direction as the total wind (figure not shown), thus enhancing the low-level maritime current which is supplying of moisture the coastal environment. In general terms, the wind pattern shown in Figure 6.22b exhibits a cyclonic circulation over the western Mediterranean, in agreement with the

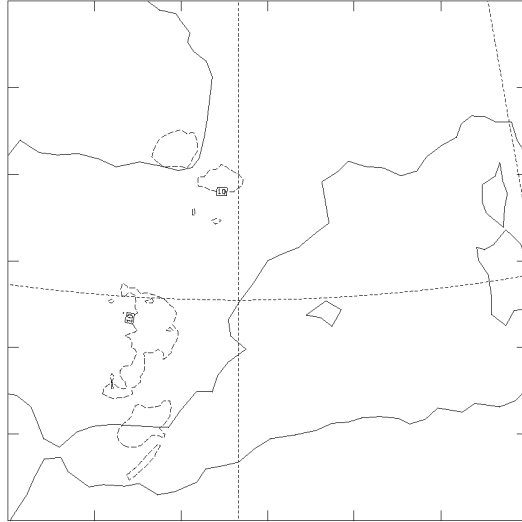
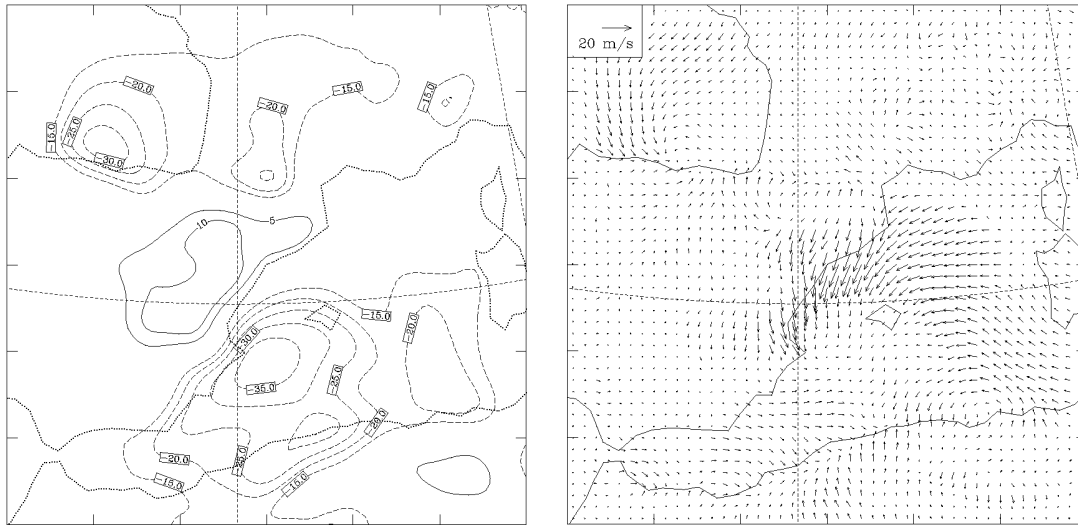


Figure 6.21: Forecast total precipitation from 06 UTC 9 October 1994 to 06 UTC 10 October 1994 for the experiment without orography and without evaporation from the sea. Contour interval is 20 mm starting at 20 mm (continuous line). Dashed contour represents 10 mm.

geopotential anomalies produced by the orography. The orographic action on the 1000 hPa temperature, (figure not shown), represents a warming effect over south Mediterranean and a cooling effect over northeastern Spain. The combination of both effects explains the accentuated temperature gradient over eastern Spain and between Catalonia and the Balearic Islands (Figure 6.18a). For the rainfall, the effect is important, but mainly limited to the interior relief systems (Figure 6.22c). This is in agreement with the model initial conditions for relative humidity at low levels (not shown) which indicates high values of relative humidity over eastern Spain but not over the Mediterranean.

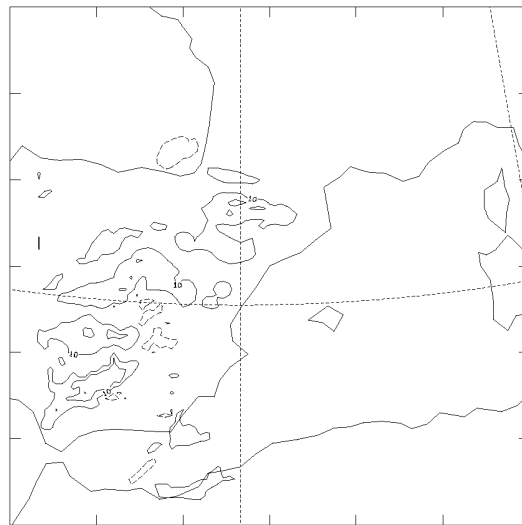
The effect of the evaporation from the sea on geopotential, wind and temperature at surface is negligible. On the accumulated rainfall it is, as expected, mainly positive. In this case it also affects moderately coastal areas of Catalonia, Valencia and eastern Andalucía (Figure 6.23). It seems that, without presence of orography, the evaporation from the sea does not contribute decisively to the rainfall field.

The most decisive role to define the coastal rainfall maximum in the Valencia area was exerted by the synergistic factor (see Figure 6.24a). Other positive signals exist over the sea and coastal zones, and the action is suppressive in many interior areas. Therefore, it seems that in its initial state, the low atmosphere over the sea did not have enough moisture content to readily feed the coastal convection. Evaporation heat fluxes during the course of the simulation from the Mediterranean are very high (Figure 6.24b), charging of moisture the air parcels that interact downstream with the coastal topography. The effect of the interactive factor on the wind field (not shown) is also weak in this case. It is most notable over Valencia and south Catalonia where it acts producing a slight upslope component (opposite to the orographic action), probably because moist flows present smaller effective stability and therefore are less susceptible to blocking. The effect on the 1000 hPa geopotential is weak and only slightly significant over south Valencia where a negative signal appears, in agreement with the effect on the surface wind field.



(a) Geopotential 1000 hPa

(b) Surface wind



(c) Total precipitation

Figure 6.22: Effect of the orography at the end of the simulation (06 UTC 10 October 1994): (a) on the geopotential field at 1000 hPa (in gpm); (b) on the surface wind field; (c) on the total precipitation (contour interval is 20 mm starting at 10 mm, continuous line, and at -10 mm, dashed line).

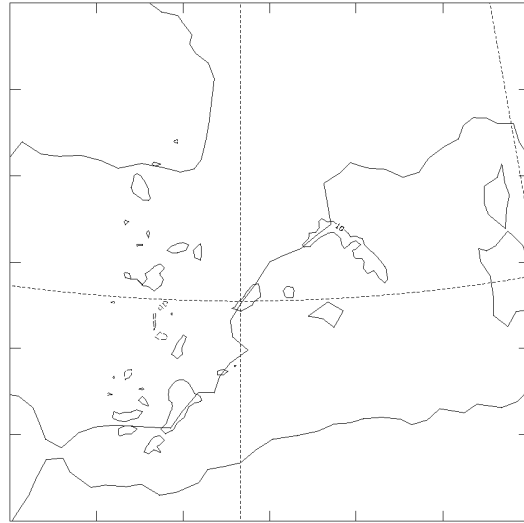
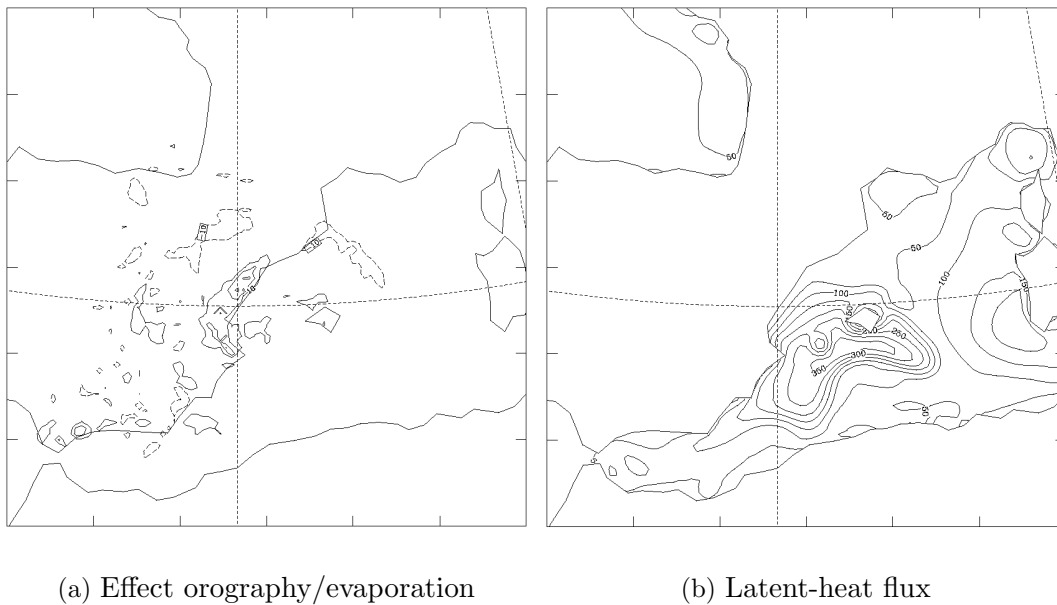


Figure 6.23: Effect of the evaporation from the sea at the end of the simulation (06 UTC 10 October 1994) on the total precipitation (contour interval is 20 mm starting at 10 mm, continuous line, and at -10 mm, dashed line).



(a) Effect orography/evaporation

(b) Latent-heat flux

Figure 6.24: (a) Effect of the interaction orography/evaporation at the end of the simulation (06 UTC 10 October 1994) on the total precipitation (contour interval is 20 mm starting at 10 mm, continuous line, and at -10 mm, dashed line). (b) Latent-heat flux from the sea at the end of the simulation (06 UTC 10 October 1994) (contour interval is 50 W m^{-2} starting at 50 W m^{-2}).

6.5 Results for 10 October

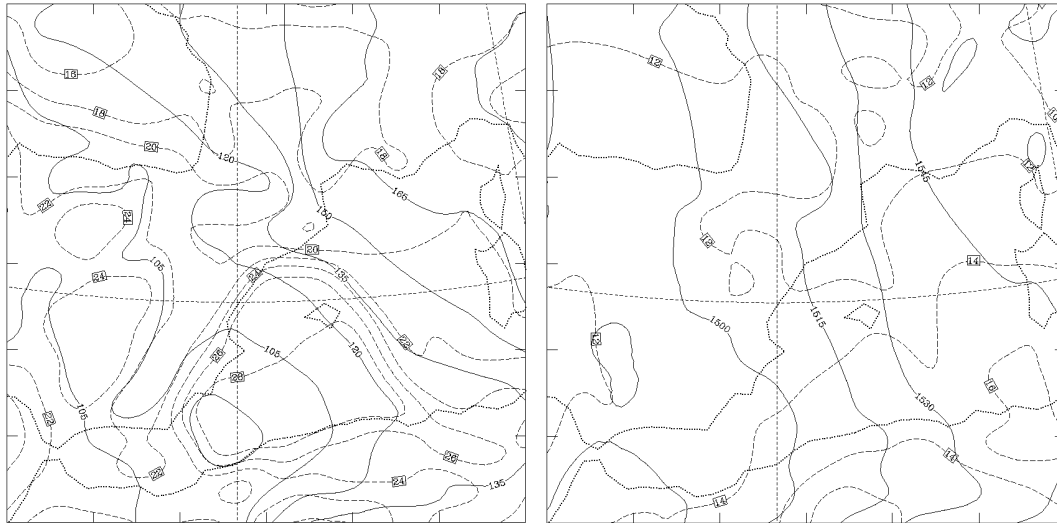
Figure 6.25 shows the 18 hours forecast fields at 18 UTC 10 October. At low levels (Figure 6.25a), it is seen that the low located over south Spain (see Figure 6.18a) has displaced to the east and has weakened. However, the strong flux from the southeast over the Mediterranean remains practically over the same area that 12 hours before, blowing towards the northern part of the Catalonia coast. The warm tongue over the western Mediterranean, although less intense, maintains its structure and then warm advection continues over Catalonia. The orographic pressure dipole about the Pyrenees is still present. At 850 hPa (Figure 6.25b) the geopotential gradient over the Mediterranean has weakened but the flux remains from the south with the strongest values located over north Catalonia and south France. At upper levels (Figures 6.25c and d) the flux keeps its south-southwest component but it is much weaker than 12 hours before (Figures 6.18c and d). This fact can explain why the orographic effects on the surface pressure field in the lee of the Atlas are smoother than the day before, as it will be shown later.

On this day the heavy rains affected northern Valencia and south Catalonia as on 9 October, but in contrast, the coastal part of northern Catalonia was also extensively affected by convection whereas southeastern Spain was free of important rains (see Figure 1.12b). This rainfall spatial distribution is well captured by the mesoscale model, as can be seen in Figure 6.26a. A coastal band of more than 40 mm, resembling the observed pattern, is forecast by the model from central Valencia to northern Catalonia. Quantitatively, this forecast is also better than for the previous day, since a large area exceeding 60 mm is obtained in Catalonia (peak values exceed 100 mm). In this case, the forecast total rainfall is also essentially convective. In agreement with the observed evolution of the episode, the major part of the rainfall is forecast during the first half of the day (Figure 6.26b).

The main physical arguments derived for 9 October also apply for 10 October. When considering the basic simulation f_0 , less than 10 mm are given by the model in all the area of interest, including sea zones. This means that the considered factors should be fundamental for the rainfall distribution and amounts. The isolated effect of the topography on the accumulated rainfall results very important (Figure 6.27a). This effect practically explains the forecast rainfall in all zones except in coastal Catalonia and over the sea (compare with Figure 6.26a). The orographic effect on the surface wind field at 18 UTC (Figure 6.27b) shows similar actions that 12 hours before, but the blocking and associated convergences appear more concentrated in the Catalonia area and are less intense. The effect on the 1000 hPa geopotential field at 18 UTC is shown in Figure 6.27c. Comparing with Figure 6.22a, it is deduced that the orographic effect, both by Atlas and by Pyrenees, is not so marked at this time. This can be attributed to the weakening of the southerly flux at upper levels.

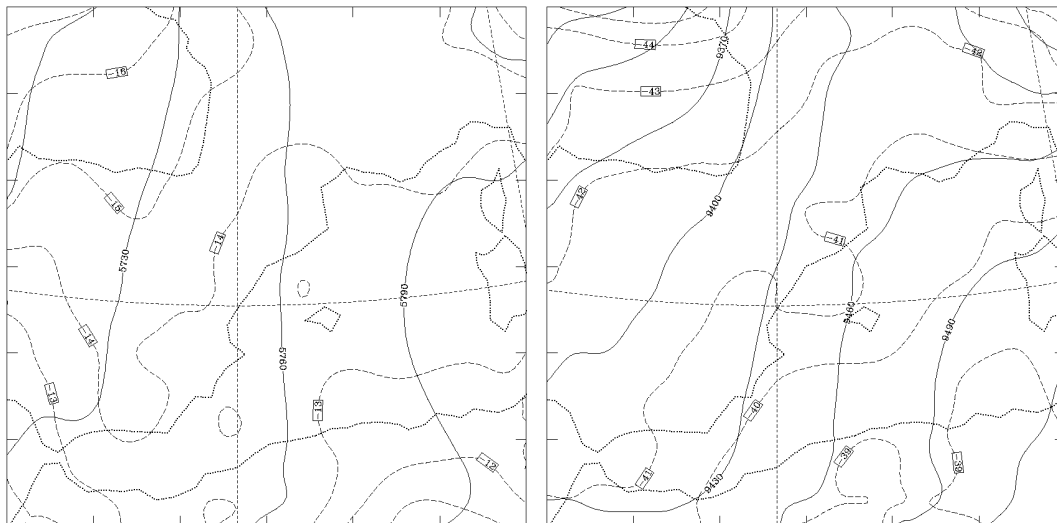
The effect of the evaporation from the sea on the rainfall is essentially positive and helps to explain the rainfall structure depicted in Figure 6.26a over the sea, south of the Balearic Islands. Only very weak actions on the low-level flow and geopotential can be attributed to the evaporation. This effect becomes once again the weakest one of the three and it is not shown.

The effect of the interaction orography/evaporation turns to be the most important for explaining the rainfall north of the Balearic Islands and in particular the coastal



(a) 1000 hPa

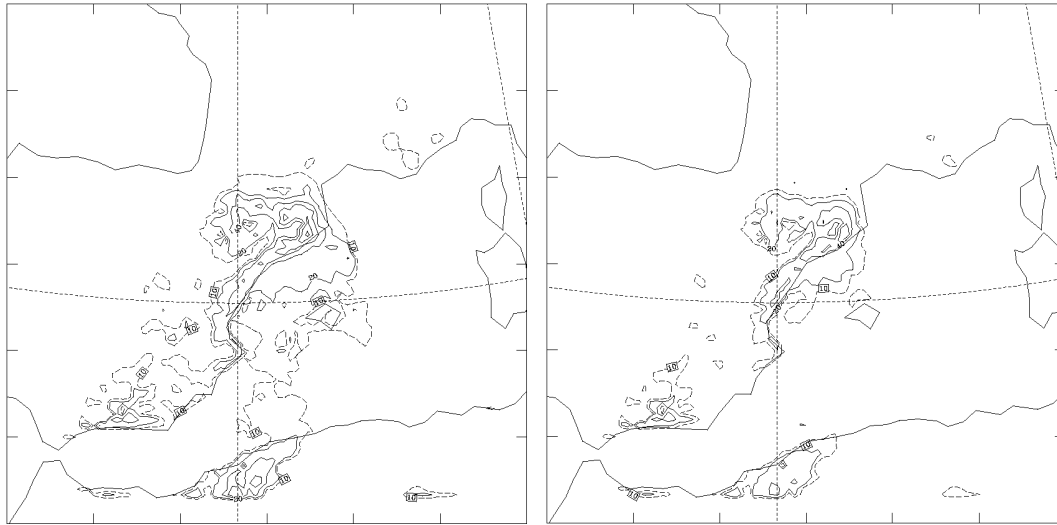
(b) 850 hPa



(c) 500 hPa

(d) 300 hPa

Figure 6.25: Forecast fields at 18 UTC 10 October 1994, showing height (gpm, continuous line) and temperature ($^{\circ}\text{C}$, dashed line): (a) 1000 hPa, (b) 850 hPa, (c) 500 hPa, (d) 300 hPa.



(a) 24 h rainfall

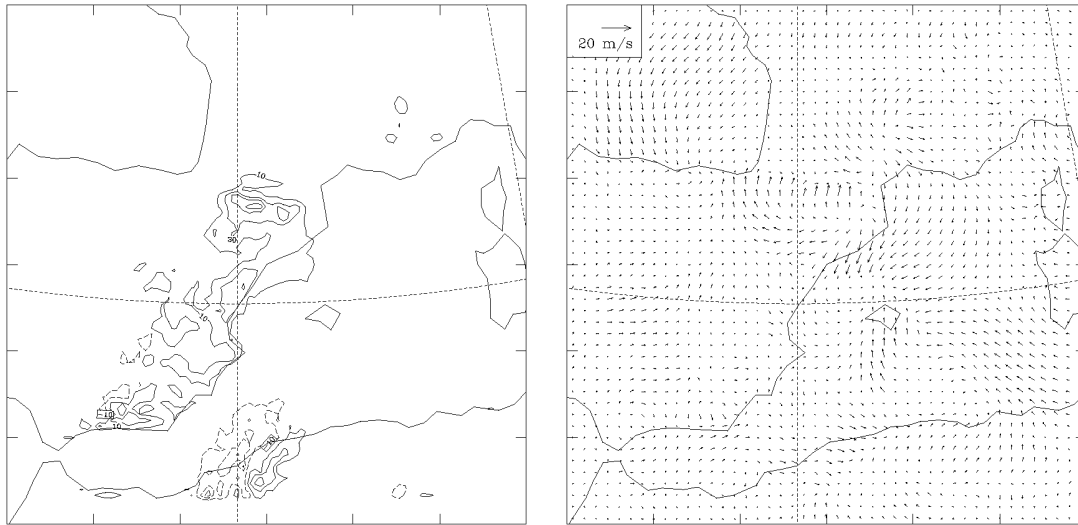
(b) 12 h rainfall

Figure 6.26: Forecast total precipitation: (a) from 06 UTC 10 October 1994 to 06 UTC 11 October 1994; (b) from 06 UTC 10 October 1994 to 18 UTC 10 October 1994. Contour interval is 20 mm starting at 20 mm (continuous line). Dashed contour represents 10 mm.

maxima of Catalonia (Figure 6.28). Correspondingly, its action is suppressive downstream over interior lands. The great importance of the synergistic effect over coastal Catalonia can be attributed to the model initial conditions of wind and relative humidity at low levels (Figures 6.29a and b). Both figures show that the flux impinging over Catalonia during the first hours of simulation must be “dry” unless evaporation from the sea is allowed. The evaporation increases the relative humidity of the air parcels flowing over the Mediterranean and the coastal mountains of Catalonia are able to develop convection. The interaction effect on the surface wind field is only remarkable over the sea close to the Catalonia coast. It acts in opposite sense that the orography, since blocking is less strong for humid air than for dry air. The effect on the 1000 hPa geopotential is generally weak, but a negative signal appears over south Catalonia.

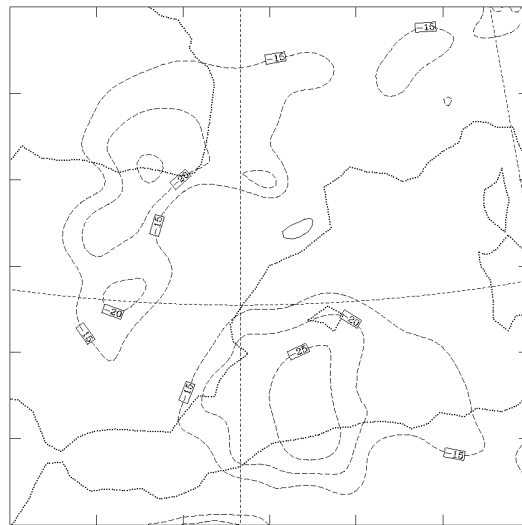
6.6 Conclusions

The meteorological situation in which the Tarragona heavy precipitation event occurred has been presented. At low levels, it was characterized by an anticyclone over Europe and a trough over the Algerian coast which combined to produce warm and humid easterly flux impinging over the coastal orography of eastern Spain. At upper levels, there was a synoptic wave with a trough to the southwest of Spain and a negatively tilted ridge over the western Mediterranean. A thermal ridge was also present over eastern Spain and the western Mediterranean. Meteosat images show that the development of the convective systems producing the heaviest precipitation occurred in the rear of the ridge axis and far from the trough. The convection developed over the Valencia area and



(a) Total precipitation

(b) Surface wind



(c) Geopotential 1000 hPa

Figure 6.27: Effect of the orography: (a) on the total precipitation at the end of the simulation (06 UTC 11 October 1994) (contour interval is 20 mm starting at 10 mm, continuous line, and at -10 mm, dashed line); (b) on the surface wind field on 18 UTC 10 October 1994; (c) on the geopotential field at 1000 hPa (in gpm) on 18 UTC 10 October 1994.

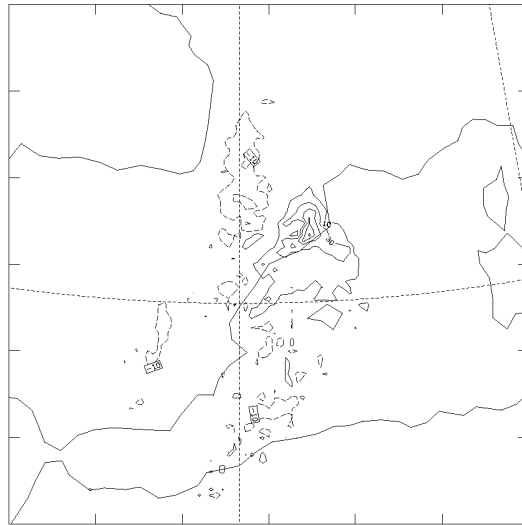
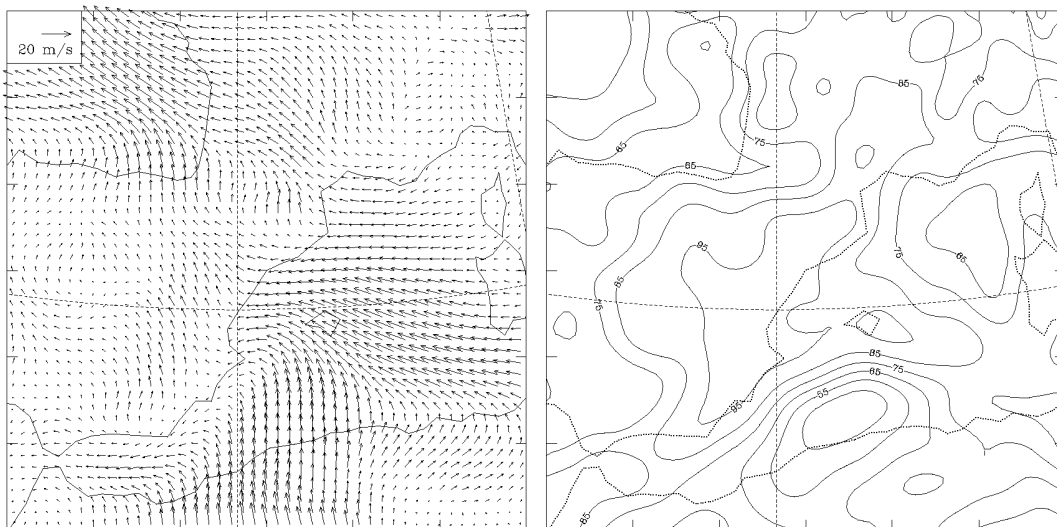


Figure 6.28: Effect of the interaction orography/evaporation on the total precipitation at the end of the simulation (06 UTC 11 October 1994) (contour interval is 20 mm starting at 10 mm, continuous line, and at -10 mm, dashed line).



(a) Wind field

(b) Relative humidity

Figure 6.29: (a) 1000 hPa wind field at the start of the simulation (00 UTC 10 October 1994). (b) 1000 hPa relative humidity (%) at the start of the simulation (00 UTC 10 October 1994).

then moved northeastwards along the Spanish coast, remaining stationary during several hours over south Catalonia.

The diagnostic study of the event at synoptic scale, using ECMWF data, reveals the presence over eastern Spain and the western Mediterranean of enough ingredients for the development and maintenance of convection able to produce heavy rain. Composite charts including quasigeostrophic upward forcing at 850 hPa, convergence of water vapour between 1000 and 850 hPa, and convective instability between 1000 and 500 hPa show that these ingredients overlapped over eastern Spain. The overlapping areas represent the zones where subsynoptic mechanisms may be more effective for the trigger of convective cells. The analysis of the available radiosonde data close to the area of interest show that the results obtained from the ECMWF data are quite representative of the actual environment. The radiosoundings also show that there was high humidity in all the troposphere, representing a favourable environment for the precipitation efficiency. The comparison between the radiosonde data from Palma (Balearic Islands) and Zaragoza (inland Spain) demonstrates that the air mass over the Mediterranean is representative of the environment in which the convection developed, and that it is clearly separated from the much more stable air mass of inland Spain.

Subsynoptic analyses based on Meteosat images and all the available surface and upper air data, demonstrate the strong influence of the orography on the pressure and wind distributions. In particular, the Atlas range develops a shallow low over the south of the western Mediterranean and the Pyrenees causes a pressure dipole with the mesohigh over Catalonia. Both pressure anomalies combine to focalize and intensify the low level moist flux towards the Spanish coast, where the orography provides lifting to the humid parcels. The interaction of the easterly flux with the outflow boundary of the Pyrenean mesohigh can explain the stationarity of the convection when it reached south Catalonia. A secondary weak trough identified on the 500 hPa maps, which translated between the trough and the ridge axes, could have assisted the low levels lifting mechanisms to trigger the convection.

The meteorological scenario of the event resembles, in many aspects, the scenario described by Maddox et al. (1979) as the “mesohigh event” for flash floods in USA. However, the mesolow and mesohigh that interact to develop stationary convection have, in our case, an orographic origin.

The performed numerical simulations have shown, once again, that a mesoscale model is able to capture reasonably well the spatial details of the precipitation field. However, quantitative precipitation forecast is worse, since the recorded maxima are underestimated [similar behaviour was obtained by Codina et al. (1997) with another numerical model (the MASS model)]. The predicted geopotential and temperature fields at low levels display a low pressure area over the Algerian coast, a pressure dipole about the Pyrenees, and a warm air tongue extending from Africa towards the Spanish coast. Such structures are supported by the subjective sub-synoptic analyses and have been associated with the important Atlas and Pyrenees orographic systems.

On the other hand, the investigation by means of numerical simulations of the effects by the orography and the evaporation from the sea has shown that:

a) The orography is the responsible for the development of the shallow low in the lee of the Atlas over the Algerian coast, as well as for the pressure dipole about the Pyrenees.

These structures, which are more noticeable when the upper levels flow is strong, lead to an intensification of the pressure gradient over the western Mediterranean and therefore to an enhancement of the easterly flux towards the Spanish coasts. In addition, the orography is also responsible for the warm air anomaly present at low levels over the south of the western Mediterranean. This warm air tongue and the easterly flux combine to reinforce the warm advection towards the Spanish coastal orography.

b) The evaporation from the sea does not produce, when orography is not present, any remarkable effect on the precipitation, geopotential and wind fields.

c) The combination orography/evaporation was the most decisive factor for the spatial distribution of rainfall in the Tarragona event. In particular, it is responsible for the coastal maxima located in northern Valencia (9 October) and Catalonia (10 October). For Catalonia and Piedmont events (chapter 5), the combined effect was not so relevant because the air mass advected towards the coastal areas was already charged of enough moisture. However, the present result illustrates the great importance that latent heat fluxes during the course of the simulation may have in other cases, and suggests that quantitative precipitation forecasts in the western Mediterranean area may be especially sensitive to sea surface temperature.

Chapter 7

CONCLUSIONS AND PERSPECTIVES

With this work, we try to contribute with new understanding to the context of Mediterranean Meteorology. We have focused our efforts (principally numerical modelling) on two important topics: the characteristic breeze circulation in the island of Mallorca and its effects on the pollutants released over the coast; and the problem of heavy precipitations in the western Mediterranean region, with more emphasis in Mediterranean Spain.

The results of chapter 3 show the ability of the mesoscale models to reproduce sea breeze circulations on small islands like Mallorca, where the orography is complex and becomes fundamental in the full structure of the circulation.

The general structure and diurnal cycle are well reproduced by the model and show general aspects developed by theoretical studies. The convergence zones are well located as well as the blocking action by the principal mountain range of Mallorca. Some small and new structures have appeared in the model results: a small and shallow cyclonic circulation in the centre and another one over the west of the island. These systems move from their genesis areas during the process of the decay of the sea breeze and become important in the remaining circulation. The available wind observations over Mallorca seem to contain some signs of these vortex, but they are not dense enough to effectively prove and describe these atmospheric structures and their evolution. The use of dense observational systems, operating for example during a month of July, would be highly valuable to investigate the small scale components embedded within the breeze circulation. They could be also very helpful to better describe the structure and evolution of the boundary layer during the breeze cycle. Both aspects are important mechanisms for the transport and mixing of pollutants.

Although the presented simulation of the full breeze, entirely produced by differential heating forcing, matches well with observations, it must be just considered as a first approximation due to the fact that the actual breeze can be enhanced, reduced or modified by the synoptic flux. Simulations with different synoptic fluxes would help to know their action on the main features of the breeze. However, the results presented in this work probably represent the best known, at the moment, about the breeze in the island of Mallorca, and can serve as a guide to potential users such as sailors, or help for others studies such as environmental applications.

In this sense, our numerical experiments designed to study the impact of extant and hypothetical coastal sources of pollutants represent a new effort in Mallorca. Our results could help to improve the present disposition of the few pollutant measurement sites, and to improve the design of a future sampling network for air quality control in Mallorca. At the same time, our work could be taken as a reference point to continue the discussion about the impact of future coastal power plants and industries on small islands.

With respect to the study developed in chapter 4, we think that regional models on daily rainfall realizations as that obtained for Mediterranean Spain could be taken into consideration for weather forecasting tasks in the region. Precipitation is a very complex variable, being the final result of a wide range of atmospheric scales and their interactions. For that reason, accurate rainfall forecasts can not be given directly by operational large-scale numerical weather prediction models. Rather, the forecaster has to use the model outputs in combination with regional conceptual models on rainfall distribution, which in the case of the western Mediterranean are intimately related with the topography. Undoubtedly, once we determine the fundamental synoptic (or sub-synoptic) circulation patterns leading to each of the pattern groups found in chapter 4 (this work is under development at present), new predictive elements will be available for the regional forecaster. The distinction we have made between total and torrential rainfalls may have particular sense when searching the governing atmospheric structures, since discriminant factors of the latter type of rainfalls could be obtained. Moreover, the synoptic climatology started in chapter 4 may contribute to assess the impact of future tendencies of the general circulation on the rainfall regimes and torrenciality in Mediterranean Spain.

The numerical study developed in chapters 5 and 6 marks a new effort to address the feasibility of operational mesoscale modeling for flash flood situations, notably in the western Mediterranean region. The obtained results appear to validate our basic hypothesis. That is, it appears that the combination of the synoptic-scale structures associated with the region's heavy rainfall events and the strong topographic influences combine to provide an opportunity for improved forecasting through the use of mesoscale model simulations. If operational forecasters had the model results of chapters 5 and 6 available to them in real-time, we believe they would have found this to be useful information in making their forecasts. However, this study by itself does not constitute a definitive answer. That is, after only three case studies, we are not prepared to make an unqualified recommendation for the implementation of operational mesoscale models in the region. There are several issues yet to be addressed before it would be appropriate to make such a recommendation.

Clearly, it is necessary to validate more extensively the notion that most heavy rainfalls in the region share similar synoptic-scale structures (characterized by a strong synoptic-scale trough or closed cyclone at upper levels to the west of the threat area, and warm, moist advection at low levels impinging over the topography). It is unrealistic to expect that all heavy precipitation events fit this pattern, but it would be valuable to have some quantitative idea of the frequency at which such events do arise in broadly similar synoptic-scale patterns. In order to make good use of mesoscale model guidance, then, a forecaster needs to know in what circumstances the model is likely to be successful and when it is likely to fail. For our three cases, the precipitation guidance was quite good,

since these cases were dominated by the topographic modulation. If, on the other hand, for successful simulations there are important mesoscale details that must be specified accurately in the initial conditions, such cases are less likely to be well-simulated (Stensrud and Fritsch 1994). This fact was shown in Romero et al. (1998a) for one case of heavy precipitation in eastern Spain (Menorca case of the ANOMALIA project). That event was produced by a mesoscale convective system (MCS) triggered over the open seas of the western Mediterranean, but the SALSA model failed to develop the system. However, the convective storm environment was apparently well-simulated; it is possible that the simulation only lacked mesoscale initial data (such as preexisting convergence lines) to capture the development of the convection. Would an operational model produce similar results? If there was a way to introduce the mesoscale details artificially (e.g., by manual intervention during the initialization; see Spencer and Stensrud 1998), would the model then produce useful precipitation guidance? These questions remain unanswered.

Our study began with the a priori knowledge that each case did, in fact, involve a heavy rainfall event. A forecaster does not have such knowledge, of course. This leads to another important unanswered question. How often would an operational mesoscale model be successful in recognizing situations where the synoptic pattern apparently fits that of a heavy rainfall event but the event does not happen? Another set of simulations is needed with events that are at least superficially similar to our heavy rainfall cases but wherein no significant rainfalls occur. Large amplitude gravity waves, but with no appreciable precipitation, have been observed in the western Mediterranean region in similar synoptic patterns (Ramis and Jansà 1983; Monserrat et al. 1991). This problem (the forecast of a non-event in an apparently threatening synoptic situation) can be very challenging to an operational forecaster (see Stensrud and Maddox 1988).

The satellite images (Figures 5.3, 5.19, and 6.3) and the numerical simulations show that convection was present (if not dominant) in all three of our cases. The importance of convection to the region's heavy precipitation meteorology is well-known (García-Dana et al. 1982). Given the dominant role of deep moist convection, any implementation of a mesoscale model must include careful consideration of how to treat deep convection in the simulations. The parameterizations used in this study (i.e., those of Emanuel 1991, and Kain and Fritsch 1990) seem to have done reasonably well, with the best performance apparently obtained with the second scheme. Nevertheless, the successful representation of cumulus convection is far from being a closed book; the superiority of any convective parameterization or even the explicit calculation of convective processes depends on such issues as model resolution, the region of application, peculiarities associated with particular events, and computational expense. More simulations of cases using different methods for accounting for convection are needed to evaluate which approach is most appropriate for the western Mediterranean region. The evaluation, moreover, should not be limited to the success of the precipitation prediction alone. Various low-level wind flows that are associated with the region's topography (Autan, Cierzo, Tramontana, etc.; see Bougeault et al. 1990) are an important issue in the region's weather and a successful mesoscale model needs to provide guidance about those processes, as well.

In our cases, it appears that some simple diagnostic outputs can be a valuable supplement to precipitation forecasts. As shown clearly from our factor separation experiments, the evaluation of upslope flow and consideration of sea surface water vapor flux can be

quite pertinent for the region. Orographically induced mesoscale pressure systems, notably by the Atlas and Pyrenees, have been shown also to be very important. These circulations can produce or enhance surface flows leading directly towards specific zones where convection focuses, and/or develop convergence at low levels over the sea where convection can trigger. Diagnostics relevant to these factors are both easy to do and likely to be informative to forecasters.

The QPF (quantitative precipitation forecast) capability of the mesoscale model we used is certainly encouraging but the magnitudes of the simulated precipitation tend to be underestimates, especially with respect to the highly localized peak amounts in convective situations (Catalonia and Tarragona events). In fact, it is these peak values that typically are responsible for many of the flash floods that produce significant damage and numerous casualties in the region. The attained progress in QPFs has been slow compared with the improvement experienced in numerical predictions of large-scale circulation patterns (see Olson et al. 1995). Obviously, the model resolution is at least partly responsible for this. The use of non-hydrostatic high-resolution models in regions of complex orography represents a promising line of research. However, we believe there is still reason to explore the possibility of improving this facet of meso- β scale models. Riosalido (1990) has shown that most of the flash flood events in the western Mediterranean region can be attributed to quasistationary MCSs. Within such systems, individual convective storm cells may move rapidly, but the area where storms attain maturity and produce heavy rain remains nearly stationary. It appears that slow rainfall system movement occurs when system movement due to propagation is opposed to cell movement. That is, new convective developments (typically forced by the topography, or occurring along outflow boundaries produced by existing and previous convective cells) occur preferentially in a confined area. Any efforts directed to the identification of the mechanisms controlling the development, movement and precipitation efficiency of the MCSs has the potential to improve QPF (Spencer and Stensrud 1998).

APPENDIX

List of Symbols

B	vertical scale factor given by $B = -\frac{gP}{\pi R_v T \sigma'}$
C_i	concentration of the chemical substance
C_p	specific heat at constant pressure
C_ϵ	coefficient for the TKE dissipation term
$D_{\pi u}, D_{\pi v}, D_S, D_W, D_{\pi q_r}, D_{\pi N_r}, D_{\pi e}, D_{\pi C_i}$	horizontal diffusion terms
e	turbulent kinetic energy
e_s	saturation vapor pressure
f	Coriolis parameter
$F_{\pi u}, F_{\pi v}, F_S, F_W, F_{\pi q_r}, F_{\pi N_r}, F_{\pi e}, F_{\pi C_i}$	turbulent mixing terms
g	acceleration of gravity
H	entropy
k	Von Karman constant
$K_m, K_\theta, K_e, K_{ex}$	exchange coefficients
l_k	mixing length scale
l_ϵ	dissipation length scale
L	Monin-Obukhov length
L_v	latent heat
m	map scale factor
N_r	number of raindrops concentration
P	pressure
P_0	reference pressure = 1000 hPa
P_s	surface pressure
P_t	pressure at the upper boundary
\hat{P}	$\left(\frac{P}{P_0}\right)^{R_v/C_p}$
q_{cw}	cloud water mixing ratio
q_r	rainwater mixing ratio
q_v	water vapor mixing ratio
q_{vs}	saturation water vapor mixing ratio
r_a	atmospheric resistance
r_c	canopy/vegetation resistance
r_d	deposition layer resistance
r_{na}	nonatmospheric resistance
R_L	incoming longwave radiation at the surface
R_S	incoming solar radiation at the surface
R_v	universal gas constant
S	entropy variable defined by $S = \pi H$
$S_S, S_W, S_{\pi q_r}, S_{\pi N_r}, S_{\pi C_i}$	source-sink terms
t	time

T	temperature
T_0	reference temperature = 273.16 K
T_s	saturation temperature
T^*	virtual temperature
u	wind component along the x-coordinate
u_*	friction velocity
v	wind component along the y-coordinate
v_d	dry deposition velocity
W	moisture variable defined by $W = \pi(q_v + q_{cw})$
x	coordinate in the west-east direction
y	coordinate in the south-north direction
z_0	roughness length
z_s	reference height
Δt	time step
Δx	horizontal grid length
γ_{cg}	temperature countergradient
π	$(P_s - P_t)$
σ	pressure coordinate defined by $\sigma = (P - P_t)/\pi$
σ'	$d\sigma/d\nu$
ν	vertical coordinate related with σ by $\sigma = (4\nu - \nu^4)/3$
$\dot{\nu}$	vertical velocity
ϕ	geopotential
ρ	density of air
ρ_l	density of liquid water
θ	potential temperature
θ_v	virtual potential temperature. $\theta_v = \theta(1 + 0.61q_v)$

REFERENCES

Alonso, S., A. Portela, and C. Ramis, 1994: First considerations on the structure and development of the Iberian thermal low. *Ann. Geophys.*, **12**, 457-468.

Alpert, P., M. Tsidulko, and U. Stein, 1995: Can sensitivity studies yield absolute comparisons for the effects of several processes?. *J. Atmos. Sci.*, **52**, 597-601.

Anderberg, M. R., 1973: *Cluster analysis for applications*. Academic Press, 359 pp.

Anthes, R. A., and T. T. Warner, 1974: *Prediction of mesoscale flows over complex terrain*. ECOM Technical Report No. 5532, White Sands Missile Range, New Mexico, 88002.

Arakawa, A., and W. H. Schubert, 1974: Interaction of a cumulus cloud ensemble with the large-scale environment. Part I. *J. Atmos. Sci.*, **31**, 674-701.

Atkinson, B. W., 1981: *Mesoscale atmospheric circulations*. Academic Press, New York, 495 pp.

Baker, C. B., J. K. Eischeid, T. R. Karl, and H. F. Diaz, 1995: The quality control of long-term climatological data using objective data analysis. /linebreak (available from <http://www.ncdc.noaa.gov/gcps/papers/qc1/qc.html>).

Barnes, S. L., 1985: Omega Diagnosis as a Supplement to LFM/MOS Guidance in Weakly Forced Convective Situations. *Mon. Wea. Rev.*, **113**, 2122-2141.

Barnes, S. L., and C. W. Newton, 1986: *Thunderstorms in the Synoptic Setting. Thunderstorm. Morphology and Dynamics*. 2nd Edit, E. Kessler Ed., Univ. Oklahoma Press, 75-112.

Bärring, L., 1987: Spatial patterns of daily rainfall in central Kenya: Application of principal component analysis, common factor analysis and spatial correlation. *Int. J. Climatol.*, **7**, 267-290.

Beard, K. V., and H. R. Pruppacher, 1969: A determination of the terminal velocity and drag of small water drops by means of a wind tunnel. *J. Atmos. Sci.*, **26**, 1066-1072.

Benjamin, S. G., and T. N. Carlson, 1986: Some effects of surface heating and topography on the regional severe storm environment. Part I: Three-dimensional simulations. *Mon. Wea. Rev.*, **114**, 307-329.

Berry, E. X., 1967: Cloud droplet growth by collection. *J. Atmos. Sci.*, **24**, 688-701.

Berry, E. X., and R. L. Reinhardt, 1973: *Modeling of condensation and collection within clouds*. D.R.I. Phys. Sci. Pub. No.16, University of Nevada.

Berry, E. X., and M. P. Pranger, 1974: Equations for calculating the terminal velocities of water drops. *J. Appl. Meteor.*, **13**, 108-113.

Bessemoulin, P., P. Bougeault, A. Genovés, A. Jansà, and D. Puech, 1993: Mountain pressure drag during PYREX. *Beitr. Phys. Atmosph.*, **66**, 305-325.

Bhumralkar, C. M., 1975: Numerical experiments on the computation of ground surface temperature in an atmospheric general circulation model. *J. Appl. Meteor.*, **14**, 1246-1258.

Blackadar, A. K., 1976: *Modeling the nocturnal boundary layer*. Proceedings of the Third Symposium on Atmospheric Turbulence, Diffusion and Air Quality, American Meteorological Society, Boston, 46-49.

Bonell, M., and G. N. Sumner, 1992: Autumn-winter daily precipitation areas in Wales, 1982/83 to 1986/87. *Int. J. Climatol.*, **12**, 77-102.

Bougeault, P., and P. Lacarrère, 1989: Parameterization of orographic induced turbulence in a mesobeta scale model. *Mon. Wea. Rev.*, **117**, 1872-1890.

Bougeault, P., A. Jansà, B. Benech, B. Carissimo, J. Pelon, and E. Richard, 1990: Momentum budget over the Pyrenees: the PYREX experiment. *Bull. Amer. Meteor. Soc.*, **71**, 806-818.

Brooks, H. E., C. A. Doswell III, and J. Cooper, 1994: On the environments of tornadic and nontornadic environments. *Wea. Forecasting*, **9**, 606-618.

Businger, J. A., J. C. Wyngaard, Y. Izumi, and E. F. Bradley, 1971: Flux-profile relationship in the atmospheric surface layer. *J. Atmos. Sci.*, **28**, 181-189.

Buzzi, A., and N. Tartaglione, 1996: Some aspects of the Piedmont flood: Frontal splitting and role of humid processes. *MAP Newsletter*, **5**, 38-39.

Cacciamani, C., S. Tibaldi, and S. Nanni, 1994: Mesoclimatology of winter temperature and precipitation in the Po Valley of northern Italy. *Int. J. Climatol.*, **14**, 777-814.

Cattell, R. B., 1966. The scree test for the number of PCs. *Mult. Behav. Res.*, **1**, 245-276.

Chaumerliac, N., E. Richard, J. P. Pinty, and E. C. Nickerson, 1987: Sulfur scavenging in a mesoscale model with quasi-spectral microphysics: Two-dimensional results for continental and maritime clouds. *J. Geophys. Res.*, **92**, 3114-3126.

Chaumerliac, N., R. Rosset, M. Renard, and E. C. Nickerson, 1992: The transport and redistribution of atmospheric gases in regions of frontal rain. *J. Atmos. Chemistry*, **14**, 43-51.

Clapp, R., and G. Hornberger, 1978: Empirical equations for some soil hydraulic properties. *Water Resour. Res.*, **14**, 601-604.

Codina, B., M. Aran, S. Young, and A. Redao, 1997: Prediction of a mesoscale convective system over Catalonia (northeastern Spain) with a nested numerical model. *Meteorol. Atmos. Phys.*, **62**, 9-22.

Conrad, V., and L. W. Pollack, 1962: *Methods in climatology*. Harvard University Press, Cambridge-Massachusetts.

Creutin, J. D., and C. Obled, 1982: Objective analyses and mapping techniques for rainfall fields, an objective comparison. *Water Resources Research*, **18**, 413-431.

Davies, H. C., 1976: A lateral boundary formulation for multi-level prediction models. *Quart. J. R. Meteor. Soc.*, **102**, 405-418.

Davies-Jones, R. D., D. Burgess, and M. Foster, 1990: *Test of helicity as a tornado forecast parameter*. Preprints, 16th Conf. on Severe Local Storms. Kananaskis Park, Alberta, Canada, Amer. Meteor. Soc., 588-592.

Davis, C. G., S. S. Bunker, and J. P. Mutschlecner, 1984: Atmospheric transport models for complex terrain. *J. Climate Appl. Meteor.*, **23**, 235-238.

Deardorff, J. W., 1972: Theoretical expressions for the counter gradient vertical heat flux. *J. Geophys. Res.*, **30**, 5900-5904.

Deardorff, J. W., 1978: Efficient prediction of ground surface temperature and moisture, with inclusion of a layer of vegetation. *J. Geophys. Res.*, **83**, 1889-1903.

De Rivas, E. K., 1972: On the use of nonuniform grids in finite difference equations. *J. Comput. Phys.*, **10**, 202-210.

De Ruffray, P., H. Brisse, and G. Granjean, 1981: Un procédé d'estimation des données manquantes fondé sur les corrélations climatiques entre postes voisins. *La Météorologie*, **24**, 47-60.

Doswell, C. A., 1987: The distinction between large-scale and mesoscale contribution to severe convection: A case study example. *Wea. Forecasting*, **2**, 3-16.

Doswell, C. A. III, H. E. Brooks, and R. A. Maddox, 1996: Flash flood forecasting: An ingredients-based methodology. *Wea. Forecasting*, **11**, 560-581.

Doswell, C. A. III, C. Ramis, R. Romero, and S. Alonso, 1998: A diagnostic study of three heavy precipitation episodes in the western Mediterranean region. *Wea. Forecasting*, (in press).

Dufour, L., and J. Van Mieghem, 1975: *Thermodynamique de l'atmosphere*. Institut Royal Meteorologique de Belgique, Brussels.

Emanuel, K. A., 1983: On assessing local conditional symmetric instability from atmospheric soundings. *Mon. Wea. Rev.*, **111**, 2016-2033.

Emanuel, K. A., 1991: A scheme for representing cumulus convection in large-scale models. *J. Atmos. Sci.*, **48**, 2313-2335.

Endlich, R. M., 1967: An iterative method for altering the kinematic properties of wind fields. *J. Appl. Meteorol.*, **6**, 837-844.

Everitt, B., 1979: Unsolved problems in cluster analysis. *Biometrics*, **35**, 169-181.

Farrel, R. J., and T. N. Carlson, 1989: Evidence for the role of the Lid and Under-running in an outbreak of tornadic thunderstorms. *Mon. Wea. Rev.*, **117**, 857-871.

Fernández, C., M. A. Gaertner, C. Gallardo, and M. Castro, 1995: Simulation of a long-lived meso- β scale convective system over the mediterranean coast of Spain. Part I: Numerical predictability. *Meteorol. Atmos. Phys.*, **56**, 157-179.

Ferretti, R., G. Visconti, and F. Giorgi, 1993: Chemistry and transport of sulphur compounds from large oil fires studied with a 2D mesoscale model. *Ann. Geophys.*, **11**, 68-77.

Font, I., 1983: *Climatología de España y Portugal*. Instituto Nacional de Meteorología, Apartado 285, 28071, Madrid, 296 pp.

Frank, W. M., 1983: The cumulus parameterization problem. *Mon. Wea. Rev.*, **111**, 1859-1871.

Fritsch, J. M., C. F. Chappell, and L. R. Hoxit, 1976: The use of large-scale budgets for convective parameterization. *Mon. Wea. Rev.*, **104**, 1408-1418.

Fritsch, J. M., and C. F. Chappell, 1980: Numerical prediction of convectively driven mesoscale pressure systems. Part I: Convective parameterization. *J. Atmos. Sci.*, **37**, 1722-1733.

Gandin, L. S. 1963: *Objective analysis of meteorological fields*. Gidrometeorologicheskoe Izdatel'stvo, Leningrado, 242 pp.

García-Dana, F., R. Font, and A. Rivera, 1982: *Meteorological situation during the heavy rain event in the eastern zone of Spain during October-82*. Instituto Nacional de Meteorología, Madrid.

Georgelin, M., E. Richard, M. Petitdidier, and A. Druilhet, 1994: Impact of subgrid-scale orography parameterization on the simulation of orographic flows. *Mon. Wea. Rev.*, **122**, 1509-1522.

Gifford, F., 1968: An outline of theories of diffusion in the lower layers of the atmosphere. *Meteorology and Atomic Energy*. H. Slade Ed., 65-116.

Gong, X., and M. B. Richman, 1995: On the application of cluster analysis to growing season precipitation data in North America east of the Rockies. *J. Climate.*, **8**, 897-931.

Guijarro, J. A., 1986: *Contribución a la bioclimatología de Baleares*. Ph. D. Thesis., Univ. de les Illes Balears, Palma, 301 pp.

Gunn, R., and G. D. Kinzer, 1949: The terminal velocity of fall for water droplets in stagnant air. *J. Meteor.*, **6**, 243-248.

Hakim, G. J., and L. W. Uccellini, 1992: Diagnosing coupled Jet Streak circulations for a northern plains snow band from the operational nested-grid model. *Wea. Forecasting*, **7**, 26-48.

Hearn, D., 1989: ISC modelling of sulfur dioxide concentrations in the Latrobe valley. *Man and his Ecosystem*. L. J. Brassler and W. C. Mulder Ed., Elsevier Sci. Publ., 269-273.

Hewson, E. W., and L. E. Olsson, 1967: Lake effects on air pollution dispersion. *J. Air Poll. Cont. Assoc.*, **17**, 757-761.

Holton, J. R., 1993: *An Introduction to Dynamic Meteorology*. Third Edition, Academic Press, 511 pp.

Hoskins, B. J., and M. A. Pedder, 1980: The diagnosis of middle latitude synoptic development. *Q. J. R. Meteorol. Soc.*, **106**, 707-719.

Jansà, J. M., and E. Jaume, 1946: The sea breeze regime in the Mallorca island. *Rev. de Geofísica*, **19**, 304-328.

Jansà, A., C. Ramis, and S. Alonso, 1986: The Mediterranean thunderstorm on 15 November 1985: triggering mechanism. *Rev. Meteorol.*, **8**, 7-19.

Jolliffe, I. T., 1986: *Principal component analysis*. Springer-Verlag, New York, 271 pp.

Kain, J. S., and J. M. Fritsch, 1990: A one-dimensional entraining/detraining plume model and its application in convective parameterization. *J. Atmos. Sci.*, **47**, 2784-2802.

Kidson, J. W., 1994: Relationship of New Zealand daily and monthly weather patterns to synoptic weather types. *Int. J. Climatol.*, **14**, 723-737.

King, D. S., and S. S. Bunker, 1984: Application of atmospheric transport models for complex terrain. *J. Climate Appl. Meteor.*, **23**, 239-246.

Kreitzberg, C. W., and D. J. Perkey, 1976: Release of potential instability. Part I: A sequential plume model within a hydrostatic primitive equation model. *J. Atmos. Sci.*, **33**, 456-475.

Lionetti, M., 1996: The Italian floods of 4-6 November 1994. *Weather*, **51**, 18-27.

Llasat, M. C., 1987: *Heavy rain events in Catalonia: genesis, evolution and mechanism*. Ph. D. Thesis., Univ. of Barcelona Press, Barcelona, 250 pp.

Louis, J. F., 1979: A parametric model of vertical eddy fluxes in the atmosphere. *Bound. Layer Meteor.*, **17**, 187-202.

Lyons, W. A., 1975: *Turbulent diffusion and pollutant transport in shoreline environments*. In D. Haugen Ed., *Lectures on Air Pollution and Environmental Impact Analyses*, Boston: American Meteorological Society.

Maddox, R. A., C. F. Chappell, and L. R. Hoxit, 1979: Synoptic and meso- α scale aspects of flash flood events. *Bull. Amer. Meteor. Soc.*, **60**, 115-123.

Maddox, R., 1980: Mesoscale convective complexes. *Bull. Amer. Meteor. Soc.*, **61**, 1374-1387.

Mahfouf, J. F., E. Richard, and P. Mascart, 1987a: The influence of soil and vegetation on the development of mesoscale circulations. *J. Climate Appl. Meteor.*, **26**, 1483-1495.

Mahfouf, J. F., E. Richard, P. Mascart, E. C. Nickerson, and R. Rosset, 1987b: A comparative study of various parameterizations of the planetary boundary layer in a numerical mesoscale model. *J. Climate Appl. Meteor.*, **26**, 1671-1695.

Mahrer, Y., and R. A. Pielke, 1977: The effects of topography on the sea and land breezes in a two-dimensional numerical model. *Mon. Wea. Rev.*, **105**, 1151-1162.

Markowitz, A. H., 1976: Raindrop size distribution expressions. *J. Appl. Meteor.*, **15**, 1029-1031.

McCumber, M. C., 1980: *A numerical simulation of the influence of heat and moisture*

fluxes upon mesoscale circulations. Ph. D. dissertation, University of Virginia, 255 pp.

McCumber, M. C., and R. A. Pielke, 1981: Simulation of the effects of surface fluxes of heat and moisture in a mesoscale numerical model: 1. Soil Layer. *J. Geophys. Res.*, **86**, 9929-9938.

McNulty, R. P., 1995: Severe and convective weather: a central region forecasting challenge. *Wea. Forecasting*, **10**, 187-202.

McVehil, G. E., 1989: Model estimates of provincial scale atmospheric sulphur dioxide (SO₂) and oxides of nitrogen (NO_x) in Alberta. *Acidic deposition: Sulphur and nitrogen oxides*. A. H. Legge and S. U. Krupa Ed., CRC Press, Inc., 433-475.

Meteorological Office, 1962: *Weather in the Mediterranean*. Air Ministry, Vol. 1, 362 pp.

Miró-Granada, J., 1974: Les crues catastrophiques sur le Méditerranée occidentale. *AMS-AISH Public.*, **12**, 119-132.

Monserrat, S., C. Ramis, and J. A. Thorpe, 1991: Large amplitude pressure oscillations in the western Mediterranean. *Geoph. Res. Letter.*, **18**, N2, 183-186.

Murray, F. W., 1967: On the computation of saturation vapor pressure. *J. Appl. Meteor.*, **6**, 203-204.

Nickerson, E. C., and E. L. Magaziner, 1976: *A three-dimensional simulation of winds and non-precipitating orographic clouds over Hawaii*. NOAA Technical Report ERL 377-APCL 39, 35 pp.

Nickerson, E. C., 1979: On the numerical simulation of airflow and clouds over mountainous terrain. *Beitr. Phys. Atmos.*, **52**, 161-177.

Nickerson, E. C., E. Richard, R. Rosset, and D. R. Smith, 1986: The numerical simulation of clouds, rain and airflow over the Vosges and Black Forest mountain: a meso- β model with parameterized microphysics. *Mon. Wea. Rev.*, **114**, 398-414.

Olson, D. A., N. W. Junker, and B. Korty, 1995: Evaluation of 33 years of quantitative precipitation forecasting at the NMC. *Wea. and Forecasting*, **10**, 498-511.

Paccagnella, T., S. Tibaldi, R. Buizza, and S. Scoccianti, 1992: High-resolution numerical modelling of convective precipitation over Northern Italy. *Meteorol. Atmos. Phys.*, **50**, 143-163.

Pasquill, F., 1974: *Atmospheric Diffusion*. 2nd ed., Wiley & Sons, 429 pp.

Paulhus, J. L. H., and M. A. Kohler, 1952: Interpolation of missing precipitation records. *Mon. Wea. Rev.*, **80**, 129-133.

Pedder, M. A., 1989: Limited area kinematic analysis by a multivariate statistical interpolation method. *Mon. Wea. Rev.*, **117**, 1695-1708.

Petterssen, S., 1956: *Weather analysis and forecasting (vol I)*. McGraw-Hill Company, New York, 428 pp.

Piedelievre, J. P., L. Musson-Genon, and F. Bompay, 1990: MEDIA-An eulerian model of atmospheric dispersion: First validation on the Chernobyl release. *J. Appl. Meteor.*, **29**, 1205-1220.

Pielke, R. A., 1984: *Mesoscale meteorological modeling*. Academic Press, Orlando, 612 pp.

Pinty, J. P., 1984: *Une méthode variationnelle d'ajustement des champs de masse et de vent*. Note 72 de l'I.O.P.G., Université de Clermont II.

Pinty, J. P., P. Mascart, E. Richard, and R. Rosset, 1989: An investigation of mesoscale flows induced by vegetation inhomogeneities using an evapotranspiration model calibrated against HAPEX-MOBILHY data. *J. Appl. Meteor.*, **28**, 976-992.

Preisendorfer, R. W., 1988: *Principal component analysis in meteorology and oceanography*, Elsevier, New York, 425 pp.

Ramis, C., 1976: *Climatology of the upper air over Mallorca*. Univ. de Barcelona, 66 pp.

Ramis, C., and A. Jansà, 1983: Meteorological conditions simultaneous to large sea level oscillations in the western Mediterranean. *Rev. de Geofísica*, **39**, 35-42.

Ramis, C., A. Jansà, S. Alonso, and M. A. Heredia, 1986: Convection over the western Mediterranean. Synoptic study and remote observation. *Rev. de Meteorología.*, **7**, 59-82.

Ramis, C., and S. Alonso, 1988: Sea breeze convergence line in Mallorca. A satellite observation. *Weather*, **43**, 288-293.

Ramis, C., A. Jansà, and S. Alonso, 1990: Sea breeze in Mallorca. A numerical study. *Meteorol. Atmos. Phys.*, **42**, 249-258.

Ramis, C., M. C. Llasat, A. Genovés, and A. Jansà, 1994: The October-1987 floods in Catalonia: Synoptic and Mesoscale Mechanisms. *Meteor. Applicat.*, **1**, 337-350.

Ramis, C., S. Alonso, and M. C. Llasat, 1995: A comparative study of two cases of

heavy rain in Catalonia. *Surv. in Geophys.*, **16**, 141-161.

Ramis, C., and R. Romero, 1995: A first numerical simulation of the development and structure of the sea breeze in the island of Mallorca. *Ann. Geophys.*, **13**, 981-994.

Ramis, C., 1995: Las observaciones de la atmósfera libre en Mallorca: una breve historia y algunos resultados. *Revista de Ciència*, **17**, 41-58.

Ramis, R., R. Romero, V. Homar, S. Alonso, and M. Alarcón, 1998: Diagnosis and numerical simulation of a torrential precipitation event in Catalonia (Spain). *Meteorol. Atmos. Phys.*, (submitted).

Raymond, D. J., and A. M. Blyth, 1986: A stochastic model for nonprecipitating cumulus clouds. *J. Atmos. Sci.*, **43**, 2708-2718.

Reiter, E. R., 1975: *Handbook for forecasters in the Mediterranean*, Naval Postgraduate School, Monterey, California.

Richard, E., J. P. Pinty, and N. Chaumerliac, 1985: *Simulations d'ondes de montagne hydrostatiques bidimensionnelles*. Note I.O.P.G. number 82, 41 pp.

Richard, E., N. Chaumerliac, and J. F. Mahfouf, 1986: Numerical simulation of orographic enhancement of rain with a mesoscale model. *J. Climate Appl. Meteor.*, **26**, 661-669.

Richard, E., P. Mascart, and E. C. Nickerson, 1989: The role of surface friction in downslope windstorms. *J. Appl. Meteor.*, **28**, 241-251.

Richmann, M. B., 1986: Rotation of principal components. *J. Climatol.*, **6**, 293-335.

Riosalido, R., 1990: *Characterization of mesoscale convective systems by satellite pictures during PREVIMET MEDITERRANEO-89*. Segundo Simposio Nacional de Predicción. Instituto Nacional de Meteorología, Apartado 285, 28071, Madrid, 135-148.

Robinson, G. D., 1967: Some current projects for global meteorological observation and experiment. *Quart. J. R. Meteor. Soc.*, **93**, 409-418.

Robinson, M. K., R. A. Bauer, and E. H. Schroeder, 1979: *Atlas of North Atlantic - Indian Ocean monthly mean temperatures and mean salinities of the surface layer*. Naval oceanographic office reference publication 18, Department of the Navy, Washington, D.C. 20373.

Rockwood, A. A., and R. A. Maddox, 1988: Mesoscale and synoptic interactions leading to intense convection: the case of 7 June 1982. *Wea. Forecasting*, **3**, 51-68.

Romero, R., S. Alonso, E. C. Nickerson, and C. Ramis, 1995: The influence of vegetation on the development and structure of mountain waves. *J. Appl. Meteor.*, **34**, 2230-2242.

Romero, R., and C. Ramis, 1996: A numerical study of the transport and diffusion of coastal pollutants during the breeze cycle in the island of Mallorca. *Ann. Geophys.*, **14**, 351-363.

Romero, R., C. Ramis, and S. Alonso, 1997: Numerical simulation of an extreme rainfall event in Catalonia: Role of orography and evaporation from the sea. *Quart. J. Roy. Meteor. Soc.*, **123**, 537-559.

Romero, R., C. Ramis, S. Alonso, C. A. Doswell III, and Stensrud, D. J., 1998a: Mesoscale model simulations of three heavy precipitation events in the western Mediterranean region. *Mon. Wea. Rev.*, (in press).

Romero, R., J. A. Guijarro, C. Ramis, and S. Alonso, 1998b: A 30 year (1964-1993) daily rainfall data base for the Spanish mediterranean regions: First exploratory study., *Int. J. Climatol.*, (in press).

Romero, R., C. Ramis, and J. A. Guijarro, 1998c: Daily rainfall patterns in the Spanish mediterranean area: An objective classification. *Int. J. Climatol.*, (in press).

Romero, R., C. Ramis, and S. Alonso, 1998d: Performance of two cumulus convection parameterizations for two heavy precipitation events in the western Mediterranean. *Meteorol. Atmos. Phys.*, (in press).

Schlesinger, R. F., L. W. Uccellini, and D. R. Johnson, 1983: The effects of the Asselin time filter on numerical solutions to the linearized shallow-water wave equations. *Mon. Wea. Rev.*, **111**, 455-467.

Schofield, R. A., and J. F. W. Purdom, 1986: The use of satellite data for mesoscale analyses and forecasting applications. *In Mesoscale Meteorology and Forecasting*. P. S. Ray Ed., American Meteorological Society, Boston, 118-150.

Sehmel, G. A., 1980: Particle and gas dry deposition: A review. *Atmos. Environ.*, **14**, 983-1011.

Shafir, U., and M. Neiburger, 1963: Collision efficiencies of two spheres falling in a viscous medium. *J. Geophys. Res.*, **68**, 4114-4148.

Shapiro, R., 1970: Smoothing, filtering and boundary effects. *Rev. Geophys. Space Phys.*, **8**, 359-387.

Shearman, R. J., 1975: Computer quality control of daily and monthly rainfall data.

The Met. Mag., **104**, 102-108.

Slinn, W. G. N., L. Hasse, B. B. Hicks, A. W. Hogan, D. Lal, P. S. Liss, K. O. Munnich, G. A. Sehmel, and O. Vittori, 1978: Some aspects of the transfer of atmospheric trace constituents past the air-sea interface. *Atmos. Environ.*, **12**, 2055-2087.

Smith, R. B., 1989: Hydrostatic airflow over mountains. *Advances in Geophysics*. **31**, 1-41.

Spackman, E. A., and F. Singleton, 1982: Recent developments in the quality control of climatological data. *The Met. Mag.*, **111**, 301-311.

Spencer, P. L., and D. J. Stensrud, 1998: Simulating flash flood events: Importance of the sub-grid representation of convection. *Mon. Wea. Rev.*, (submitted).

STATISTICA, 1994. *STATISTICA for Windows (Volume III): Statistics II*. StatSoft Inc., Tulsa OK.

Stein, U., and P. Alpert, 1993: Factor separation in numerical simulations. *J. Atm. Sci.*, **50**, 2107-2115.

Stensrud, D. J., and R. A. Maddox, 1988: Opposing mesoscale circulations: A case study. *Wea. and Forecasting*, **3**, 189-204.

Stensrud, D. J., and J. M. Fritsch, 1994: Mesoscale convective systems in weakly forced large-scale environments. Part III: Numerical simulations and implications for operational forecasting. *Mon. Wea. Rev.*, **122**, 2084-2104.

Sumner, G., C. Ramis, and J. A. Guijarro, 1993: The spatial organization of daily rainfall over Mallorca. *Int. J. Climatol.*, **13**, 89-109.

Sumner, G., J. A. Guijarro, and C. Ramis, 1995a: The impact of surface circulations on the daily rainfall over Mallorca. *Int. J. Climatol.*, **15**, 673-696.

Sumner, G., C. Ramis, and J. A. Guijarro, 1995b: Daily rainfall domains in Mallorca, Spain (1986-1989). *Theor. Appl. Climatol.*, **51**, 199-221.

Sumner, G., 1996: Daily precipitation patterns over Wales: towards a detailed precipitation climatology. *Trans. Inst. Br. Geogr.*, **21**, 157-176.

Therry, G., and P. Lacarrère, 1983: Improving the eddy-kinetic energy model for planetary boundary layer description. *Bound. Layer Meteor.*, **25**, 63-88.

Tudurí, E. and Ramis, C. 1997: The environments of significant convective events in the western Mediterranean. *Wea. and Forecasting*, **12**, 294-306.

Uccellini, L.W., 1975: A case study of apparent gravity waves initiation of severe convection storms. *Mon. Wea. Rev.*, **103**, 497-513.

Uccellini, L. W., and D. R. Johnson, 1979: The coupling of upper and lower Jet Streaks and implications for the development of severe convective storms. *Mon. Wea. Rev.*, **107**, 682-703.

Uliasz, M., 1993: The atmospheric mesoscale dispersion modeling system. *J. Appl. Meteor.*, **32**, 139-149.

Vergeiner, I., R. Steinacker, and E. Dreiseitl, 1982: The south foehn case 4/5 May 1982. *Alpex Preliminary Scientific Results*. J. P. Kuettner Ed., GARP-ALPEX n 7, WMO, 143-154.

Ward, J. H., 1963: Hierarchical grouping to optimize an objective function. *J. Amer. Stat. Assoc.*, **58**, 236-244.

Warner, T. T., R. A. Anthes, and A. L. McNab, 1978: Numerical simulations with a three-dimensional mesoscale model. *Mon. Wea. Rev.*, **106**, 1079-1099.

Wesely, M. L., and B. B. Hicks, 1977: Some factors that affect deposition rates of SO₂ and similar gases on vegetation. *J. APCA*, **27**, 1110-1116.

White, D., M. Richman, and B. Yarnal, 1991: Climate regionalization and rotation of principal components. *Int. J. Climatol.*, **11**, 1-25.

WMO Unesco, 1970: *Climatic Atlas of Europe*. Cartographia, Hungary, SC.69/C.8.

Yamada, T., S. Bunker, and M. Moss, 1992: Numerical simulations of atmospheric transport and diffusion over coastal complex terrain. *J. Appl. Meteor.*, **31**, 565-578.

Young, K. C., 1992: A three-way model for interpolating monthly precipitation values. *Mon. Wea. Rev.* **120**, 2561-2569.